

# **Journal of Mechanics of Materials and Structures**

**Volume 14, No. 4**

**July 2019**



# JOURNAL OF MECHANICS OF MATERIALS AND STRUCTURES

[msp.org/jomms](http://msp.org/jomms)

Founded by Charles R. Steele and Marie-Louise Steele

## EDITORIAL BOARD

ADAIR R. AGUIAR	University of São Paulo at São Carlos, Brazil
KATIA BERTOLDI	Harvard University, USA
DAVIDE BIGONI	University of Trento, Italy
MAENGHYO CHO	Seoul National University, Korea
HUILING DUAN	Beijing University
YIBIN FU	Keele University, UK
IWONA JASIUK	University of Illinois at Urbana-Champaign, USA
DENNIS KOCHMANN	ETH Zurich
MITSUTOSHI KURODA	Yamagata University, Japan
CHEE W. LIM	City University of Hong Kong
ZISHUN LIU	Xi'an Jiaotong University, China
THOMAS J. PENCE	Michigan State University, USA
GIANNI ROYER-CARFAGNI	Università degli studi di Parma, Italy
DAVID STEIGMANN	University of California at Berkeley, USA
PAUL STEINMANN	Friedrich-Alexander-Universität Erlangen-Nürnberg, Germany
KENJIRO TERADA	Tohoku University, Japan

## ADVISORY BOARD

J. P. CARTER	University of Sydney, Australia
D. H. HODGES	Georgia Institute of Technology, USA
J. HUTCHINSON	Harvard University, USA
D. PAMPLONA	Universidade Católica do Rio de Janeiro, Brazil
M. B. RUBIN	Technion, Haifa, Israel

## PRODUCTION [production@msp.org](mailto:production@msp.org)

SILVIO LEVY Scientific Editor


Cover photo: Mando Gomez, [www.mandolux.com](http://www.mandolux.com)

See [msp.org/jomms](http://msp.org/jomms) for submission guidelines.

JoMMS (ISSN 1559-3959) at Mathematical Sciences Publishers, 798 Evans Hall #6840, c/o University of California, Berkeley, CA 94720-3840, is published in 10 issues a year. The subscription price for 2019 is US \$635/year for the electronic version, and \$795/year (+\$60, if shipping outside the US) for print and electronic. Subscriptions, requests for back issues, and changes of address should be sent to MSP.

JoMMS peer-review and production is managed by EditFlow® from Mathematical Sciences Publishers.

PUBLISHED BY

 **mathematical sciences publishers**  
nonprofit scientific publishing

<http://msp.org/>

© 2019 Mathematical Sciences Publishers

## EXTENDED HIGHER-ORDER SANDWICH PANEL THEORY FOR PLATES WITH ARBITRARY ASPECT RATIOS

FAISAL SIDDIQUI AND GEORGE A. KARDOMATEAS

A new extended higher-order sandwich panel theory (EHSAPT) for orthotropic elastic sandwich plates is formulated. This new theory extends the one-dimensional extended higher-order sandwich panel beam theory to two dimensions and applies it to plate structures. In this theory, the compressibility of the soft core in the transverse direction is taken into consideration. The in-plane displacements are third-order and the transverse displacement is second-order in the transverse coordinate respectively. This arrangement allows the theory to take the axial, shear and transverse normal stresses in the core in consideration. In order to derive the governing equations and associated boundary conditions, eleven generalized coordinates are considered. Each face sheet has three generalized coordinates (two in-plane and one transverse displacement respectively) and the core has five generalized coordinates which include three displacements and two independent rotations. The governing equations and boundary conditions are derived using a variational approach such that all core/face sheet displacement compatibility conditions are satisfied.

### 1. Introduction

Typical sandwich panels consist of two metallic or composite thin face sheets separated by a honeycomb or foam core. This configuration gives the sandwich panel high stiffness and strength, and enables excellent energy absorption capabilities with little resultant weight penalty. This makes the sandwich structure a preferred material of choice in a lot of applications including aerospace, naval, wind turbines and civil industries. Many of the currently used methods of analysis on sandwich structures assume a noncompressible core and are categorized as the classical and the first-order shear models when shear effects are taken into consideration [Plantema 1966; Allen 1969]. The assumptions on these theories are only adequate if the core is made of a high-strength and stiff material; but in many cases when the core is a more compliant and softer material, the predictions from these theories become more and more inaccurate especially under quasistatic loading [Phan et al. 2012]. Experimental results have also shown that the core can undergo significant transverse deformation under a sudden impulsive load [Gardner et al. 2012; Jackson and Shukla 2011; Nemat-Nasser et al. 2007; Tekalur et al. 2009; Wang et al. 2009]. This implies that in order to get accurate results the transverse deformation and shear stresses in the core must be taken into consideration.

Keeping in view the importance of accurate prediction of failure modes, some of the recent computational models have considered transverse compressibility in the core. Frostig et al. [1992] proposed a theory for sandwich panels in which the resulting shear strain in the core is constant and the resulting

---

*Keywords:* Sandwich panel, plate, arbitrary aspect ratios, EHSAPT.

transverse normal strain in the core is linear in  $z$ ; however, this model was only formulated for a one-dimensional beam (HSAPT). Hohe et al. [2006] developed a model for sandwich plates in which the transverse normal strain is constant along the transverse coordinate  $z$ , and the shearing strains are first-order in  $z$ . Also, Li and Kardomateas [2008] explored a higher-order theory for plates in which the transverse normal strain in the core is of third-order in  $z$ , and the shear strains in the core are of fourth-order in  $z$ .

The accuracy of any of these models can be readily assessed because an elasticity solution already exists. Pagano [1970] presented a three-dimensional elasticity solution for laminated rectangular plates for the following cases:

- (1) *Orthotropic material*: the cubic characteristic equation has a negative discriminant and results in real and unequal roots.
- (2) *Isotropic material*: the cubic characteristic equation has a zero discriminant and results in real and equal roots.

Kardomateas [2008] then presented the solution for the case of positive discriminant, in which two of the roots are complex conjugates. This is actually a case frequently encountered in sandwich construction in which the orthotropic core is stiffer in the transverse direction than the in-plane directions.

In this paper we present an advanced new extended higher-order sandwich panel theory (EHSAPT), which is a two-dimensional extension of the EHSAPT beam model presented in [Phan et al. 2012]. In that reference the authors extended the HSAPT given in [Frostig et al. 1992] for beams, to allow for the transverse shear distribution in the core to acquire the proper distribution as the core stiffness increases as a result of nonnegligible in-plane stresses. The current paper extends the concept of Phan et al. [2012] and applies it to two-dimensional plate structures. The theory assumes a transverse displacement in the core that varies as a second-order equation in  $z$ , and in-plane displacements that are of third-order in  $z$ . The novelty of this approach is that it allows for five generalized coordinates in the core (the in-plane and transverse displacements and two independent rotations).

The theory is formulated for a sandwich panel with a symmetric layout. The major assumptions of the theory are as follows:

- (1) The face sheets satisfy the Kirchhoff assumptions, and their thicknesses are small compared with the overall thickness of the sandwich section; they undergo large displacements with moderate rotations.
- (2) The core is compressible in the transverse and axial directions (transverse displacement is second-order in  $z$  and in-plane displacements are third-order in  $z$ ); it has in-plane, transverse and shear rigidities; and it undergoes large displacements.
- (3) The bonding between the face sheets and core is assumed to be perfect.

## 2. Derivation of EHSAPT theory

We consider a sandwich plate with two identical face sheets of thickness  $f$  and a core of thickness  $2c$ . The cartesian coordinate system is placed in the middle plane of the sandwich plate as shown in Figure 1.

The corresponding displacements are denoted by  $(u, v, w)$ . Subscript  $t$ ,  $b$  and  $c$  refer to the top face sheet, bottom face sheet and core. Subscript 0 refers to the middle surface of the respective phase. The total thickness of the plate is given by  $h_{\text{tot}} = 2f + 2c$ .

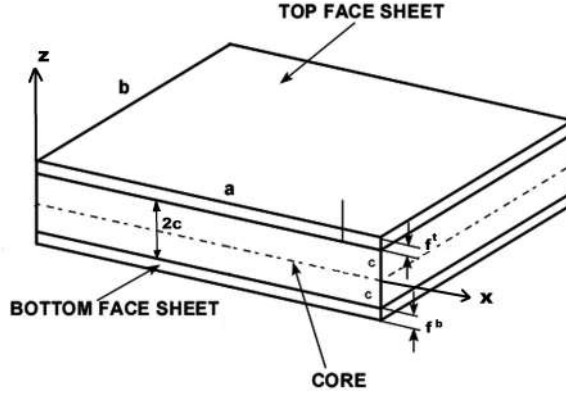


**Figure 1.** Geometric configuration of the plate.

**2A. Displacements and strains.** It is highlighted that the following functions depend on  $x$ ,  $y$ ,  $z$  and  $t$  and this functional dependence will not be explicitly written in the equations that follow in favor of conserving writing space:

$$\begin{aligned}
 u^{t,b,c} &= u^{t,b,c}(x, y, z, t), & u_0^{t,b,c} &= u_0^{t,b,c}(x, y, t), & \psi_0^c &= \psi_0^c(x, y, t), & u_2^c &= u_2^c(x, y, t), \\
 u_3^c &= u_3^c(x, y, t), \\
 v^{t,b,c} &= v^{t,b,c}(x, y, z, t), & v_0^{t,b,c} &= v_0^{t,b,c}(x, y, t), & \phi_0^c &= \phi_0^c(x, y, t), & v_2^c &= v_2^c(x, y, t), \\
 v_3^c &= v_3^c(x, y, t), \\
 w^{t,b,c} &= w^{t,b,c}(x, y, z, t), & w_1^c &= w_1^c(x, y, t), & w_2^c &= w_2^c(x, y, t).
 \end{aligned}$$

**2A.1. Displacements of the face sheets.** The face sheets are assumed to satisfy the Kirchhoff–Love assumptions and their thickness is assumed to be small as compared to the overall thickness of the plate. The displacements are represented as

$$u^t = u_0^t - \zeta^t w_{,x}^t, \quad (2-1a)$$

$$v^t = v_0^t - \zeta^t w_{,y}^t, \quad (2-1b)$$

$$w^t = w^t. \quad (2-1c)$$

Similarly, for the bottom face sheet,

$$u^b = u_0^b - \zeta^b w_{,x}^b, \quad (2-2a)$$

$$v^b = v_0^b - \zeta^b w_{,y}^b, \quad (2-2b)$$

$$w^b = w^b, \quad (2-2c)$$

where  $\zeta^{t,b} = z \mp (c + f^{t,b}/2)$ .



The nonlinear strain-displacement relations are

$$[\epsilon^{t,b}] = \begin{bmatrix} \epsilon_{xx}^{t,b} \\ \epsilon_{yy}^{t,b} \\ \gamma_{xy}^{t,b} \end{bmatrix} = [\epsilon_0] + \zeta [\kappa] = \begin{bmatrix} \epsilon_{0x} + \zeta \kappa_x \\ \epsilon_{0y} + \zeta \kappa_y \\ \gamma_{0xy} + \zeta \kappa_{xy} \end{bmatrix}, \quad (2-3a)$$

$$[\epsilon_0] = \begin{bmatrix} \epsilon_{0x} \\ \epsilon_{0y} \\ \gamma_{0xy} \end{bmatrix} = \begin{bmatrix} u_{0,x} + \frac{1}{2} w_{,x}^2 \\ v_{0,y} + \frac{1}{2} w_{,y}^2 \\ u_{0,y} + v_{0,x} + w_{,x} w_{,y} \end{bmatrix}. \quad (2-3b)$$

Moreover,  $[\kappa]$  is the curvature matrix and can be given as

$$[\kappa] = \begin{bmatrix} \kappa_x \\ \kappa_y \\ \kappa_{xy} \end{bmatrix} = \begin{bmatrix} -w_{,xx} \\ -w_{,yy} \\ -2w_{,xy} \end{bmatrix}. \quad (2-3c)$$

**2A.2. Displacements for the higher-order core.** First-order approximation of the classical sandwich panel theory neglects the transverse deformation of the core and leads to erroneous results in many practical cases. However, in many instances it becomes essential to capture the core compressibility effects and thus we use a higher-order definition of the in-plane and transverse deformation of the core in terms of the transverse coordinate:

$$u^c = u_0^c + \psi_0^c z + u_2^c z^2 + u_3^c z^3, \quad (2-4a)$$

$$v^c = v_0^c - \phi_0^c z + v_2^c z^2 + v_3^c z^3, \quad (2-4b)$$

$$w^c = w_0^c + w_1^c z + w_2^c z^2. \quad (2-4c)$$

In these equations  $u_0^c$ ,  $v_0^c$  and  $w_0^c$  are the in-plane and transverse displacements and  $\phi_0^c$  and  $\psi_0^c$  are the rotations about the  $x$ -axis and  $y$ -axis, respectively. Also,  $u_2^c$ ,  $u_3^c$ ,  $v_2^c$ ,  $v_3^c$ ,  $w_1^c$  and  $w_2^c$  are the in-plane and transverse unknown functions to be determined by enforcing displacement compatibility conditions at the core/face sheets interface. We therefore enforce compatibility at  $z = \pm c$  and after some algebraic calculations, the following core displacement field is obtained:

$$u^c = u_0^c + z\psi_0^c - \frac{z^3}{4c^3} [2u_0^b - 2u_0^t + 4c\psi_0^c - f^b w_{,x}^b - f^t w_{,x}^t] - \frac{z^2}{4c^2} [-2u_0^b - 2u_0^t + 4u_0^c + f^b w_{,x}^b - f^t w_{,x}^t], \quad (2-5a)$$

$$v^c = v_0^c - z\phi_0^c - \frac{z^3}{4c^3} [2v_0^b - 2v_0^t - 4c\phi_0^c - f^b w_{,y}^b - f^t w_{,y}^t] - \frac{z^2}{4c^2} [-2v_0^b - 2v_0^t + 4v_0^c + f^b w_{,y}^b - f^t w_{,y}^t], \quad (2-5b)$$

$$w^c = w_0^c - \frac{z^2}{2c^2} [-w^b - w^t + 2w_0^c] - \frac{z}{2c} [w^b - w^t]. \quad (2-5c)$$

It is highlighted that in developing their higher-order theories, Li and Kardomateas [2008] and Phan et al. [2012] assumed that the core undergoes large rotation with a small displacement and therefore

neglected the in-plane strains. However, the current theory does not make any such assumptions and we consider all six strains in the core. This leads to the following six strain-displacement relations for the core:

$$\begin{aligned} \epsilon_{xx}^c = & u_{0,x}^c + z\psi_{0,x}^c - \frac{z^3}{4c^3}[2u_{0,x}^b - 2u_{0,x}^t + 4c\psi_{0,x}^c - f^b w^b_{,xx} - f^t w^t_{,xx}] \\ & - \frac{z^2}{4c^2}[-2u_{0,x}^b + 4u_{0,x}^c - 2u_{0,x}^t + f^b w^b_{,xx} - f^t w^t_{,xx}]\psi_{0,x}^c, \quad (2-6a) \end{aligned}$$

$$\begin{aligned} \epsilon_{yy}^c = & v_{0,y}^c - z\phi_{0,y}^c - \frac{z^3}{4c^3}[2v_{0,y}^b - 2v_{0,y}^t - 4c\phi_{0,y}^c - f^b w^b_{,yy} - f^t w^t_{,yy}] \\ & - \frac{z^2}{4c^2}[-2v_{0,y}^b + 4v_{0,y}^c - 2v_{0,y}^t + f^b w^b_{,yy} - f^t w^t_{,yy}], \quad (2-6b) \end{aligned}$$

$$\epsilon_{zz}^c = -\frac{z}{c^2}[2w_0^c - w^b - w^t] - \frac{1}{2c}[w^b - w^t] \quad (2-6c)$$

$$\begin{aligned} \gamma_{xy}^c = & u_{0,y}^c + z\psi_{0,y}^c + v_{0,x}^c - z\phi_{0,x}^c - \frac{z^3}{4c^3}[2u_{0,y}^b - 2u_{0,y}^t + 4c\psi_{0,y}^c - f^b w^b_{,xy} - f^t w^t_{,xy}] \\ & - \frac{z^3}{4c^3}[2v_{0,x}^b - 2v_{0,x}^t - 4c\phi_{0,x}^c - f^b w^b_{,xy} - f^t w^t_{,xy}] \\ & - \frac{z^2}{4c^2}[-2u_{0,y}^b + 4u_{0,y}^c - 2u_{0,y}^t + f^b w^b_{,xy} - f^t w^t_{,xy}] \\ & - \frac{z^2}{4c^2}[-2v_{0,x}^b + 4v_{0,x}^c - 2v_{0,x}^t + f^b w^b_{,xy} - f^t w^t_{,xy}], \quad (2-6d) \end{aligned}$$

$$\begin{aligned} \gamma_{xz}^c = & \psi_0^c + w_{0,x}^c - \frac{z^2}{2c^2}[2w_{0,x}^c - w^b_{,x} - w^t_{,x}] - \frac{z}{2c}[w^b_{,x} - w^t_{,x}] \\ & - \frac{3z^2}{4c^3}[2u_0^b - 2u_0^t + 4c\psi_0^c - f^b w^b_{,x} - f^t w^t_{,x}] \\ & - \frac{z}{2c^2}[-2u_0^b + 4u_0^c - 2u_0^t + f^b w^b_{,x} - f^t w^t_{,x}], \quad (2-6e) \end{aligned}$$

$$\begin{aligned} \gamma_{yz}^c = & -\phi_0^c + w_{0,y}^c - \frac{z^2}{2c^2}[2w_{0,y}^c - w^b_{,y} - w^t_{,y}] - \frac{z}{2c}[w^b_{,y} - w^t_{,y}] \\ & - \frac{3z^2}{4c^3}[2v_0^b - 2v_0^t - 4c\phi_0^c - f^b w^b_{,y} - f^t w^t_{,y}] \\ & - \frac{z}{2c^2}[-2v_0^b + 4v_0^c - 2v_0^t + f^b w^b_{,y} - f^t w^t_{,y}]. \quad (2-6f) \end{aligned}$$

**2A.3. Constitutive relations.** We assume that the face sheets are composite laminates and the core is fully orthotropic. The stress-strain relations for the top and bottom sheets read as

$$\begin{bmatrix} \sigma_{xx}^{t,b} \\ \sigma_{yy}^{t,b} \\ \tau_{xy}^{t,b} \end{bmatrix} = \begin{bmatrix} C_{11}^{t,b} & C_{12}^{t,b} & C_{16}^{t,b} \\ C_{12}^{t,b} & C_{22}^{t,b} & C_{26}^{t,b} \\ C_{16}^{t,b} & C_{26}^{t,b} & C_{66}^{t,b} \end{bmatrix} \begin{bmatrix} \epsilon_{xx}^{t,b} \\ \epsilon_{yy}^{t,b} \\ \gamma_{xy}^{t,b} \end{bmatrix}, \quad (2-7a)$$

where  $C_{ij}$  ( $i, j = 1, 2, 6$ ) are the plane stress reduced stiffness coefficients. The core is considered to be

fully orthotropic:

$$\begin{bmatrix} \sigma_{xx}^c \\ \sigma_{yy}^c \\ \sigma_{zz}^c \\ \tau_{yz}^c \\ \tau_{xz}^c \\ \tau_{xy}^c \end{bmatrix} = \begin{bmatrix} C_{11}^c & C_{12}^c & C_{13}^c & 0 & 0 & 0 \\ C_{12}^c & C_{22}^c & C_{23}^c & 0 & 0 & 0 \\ C_{13}^c & C_{23}^c & C_{33}^c & 0 & 0 & 0 \\ 0 & 0 & 0 & C_{44}^c & 0 & 0 \\ 0 & 0 & 0 & 0 & C_{55}^c & 0 \\ 0 & 0 & 0 & 0 & 0 & C_{66}^c \end{bmatrix} \begin{bmatrix} \epsilon_{xx}^c \\ \epsilon_{yy}^c \\ \epsilon_{zz}^c \\ \gamma_{yz}^c \\ \gamma_{xz}^c \\ \gamma_{xy}^c \end{bmatrix}. \quad (2-7b)$$

Since the face sheets are laminated composite plates with the face sheets composed of multiple laminas, each fiber angle of an individual lamina can be chosen independently. The following constitutive relations are defined:

$$\chi(\theta) = \begin{bmatrix} 1 & 1 & \cos \theta & \cos 4\theta \\ 1 & 1 & -\cos \theta & \cos 4\theta \\ 1 & -1 & 0 & -\cos 4\theta \\ 0 & 1 & 0 & -\cos 4\theta \\ 0 & 0 & \frac{1}{2} \sin 2\theta & \sin 4\theta \\ 0 & 0 & \frac{1}{2} \sin 2\theta & -\sin 4\theta \end{bmatrix}. \quad (2-8)$$

Similarly, the following four material invariants are defined:

$$\begin{aligned} \alpha_1 &= \frac{E_1 + E_2 + 2\nu_{12}E_2}{4\alpha_0}, & \alpha_2 &= \frac{E_1 + E_2 - 2\nu_{12}E_2}{8\alpha_0} + \frac{G_{12}}{2}, \\ \alpha_3 &= \frac{E_1 - E_2}{2\alpha_0}, & \alpha_4 &= \frac{E_1 + E_2 - 2\nu_{12}E_2}{8\alpha_0} - \frac{G_{12}}{2}, \end{aligned}$$

where  $\alpha_0 = 1 - \nu_{12}E_2/E_1$ . Next, we define an array of the lamina stiffness coefficients such that

$$C = \{C_{11}, C_{22}, C_{12}, C_{66}, C_{16}, C_{26}\}^T. \quad (2-9)$$

We then define an array of the material invariants as

$$\alpha = \{\alpha_1, \alpha_2, \alpha_3, \alpha_4\}^T. \quad (2-10)$$

Therefore

$$[C(\theta)] = [\chi(\theta)]\{\alpha\}. \quad (2-11)$$

Hence depending upon the angle of individual laminas, the material coefficients for the face sheets are defined. Next, the stress and moment resultants for the facesheets are defined as

$$[N^{t,b}] = \begin{bmatrix} N_{xx}^{t,b} \\ N_{yy}^{t,b} \\ N_{xy}^{t,b} \end{bmatrix} = \begin{bmatrix} N_{xx}^{t,b^1} \\ N_{yy}^{t,b^1} \\ N_{xy}^{t,b^1} \end{bmatrix} + \begin{bmatrix} N_{xx}^{t,b^2} \\ N_{yy}^{t,b^2} \\ N_{xy}^{t,b^2} \end{bmatrix} = \int_c^{c+f^{t,b}/2} [\sigma^{t,b^1}] dz + \int_{c+f^{t,b}/2}^{c+f^{t,b}} [\sigma^{t,b^2}] dz. \quad (2-12)$$



Similarly

$$[M^{t,b}] = \begin{bmatrix} M_{xx}^{t,b} \\ M_{yy}^{t,b} \\ M_{xy}^{t,b} \end{bmatrix} = \begin{bmatrix} M_{xx}^{t,b^1} \\ M_{yy}^{t,b^1} \\ M_{xy}^{t,b^1} \end{bmatrix} + \begin{bmatrix} M_{xx}^{t,b^2} \\ M_{yy}^{t,b^2} \\ M_{xy}^{t,b^2} \end{bmatrix} = \int_c^{c+f^{t,b}/2} [\sigma^{t,b^1}] \zeta^{t,b} dz + \int_{c+f^{t,b}/2}^{c+f^{t,b}} [\sigma^{t,b^2}] \zeta^{t,b} dz. \quad (2-13)$$

For the core the following resultants are defined:

$$[N^c] = \begin{bmatrix} N_{xx}^c \\ N_{yy}^c \\ N_{zz}^c \\ N_{xy}^c \\ Q_x^c \\ Q_y^c \end{bmatrix} = \int_{-c}^c \begin{bmatrix} \sigma_{xx}^c \\ \sigma_{yy}^c \\ \sigma_{zz}^c \\ \sigma_{xy}^c \\ \sigma_{xz}^c \\ \sigma_{yz}^c \end{bmatrix} dz, \quad \text{for the core.} \quad (2-14a)$$

Similarly, the following resultants are also defined for the core:

$$\begin{bmatrix} M_{xx}^c \\ M_{yy}^c \\ M_{zz}^c \\ M_{xy}^c \\ M_{yz}^c \\ M_{xz}^c \end{bmatrix} = \int_{-c}^c \begin{bmatrix} \sigma_{xx}^c \\ \sigma_{yy}^c \\ \sigma_{zz}^c \\ \sigma_{xy}^c \\ \sigma_{yz}^c \\ \sigma_{xz}^c \end{bmatrix} z dz, \quad \begin{bmatrix} R_{xx}^c \\ R_{yy}^c \\ R_{xy}^c \\ R_{yz}^c \\ R_{xz}^c \end{bmatrix} = \int_{-c}^c \begin{bmatrix} \sigma_{xx}^c \\ \sigma_{yy}^c \\ \sigma_{xy}^c \\ \sigma_{yz}^c \\ \sigma_{xz}^c \end{bmatrix} z^2 dz, \quad \begin{bmatrix} P_{xx}^c \\ P_{yy}^c \\ P_{xy}^c \end{bmatrix} = \int_{-c}^c \begin{bmatrix} \sigma_{xx}^c \\ \sigma_{yy}^c \\ \sigma_{xy}^c \end{bmatrix} z^3 dz. \quad (2-14b)$$

Also

$$I_i = \int_{-h/2}^{h/2} \rho(z)^i dz \quad (i = 0, 1, 2, 3, \dots, 6). \quad (2-15)$$

**2B. Governing differential equations.** The governing differential equations and associated boundary conditions can be derived using the Hamilton's principle. The sandwich panel is subjected to a transverse load  $q(x, y, t)$  on the top and bottom face sheets. Let the strain energy be denoted by  $U$ , the kinetic energy by  $K$  and the external work by  $W$ . The variational principle states that

$$\delta[T - (U - W)] = 0, \quad (2-16)$$

in which the first variation of the energy functionals can be written as

$$\begin{aligned} \delta U = & \int_0^t \int_0^b \int_0^a \left[ \int_c^{c+f^t} (\sigma_{xx}^t \delta \epsilon_{xx}^t + \sigma_{yy}^t \delta \epsilon_{yy}^t + \tau_{xy}^t \delta \gamma_{xy}^t) dz \right. \\ & + \int_{-c}^c (\sigma_{xx}^c \delta \epsilon_{xx}^c + \sigma_{yy}^c \delta \epsilon_{yy}^c + \sigma_{zz}^c \delta \epsilon_{zz}^c + \tau_{xy}^c \delta \gamma_{xy}^c + \tau_{xz}^c \delta \gamma_{xz}^c + \tau_{yz}^c \delta \gamma_{yz}^c) dz \\ & \left. + \int_{-c-f^b}^{-c} (\sigma_{xx}^b \delta \epsilon_{xx}^b + \sigma_{yy}^b \delta \epsilon_{yy}^b + \tau_{xy}^b \delta \gamma_{xy}^b) dz \right] dx dy, \quad (2-17) \end{aligned}$$

$$\delta T = \int_0^t \int_0^b \int_0^a \left[ \int_c^{c+f^t} \rho^t (\dot{u}^t \delta \dot{u}^t + \dot{v}^t \delta \dot{v}^t + \dot{w}^t \delta \dot{w}^t) dz + \int_{-c}^c \rho^c (\dot{u}^c \delta \dot{u}^c + \dot{v}^c \delta \dot{v}^c + \dot{w}^c \delta \dot{w}^c) dz + \int_{-c-f^b}^{-c} \rho^b (\dot{u}^b \delta \dot{u}^b + \dot{v}^b \delta \dot{v}^b + \dot{w}^b \delta \dot{w}^b) dz \right] dx dy dt, \quad (2-18)$$

and the work done by external forces is

$$\delta W = \int_0^t \int_0^b \int_0^a q^t(x, y, t) \delta w^t + q^b(x, y, t) \delta w^b dx dy dt, \quad (2-19)$$

where  $\rho$  is the mass density and dot above the variables represents differentiation with respect to time;  $q^t(x, y, z)$  and  $q^b(x, y, z)$  are the distributed transverse load on top and bottom face sheets, respectively;  $\delta w^t$  and  $\delta w^b$  represents the virtual transverse displacements of top and bottom face sheets, respectively. Equating time derivatives equal to zero would recover the governing differential equations and associated boundary conditions for a static case.

**2B.1. Equations of motion.** The governing equations and associated boundary conditions can be obtained by substituting the strain-displacement relations ((2-3) and (2-6)) and stress-strain relations (2-7) in the first variations of the energy functionals. We make use of the stress and moment resultants defined by using (2-12), (2-13) and (2-14), respectively. We then employ Green's theorem to relieve the primary variables of derivatives. This results in eleven governing equations: three for each face sheet and five for the core. Also, boundary conditions are acquired as a result of the process:

$$\delta u_0^b : 4\alpha_2 M_{xz}^c - 6\alpha_3 R_{xz}^c - N_{xy,y}^b + 2\alpha_3 P_{xy,y}^c - 2\alpha_2 R_{xy,y}^c - N_{xx,x}^b + 2\alpha_3 P_{xx,x}^c - 2\alpha_2 R_{xx,x}^c + \beta_1 \ddot{u}_0^b - 2\beta_2 \ddot{u}_0^c + 4\beta_3 \ddot{u}_0^t + 2\beta_5 \ddot{\psi}_0^c - \beta_4 \ddot{w}_{,x}^b + 2f^t \beta_3 \ddot{w}_{,x}^t = 0, \quad (2-20a)$$

$$\delta v_0^b : 4\alpha_2 M_{yz}^c - 6\alpha_3 R_{yz}^c - N_{yy,y}^b + 2\alpha_3 P_{yy,y}^c - 2\alpha_2 R_{yy,y}^c - N_{xy,x}^b + 2\alpha_3 P_{xy,x}^c - 2\alpha_2 R_{xy,x}^c + \beta_1 \ddot{v}_0^b + 2\beta_2 \ddot{v}_0^c + 4\beta_3 \ddot{v}_0^t - 2\beta_5 \ddot{\phi}_0^c - \beta_4 \ddot{w}_{,y}^b + 2f^t \beta_3 \ddot{w}_{,y}^t = 0, \quad (2-20b)$$

$$\begin{aligned} \delta w^b : 4\alpha_2 M_{zz}^c - \alpha_1 N_{zz}^c + (\alpha_1 + 2f^b \alpha_2)(M_{xz,x}^c + M_{yz,y}^c) - 2M_{xy,xy}^b - M_{xx,xx}^b \\ + f^b \alpha_3 (P_{xx,xx}^c + P_{yy,yy}^c + 2P_{xy,xy}^c) - f^b \alpha_2 (R_{xx,xx}^c + R_{yy,yy}^c + 2R_{xy,xy}^c) \\ - R_{xz,x}^c (2\alpha_2 + 3f^b \alpha_3) + \beta_6 \ddot{w}^b - \beta_7 \ddot{w}_0^c - \beta_8 \ddot{w}^t + \beta_4 (\ddot{u}_{0,x}^b + \ddot{v}_{0,y}^b) \\ + f^b \beta_2 (\ddot{u}_{0,x}^c + \ddot{v}_{0,y}^c) + 2f^b \beta_3 (\ddot{u}_{0,x}^t + \ddot{v}_{0,y}^t) + f^b \beta_5 (\ddot{\psi}_{0,x}^c - \ddot{\phi}_{0,y}^c) \\ + f^b f^t \beta_3 (\ddot{w}_{,xx}^t + \ddot{w}_{,yy}^t) - \beta_9 (\ddot{w}_{,xx}^b + \ddot{w}_{,yy}^b) = q^b[x, y, t], \end{aligned} \quad (2-20c)$$

$$\delta u_0^t : 4\alpha_2 M_{xz}^c + 6\alpha_3 R_{xz}^c - N_{xy,y}^t - 2\alpha_3 P_{xy,y}^c - 2\alpha_2 R_{xy,y}^c - N_{xx,x}^t - 2\alpha_3 P_{xx,x}^c - 2\alpha_2 R_{xx,x}^c + 4\beta_3 \ddot{u}_0^b + 2\xi_2 \ddot{u}_0^c + \xi_1 \ddot{u}_0^t + 2\xi_5 \ddot{\psi}_0^c - 2f^b \beta_3 \ddot{w}_{,x}^b + \xi_4 \ddot{w}_{,x}^t = 0, \quad (2-20d)$$

$$\delta v_0^t : 4\alpha_2 M_{yz}^c + 6\alpha_3 R_{yz}^c - N_{yy,y}^t - 2\alpha_3 P_{yy,y}^c - 2\alpha_2 R_{yy,y}^c - N_{xy,x}^t - 2\alpha_3 P_{xy,x}^c - 2\alpha_2 R_{xy,x}^c + 4\beta_3 \ddot{v}_0^b + 2\xi_2 \ddot{v}_0^c + \xi_1 \ddot{v}_0^t - 2\xi_5 \ddot{\phi}_0^c - 2f^b \beta_3 \ddot{w}_{,y}^b + \xi_4 \ddot{w}_{,y}^t = 0, \quad (2-20e)$$

$$\begin{aligned}
\delta w^t : \quad & 4\alpha_2 M_{zz}^c + \alpha_1 N_{zz}^c - (\alpha_1 + 2f^t \alpha_2)(M_{yz,y}^c - M_{xz,x}^c) - 2M_{xy,xy}^t - M_{xx,xx}^t \\
& + f^t \alpha_3 (P_{yy,yy}^c + P_{xx,xx}^c + 2P_{xy,xy}^c) + f^t \alpha_2 (R_{yy,yy}^c + 2R_{xy,xy}^c + R_{xx,xx}^c) \\
& - R_{xz,x}^c (2\alpha_2 + 3\alpha_3 f^t) - \beta_8 \ddot{w}^b + \xi_7 \ddot{w}_0^c + \xi_6 \ddot{w}^t + f^b f^t \beta_3 (\ddot{w}_{,yy}^b + \ddot{w}_{,xx}^b) \\
& - 2f^t \beta_3 (\ddot{w}_{0,x}^b + \ddot{w}_{0,x}^b) - f^t \xi_2 (\ddot{w}_{0,x}^c + \ddot{v}_{0,y}^c) - \xi_4 (\ddot{w}_{0,x}^t + \ddot{v}_{0,y}^t) \\
& - f^t \xi_5 (\ddot{\phi}_{0,y}^c + \ddot{\psi}_{0,x}^c) - \xi_9 (\ddot{w}_{,yy}^t + \ddot{w}_{,xx}^b) = q^t[x, y, t], \quad (2-20f)
\end{aligned}$$

$$\begin{aligned}
\delta u_0^c : \quad & 8\alpha_2 M_{xz}^c + N_{xy,y}^c - 4\alpha_2 R_{xy,y}^c + N_{xx,x}^c - 4\alpha_2 R_{xx,x}^c - 2\beta_2 \ddot{u}_0^b - \Delta_1 \ddot{u}_0^c - 2\beta_2 \ddot{u}_0^t \\
& - \Delta_2 \ddot{\psi}_0^c + \beta_2 f^b \ddot{w}_{,x}^b - \beta_2 f^t \ddot{w}_{,x}^t = 0, \quad (2-20g)
\end{aligned}$$

$$\begin{aligned}
\delta v_0^c : \quad & 8\alpha_2 M_{yz}^c + N_{yy,y}^c - 4\alpha_2 R_{yy,y}^c + N_{xy,x}^c - 4\alpha_2 R_{xy,x}^c - 2\beta_2 \ddot{v}_0^b - \Delta_1 \ddot{v}_0^c - 2\beta_2 \ddot{v}_0^t \\
& + \Delta_2 \ddot{\phi}_0^c + \beta_3 f^b \ddot{w}_{,y}^b - \beta_3 f^t \ddot{w}_{,y}^t = 0, \quad (2-20h)
\end{aligned}$$

$$\delta w_0^c : \quad 8\alpha_2 M_{zz}^c + Q_{y,y}^c - 4\alpha_2 R_{yz,y}^c + Q_{x,x}^c - 4\alpha_2 R_{xz,x}^c + \beta_7 \ddot{w}^b - \Delta_1 \ddot{w}_0^c - \xi_7 \ddot{w}^t = 0, \quad (2-20i)$$

$$\begin{aligned}
\delta \phi_0^c : \quad & -Q_y^c + 12R_{yz}^c - M_{xy,x}^c + M_{yy,y}^c - 4\alpha_2 P_{yy,y}^c - 4\alpha_2 P_{xy,x}^c - 2\beta_5 \ddot{v}_0^b - \Delta_2 \ddot{v}_0^c \\
& + 2\xi_5 \ddot{v}_0^t + \Delta_4 \ddot{\phi}_0^c + f^b \beta_5 \ddot{w}_{,y}^b + f^t \xi_5 \ddot{w}_{,y}^t = 0, \quad (2-20j)
\end{aligned}$$

$$\begin{aligned}
\delta \psi_0^c : \quad & Q_x^c - 12R_{xz}^c - M_{xy,y}^c - M_{xx,x}^c + 4\alpha_2 P_{xx,x}^c + 4\alpha_2 P_{xy,y}^c + 2\beta_5 \ddot{u}_0^b + \Delta_2 \ddot{u}_0^c \\
& + 2\xi_5 \ddot{u}_0^t + \Delta_4 \ddot{\psi}_0^c - f^b \beta_5 \ddot{w}_{,x}^b + f^t \xi_5 \ddot{w}_{,x}^t = 0, \quad (2-20k)
\end{aligned}$$

where  $\alpha_1 = 1/2c$ ,  $\alpha_2 = 1/4c^2$ ,  $\alpha_3 = 1/4c^3$ , and

$$\begin{aligned}
\beta_1 &= \frac{4c^6 I_0^b + c^2 I_4^c - 2c I_5^c + I_6^c}{4c^6}, \quad \beta_2 = \frac{c^4 I_2^c - c^3 I_3^c - c^2 I_4^c + c I_5^c}{4c^6}, \quad \beta_3 = \frac{c^2 I_4^c - I_6^c}{16c^6}, \\
\beta_4 &= \frac{8c^7 I_0^b + 4c^6 f^b I_0^b + 8c^6 I_1^b + c^2 f^b I_4^c - 2c f^b I_5^c + f^b I_6^c}{8c^6}, \quad \beta_5 = \frac{c^3 I_3^c - c^2 I_4^c - c I_5^c + I_6^c}{4c^5}, \\
\beta_6 &= \frac{4c^4 I_0^b + c^2 I_2^c - 2c I_3^c + I_4^c}{4c^4}, \quad \beta_7 = \frac{c^3 I_1^c - c^2 I_2^c - c I_3^c + I_4^c}{2c^4}, \quad \beta_8 = \frac{c^2 I_2^c - I_4^c}{4c^4}, \\
\beta_9 &= \frac{16c^8 I_0^b + 16c^7 f^b I_0^b + 4c^6 f^b I_1^b + 32c^7 I_1^b + 16c^6 f^b I_1^b + 16c^6 I_2^b + c^2 f^b I_4^c - 2c f^b I_5^c + f^b I_6^c}{16c^6}, \\
\Delta_1 &= \frac{c^4 I_0^c - 2c^2 I_2^c + I_4^c}{c^4}, \quad \Delta_2 = \frac{c^4 I_1^c - 2c^2 I_3^c + I_5^c}{c^4}, \quad \Delta_4 = \frac{c^4 I_2^c - 2c^2 I_4^c + I_6^c}{c^4}, \\
\xi_1 &= \frac{4c^6 I_0^t + c^2 I_4^c + 2c I_5^c + I_6^c}{4c^6}, \quad \xi_2 = \frac{c^4 I_2^c + c^3 I_3^c - c^2 I_4^c - c I_5^c}{4c^6}, \\
\xi_4 &= \frac{8c^7 I_0^t + 4c^6 f^t I_0^t - 8c^6 I_1^t + c^2 f^t I_4^c + 2c f^t I_5^c + f^t I_6^c}{8c^6},
\end{aligned}$$

$$\xi_5 = \frac{c^4 I_3^c + c^3 I_4^c - c^2 I_5^c - c I_6^c}{4c^6}, \quad \xi_6 = \frac{4c^4 I_0^t + c^2 I_2^c + 2c I_3^c + I_4^c}{4c^6}, \quad \xi_7 = \frac{c^3 I_1^c + c^2 I_2^c - c I_3^c - I_4^c}{2c^4},$$

$$\xi_9 = \frac{16c^8 I_0^t + 16c^7 f^t I_0^t + 4c^6 f^{t^2} I_0^t - 32c^7 I_1^t - 16c^6 I_1^t + 16c^6 I_2^b + c^2 f^{t^2} I_4^c + 2c f^{t^2} I_5^c + f^{t^2} I_6^c}{16c^6}.$$

The associated boundary conditions at  $x = 0, a$  read as

$$\begin{aligned} u_0^b &= \tilde{u}^b, & \text{or} & \quad \tilde{N}_{xx}^b = N_{xx}^b - 2\alpha_3 P_{xx}^c + 2\alpha_2 R_{xx}^c, \\ u_0^c &= \tilde{u}^c, & \text{or} & \quad \tilde{N}_{xx}^c = N_{xx}^c - 4\alpha_2 R_{xx}^c, \\ u_0^t &= \tilde{u}^t, & \text{or} & \quad \tilde{N}_{xx}^t = N_{xx}^t + 2\alpha_3 P_{xx}^c + 2\alpha_2 R_{xx}^c, \\ v_0^b &= \tilde{v}^b, & \text{or} & \quad \tilde{N}_{yy}^b = N_{yy}^b - 2\alpha_3 P_{xy}^c + 2\alpha_2 R_{xy}^c, \\ v_0^c &= \tilde{v}^c, & \text{or} & \quad \tilde{N}_{yy}^c = N_{yy}^c - 4\alpha_2 R_{xy}^c, \\ v_0^t &= \tilde{v}^t, & \text{or} & \quad \tilde{N}_{yy}^t = N_{yy}^t + 2\alpha_3 P_{xy}^c + 2\alpha_2 R_{xy}^c, \\ w^b &= \tilde{w}^b, & \text{or} & \quad \tilde{Q}_x^b = -\alpha_1 M_{xz}^c - 2\alpha_2 f^b M_{xz}^c + 2\alpha_2 R_{xz}^c + 3\alpha_3 f^b R_{xz}^c - \beta_4 \ddot{u}_0^b - f^b \beta_2 \ddot{u}_0^c \\ & & & \quad - 2\beta_3 f^b \ddot{u}_0^t - \beta_5 \ddot{\psi}_0^c + M_{xy,y}^b - f^b \alpha_3 P_{xy,y}^c + \alpha_2 f^b R_{xy,y}^c \\ & & & \quad + M_{xx,x}^b - \alpha_3 f^b P_{xx,x}^c + \alpha_2 f^b R_{xx,x}^c + \beta_9 \ddot{w}_{,x}^b + f^b f^t \beta_3 \ddot{w}_{,x}^t, \\ w^{b,y} &= \tilde{w}_{,y}^b, & \text{or} & \quad \tilde{M}_{xy}^b = -M_{xy}^b + \alpha_3 f^b P_{xy}^c - \alpha_2 f^b R_{xy}^c, \\ w_0^c &= \tilde{w}^c, & \text{or} & \quad \tilde{Q}_x^c = Q_x^c - 4\alpha_2 R_{xz}^c, \\ \psi_0^c &= \tilde{\psi}_0^c, & \text{or} & \quad \tilde{M}_{xx}^c = M_{xx}^c - 4\alpha_2 P_{xx}^c, \\ \phi_0^c &= \tilde{\phi}_0^c, & \text{or} & \quad \tilde{M}_{xy}^c = -M_{xy}^c + 4\alpha_2 P_{xy}^c, \\ w^t &= \tilde{w}^t, & \text{or} & \quad \tilde{Q}_x^t = \alpha_1 M_{xz}^c + 2\alpha_2 f^t M_{xz}^c + 2\alpha_2 R_{xz}^c + 3\alpha_3 f^t R_{xz}^c + 2f^t \beta_3 \ddot{u}_0^b + f^t \xi_2 \ddot{u}_0^c \\ & & & \quad + \xi_4 \ddot{u}_0^t + \xi_5 \ddot{\psi}_0^c + M_{xy,y}^t - f^t \alpha_3 P_{xy,y}^c - f^t \alpha_2 R_{xy,y}^c \\ & & & \quad + M_{xx,x}^t - f^t \alpha_3 P_{xx,x}^c - f^t \alpha_2 R_{xx,x}^c - f^b f^t \beta_3 \ddot{w}_{,x}^b + \xi_9 \ddot{w}_{,x}^t, \\ w^{t,y} &= \tilde{w}_{,y}^t, & \text{or} & \quad \tilde{M}_{xy}^t = -M_{xy}^t + \alpha_3 f^t P_{xy}^c + \alpha_2 f^t R_{xy}^c, \end{aligned}$$

where the tilde accent denotes the known external boundary values. Similar equations can be written for  $y = 0, b$ .

### 3. Conclusion

In this paper, a new higher order sandwich panel plate theory (EHSAPT) is presented. This is a two dimensional extension of the one dimensional theory presented in [Phan et al. 2012]. In this derivation both the core compressibility effects and the core shear stresses are considered, the theory also allows for nonzero axial stresses in the core. In order to capture all these effects, eleven generalized coordinates are defined with five generalized coordinates for the core and three each for the two face sheets. The equations are derived using a variational approach and associated boundary conditions are presented.

## References

- [Allen 1969] H. J. Allen, *Analysis and design of structural sandwich panels*, Pergamon, Oxford, 1969.
- [Frostig et al. 1992] Y. Frostig, M. Baruch, O. Vilnay, and I. Sheinman, “High-order theory for sandwich-beam behavior with transversely flexible core”, *J. Eng. Mech. (ASCE)* **118**:5 (1992), 1026–1043.
- [Gardner et al. 2012] N. Gardner, E. Wang, P. Kumar, and A. Shukla, “Blast mitigation in a sandwich composite using graded core and polyurea interlayer”, *Exp. Mech.* **52**:2 (2012), 119–133.
- [Hohe et al. 2006] J. Hohe, L. Librescu, and S. Y. Oh, “Dynamic buckling of flat and curved sandwich panels with transversely compressible core”, *Compos. Struct.* **74**:1 (2006), 10–24.
- [Jackson and Shukla 2011] M. Jackson and A. Shukla, “Performance of sandwich composites subjected to sequential impact and air blast loading”, *Compos. B Eng.* **42**:2 (2011), 155–166.
- [Kardomateas 2008] G. A. Kardomateas, “Three-dimensional elasticity solution for sandwich plates with orthotropic phases: the positive discriminant case”, *J. Appl. Mech. (ASME)* **76**:1 (2008), art. id. 014505.
- [Li and Kardomateas 2008] R. Li and G. A. Kardomateas, “Nonlinear high-order core theory for sandwich plates with orthotropic phases”, *AIAA J.* **46**:11 (2008), 2926–2934.
- [Nemat-Nasser et al. 2007] S. Nemat-Nasser, W. J. Kang, J. D. McGee, W.-G. Guo, and J. B. Isaacs, “Experimental investigation of energy-absorption characteristics of components of sandwich structures”, *Int. J. Impact Eng.* **34**:6 (2007), 1119–1146.
- [Pagano 1970] N. J. Pagano, “Exact solutions for rectangular bidirectional composites and sandwich plates”, *J. Compos. Mater.* **4**:1 (1970), 20–34.
- [Phan et al. 2012] C. N. Phan, Y. Frostig, and G. A. Kardomateas, “Analysis of sandwich beams with a compliant core and with in-plane rigidity: extended high-order sandwich panel theory versus elasticity”, *J. Appl. Mech. (ASME)* **79**:4 (2012), art. id. 041001.
- [Plantema 1966] F. J. Plantema, *Sandwich construction: the bending and buckling of sandwich beams, plates, and shells*, Wiley, New York, 1966.
- [Tekalur et al. 2009] S. A. Tekalur, A. E. Bogdanovich, and A. Shukla, “Shock loading response of sandwich panels with 3-D woven E-glass composite skins and stitched foam core”, *Compos. Sci. Technol.* **69**:6 (2009), 736–753.
- [Wang et al. 2009] E. Wang, N. Gardner, and A. Shukla, “The blast resistance of sandwich composites with stepwise graded cores”, *Int. J. Solids Struct.* **46**:18–19 (2009), 3492–3502.

Received 27 Nov 2018. Revised 25 Apr 2019. Accepted 4 Jun 2019.

FAISAL SIDDIQUI: [faisals@gatech.edu](mailto:faisals@gatech.edu)

Georgia Institute of Technology, Atlanta, GA, United States

GEORGE A. KARDOMATEAS: [george.kardomateas@aerospace.gatech.edu](mailto:george.kardomateas@aerospace.gatech.edu)

Georgia Institute of Technology, Atlanta, GA, United States



# APPLICATIONS OF EXTENDED HIGHER ORDER SANDWICH PANEL THEORY FOR PLATES WITH ARBITRARY ASPECT RATIOS

FAISAL SIDDIQUI AND GEORGE A. KARDOMATEAS

In this paper, solutions for a transversely loaded simply supported case with several different plate configurations based on extended higher-order sandwich panel theory (EHSAPT) are outlined and numerical results are presented. The results are also compared to established elasticity solutions and validation of EHSAPT for plates of arbitrary aspect ratios is made. The results are also compared to existing classical and first-order shear models for completeness. The results show excellent agreement both for displacements and stresses through the core. Analytical formulations and solutions to the natural frequency analysis of simply supported composite sandwich plates are also presented. The effects of variation of geometrical parameters of the structure on the natural frequency are also studied.

## 1. Introduction

This paper deals with the application of extended higher-order sandwich panel theory for plates with arbitrary aspect ratios derived in the companion paper [SK 2019]. The face sheets are made up of two individual laminas, each of which can have different layouts. The results have been presented for a transversely loaded simply supported sandwich panel, for static and dynamic cases, and are then compared to the classical model, the first order shear model [Plantema 1966; Allen 1969] and elasticity solutions [Kardomateas and Phan 2011; Kardomateas 2008; Noor 1973]. After establishing accuracy of the theory we then study the effects of varying certain geometric parameters on the fundamental natural frequency of the structure.

SK [2019] proposed an extended higher-order sandwich panel theory for sandwich plates with arbitrary aspect ratios considering a transverse displacement in the core that varies as a second-order equation in  $z$  and the in-plane displacements that are of third order in  $z$ , the transverse coordinate.

A higher-order sandwich panel theory (HSAPT) for one-dimensional beam was proposed in [Frostig et al. 1992], which considers the shear strain in the core to be constant while the resulting normal strain in the core is linear in  $z$ . Another model presented by Hohe et al. [2006] for sandwich plate considers the resulting transverse normal strain as constant in the transverse coordinate,  $z$ , while the shear strains are first order in  $z$ . Another higher-order theory proposed by Li and Kardomateas [2008] considers the transverse normal strain as third order in  $z$ , and the shear strains as fourth order in the transverse coordinate. Phan et al. [2012] extended the HSAPT theory [Frostig et al. 1992] for beams that allows for the transverse shear distribution in the core to acquire the proper distribution as the core stiffness increases as a result of nonnegligible in-plane stresses. The HSAPT model is incapable of capturing the in-plane stresses and assumes negligible in-plane rigidity. The current research extends that concept and applies it to two-dimensional plate structures with variable aspect ratios. This approach allows for five

*Keywords:* sandwich panel, plate, arbitrary aspect ratio, EHSAPT.



generalized coordinates in the core. Noor [1973] presented an exact three dimensional elasticity solution for the free vibration analysis of isotropic, orthotropic and anisotropic composite laminated plates which serves as a benchmark for comparison with these extended higher order theories.

## 2. Application of EHSAPT to a simply supported sandwich plate: static case

We consider a sandwich plate with two identical face sheets of thickness  $f$  and a core of thickness  $2c$  respectively. The cartesian coordinate system is placed in the middle plane of the sandwich plate as shown in Figure 1. The corresponding displacements are denoted  $(u, v, w)$ . The subscripts  $t, b$  and  $c$  refer to the top face sheet, bottom face sheet and the core respectively. Similarly, the subscript 0 refers to the middle surface of the respective phase. The total thickness of the plate is given by  $h_{\text{tot}} = 2f + 2c$ .

In order to compare the results of EHSAPT with other available theories, the case of a simply supported plate will be studied. The following boundary conditions are applied [SK 2019]: For  $x = 0, a$ ,

$$u_0^t = u_0^c = u_0^b = 0, \quad v_0^t = v_0^c = v_0^b = 0, \quad w^t = w_0^c = w^b = 0, \quad \tilde{M}^t = \tilde{M}^c = \tilde{M}^b = 0. \quad (2-1)$$

Similar boundary conditions can be written for the other two ends of the plate at  $y = 0, b$ .

The displacements can be written in the form

$$u_0^t = U^T \cos \frac{m\pi x}{a} \sin \frac{n\pi y}{b}, \quad u_0^c = U^C \cos \frac{m\pi x}{a} \sin \frac{n\pi y}{b}, \quad u_0^b = U^B \cos \frac{m\pi x}{a} \sin \frac{n\pi y}{b}, \quad (2-2a)$$

$$v_0^t = V^T \sin \frac{m\pi x}{a} \cos \frac{n\pi y}{b}, \quad v_0^c = V^C \sin \frac{m\pi x}{a} \cos \frac{n\pi y}{b}, \quad v_0^b = V^B \sin \frac{m\pi x}{a} \cos \frac{n\pi y}{b}, \quad (2-2b)$$

$$w^t = W^T \sin \frac{m\pi x}{a} \sin \frac{n\pi y}{b}, \quad w_0^c = W^C \sin \frac{m\pi x}{a} \sin \frac{n\pi y}{b}, \quad w^b = W^B \sin \frac{m\pi x}{a} \sin \frac{n\pi y}{b}, \quad (2-2c)$$

$$\phi = \Phi \sin \frac{m\pi x}{a} \cos \frac{n\pi y}{b}, \quad \psi = \Psi \cos \frac{m\pi x}{a} \sin \frac{n\pi y}{b}. \quad (2-2d)$$

Here  $U^T, U^C, U^B, V^T, V^C, V^B, W^T, W^C, W^B, \Phi$  and  $\Psi$  are constants to be determined. Substituting equations (2-2) into the governing differential equations [SK 2019] results in a system of eleven equations for the eleven unknown constants:  $U^T, U^C, U^B, V^T, V^C, V^B, W^T, W^C, W^B, \Phi$  and  $\Psi$ .

**2A. Numerical results and case study.** In this section, we present the numerical results for several typical sandwich configurations. The results are compared to the classical model, the first-order shear model and established elasticity solutions. In the following we assume a sinusoidal transverse loading

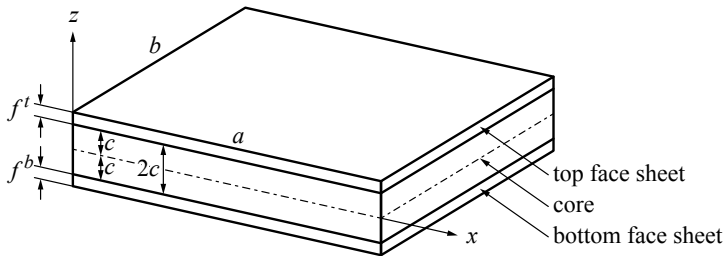


**Figure 1.** Geometric configuration of the plate.

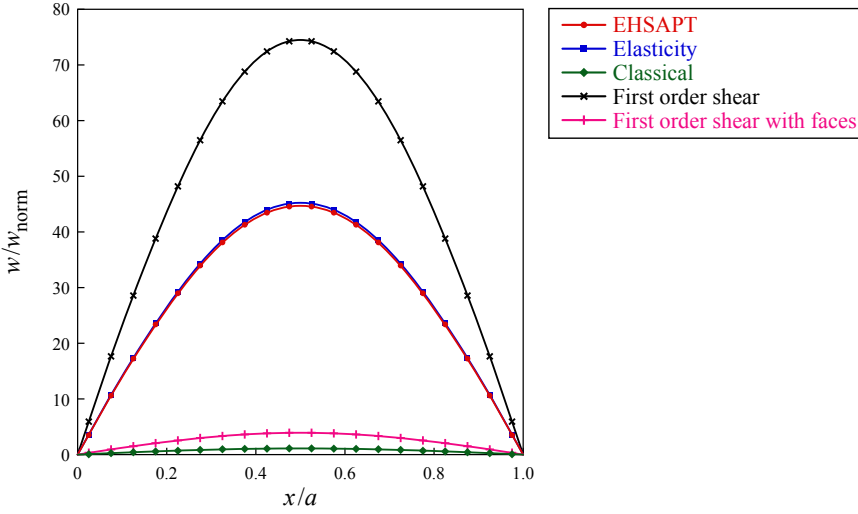


**Figure 2.** Transverse displacement  $w^t$  at the top face  $z = c + f^t$  at  $y = \frac{1}{2}b$  for  $a = b = 5h_{\text{tot}}$ .

on the top face sheet of the form

$$q(x, y) = q_0 \sin \frac{\pi x}{a} \sin \frac{\pi y}{b}, \quad 0 \leq x \leq a, \quad 0 \leq y \leq b, \quad (2-3)$$

where  $q_0$  is the magnitude of the load applied which is taken to be  $10^6$ . Let us consider a sandwich configuration consisting of unidirectional graphite/epoxy faces with moduli (in GPa) of  $E_1^f = 181.0$ ,  $E_2^f = E_3^f = 10.3$ ,  $G_{12}^f = G_{31}^f = 7.17$  and  $G_{23}^f = 5.96$  and Poisson's ratio of  $\nu_{12}^f = 0.277$ ,  $\nu_{31}^f = 0.016$  and  $\nu_{32}^f = 0.4$ . The core is made up of hexagonal glass/phenolic honeycomb with moduli (in GPa) of  $E_1^c = E_2^c = 0.032$ ,  $E_3^c = 0.300$ ,  $G_{23}^c = G_{31}^c = 0.048$ , and  $G_{12}^c = 0.013$  and Poisson's ratio of  $\nu_{12}^c = \nu_{31}^c = \nu_{32}^c = 0.250$ .

The two face sheets are assumed to be identical with a thickness of  $f_t = f_b = f = 2$  mm. The core thickness is  $2c = 16$  mm. The total thickness of the plate is defined to be  $h_{\text{tot}} = 2f + 2c$ . In the following results, the displacements are normalized with  $100 \times h_{\text{tot}} q_0 / E_1^f$  and the normal stresses with  $q_0 a^2 / h_{\text{tot}}^2$ .

Two plate configurations are considered with  $a = b = 5h_{\text{tot}}$  and  $a = b = 20h_{\text{tot}}$  respectively. Plotted in Figure 2 is the normalized displacement at the top face sheet as a function of  $x$  at  $y = \frac{1}{2}b$ . In this figure we also show the predictions of the classical plate theory as well as the first-order shear theories; for the latter, there are two versions: one that is based only on the core shear stiffness and one that includes the face sheet stiffnesses. From Figure 2, we can see that both the classical and the first-order shear theories seem to be inadequate. The classical theory is too nonconservative and can sometimes hardly make any difference. On the other hand, the first-order shear theory where shear is assumed to be carried exclusively by the core is too conservative; this clearly demonstrates the need for higher-order theories in dealing with sandwich plate structures. In this regard the EHSAPT theory gives a profile which is essentially identical to the elasticity solution. In Figure 2 we can also see the effect of transverse shear, which is an important feature of sandwich structures.

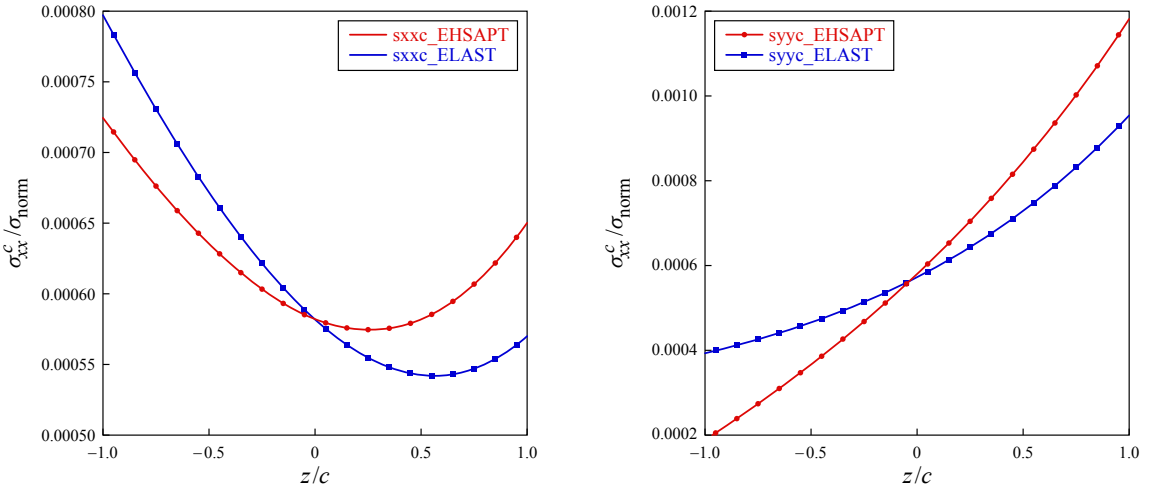


**Figure 3.** Through-thickness distribution in the core of the axial stress:  $\sigma_{xx}$  (left) and  $\sigma_{yy}$  (right) at  $x = \frac{1}{2}a$  and  $y = \frac{1}{2}b$ ; case of  $a = b = 5h_{\text{tot}}$ .

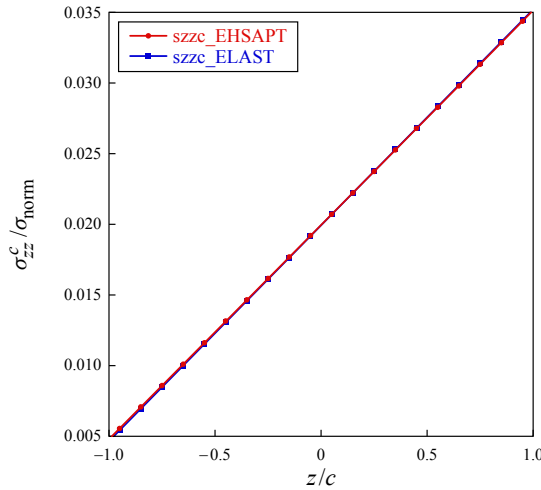


**Figure 4.** Through-thickness distribution in the core of the transverse normal stress  $\sigma_{zz}$  at  $x = \frac{1}{2}a$  and  $y = \frac{1}{2}b$ ; case of  $a = b = 5h_{\text{tot}}$ .

The distribution of the axial stresses  $\sigma_{xx}$  and  $\sigma_{yy}$  in the core as a function of  $z$  at the midspan location,  $x = \frac{1}{2}a$  and  $y = \frac{1}{2}b$  (where the bending moment is maximum) is plotted in Figure 3. Note that for both elasticity and the extended high-order theory, there is no symmetry with regard to the midplane ( $z = 0$ ).

The through-thickness distribution of the transverse normal stress in the core,  $\sigma_{zz}$ , at the midspan location,  $x = \frac{1}{2}a$  and  $y = \frac{1}{2}b$ , is shown in Figure 4. It can be seen that the elasticity curve is in perfect agreement with the EHSAPT curve and both are nearly linear.

Plotted in Figures 5, 6 and 7 are the normalized displacement, axial stresses and the transverse normal stress respectively for the case of  $a = b = 20h_{\text{tot}}$ .

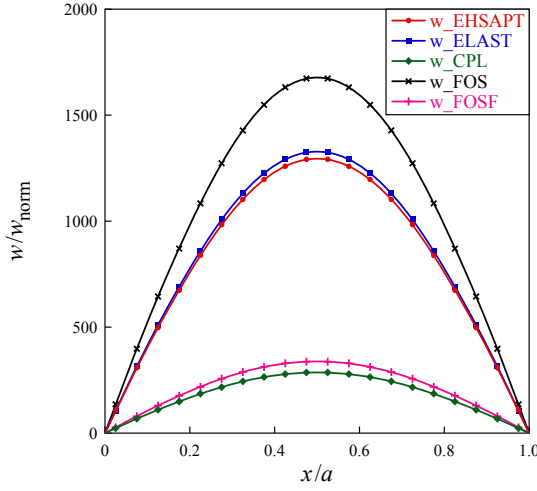


**Figure 5.** Transverse displacement  $w^t$  at the top face  $z = c + f^t$  at  $y = \frac{1}{2}b$  for  $a = b = 20h_{\text{tot}}$ .

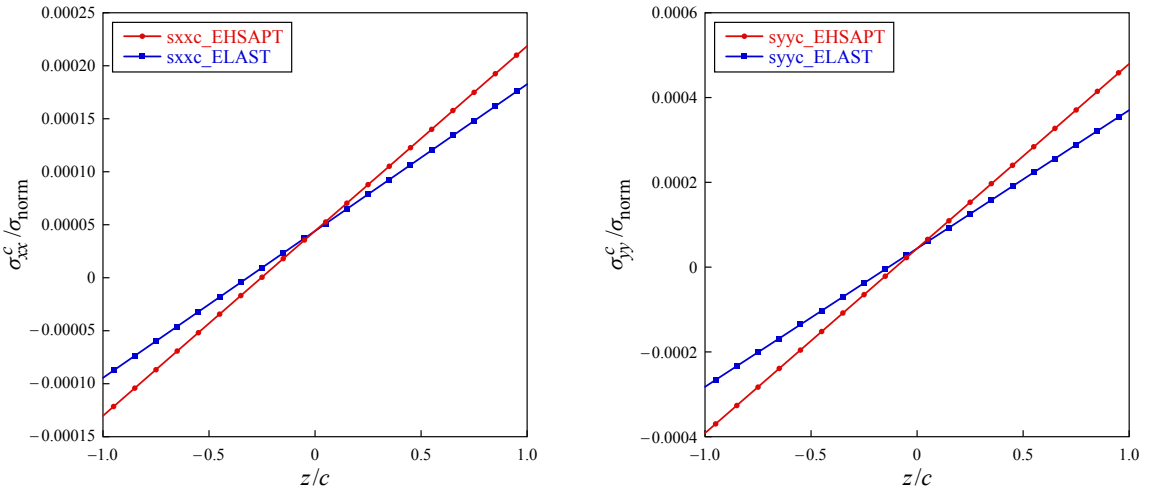


**Figure 6.** Through-thickness distribution in the core of the axial stress:  $\sigma_{xx}$  (left) and  $\sigma_{yy}$  (right) at  $x = \frac{1}{2}a$  and  $y = \frac{1}{2}b$ ; case of  $a = b = 20h_{\text{tot}}$ .

### 3. Application of EHSAPT to a simply supported sandwich plate: dynamic case

The dynamic case of a simply supported rectangular plate on all four edges is considered and boundary conditions mentioned in (2-1) are applied at  $x = 0, a$ . Similar boundary conditions can be written for the other two ends of the plate at  $y = 0, b$ .

The displacements for the dynamic case can be written in the form

$$u_0^t = U^T \cos \frac{m\pi x}{a} \sin \frac{n\pi y}{b} e^{i\omega t}, \quad u_0^c = U^C \cos \frac{m\pi x}{a} \sin \frac{n\pi y}{b} e^{i\omega t}, \quad u_0^b = U^B \cos \frac{m\pi x}{a} \sin \frac{n\pi y}{b} e^{i\omega t}, \quad (3-1a)$$

$$v_0^t = V^T \sin \frac{m\pi x}{a} \cos \frac{n\pi y}{b} e^{i\omega t}, \quad v_0^c = V^C \sin \frac{m\pi x}{a} \cos \frac{n\pi y}{b} e^{i\omega t}, \quad v_0^b = V^B \sin \frac{m\pi x}{a} \cos \frac{n\pi y}{b} e^{i\omega t}, \quad (3-1b)$$

$$w^t = W^T \sin \frac{m\pi x}{a} \sin \frac{n\pi y}{b} e^{i\omega t}, \quad w_0^c = W^C \sin \frac{m\pi x}{a} \sin \frac{n\pi y}{b} e^{i\omega t}, \quad w^b = W^B \sin \frac{m\pi x}{a} \sin \frac{n\pi y}{b} e^{i\omega t}, \quad (3-1c)$$

$$\phi = \Phi \sin \frac{m\pi x}{a} \cos \frac{n\pi y}{b} e^{i\omega t}, \quad \psi = \Psi \cos \frac{m\pi x}{a} \sin \frac{n\pi y}{b} e^{i\omega t}. \quad (3-1d)$$

Substituting equations (3-1) into the governing differential equations [SK 2019] results in a system of eleven equations which are collected to obtain

$$([K] - \lambda[M])\{u_0^b \ u_0^c \ u_0^t \ v_0^b \ v_0^c \ v_0^t \ w^b \ w_0^c \ w^t \ \phi \ \psi\}^T = 0, \quad \text{where } \lambda = \omega^2, \quad (3-2)$$

where  $[K]$  and  $[M]$  are the stiffness and mass matrices respectively.

**3A. Numerical results and case study.** In this section, the numerical results for several different geometric configurations are presented and a parametric study to analyze the free response of laminated composite plates is carried out. In order to make the comparison with an existing elasticity solution provided by Noor [1973], a simply supported square laminated plate with the face sheets and core constructed from the same material is considered. It should be noted that uniform material properties have been chosen to validate the current formulation against the elasticity solution, which does not exist for sandwich configurations. Two different symmetric layouts with respect to the middle plane such that the fiber orientations of the laminae alternate between  $0^\circ$  and  $90^\circ$  with respect to the  $x$ -axis are studied and compared to the elasticity solution. The following material properties are used:

$$E_1/E_2 = 3, \quad E_2 = E_3, \quad G_{12} = G_{13} = 0.6E_2, \quad G_{23} = 0.5E_2, \quad \nu_{12} = \nu_{13} = \nu_{23} = 0.25.$$

Following the Navier's solution procedure [Reddy 2006] the assumed displacement functions are substituted (3-1) into the governing differential equations [SK 2019], and the resulting eigensystem is solved. The nondimensionalized frequency are evaluated as:

$$\bar{\lambda} = (\omega b^2/h)\sqrt{\rho/E_2},$$

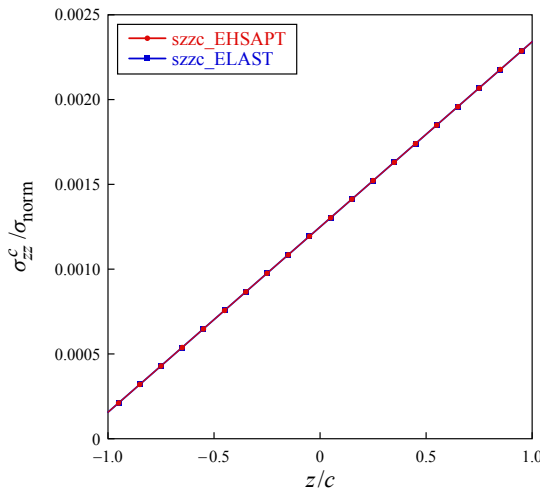


**Figure 7.** Through-thickness distribution in the core of the transverse normal stress  $\sigma_{zz}$  at  $x = \frac{1}{2}a$  and  $y = \frac{1}{2}b$ ; case of  $a = b = 20h_{\text{tot}}$ .

lamination and # of layers	elasticity	EHSAPT
0/90/0	6.6185	6.56874
0/90/0/90/0	6.6468	6.6521

**Table 1.** Nondimensionalized fundamental frequencies,  $\bar{\lambda} = (\omega b^2/h)\sqrt{\rho/E_2}$  for a simply supported square plate with  $a/h = 5$ .

where  $\omega$  is the circular frequency.

Table 1 shows that the results from EHSAPT closely match the elasticity solutions and provide us the necessary basis to verify our results and carry out a parametric study and analyze the variation of the fundamental natural frequency vis-à-vis changes in various geometric and material parameters.

#### 4. Parametric study

The variation of fundamental frequency with respect to the following parameters is studied:

$a/h$  side-to-thickness ratio

$t_c/t_f$  thickness of the core to thickness of face-sheets

$a/b$  aspect ratio

$E_1^c/E_2^c$  degree of orthotropy of the core

$E_1^f/E_2^f$  degree of orthotropy of the flanges

**4A. 5-Ply symmetric laminate with typical material properties.** Considering the material properties of individual layers in the flanges and the core are typical of high fibrous composites,

$$\begin{aligned} E_2^f = E_3^f, \quad G_{12}^f = G_{13}^f = 0.6E_2^f, \quad G_{23}^f = 0.5E_2^f, \quad \nu_{12}^f = \nu_{13}^f = \nu_{23}^f = 0.25, \\ E_2^c = E_3^c, \quad G_{12}^c = G_{13}^c = 0.6E_2^c, \quad G_{23}^c = 0.5E_2^c, \quad \nu_{12}^c = \nu_{13}^c = \nu_{23}^c = 0.25. \end{aligned}$$

Additionally we consider three different symmetric layouts of the composite sandwich laminate:

- 0/90/core/90/0
- 0/60/core/60/0
- 0/45/core/45/0

Initially, considering the variation of the normalized fundamental natural frequency with the side to thickness ratio for a simply supported square plate with  $t_c/t_f = 10$ ,  $E_1^f/E_2^f = 3$  and  $E_1^c/E_2^c = 10$ , in Figure 8, left, it can be seen that as the side to thickness ratio increases, the natural frequency also starts to increase for all three laminates considered. It can be seen that the highest fundamental natural frequency is achieved in the case of the 0/45/core/45/0 symmetric layout for any given  $a/h$  ratio. Moreover, the increase in natural frequency with an increase in side-to-thickness ratio can be explained by the fact that the sandwich plates are not assumed to be infinitely stiff through the thickness since the shear terms are included in the analytical plate model. The effect of the shear deformation results in a decrease in normalized natural frequency. This effect is more pronounced when the thickness,  $h$  of the plate increases, which can also be symbolized by an increase in  $a/h$  ratio.

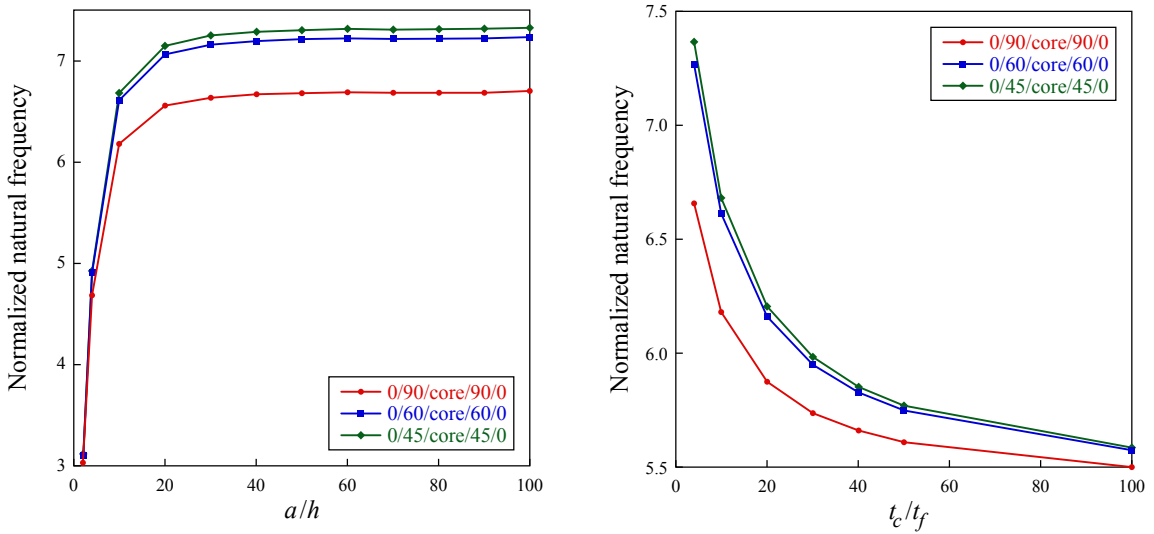


**Figure 8.** Fundamental natural frequency versus  $a/h$  ratio (left) and  $t_c/t_f$  ratio (right).

Next, the variation of the normalized fundamental natural frequency with the thickness of the core to thickness of the face-sheets for a simply supported square plate with  $a/h = 10$ ,  $E_1^f/E_2^f = 3$  and  $E_1^c/E_2^c = 10$  is analyzed and depicted in Figure 8, right. It is known that an increase in stiffness of the sandwich plate results in an increased normalized natural frequency. A similar behavior for various laminates is observed. It can be seen that as the core thickness increases in relation to the thickness of the face-sheets the fundamental natural frequency starts to decrease. Again it can be seen that the highest fundamental natural frequency is achieved in the case of the 0/45/core/45/0 symmetric layout for any given  $t_c/t_f$  ratio.

In the next case, the variation of the fundamental natural frequency with the aspect ratio of the simply supported plate with  $t_c/t_f = 10$ ,  $a/h = 10$ ,  $E_1^f/E_2^f = 3$  and  $E_1^c/E_2^c = 10$  is considered and presented in Figure 9, left. It can be seen that as the aspect ratio increases (that is, as the plate becomes narrower), its fundamental natural frequency starts to decrease. In this case the layout of the laminate does not seem to have a significant effect on the natural frequency of the laminate composite plate.

The effect of variation of the degree of orthotropy of the core for a simply supported square laminated plate with  $t_c/t_f = 10$ ,  $a/h = 10$  and  $E_1^f/E_2^f = 3$  is shown in Figure 9, right. It can be seen that as the degree of orthotropy of the core increases the fundamental natural frequency of the plate starts to decrease and the isotropic core provides the highest natural frequency for any laminate layout. Again the 0/45/core/45/0 layout seems to provide the highest fundamental natural frequency for any given  $E_1^c/E_2^c$  ratio.

Finally, the effect of varying the degree of orthotropy of the flanges for a simply supported square plate with an isotropic core and  $t_c/t_f = 10$  and  $a/h = 10$  is considered and presented Figure 10. It can be seen that as the ratio  $E_1^f/E_2^f$  increases the fundamental natural frequency of the plate also increases and hence it can be concluded that a combination of a isotropic core and highly orthotropic flanges provides the highest fundamental natural frequency.



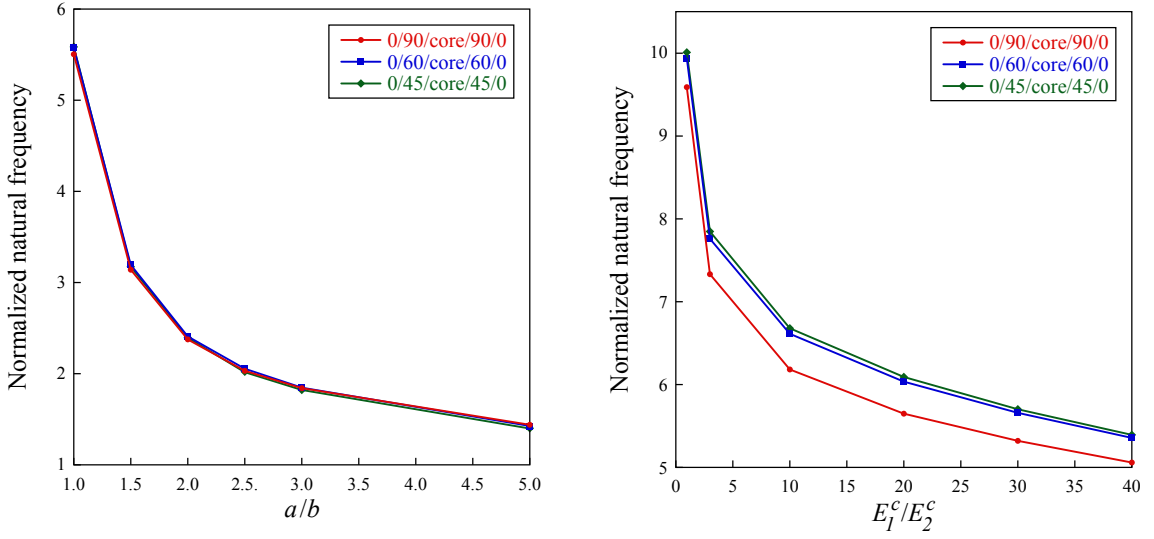


**Figure 9.** Fundamental natural frequency versus aspect ratio (left) and  $E_1^c/E_2^c$  ratio (right).

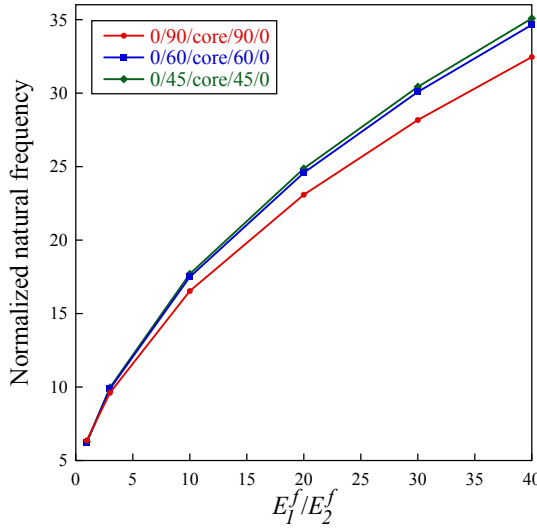


**Figure 10.** Fundamental natural frequency versus variation in the  $E_1^f/E_2^f$  ratio.

**4B. 3-ply symmetric graphite-epoxy T300/934 laminate.** We now consider a 3-ply laminate graphite-epoxy T300/934 with the following material properties:

- Face sheets:

$$\begin{aligned}
 E_1^f &= 19 \cdot 10^6 \text{ psi (131 GPa)}, & E_2^f &= 1.5 \cdot 10^6 \text{ psi (10.34 GPa)}, & E_2^f &= E_3^f, \\
 G_{12}^f &= 1 \cdot 10^6 \text{ psi (6.895 GPa)}, & G_{13}^f &= 0.90 \cdot 10^6 \text{ psi (6.205 GPa)}, & G_{23}^f &= 1 \cdot 10^6 \text{ psi (6.895 GPa)}, \\
 \nu_{12}^f &= 0.25, & \nu_{13}^f &= 0.22, & \nu_{23}^f &= 0.49, \\
 \rho^f &= 0.057 \text{ lb/inch}^3 (1627 \text{ kg/m}^3).
 \end{aligned}$$

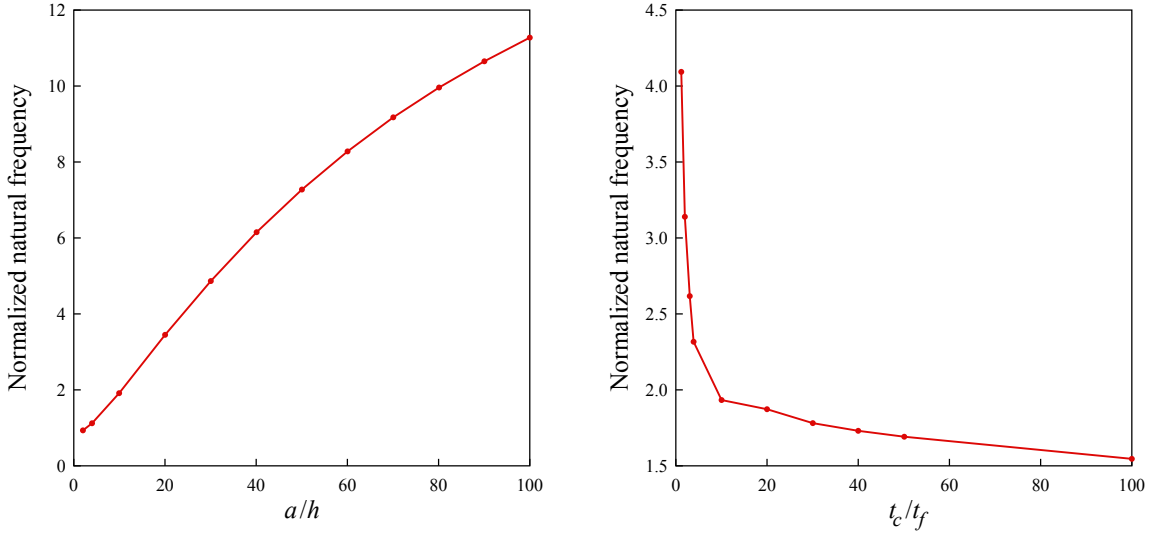


**Figure 11.** Normalized fundamental frequency versus side-to-thickness ratio  $a/h$  (left) and thickness of core to thickness of face sheet  $t_c/t_f$  (right) of a simply supported 3-ply square plate.

- Core properties (isotropic):

$$E_1^c = E_2^c = E_3^c = 2G^c = 1000 \text{ psi } (6.89 \times 10^{-3} \text{ GPa}),$$

$$G_{12}^c = G_{13}^c = G_{23}^c = 500 \text{ psi } (3.45 \times 10^{-3} \text{ GPa}),$$

$$\nu_{12}^c = \nu_{13}^c = \nu_{23}^c = 0,$$

$$\rho^c = 0.3403 \times 10^{-2} \text{ lb/inch}^3 \text{ (97 kg/m}^3\text{)}.$$

Initially, considering the variation of the normalized fundamental natural frequency with the side to thickness ratio ( $a/h$ ) for a simply supported square plate with  $t_c/t_f = 10$ . In [Figure 11](#), left, it can be observed that the natural frequency increases as  $a/h$  increases. This is because the sandwich plate is considered to be infinitely rigid through the thickness.

Now, considering the variation of the normalized fundamental natural frequency with the thickness of the core to thickness of the face-sheets for a simply supported square plate with  $a/h = 10$ . In [Figure 11](#), right, it can again be seen that as the core thickness increases in relation to the thickness of the face sheets the fundamental natural frequency starts to decrease.

Finally, considering the variation of the fundamental natural frequency with the aspect ratio of the simply supported plate with  $t_c/t_f = 10$  and  $a/h = 10$ . In [Figure 12](#) as expected, it can be seen that as the aspect ratio increases the fundamental natural frequency starts to decrease. This result again matches the behavior as predicted in [Figure 9](#).

## 5. Conclusion

This paper presents the applications and validation of extended higher-order sandwich panel theory for plates with arbitrary aspect ratios presented in [\[SK 2019\]](#). The results have been presented for a

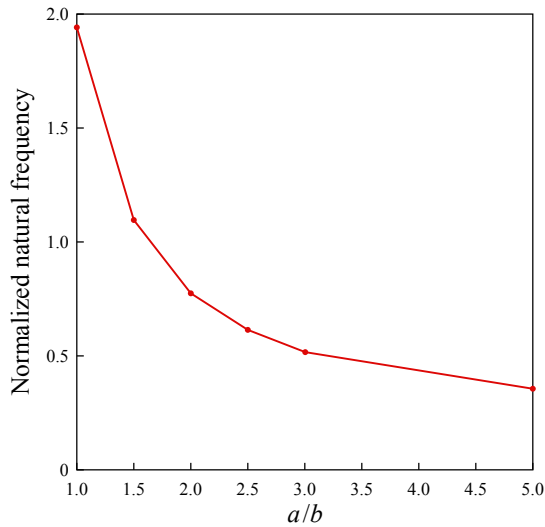


**Figure 12.** Normalized fundamental frequency versus aspect ratio ( $a/b$ ) of a simply supported 3-ply plate.

transversely loaded simply supported sandwich panel and are then compared to the classical model, the first-order shear model [Plantema 1966; Allen 1969] and elasticity solutions [Kardomateas and Phan 2011; Kardomateas 2008]. It is quite evident that the EHSAPT theory generates very good results which are in excellent agreement with the elasticity solution. These results also highlight the shortcomings of the incumbent classical and first-order shear models.

It is highlighted that some of the other recently presented higher order sandwich panel theories present very good results for the displacement profile but stresses through the core show inconsistencies when compared to elasticity solutions. The same can be seen by comparing the results obtained by Li and Kardomateas [2008]. It can be seen that his theory generates a very closely matched displacement profile but the transverse normal stress through the core ( $\sigma_{zz}^c$ ) does not match the elasticity solution and underestimates the stress at the face sheet and core interface. It is highlighted that through the thickness, transverse normal stress in the core can play a very crucial role in failure modes of the sandwich plate and debonding at the interfaces, local wrinkling and core crushing are some serious repercussions of inaccurate results. The present EHSAPT theory on the other hand not only generates excellent results for the displacement solution but also shows superior agreement with the exact solution for stresses. Therefore, this new theory is expected to have wide implications in the analysis of sandwich plate structures.

Analytical formulations and solutions to the natural frequency analysis of simply supported composite sandwich laminated plates based on a higher-order theory is presented. The displacement field takes into account the compressibility effects in the core which allows us to take the axial, shear and transverse normal stresses in the core into consideration. For laminated composite plates the solutions of this higher-order refined theory are found to be in excellent agreement with the three-dimensional elasticity solution.

A parametric study was then carried out to analyze the effect of varying the various geometric parameters and material properties on the fundamental natural frequency of laminated composite sandwich

plates with three different symmetric layouts. This study could suggest some guidelines for sandwich plate optimal design.

## References

- [Allen 1969] H. J. Allen, *Analysis and design of structural sandwich panels*, Pergamon, Oxford, 1969.
- [Frostig et al. 1992] Y. Frostig, M. Baruch, O. Vilnay, and I. Sheinman, “High-order theory for sandwich-beam behavior with transversely flexible core”, *J. Eng. Mech. (ASCE)* **118**:5 (1992), 1026–1043.
- [Hohe et al. 2006] J. Hohe, L. Librescu, and S. Y. Oh, “Dynamic buckling of flat and curved sandwich panels with transversely compressible core”, *Compos. Struct.* **74**:1 (2006), 10–24.
- [Kardomateas 2008] G. A. Kardomateas, “Three-dimensional elasticity solution for sandwich plates with orthotropic phases: the positive discriminant case”, *J. Appl. Mech. (ASME)* **76**:1 (2008), art. id. 014505.
- [Kardomateas and Phan 2011] G. A. Kardomateas and C. N. Phan, “Three-dimensional elasticity solution for sandwich beams/wide plates with orthotropic phases: the negative discriminant case”, *J. Sandw. Struct. Mater.* **13**:6 (2011), 641–661.
- [Li and Kardomateas 2008] R. Li and G. A. Kardomateas, “Nonlinear high-order core theory for sandwich plates with orthotropic phases”, *AIAA J.* **46**:11 (2008), 2926–2934.
- [Noor 1973] A. K. Noor, “Free vibrations of multilayered composite plates”, *AIAA J.* **11**:7 (1973), 1038–1039.
- [Phan et al. 2012] C. N. Phan, Y. Frostig, and G. A. Kardomateas, “Analysis of sandwich beams with a compliant core and with in-plane rigidity: extended high-order sandwich panel theory versus elasticity”, *J. Appl. Mech. (ASME)* **79**:4 (2012), art. id. 041001.
- [Plantema 1966] F. J. Plantema, *Sandwich construction: the bending and buckling of sandwich beams, plates, and shells*, Wiley, New York, 1966.
- [Reddy 2006] J. N. Reddy, *Theory and analysis of elastic plates and shells*, 2nd ed., CRC, Boca Raton, FL, 2006.
- [SK 2019] F. Siddiqui and G. A. Kardomateas, “Extended higher order sandwich panel theory for plates with arbitrary aspect ratios”, *J. Mech. Mater. Struct.* **14**:4 (2019).

Received 4 Dec 2018. Revised 24 Apr 2019. Accepted 4 Jun 2019.

FAISAL SIDDIQUI: [faisals@gatech.edu](mailto:faisals@gatech.edu)  
Georgia Institute of Technology, Atlanta, GA, United States

GEORGE A. KARDOMATEAS: [george.kardomateas@aerospace.gatech.edu](mailto:george.kardomateas@aerospace.gatech.edu)  
Georgia Institute of Technology, Atlanta, GA, United States

## INSTABILITIES IN THE FREE INFLATION OF A NONLINEAR HYPERELASTIC TOROIDAL MEMBRANE

SAIRAM PAMULAPARTHI VENKATA AND PRASHANT SAXENA

We study an incompressible nonlinear hyperelastic thin-walled toroidal membrane of circular cross-section subjected to inflation due to a uniform pressure, comparing three elastic constitutive models (neo-Hookean, Mooney–Rivlin, and Ogden) and different torus shapes. A variational approach is used to derive the equations of equilibrium and bifurcation. An analysis of the pressure–deformation plots shows occurrence of the well-known limit point (snap-through) instabilities in the membrane. Calculations are performed to study the elastic buckling point to predict bifurcation of the solution corresponding to the loss of symmetry. Tension field theory is employed to study the wrinkling instability that, in this case, typically occurs near the inner regions of tori with large aspect ratios.

### 1. Introduction

Nonlinear elastic membranes are widely used to make engineering structures and occur naturally as biological tissues. Air bags, diaphragm valves, balloons, and soft tissues like skin, arterial walls, and cell walls are some examples. Large deformation due to inflation in membranes is typically associated with several instability modes and the behaviour strongly depends on the geometric and material nonlinearities. Here we study the inflation of an incompressible toroidal membrane under hydrostatic pressure and the instabilities accompanying large deformation. We present new results and analyses for different constitutive models, limit points, buckling, and wrinkling instabilities.

Axisymmetric deformations of toroidal membranes have been studied for several decades, for example, see the early works [Clark 1950; Jordan 1962; Liepins and Sanders 1963]. By using perturbation technique, an approximate solution for a thick-walled toroidal membrane made of neo-Hookean material is given in [Kydoniefs and Spencer 1965] and for a thin-walled toroidal membrane in [Kydoniefs and Spencer 1967]. Yang and Feng [1970] examined the problems concerning large axisymmetric deformations of nonlinear membranes of Mooney–Rivlin type by employing standard numerical techniques. Hill [1980] determined analytical solutions for a thick-walled toroidal membrane using the Mooney–Rivlin model. Asymptotic behaviour of a nonlinear torus was studied in [Bonadies 1987] using an assumption that overall radius of the torus is large in comparison to the radius of larger circle generating the torus. Application of finite-element formulation to numerically analyse axisymmetric incompressible nonlinear elastic membranes of general shape which exhibit finite strains can be found in the works [Wriggers and Taylor 1990; Gruttmann and Taylor 1992; Bařar and Itskov 1998]. Numerical studies by Holzapfel et al. [1996] and Humphrey [1998] shine light on remarkable success of the finite-element approach to understand axisymmetric nonlinear behaviour of anisotropic biomembranes and cells under

MSC2010: 74B20, 74G60, 74K15.

Keywords: membrane, limit point, wrinkling, bifurcation, nonlinear elasticity, finite deformation.

finite strain. Shang and Cheng [1991] employed Runge–Kutta numerical method followed by Newton–Raphson iterative technique to study axisymmetric deformation of hyperelastic toroidal membrane with finite strains by considering the volume of the gas inside the torus (monotonic function) as a control parameter instead of internal pressure (nonmonotonic function). Papargyri [1995] examined a pressurised compressible thin-walled nonlinear toroidal membrane by comparing the stability of analytical solution obtained from perturbation approach with the numerical results. Papargyri and Stavrakakis [2000] applied a numerical scheme to study an incompressible thin-walled nonlinear torus under internal pressure for different elastic constitutive models. Papargyri [2005] developed a finite-element method to numerically determine stresses and deformations in both compressible and incompressible thin-walled toroidal membrane under static inflation using Levenberg–Marquardt algorithm. By varying the geometric and material parameters, Tamadapu and DasGupta [2012] studied in-plane deformations in homogeneous inflated elastic toroidal membranes made of neo-Hookean and Mooney–Rivlin materials using discretisation methods for both isotropic and anisotropic cases. A direct integration method coupled with Nelder–Mead optimisation technique was formulated to determine numerical solutions for toroidal membranes in [Tamadapu and DasGupta 2014; Roychowdhury and DasGupta 2015].

Typical deformation characteristics of membranes under inflation involve the phenomenon of limit point or snap-through instability. A peak pressure is reached for a given deformation beyond which the membrane inflates rapidly with the slightest increase in pressure. These instabilities have been widely studied for membranes of various shapes [Benedict et al. 1979; Dreyer et al. 1982; Carroll 1987; Khayat et al. 1992; Müller and Struchtrup 2002]. Kanner and Horgan [2007] investigated the effect of strain-hardening on limit point instability in thin-walled spherical and cylindrical shells for different constitutive models and material parameters. Tamadapu et al. [2013] analysed the effects of geometric and material parameters on limit point pressure and the associated instabilities during inflation of incompressible nonlinear elastic membranes of Mooney–Rivlin type, including the torus. Reddy and Saxena [2017; 2018] employed both analytical and numerical schemes to study limit point instability in toroidal and cylindrical magnetoelastic membranes. Application of bifurcation theory to study buckling problems in the case of a general elastic deformation is a well-developed research area; see, for example, the classical works [Koiter 1945; Budiansky 1974].

During the process of stretching, a local structural instability in the form of wrinkling is typically observed in thin-walled elastic membranes for certain geometries and material parameters [Harold 1970; Szyszkowski and Glockner 1987; Jenkins et al. 1998]. Due to unequal stretching in the principal directions during inflation, compressive stresses may develop in certain regions of the membrane causing out of plane displacements. According to the tension field theory [Pipkin 1986], the wrinkles orient along the direction of the positive principal stress and the wrinkling occurs in the direction of negative principal stress. The component of principal stress along the direction of wrinkling is considered to be zero by Pipkin [1986]. Steigmann [1990] extended this theory to nonlinear elastic membranes and developed analytical functions to obtain information about stretch and the alignment of tension lines in membranes undergoing wrinkling. It is to be noted that, as no bending stiffness is assigned to the membrane, the amplitude and wavelength of the wrinkles cannot be computed by using this theory. Research on the wrinkling of membranes include [Stein and Hedgepeth 1961; Wu 1974; 1978; Wu and Canfield 1981; Mansfield 1981; Zak 1982; Haughton and McKay 1995; Epstein 1999; Saxena et al. 2019], to name a few. Axisymmetric deformations of tense and wrinkled zones in thin-walled

elastic isotropic membranes were found in Li and Steigmann [1995a; 1995b] using relaxed form of Ogden's three-terms strain energy model, by Roxburgh [1995] using relaxed form of Mooney–Rivlin strain energy function, and by Steigmann [2005] using relaxed form of Varga strain energy function. Wong and Pellegrino [2006] proposed an analytical method to determine the location of wrinkles and quantify the geometrical patterns such as amplitude and wavelength in linear elastic membranes. Nayyar et al. [2011] and Barsotti [2015] applied finite-element methods to study wrinkling in thin-walled elastic membranes. Patil et al. [2015] used a combination of standard and relaxed strain energy density functions to numerically determine the nonlinear axisymmetric deformations in tensed and wrinkled regions for an incompressible cylindrical membrane with nonuniform thickness. The numerical analysis was performed by applying finite difference method coupled with the Newton–Raphson iterative technique.

Here we analyse the influence of geometry and material parameters on axisymmetric deformations, limit points, bifurcation points, and wrinkling of inflated isotropic hyperelastic toroidal membrane under a uniform hydrostatic pressure. The two-point boundary value problem obtained from the equilibrium equations is converted to an initial value problem. Then, for a given deformation of a point on the outer equator of the membrane, the shooting method is employed to capture the unknown initial conditions using Nelder–Mead optimisation coupled with direct integration to solve the resulting equilibrium equations. We apply the classical theory of instability developed by Koiter [1945] and Budiansky [1974] by considering pressure as the loading parameter to compute the bifurcation point at which the symmetric fundamental solution becomes unstable. It is observed that bifurcation for torus of neo-Hookean type typically occurs very close to the limit point for the first mode except for the smallest aspect ratio case in which it occurs post limit point for the second mode. Location of wrinkled region is computed using an iterative process based on a kinematic condition that helps in an accurate recomputation of the entire solution using a coupled form of standard and relaxed energy to determine the membrane deformation.

Remainder of this paper is organised as follows. In Section 2, we formulate the problem statement along with the necessary kinematical equations for the reference and deformed configurations of the toroidal membrane. In Section 3, we formulate the governing equations of elastic equilibrium using the first variation of the total potential energy functional. We introduce three different elastic constitutive models (Ogden, Mooney–Rivlin, and neo-Hookean) used for computations and also derive the governing equations corresponding to wrinkling by using relaxed strain energy density. In Section 4, second variation of the strain-energy functional is derived for the neo-Hookean model to compute critical pressure for buckling. We discuss the numerical procedure used for computations and present our results and analysis in Section 5. Finally, we present the conclusions in Section 6.

## 2. Kinematics of deformation

Consider the reference and deformed configurations of an isotropic incompressible hyperelastic thin-walled toroidal membrane of a circular cross-section as shown in Figure 1. Smaller radius is  $R_s$  and the radius of revolution is  $R_b$  in the reference configuration. The toroidal membrane is inflated by an internal hydrostatic pressure. Thickness of the undeformed and deformed membranes are denoted by  $T$  and  $t$ , respectively related by the stretch ratio  $\lambda_3 = t/T$ . The thinness assumption requires  $T \ll R_s$ . Profile of the midsurface of torus in the deformed configuration can be traced using two functions  $\tilde{q}$  and  $\tilde{\eta}$  as shown in the figure. The torus is symmetric about the  $Y^1$ - $Y^2$  plane, hence we constrain the solution





### 3. Energy considerations and governing equations

**3.1. Potential energy and equilibrium equations.** The total potential energy functional  $E$  of the system of interest is given by

$$E[\varrho, \eta] = T \int_{\Omega} W dA - \int_{V_0}^{V_0 + \Delta V} \hat{P} dV, \quad (4)$$

where  $T$  is the thickness of undeformed membrane,  $\Omega$  represents the midsurface of the undeformed membrane,  $V_0$  represents the enclosed initial volume and  $\Delta V$  measures the change in the enclosed volume,  $W(\varrho, \varrho_\theta, \varrho_\phi, \eta_\theta, \eta_\phi)$  is the strain energy per unit undeformed volume, and  $\hat{P}$  is the hydrostatic pressure. Note that  $W$  has no explicit dependence on  $\eta$  since none of the principal stretch ratios depend on  $\eta$  as seen from (3).

Equation (4) can be rewritten as

$$E[\varrho, \eta] = T \int_0^{2\pi} \int_0^{2\pi} W \sqrt{G} d\theta d\phi - \int_0^{2\pi} \int_0^{2\pi} \hat{P} \mathbf{n} da \cdot \delta \mathbf{y}, \quad (5)$$

where  $\sqrt{G} = \sqrt{\det(G_{ij})} = RR_b$  and  $da = \sqrt{g} d\theta d\phi$  is the area of a differential element on the deformed surface with the unit normal  $\mathbf{n}$ . Note that the strain energy is calculated over the reference configuration while the pressure work is evaluated over the deformed configuration.

First variation of the total potential energy is given as

$$\begin{aligned} \delta E = T \int_0^{2\pi} \int_0^{2\pi} & \left[ \left[ \frac{\partial W}{\partial \varrho} \sqrt{G} - \frac{\partial}{\partial \theta} \left( \frac{\partial W}{\partial \varrho_\theta} \sqrt{G} \right) - \frac{\partial}{\partial \phi} \left( \frac{\partial W}{\partial \varrho_\phi} \sqrt{G} \right) \right] \delta \varrho \right. \\ & \left. - \left[ \frac{\partial}{\partial \theta} \left( \frac{\partial W}{\partial \eta_\theta} \sqrt{G} \right) + \frac{\partial}{\partial \phi} \left( \frac{\partial W}{\partial \eta_\phi} \sqrt{G} \right) \right] \delta \eta \right] d\theta d\phi \\ & + \int_0^{2\pi} \int_0^{2\pi} \hat{P} R_b^3 [[\varrho_\theta \delta \eta] - [\eta_\theta \delta \varrho]] d\theta d\phi. \end{aligned} \quad (6)$$

From the principle of minimum potential energy, equilibrium states are attained when  $\delta E = 0$  that results in the following Euler equations to be satisfied for evaluating the principal solution of deformation:

$$\frac{\partial}{\partial \theta} \left( \frac{\partial W}{\partial \varrho_\theta} \sqrt{G} \right) + \frac{\partial}{\partial \phi} \left( \frac{\partial W}{\partial \varrho_\phi} \sqrt{G} \right) - \frac{\partial W}{\partial \varrho} \sqrt{G} + \frac{\hat{P} R_b^3}{T} [\varrho_\theta \eta_\phi] = 0, \quad (7a)$$

$$\frac{\partial}{\partial \theta} \left( \frac{\partial W}{\partial \eta_\theta} \sqrt{G} \right) + \frac{\partial}{\partial \phi} \left( \frac{\partial W}{\partial \eta_\phi} \sqrt{G} \right) - \frac{\hat{P} R_b^3}{T} [\varrho_\theta \varrho_\phi] = 0. \quad (7b)$$

The fundamental solution is symmetric with respect to rotation about the  $Y^3$  axis resulting in  $\varrho_\phi = \eta_\phi = 0$ . Upon using this condition, (7a) is simplified to

$$\frac{\partial^2 W}{\partial \theta \partial \varrho_\theta} \gamma R - \frac{\partial W}{\partial \varrho_\theta} \gamma^2 \sin \theta - \frac{\partial W}{\partial \varrho} \gamma R + \frac{\hat{P} R_b}{T} \varrho_\theta \eta_\theta = 0, \quad (8)$$

and (7b) becomes

$$\frac{\partial^2 W}{\partial \theta \partial \eta_\theta} \gamma R - \frac{\partial W}{\partial \eta_\theta} \gamma^2 \sin \theta - \frac{\hat{P} R_b}{T} \varrho_\theta \eta_\theta = 0. \quad (9)$$

The governing equations (8) and (9) are solved using the boundary conditions which are determined based on compatibility and symmetry of the cross-section of the torus

$$\varrho_\theta(0) = \varrho_\theta(\pi) = 0, \quad \eta(0) = \eta(\pi) = 0. \quad (10)$$

**3.1.1. Elastic constitutive models.** In order to demonstrate mechanical behaviour via computations we use the three-term Ogden, Mooney–Rivlin, and neo-Hookean hyperelastic models for the elastic strain energy density  $W$  in this work. These are three very commonly used hyperelastic energy density functions in several computational studies [Holzapfel 2000]. The mathematical expressions and numerical values of the material parameters are given below.

The strain energy density for the three-term Ogden model is given by

$$W^*(\lambda_1, \lambda_2) = \sum_{j=1}^3 \frac{\mu_j}{\alpha_j} \left[ \lambda_1^{\alpha_j} + \lambda_2^{\alpha_j} + \left[ \frac{1}{\lambda_1 \lambda_2} \right]^{\alpha_j} - 3 \right], \quad (11)$$

along with the conditions  $\sum_j \mu_j \alpha_j = 2\mu$  and  $\mu_j \alpha_j > 0$ . The nondimensional parameters can be defined as  $\mu_1^* = \mu_1/\mu$ ,  $\mu_2^* = \mu_2/\mu$ ,  $\mu_3^* = \mu_3/\mu$ , where  $\mu$  is the baseline shear modulus.

Upon substituting  $\alpha_1 = 2$ ,  $\alpha_2 = -2$ , and  $\mu_3 = 0$  in (11), we arrive at the Mooney–Rivlin strain energy density given by

$$W^*(\lambda_1, \lambda_2) = \frac{1}{2}\mu_1 \left[ \lambda_1^2 + \lambda_2^2 + \frac{1}{\lambda_1^2 \lambda_2^2} - 3 \right] - \frac{1}{2}\mu_2 \left[ \frac{1}{\lambda_1^2} + \frac{1}{\lambda_2^2} + \lambda_1^2 \lambda_2^2 - 3 \right]. \quad (12)$$

Upon using  $\alpha_1 = 2$ ,  $\mu_2 = \mu_3 = 0$  in (11), we arrive at the neo-Hookean strain energy density given by

$$W^*(\lambda_1, \lambda_2) = \frac{1}{2}\mu_1 \left[ \lambda_1^2 + \lambda_2^2 + \frac{1}{\lambda_1^2 \lambda_2^2} - 3 \right]. \quad (13)$$

Upon substitution of the explicit expressions of each of the above energy density functions, the resulting governing equations (8) and (9) can be rewritten as a system of first-order ODEs in matrix form as

$$\begin{bmatrix} 1 & 0 & 0 & 0 \\ 0 & S_{22} & 0 & S_{24} \\ 0 & 0 & 1 & 0 \\ 0 & S_{42} & 0 & S_{44} \end{bmatrix} \begin{bmatrix} \mathcal{U}'_1 \\ \mathcal{U}'_2 \\ \mathcal{U}'_3 \\ \mathcal{U}'_4 \end{bmatrix} = \begin{bmatrix} \mathcal{U}_2 \\ \mathcal{V}_1 \\ \mathcal{U}_4 \\ \mathcal{V}_2 \end{bmatrix}, \quad (14)$$

where

$$\mathcal{U}_1 = \varrho, \quad \mathcal{U}_2 = \varrho_\theta = \mathcal{U}'_1, \quad \mathcal{U}'_2 = \varrho_{\theta\theta}, \quad \mathcal{U}_3 = \eta, \quad \mathcal{U}_4 = \eta_\theta = \mathcal{U}'_3, \quad \mathcal{U}'_4 = \eta_{\theta\theta}, \quad (15)$$

and the remaining terms  $S_{22}$ ,  $S_{24}$ ,  $S_{42}$ ,  $S_{44}$ ,  $\mathcal{V}_1$ ,  $\mathcal{V}_2$  for each of the constitutive models are listed in Sections A.1–A.3 in the Appendix.

**3.2. Relaxed strain energy density.** During the inflation of elastic membranes, compressive stresses might develop for certain geometries as the membrane undergoes unequal stretching in the principal directions. As membranes are no-compression structures, these in-plane negative stresses result in out of plane deformations causing wrinkling instability. According to the tension field theory, with the absence of bending stiffness in thin membranes, infinitesimally small and closely spaced wrinkles are formed due to compressive stresses. We observe the compressive stresses for certain geometries and for specific

material parameters in our study. Pipkin [1986] proposed the concept of “relaxed strain energy density” by modifying the elastic constitutive relation based on principal stretches to study the wrinkling behaviour in linear elastic membranes. This theory is extended to nonlinear elastic membranes by Steigmann [1990]. The relaxed strain energy density  $W_R$  is represented as

$$W_R = \begin{cases} W(\lambda_1, \lambda_2) & \text{if } \lambda_2 \geq w(\lambda_1) \text{ and } \lambda_1 \geq w(\lambda_2), \\ W_t(\lambda_1) & \text{if } \lambda_2 \leq w(\lambda_1) \text{ and } \lambda_1 \geq 1, \\ W_t(\lambda_2) & \text{if } \lambda_1 \leq w(\lambda_2) \text{ and } \lambda_2 \geq 1, \\ 0 & \text{if } \lambda_1 \leq 1 \text{ and } \lambda_2 \leq 1, \end{cases} \quad (16)$$

where the function  $w(\lambda)$  is termed as the “natural width in simple tension” and defined below. For any fixed value of  $\lambda_1$ , the minimum of  $W$  with respect to  $\lambda_2$  is attained at

$$\lambda_2 = \lambda_1^{-1/2} =: w(\lambda_1). \quad (17)$$

Similarly, for any fixed value of  $\lambda_2$ , the minimum of  $W$  with respect to  $\lambda_1$  is attained at

$$\lambda_1 = \lambda_2^{-1/2} = w(\lambda_2). \quad (18)$$

As compressive stresses develop in the region  $\lambda_1 \geq 1$  and  $\lambda_2 \leq w(\lambda_1)$ , we can replace the original strain energy density function  $W$  by  $W_t(\lambda_1)$  as mentioned in (16).

The terms  $S_{22}$ ,  $S_{24}$ ,  $S_{42}$ ,  $S_{44}$ ,  $\mathcal{V}_1$ ,  $\mathcal{V}_2$  in the governing equation (14) for computations in the wrinkled region should be modified according to the above-stated conditions and are given in Appendix A.4.

#### 4. Second variation of total potential energy functional

In elastic solids, we often observe critical (buckling) points for certain load values at which the equilibrium path branches out into multiple stable and/or unstable paths. These critical points are of considerable interest as the postbuckling response of the system is usually different from the initial response (principal solution). Considering the hydrostatic pressure as a loading parameter, we adopt the procedure proposed in [Budiansky 1974] to determine the critical pressure in our case of hyperelastic membrane beyond which the symmetric fundamental solution is no longer the energy minimiser. To reduce the complexity of long mathematical expressions, we study the critical pressure condition only for the neo-Hookean material model.

**4.1. Critical pressure.** The fundamental solution for  $\varrho$  and  $\eta$  is symmetric with respect to the  $Y^3$  axis and therefore has no dependence on  $\phi$ . We define critical pressure as the point where the solution loses this symmetry while retaining the symmetry with respect to the  $Y^1$ - $Y^2$  plane. Hence, we consider the bifurcation branches that include perturbations in the  $\phi$  direction. The following expansions are considered for the variables  $\varrho$  and  $\eta$ :

$$\begin{aligned} \varrho(\theta, \phi) &= \varrho_0(\theta) + \hat{\varrho}(\phi) = \varrho_0(\theta) + \Upsilon \varrho_1(\phi) + \dots \\ \eta(\theta, \phi) &= \eta_0(\theta) + \hat{\eta}(\phi) = \eta_0(\theta) + \Upsilon \eta_1(\phi) + \dots \\ \Upsilon &= \langle \hat{\varrho}, \varrho_1 \rangle = \langle \hat{\eta}, \eta_1 \rangle, \quad \langle \varrho_i, \varrho_j \rangle = \langle \eta_i, \eta_j \rangle = \begin{cases} 1 & \text{if } i = j, \\ 0 & \text{otherwise,} \end{cases} \end{aligned} \quad (19)$$

where the scalar parameter  $\Upsilon \ll 1$  measures the amount of bifurcation mode,  $\langle \bullet \rangle$  represents a suitable inner product, and  $\varrho_1$  and  $\eta_1$  represent the first bifurcation mode with  $\varrho_0$  and  $\eta_0$  being the fundamental states.

Bifurcation of the solution occurs when the second variation of the potential energy vanishes. For the current scenario, it is given as

$$\delta^2 E = E''_c U_1 \delta U = [E''_{c_{\alpha_1}} + E''_{c_{\alpha_2}} - E''_{c_{\alpha_31}} - E''_{c_{\alpha_32}} + E''_{c_{\alpha_33}} + E''_{c_{\alpha_34}}] U_1 \delta U + [-E''_{c_{\alpha_35}} + E''_{c_{\alpha_36}} + E''_{c_p}] U_1 \delta U = 0, \quad (20)$$

where we have defined several terms as below

$$E''_{c_{\alpha_1}} U_1 \delta U = 0, \quad (21)$$

$$E''_{c_{\alpha_2}} U_1 \delta U = 2\bar{\mu} T \int_0^{2\pi} \int_0^{2\pi} \frac{\varrho_{1\phi} \delta \varrho_\phi + \eta_{1\phi} \delta \eta_\phi + \varrho_1 \delta \varrho}{R^2} \sqrt{G} d\theta d\phi, \quad (22)$$

$$E''_{c_{\alpha_31}} U_1 \delta U = 2\bar{\mu} T \gamma^2 \int_0^{2\pi} \int_0^{2\pi} \frac{\mathcal{E}_{aa} \mathcal{E}_{ab}}{\mathcal{E}_{ac}^2} \sqrt{G} R^2 d\theta d\phi, \quad (23)$$

$$E''_{c_{\alpha_32}} U_1 \delta U = 2\bar{\mu} T \gamma^2 \int_0^{2\pi} \int_0^{2\pi} \frac{[\varrho_\theta \eta_\phi - \varrho_\phi \eta_\theta][\eta_{1\phi} \delta \varrho_\theta - \varrho_{1\phi} \delta \eta_\theta]}{\mathcal{E}_{ac}^2} \sqrt{G} R^2 d\theta d\phi, \quad (24)$$

$$E''_{c_{\alpha_33}} U_1 \delta U = 8\bar{\mu} T \gamma^2 \int_0^{2\pi} \int_0^{2\pi} \frac{[\varrho_\theta \eta_\phi - \varrho_\phi \eta_\theta]^2 \mathcal{E}_{aa} \mathcal{E}_{ab}}{\mathcal{E}_{ac}^3} \sqrt{G} R^2 d\theta d\phi, \quad (25)$$

$$E''_{c_{\alpha_34}} U_1 \delta U = 8\bar{\mu} T \gamma^2 \int_0^{2\pi} \int_0^{2\pi} \frac{[\varrho_\theta \eta_\phi - \varrho_\phi \eta_\theta] \mathcal{E}_{ad} \mathcal{E}_{ab}}{\mathcal{E}_{ac}^3} \sqrt{G} R^2 d\theta d\phi, \quad (26)$$

$$E''_{c_{\alpha_35}} U_1 \delta U = 2\bar{\mu} T \gamma^2 \int_0^{2\pi} \int_0^{2\pi} \frac{\varrho_1 [\varrho_\theta^2 + \eta_\theta^2] \delta \varrho + 2\varrho \varrho_1 [\varrho_\theta \delta \varrho_\theta + \eta_\theta \delta \eta_\theta]}{\mathcal{E}_{ac}^2} \sqrt{G} R^2 d\theta d\phi, \quad (27)$$

$$E''_{c_{\alpha_36}} U_1 \delta U = 8\bar{\mu} T \gamma^2 \int_0^{2\pi} \int_0^{2\pi} \frac{\varrho \varrho_1 [\varrho_\theta^2 + \eta_\theta^2][[\varrho_\theta \eta_\phi - \varrho_\phi \eta_\theta] \mathcal{E}_{aa} + \mathcal{E}_{ad}]}{\mathcal{E}_{ac}^3} \sqrt{G} R^2 d\theta d\phi, \quad (28)$$

$$E''_{c_p} U_1 \delta U = \int_0^{2\pi} \int_0^{2\pi} \hat{P} R_b^3 [\varrho_\theta \eta_1 \delta \varrho + \varrho \eta_1 \delta \varrho_\theta - \eta_\theta \varrho_1 \delta \varrho - \varrho \varrho_1 \delta \eta_\theta] d\theta d\phi, \quad (29)$$

with

$$\begin{aligned} \mathcal{E}_{aa} &= \eta_\phi \delta \varrho_\theta + \varrho_\theta \delta \eta_\phi - \eta_\theta \delta \varrho_\phi - \varrho_\phi \delta \eta_\theta, & \mathcal{E}_{ab} &= \varrho_\theta \eta_{1\phi} - \eta_\theta \varrho_{1\phi}, & \bar{\mu} &= \frac{1}{2} \mu_1, \\ \mathcal{E}_{ac} &= [\varrho_\theta \eta_\phi - \varrho_\phi \eta_\theta]^2 + \varrho^2 [\varrho_\theta^2 + \eta_\theta^2], & \mathcal{E}_{ad} &= \varrho [\varrho_\theta^2 + \eta_\theta^2] \delta \varrho + \varrho^2 [\varrho_\theta \delta \varrho_\theta + \eta_\theta \delta \eta_\theta]. \end{aligned} \quad (30)$$

Upon separating the coefficients of  $\delta \varrho$  and  $\delta \eta$ , we obtain the following governing equations for the bifurcated mode

$$\mathcal{K}_{aa} \varrho_1 + \mathcal{K}_{bb} \varrho_{1\phi\phi} + \mathcal{K}_{cc} \eta_{1\phi\phi} = 0, \quad (31)$$

and

$$\mathcal{L}_{aa} \varrho_1 + \mathcal{L}_{bb} \varrho_{1\phi\phi} + \mathcal{L}_{cc} \eta_{1\phi\phi} = 0, \quad (32)$$

Three-term Ogden model [1972]:	$\mu_1^* = 1.4910,$	$\mu_2^* = 0.0029,$	$\mu_3^* = -0.0236,$
	$\alpha_1 = 1.3,$	$\alpha_2 = 5.0,$	$\alpha_3 = -2.0,$
Mooney–Rivlin model: $\mathfrak{M} = -\frac{\mu_2}{\mu_1} = 0.1$ and $0.3.$			

**Table 1.** Nondimensional material parameters used for numerical computations.

where the bifurcation pressure is denoted as  $\widehat{P}_c$  and

$$\begin{aligned}
 \mathcal{K}_{aa} &= R\gamma\varrho^4\mathcal{N}^3 + 3R^5\gamma^3\mathcal{N}^2 + 6\varrho_\theta^2R^5\gamma^3\mathcal{N} - 2\varrho\varrho_{\theta\theta}R^5\gamma^3\mathcal{N} + 6\varrho\varrho_\theta R^4\gamma^4\mathcal{N}\sin\theta \\
 &\quad + 8\varrho\varrho_\theta[\varrho_\theta\varrho_{\theta\theta} + \eta_\theta\eta_{\theta\theta}]R^5\gamma^3 - \frac{1}{2}P_c\eta_\theta R^2\varrho^4\mathcal{N}^3, \\
 \mathcal{K}_{bb} &= -\varrho^4\gamma R\mathcal{N}^3 + \eta_\theta^2R^5\gamma^3\mathcal{N}, \quad \mathcal{K}_{cc} = -\varrho_\theta\eta_\theta R^5\gamma^3\mathcal{N}, \\
 \mathcal{N} &= \varrho_\theta^2 + \eta_\theta^2, \quad P_c = \frac{\widehat{P}_c R_b}{\bar{\mu}T}, \\
 \mathcal{L}_{aa} &= 6\varrho_\theta\eta_\theta R^5\gamma^3\mathcal{N} - 2\varrho\eta_{\theta\theta}R^5\gamma^3\mathcal{N} + 6\varrho\eta_\theta R^4\gamma^4\mathcal{N}\sin\theta + 8\varrho\eta_\theta[\varrho_\theta\varrho_{\theta\theta} + \eta_\theta\eta_{\theta\theta}]R^5\gamma^3 + \frac{1}{2}P_c\varrho^4\varrho_\theta R^2\mathcal{N}^3, \\
 \mathcal{L}_{bb} &= -\varrho_\theta\eta_\theta R^5\gamma^3\mathcal{N}, \quad \mathcal{L}_{cc} = -\gamma R\varrho^4\mathcal{N}^3 + \varrho_\theta^2R^5\gamma^3\mathcal{N}.
 \end{aligned} \tag{33}$$

Upon considering the following ansatz for  $\varrho_1$  and  $\eta_1$ :

$$\varrho_1 = \varrho_1^0 \exp(in\phi), \quad \eta_1 = \eta_1^0 \exp(in\phi), \quad \text{where } i = \sqrt{-1}. \tag{34}$$

It can be shown that a nontrivial solution for the above system of equation exists when

$$\mathcal{R}_{\text{res}} = [[\mathcal{K}_{cc}\mathcal{L}_{aa} - \mathcal{K}_{aa}\mathcal{L}_{cc}] + n^2[\mathcal{K}_{bb}\mathcal{L}_{cc} - \mathcal{K}_{cc}\mathcal{L}_{bb}]] = 0. \tag{35}$$

The residue  $\mathcal{R}_{\text{res}}$  defined above should be put to zero computationally in order to calculate the critical pressure value.

## 5. Numerical procedure, results, and discussion

Computations are performed for numerical values of the material parameters presented in Table 1.

**5.1. Calculation of fundamental solution.** The governing equations (8) and (9) for fundamental solution are subjected to boundary conditions defined by (10). They are numerically solved for three elastic constitutive models (Ogden, Mooney–Rivlin, and neo-Hookean) by following a method used for similar problems in [Tamadapu and DasGupta 2014; Reddy and Saxena 2017]. The two point boundary value problem is converted into an initial value problem with two unknown parameters ( $\varrho(0), \eta_\theta(0)$ ) at a particular nondimensional pressure  $P$ . For a given value of location of point on the outer equator of the membrane ( $\varrho(0) > 1 + \gamma$ ), we start with an initial guess for the pair ( $\eta_\theta(0), P$ ), and employ shooting method to obtain the two boundary values  $\varrho_\theta(\pi)$  and  $\eta(\pi)$  for the point on the inner edge. Ideally  $\varrho_\theta(\pi)$  and  $\eta(\pi)$  should be zero. The desired optimisation pair ( $\eta_\theta(0), P$ ) which reduces the value of the cost function,  $[\varrho_\theta(\pi)^2 + \eta(\pi)^2]^{1/2}$ , to a sufficiently small quantity ( $< \mathcal{O}(10^{-12})$ ) is obtained by using the Nelder–Mead simplex optimisation technique of two variables. This optimisation method is performed

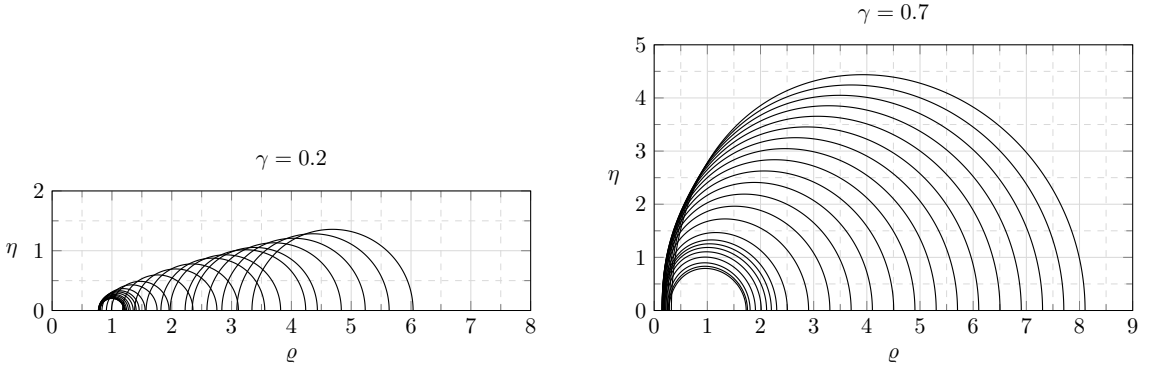


**Figure 2.** Deformation profiles of the membrane subject to inflation using Ogden energy density function for aspect ratios  $\gamma = 0.2$  and  $\gamma = 0.7$ . The nondimensional coordinates  $\varrho$  and  $\eta$  are introduced in (2). Due to symmetry, only the upper half is plotted.

using `fminsearchbnd` function with lower bounds on the guess pair  $(\{\eta_\theta(0), P\} > 0)$  in Matlab R2017b. As we capture the desired pair, we use a strong mass-state dependent `ode45` solver in Matlab R2017b to solve the set of equilibrium equations in order to obtain the values of  $\varrho$ ,  $\varrho_\theta$ ,  $\eta$ ,  $\eta_\theta$  over the domain  $\theta \in [0, \pi]$  which is finely divided into 2000 intervals.

**5.1.1. Fundamental solution, deformation profiles, and validation.** We plot the inflation profiles of the toroidal membrane for the Ogden model in Figure 2 for the aspect ratios  $\gamma = 0.2$  and  $\gamma = 0.7$ . Similar profiles are obtained for all the models, aspect ratios, and pressure values but not shown here for brevity. It can be seen from Figure 2, left, that for the small aspect ratio ( $\gamma = 0.2$ ), both the inner and the outer ends move outwards while for higher aspect ratio ( $\gamma = 0.7$ ) and Figure 2, right, inner end remains at almost the same position while the outer end moves outwards upon the increase of pressure.

Plots of  $\varrho(\pi)$  (inner end) vs.  $\varrho(0)$  (outer end) for all the three material models and several aspect ratios  $\{\gamma \in (0.2, 0.7)$  for Ogden and Mooney–Rivlin,  $\gamma \in (0.2, 0.8)$  for neo-Hookean} are presented in Figure 3. For the Ogden and neo-Hookean models, it is clearly seen that upon the increase of inflation (moving rightwards on the  $\varrho(0)$  axis), the inner end first moves slightly inwards and then moves outwards for almost all values of  $\gamma$ . Only for large aspect ratios ( $\gamma = 0.7$  for Ogden and  $\gamma = 0.7, 0.8$  for neo-Hookean), the inner end undergoes very small changes in its position. This is also expected physically since tori with large  $\gamma$  have very little room for movement of the inner end. The behaviour is different for the two Mooney–Rivlin material models as shown in Figure 3, bottom. For the cases  $\{\gamma = 0.2 \text{ to } 0.5, \mathfrak{M} = 0.1\}$  and  $\{\gamma = 0.2, \mathfrak{M} = 0.3\}$ , with an increase in pressure the inner edge moves outwards before moving inwards again for higher inflation. For all other cases, the inner edge moves further inwards monotonically upon increase of pressure.

These considerable differences in behaviours of constitutive models demonstrate the importance of selecting the right model for the material at hand. For example, behaviour of natural rubbers can usually be explained by the three-term Ogden model [1972] while that of certain soft biological tissues can be simulated by the neo-Hookean model [Horný et al. 2006]. Our results for the Mooney–Rivlin model match those presented in [Tamadapu and DasGupta 2014] for  $\mathfrak{M} = 0.3$ ,  $\gamma = 0.2$  and  $0.5$  cases, and those



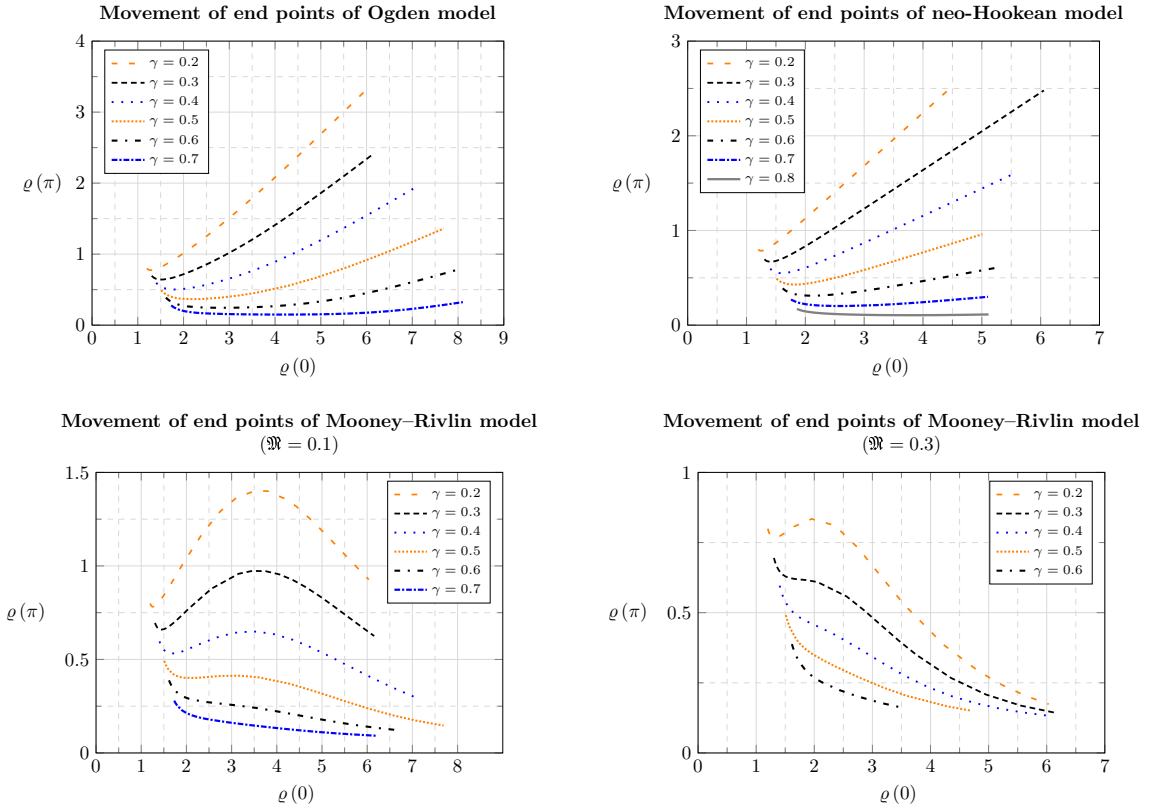


**Figure 3.** Movement of end points for different hyperelastic constitutive models during inflation of the membrane for various aspect ratios  $\gamma$ . The end  $\varrho(0)$  represents the inflation as explained in Section 5.1 and  $\varrho(\pi)$  is the inner end of the torus profile.

presented in [Reddy and Saxena 2017] for  $\mathfrak{M} = 0.1$ ,  $\gamma = 0.2$  and  $0.5$ ; thus providing a validation of the formulation and the computations.

**5.1.2. Limit point and Cauchy stress.** We compute the pressure-deformation and pressure-stress characteristics for all the three material models for the aspect ratios lying in the range  $\gamma \in (0.2, 0.8)$ . Variation of nondimensional pressure ( $P$ ) with the relative increase in volume ( $\Delta V/V$ ) of torus for three representative aspect ratios  $\gamma = 0.2, 0.4$ , and  $0.6$  is shown in Figure 4. In each of these curves we observe the classical limit point as the point at which pressure stops increasing monotonically. In a pressure controlled experiment, this generally results in a snap-through instability causing uncontrolled increase in membrane's volume likely leading to failure. However, the states beyond limit point can be reached in a volume controlled experiment.

It is evident from these curves that tori with small aspect ratios  $\gamma$  can sustain much higher pressure values for the same relative increase in volume. This effect is also visible in the limit point pressure  $P_{\text{lim}}$  plotted in Figure 5. Higher values of  $\gamma$  result in lower values of corresponding  $P_{\text{lim}}$ . We also note that with comparable values of shear modulus  $\mu$  used in the computations, Ogden material has the smallest value of  $P_{\text{lim}}$  followed by neo-Hookean and Mooney–Rivlin materials, respectively. We note that upon

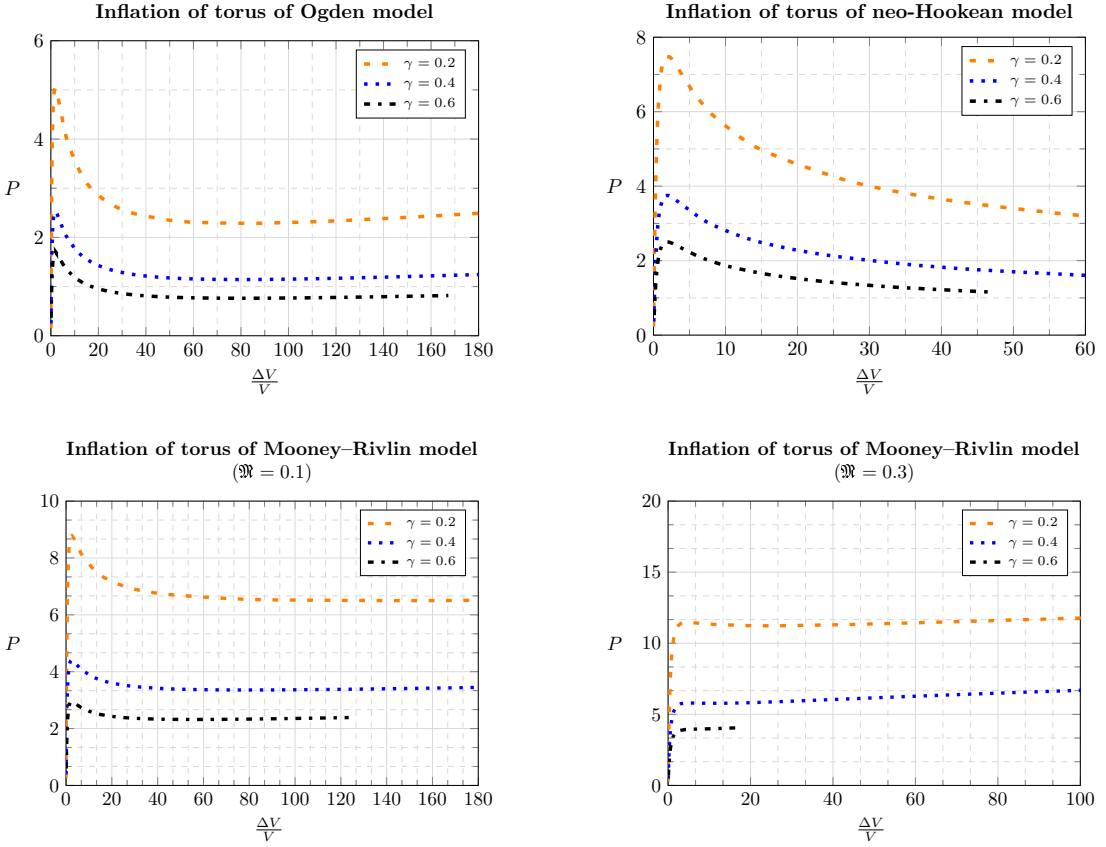


**Figure 4.** Pressure vs. volume curves for all the three material models for three different aspect ratios  $\gamma = 0.2, 0.4, 0.6$ .

increasing volume beyond the limit point, there is a consistent decline in pressure for the neo-Hookean model whereas opposite happens for Mooney–Rivlin ( $\mathfrak{M} = 0.3$ ,  $\gamma = 0.6$ ) case where pressure increases monotonically. In all the other cases (Ogden model, Mooney–Rivlin ( $\mathfrak{M} = 0.1$ ) and Mooney–Rivlin ( $\mathfrak{M} = 0.3$ ,  $\gamma = 0.2, 0.4$ )) pressure rises with volume after an initial fall at the limit point.

We also study the variation of Cauchy stresses in the membrane with inflation as computed using (43), (49), and (53). The behaviour is almost similar for all the three models and we plot a few representative results for Ogden model in Figure 6. Variation of the principal stresses  $\sigma_{\theta\theta}$  and  $\sigma_{\phi\phi}$  at the inner equator ( $\theta = \pi$ ) with the internal pressure is shown. Typically the magnitude of principal stresses along the minor circumference ( $\sigma_{\theta\theta}$ ) is larger than that of the principal stresses along the major circumference ( $\sigma_{\phi\phi}$ ). For most cases, the stresses increase monotonically with inflation, the exception being  $\sigma_{\phi\phi}(\theta = \pi)$  at  $\gamma = \{0.6, 0.7\}$ . Beyond the limit point, the stresses increase rapidly upon slight changes in pressure, likely leading to failure.

We further observe in Figure 6 that  $\sigma_{\phi\phi}$  attains a negative value for certain values of pressure for torus with  $\gamma = 0.7$ . Similar observations are made for the neo-Hookean model ( $\gamma = 0.8$ ) and Mooney–Rivlin model ( $\{\mathfrak{M} = 0.1; \gamma = 0.4, 0.5, 0.6, 0.7\}$  and  $\{\mathfrak{M} = 0.3; \gamma = 0.2, 0.3, 0.4, 0.5, 0.6\}$ ) but those results are

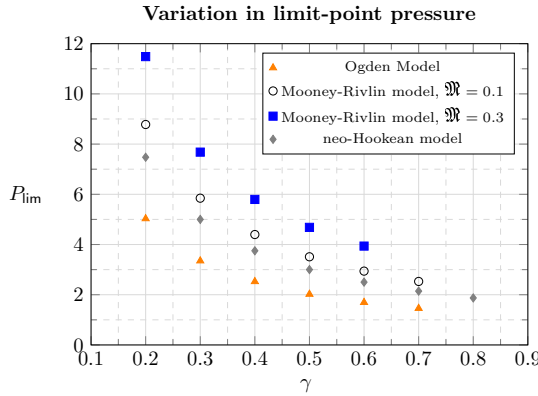


**Figure 5.** Variation of limit point pressure with aspect ratio for different elastic constitutive models.

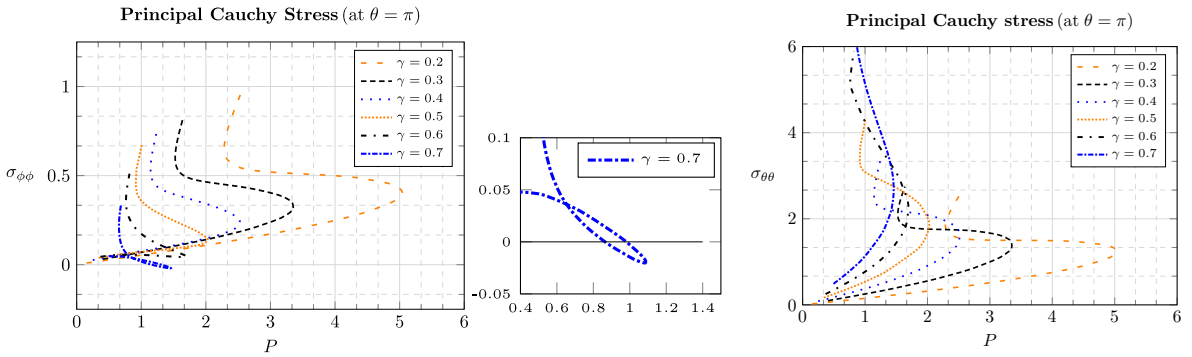


**Figure 6.** Variation of the principal stresses  $\sigma_{\theta\theta}$  and  $\sigma_{\phi\phi}$  with pressure at the inner equator ( $\theta = \pi$ ) of the torus for the Ogden material model.

not plotted here for the sake of brevity. Negative values of the principal stress indicate the occurrence of wrinkling instability and this is further explored in [Section 5.3](#).

**5.2. Calculation of critical pressure.** The fundamental solution obtained for the variables  $Q_\theta$  and  $\eta_\theta$  is used in calculating second order derivatives of  $Q$  and  $\eta$  with respect to the variable  $\theta$ . The values of  $Q_{\theta\theta}$  and  $\eta_{\theta\theta}$  in each interval are calculated by using forward difference method, i.e.,  $Q_{\theta\theta i} = (Q_{\theta i+1} - Q_{\theta i})/\Delta\theta$  where  $\Delta\theta = \pi/2000$  and  $i = 1, 2, \dots, 2000$ . The variables  $(Q, \eta)$  and their derivatives are calculated at each  $\theta_i$  for all the values of pressure during inflation process of a membrane with an aspect ratio  $\gamma$ . These values are substituted in (35) and by changing the values of the mode number  $n$  from 1 to 5, we calculate  $\mathcal{R}_{res}$  at each  $\theta_i$  for all the values of pressure and for a given aspect ratio  $\gamma$ . We repeat this process for all the values of  $\gamma \in (0.2, 0.8)$  considered in our study for the neo-Hookean material. Zeros of  $\mathcal{R}_{res}$  are searched by computing the value of pressure at which it changes sign. Only a change of order ( $> \mathcal{O}(10^{-4})$ ) in the residual value is considered to be admissible to avoid numerical errors; if the value of  $\mathcal{R}_{res}$  does not fall in the desired range we do not assign any critical value of pressure for that case. This procedure is repeated for the entire domain  $\theta \in [0, \pi]$  and the corresponding critical pressure for the point located

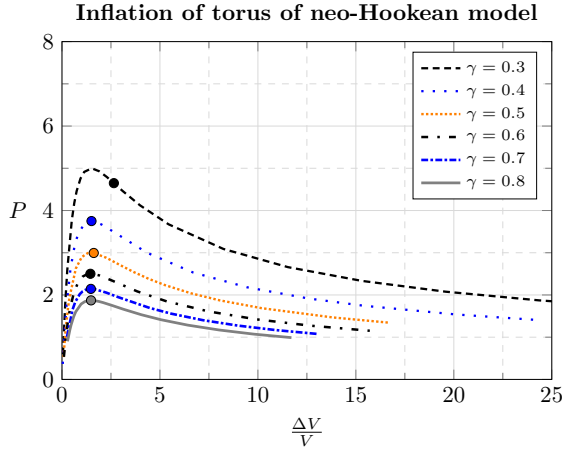


**Figure 7.** First critical points on the pressure-volume curves for the neo-Hookean model are marked with dots. For  $\gamma = 0.3$ , critical point is achieved for  $n = 2$  and occurs significantly after the limit point, while for all other cases it is achieved at  $n = 1$  very close to the limit point.

at  $\theta_i$  on the membrane is noted. The lowest of all the critical pressure values occurring at or before the limit point for a given aspect ratio is termed as critical point pressure for that membrane under inflation.

Based on our computations, we obtain critical (bifurcation) points for the cases  $\{n = 1, \gamma = 0.4, 0.5, 0.6, 0.7, 0.8\}$  and  $\{n = 2, \gamma = 0.3\}$ . All other cases lead to no solution of (35). The critical point for  $\gamma = 0.3$  occurs well after the limit point and although this configuration is difficult to access in a pressure controlled experiment, it can be achieved in a volume or mass controlled experiment [Wang et al. 2017]. For all other  $\gamma$  values, the critical points are very close (albeit not equal) to the limit point. These points are depicted graphically in Figure 7.

**5.3. Computation of wrinkling instability.** Wrinkling is achieved when the in-plane stress in any direction in the membrane reaches zero. In the negative-stress regions, we use the relaxed form of the strain energy density and the subsequently modified equations in Section 3.2 to recompute the solutions with a method similar to that employed in Section 5.1.

We start with an initial guess value for the location of onset of wrinkling region  $\theta_{\text{wr}}$  taken to be the starting location of the region  $\sigma_{\phi\phi} < 0$ . We employ standard strain energy density in the region  $0 \leq \theta \leq \theta_{\text{wr}}$  to calculate the variables  $\varrho$ ,  $\varrho_\theta$ ,  $\eta$ , and  $\eta_\theta$  at  $\theta_{\text{wr}}$  and use these as the initial conditions to determine the solution in the region  $\theta_{\text{wr}} \leq \theta \leq \pi$  employing the relaxed strain energy density function. Next, we minimise the cost function  $[\varrho_\theta(\pi)^2 + \eta(\pi)^2]^{1/2}$  to a sufficiently small quantity ( $< \mathcal{O}(10^{-12})$ ) by using the Nelder–Mead simplex optimisation technique of two variables ( $\eta_\theta(0)$ ,  $P$ ) and determine the variables over the domain  $\theta \in [0, \pi]$ . Then, we calculate  $\lambda_2^2 \lambda_1 - 1$  obtained at  $\theta_{\text{wr}}$  to check if the value is in order of ( $< \mathcal{O}(10^{-10})$ ) and this process is repeated by varying  $\theta_{\text{wr}}$  in the range  $(\frac{1}{2}\pi, \pi)$  till we get the desired solution set  $(\lambda_1, \lambda_2)$  at  $\theta_{\text{wr}}$ , since we observe that both the principal stretch ratio values are greater than one for the points on the boundary in the range  $0 \leq \theta \leq \frac{1}{2}\pi$ . The coordinate  $\theta = \theta_{\text{wr}}$  at which  $\lambda_2^2 \lambda_1 - 1 < \mathcal{O}(10^{-10})$  represents the starting location of wrinkles on the membrane.

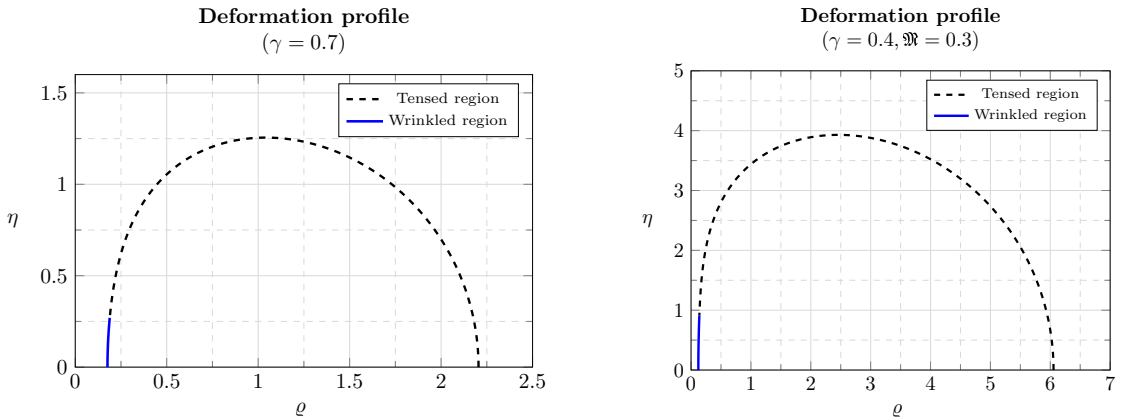


**Figure 8.** Membrane profiles upon wrinkling computed using relaxed strain energy density. Left: Ogden constitutive model (inflating pressure = 1.46,  $\varrho(0) = 2.20$ ). Right: Mooney–Rivlin model (inflating pressure = 7.62,  $\varrho(0) = 6.05$ ).

This numerical scheme is implemented in Matlab R2017b. We note that this scheme is an improvement over the traditional case where  $\theta_{\text{wr}}$  would simply be taken as the first point where  $\sigma_{\phi\phi} < 0$  based on computations made using the standard energy density function.

Wrinkling analysis is carried out for Ogden material with aspect ratio  $\gamma = 0.7$ , for Mooney–Rivlin material with  $\gamma = 0.4$ ,  $\mathfrak{M} = 0.3$ , and for neo-Hookean material with aspect ratio  $\gamma = 0.8$  after observing negative  $\sigma_{\phi\phi}$  stress values as discussed in Section 5.1.2. We observe that wrinkling occurs only in a small region near the inner equator on the membrane for all the above-mentioned cases whenever  $\sigma_{\phi\phi} < 0$ . Thus, according to the tension field theory, wrinkling happens along the  $\phi$  direction while the wrinkle lines ought to appear along the  $\theta$  direction. Membrane profiles upon wrinkling for two cases of Ogden and Mooney–Rivlin models are plotted in Figure 8.

Once the onset of wrinkling is confirmed by observing negative circumferential stress values, we recompute the entire solution using the combination of relaxed and total strain energy densities using the numerical scheme described earlier in this section. We observe that this updated solution (membrane profile and location of wrinkling) is different from the one in which  $\theta_{\text{wr}}$  is obtained using the standard strain energy. Values obtained by both the solutions and relative errors are presented in Table 2. Here  $\theta = \theta_{\text{wr}}$  is the starting point of wrinkles in the reference configuration. Maximum error in the calculations of  $\theta_{\text{wr}}$  is 0.77% or  $1.3^\circ$  for the Mooney–Rivlin material at the pressure  $P = 7.62$ . Although the error between these two approaches in this case of toroidal geometry is small, the difference in solutions is still noteworthy and might be more relevant in other constitutive models or membrane geometry.

## 6. Conclusions

In this work we have presented new analysis and results in the study of free inflation of a nonlinear hyperelastic toroidal membrane. To analyse the deformation behaviour and instabilities in free inflation of a torus under a hydrostatic pressure, toroidal membranes made of three materials (Ogden, Mooney–Rivlin, and neo-Hookean) are considered and a comparative study is conducted amongst them. We observe

model	$\varrho(0)$	$P$	standard energy density	relaxed energy density	error %
Ogden ( $\gamma = 0.7$ )	2.01	1.41	173.97°	172.98°	0.57
	2.20	1.46	173.07°	171.81°	0.73
Mooney–Rivlin ( $\gamma = 0.4, \mathfrak{M} = 0.3$ )	5.55	7.23	176.13°	175.41°	0.41
	6.05	7.62	174.42°	173.07°	0.77
neo-Hookean ( $\gamma = 0.8$ )	2.21	1.84	175.41°	174.60°	0.46
	2.31	1.87	175.41°	174.60°	0.46

**Table 2.** Error in the prediction of the parameter  $\theta_{\text{wr}}$  by standard strain energy density function.

strain-hardening behaviour in Ogden and Mooney–Rivlin material models after the limit point pressure. For the neo-Hookean model bifurcation of solution occurs well post limit point for  $\gamma = 0.3$  corresponding to the second mode, and very close to the limit point for all other aspect ratios for the first mode.

We notice that limit point pressure decreases with increase in aspect ratio and increases with increase in stiffness of the membrane. We also notice that for Mooney–Rivlin model with higher aspect ratio and a stiffer material, nondimensional pressure increases monotonically with inflation. In the compressive stress regions, we use the concept of relaxed strain energy density to study wrinkling behaviour and we observe differences between the wrinkled configuration predicted by standard strain energy density and its relaxed form.

Based on our results on critical point bifurcation and wrinkling, it can be claimed that the predicted behaviour of membrane in Figure 4 and Figure 6 for large volume cases is most likely inaccurate. The fundamental solution does not hold for the postinstability regime and a recalculation of configuration/ stress/ pressure needs to be performed. This postbuckling analysis to understand membrane's behaviour will be undertaken as future work.

## Appendix: Matrix coefficients of governing equations for various constitutive models

**A.1. Coefficients for Ogden model.** For Ogden constitutive model, the governing equation (8) gives

$$\sum_{j=1}^3 \frac{\mu_j}{\lambda_1^{\alpha_j+3} \lambda_2^{\alpha_j+1} \gamma^{2\alpha_j+2} R^{2\alpha_j+2} [\varrho_\theta^2 + \eta_\theta^2]^{3/2}} [\hat{A}_j \varrho_{\theta\theta} + \hat{B}_j \eta_{\theta\theta} + \hat{C}_j] + \left[ \frac{\hat{P} R_b}{T} \right] \varrho \eta_\theta = 0, \quad (36)$$

while the governing equation (9) results in

$$\sum_{j=1}^3 \frac{\mu_j}{\lambda_1^{\alpha_j+3} \lambda_2^{\alpha_j+1} \gamma^{2\alpha_j+2} R^{2\alpha_j+2} [\varrho_\theta^2 + \eta_\theta^2]^{3/2}} [\hat{D}_j \varrho_{\theta\theta} + \hat{E}_j \eta_{\theta\theta} + \hat{F}_j] - \left[ \frac{\hat{P} R_b}{T} \right] \varrho \varrho_\theta = 0, \quad (37)$$

where

$$\begin{aligned} \hat{A}_j = & [\alpha_j - 1][\varrho_\theta^2 + \eta_\theta^2]^{\alpha_j} \varrho^{\alpha_j} R^{\alpha_j} + [\alpha_j + 1] \gamma^{2\alpha_j} R^{2\alpha_j} \varrho_\theta^2 [\varrho_\theta^2 + \eta_\theta^2] \varrho R^2 \\ & + [[\varrho_\theta^2 + \eta_\theta^2]^{\alpha_j} \varrho^{\alpha_j} R^{\alpha_j} - \gamma^{2\alpha_j} R^{2\alpha_j}] \eta_\theta^2 [\varrho_\theta^2 + \eta_\theta^2] \varrho R^2, \end{aligned}$$

$$\begin{aligned}
 \widehat{B}_j &= [\alpha_j - 1][\varrho_\theta^2 + \eta_\theta^2]^{\alpha_j} \varrho^{\alpha_j} R^{\alpha_j} + [\alpha_j + 1]\gamma^{2\alpha_j} R^{2\alpha_j} \varrho_\theta \eta_\theta [\varrho_\theta^2 + \eta_\theta^2] \varrho R^2 \\
 &\quad - [[\varrho_\theta^2 + \eta_\theta^2]^{\alpha_j} \varrho^{\alpha_j} R^{\alpha_j} - \gamma^{2\alpha_j} R^{2\alpha_j}] \varrho_\theta \eta_\theta [\varrho_\theta^2 + \eta_\theta^2] \varrho R^2, \\
 \widehat{C}_j &= \alpha_j [\varrho_\theta R + \varrho \gamma \sin \theta] \varrho_\theta [\varrho_\theta^2 + \eta_\theta^2]^2 \gamma^{2\alpha_j} R^{2\alpha_j+1} \\
 &\quad - [[\varrho_\theta^2 + \eta_\theta^2]^{\alpha_j} \varrho^{\alpha_j} R^{\alpha_j} - \gamma^{2\alpha_j} R^{2\alpha_j}] \varrho \varrho_\theta [\varrho_\theta^2 + \eta_\theta^2]^2 \gamma R \sin \theta \\
 &\quad - [[\varrho_\theta^2 + \eta_\theta^2]^{\alpha_j/2} \varrho^{2\alpha_j} \gamma^{\alpha_j} - \gamma^{2\alpha_j} R^{2\alpha_j}] [\varrho_\theta^2 + \eta_\theta^2]^3 R^2,
 \end{aligned} \tag{38}$$

and

$$\begin{aligned}
 \widehat{D}_j &= [\alpha_j - 1][\varrho_\theta^2 + \eta_\theta^2]^{\alpha_j} \varrho^{\alpha_j} R^{\alpha_j} + [\alpha_j + 1]\gamma^{2\alpha_j} R^{2\alpha_j} \varrho_\theta \eta_\theta [\varrho_\theta^2 + \eta_\theta^2] \varrho R^2 \\
 &\quad - [[\varrho_\theta^2 + \eta_\theta^2]^{\alpha_j} \varrho^{\alpha_j} R^{\alpha_j} - \gamma^{2\alpha_j} R^{2\alpha_j}] \varrho_\theta \eta_\theta [\varrho_\theta^2 + \eta_\theta^2] \varrho R^2, \\
 \widehat{E}_j &= [\alpha_j - 1][\varrho_\theta^2 + \eta_\theta^2]^{\alpha_j} \varrho^{\alpha_j} R^{\alpha_j} + [\alpha_j + 1]\gamma^{2\alpha_j} R^{2\alpha_j} \eta_\theta^2 [\varrho_\theta^2 + \eta_\theta^2] \varrho R^2 \\
 &\quad + [[\varrho_\theta^2 + \eta_\theta^2]^{\alpha_j} \varrho^{\alpha_j} R^{\alpha_j} - \gamma^{2\alpha_j} R^{2\alpha_j}] \varrho_\theta^2 [\varrho_\theta^2 + \eta_\theta^2] \varrho R^2, \\
 \widehat{F}_j &= \alpha_j [\varrho_\theta R + \varrho \gamma \sin \theta] \eta_\theta [\varrho_\theta^2 + \eta_\theta^2]^2 \gamma^{2\alpha_j} R^{2\alpha_j+1} \\
 &\quad - [[\varrho_\theta^2 + \eta_\theta^2]^{\alpha_j} \varrho^{\alpha_j} R^{\alpha_j} - \gamma^{2\alpha_j} R^{2\alpha_j}] \varrho \eta_\theta [\varrho_\theta^2 + \eta_\theta^2]^2 \gamma R \sin \theta.
 \end{aligned} \tag{39}$$

The components of matrices in (14) for the Ogden energy density are given by

$$\begin{aligned}
 S_{22} &= \mu_1^* [\mathcal{U}_1 R^2 [\mathcal{U}_2^2 + \mathcal{U}_4^2] [[S^1] \mathcal{U}_2^2 + [S^2] \mathcal{U}_4^2]] \lambda_1^{\alpha_2+\alpha_3+6} \lambda_2^{\alpha_2+\alpha_3+2} \gamma^{2\alpha_2+2\alpha_3+4} R^{2\alpha_2+2\alpha_3+4} \\
 &\quad + \mu_2^* [\mathcal{U}_1 R^2 [\mathcal{U}_2^2 + \mathcal{U}_4^2] [[S^3] \mathcal{U}_2^2 + [S^4] \mathcal{U}_4^2]] \lambda_1^{\alpha_1+\alpha_3+6} \lambda_2^{\alpha_1+\alpha_3+2} \gamma^{2\alpha_1+2\alpha_3+4} R^{2\alpha_1+2\alpha_3+4} \\
 &\quad + \mu_3^* [\mathcal{U}_1 R^2 [\mathcal{U}_2^2 + \mathcal{U}_4^2] [[S^5] \mathcal{U}_2^2 + [S^6] \mathcal{U}_4^2]] \lambda_1^{\alpha_1+\alpha_2+6} \lambda_2^{\alpha_1+\alpha_2+2} \gamma^{2\alpha_1+2\alpha_2+4} R^{2\alpha_1+2\alpha_2+4}, \\
 S_{24} &= \mu_1^* [\mathcal{U}_1 R^2 [\mathcal{U}_2^2 + \mathcal{U}_4^2] [[S^1] \mathcal{U}_2 \mathcal{U}_4 - [S^2] \mathcal{U}_2 \mathcal{U}_4]] \lambda_1^{\alpha_2+\alpha_3+6} \lambda_2^{\alpha_2+\alpha_3+2} \gamma^{2\alpha_2+2\alpha_3+4} R^{2\alpha_2+2\alpha_3+4} \\
 &\quad + \mu_2^* [\mathcal{U}_1 R^2 [\mathcal{U}_2^2 + \mathcal{U}_4^2] [[S^3] \mathcal{U}_2 \mathcal{U}_4 - [S^4] \mathcal{U}_2 \mathcal{U}_4]] \lambda_1^{\alpha_1+\alpha_3+6} \lambda_2^{\alpha_1+\alpha_3+2} \gamma^{2\alpha_1+2\alpha_3+4} R^{2\alpha_1+2\alpha_3+4} \\
 &\quad + \mu_3^* [\mathcal{U}_1 R^2 [\mathcal{U}_2^2 + \mathcal{U}_4^2] [[S^5] \mathcal{U}_2 \mathcal{U}_4 - [S^6] \mathcal{U}_2 \mathcal{U}_4]] \lambda_1^{\alpha_1+\alpha_2+6} \lambda_2^{\alpha_1+\alpha_2+2} \gamma^{2\alpha_1+2\alpha_2+4} R^{2\alpha_1+2\alpha_2+4}, \\
 S_{42} &= \mu_1^* [\mathcal{U}_1 R^2 [\mathcal{U}_2^2 + \mathcal{U}_4^2] [[S^1] \mathcal{U}_2 \mathcal{U}_4 - [S^2] \mathcal{U}_2 \mathcal{U}_4]] \lambda_1^{\alpha_2+\alpha_3+6} \lambda_2^{\alpha_2+\alpha_3+2} \gamma^{2\alpha_2+2\alpha_3+4} R^{2\alpha_2+2\alpha_3+4} \\
 &\quad + \mu_2^* [\mathcal{U}_1 R^2 [\mathcal{U}_2^2 + \mathcal{U}_4^2] [[S^3] \mathcal{U}_2 \mathcal{U}_4 - [S^4] \mathcal{U}_2 \mathcal{U}_4]] \lambda_1^{\alpha_1+\alpha_3+6} \lambda_2^{\alpha_1+\alpha_3+2} \gamma^{2\alpha_1+2\alpha_3+4} R^{2\alpha_1+2\alpha_3+4} \\
 &\quad + \mu_3^* [\mathcal{U}_1 R^2 [\mathcal{U}_2^2 + \mathcal{U}_4^2] [[S^5] \mathcal{U}_2 \mathcal{U}_4 - [S^6] \mathcal{U}_2 \mathcal{U}_4]] \lambda_1^{\alpha_1+\alpha_2+6} \lambda_2^{\alpha_1+\alpha_2+2} \gamma^{2\alpha_1+2\alpha_2+4} R^{2\alpha_1+2\alpha_2+4}, \\
 S_{44} &= \mu_1^* [\mathcal{U}_1 R^2 [\mathcal{U}_2^2 + \mathcal{U}_4^2] [[S^1] \mathcal{U}_4^2 + [S^2] \mathcal{U}_2^2]] \lambda_1^{\alpha_2+\alpha_3+6} \lambda_2^{\alpha_2+\alpha_3+2} \gamma^{2\alpha_2+2\alpha_3+4} R^{2\alpha_2+2\alpha_3+4} \\
 &\quad + \mu_2^* [\mathcal{U}_1 R^2 [\mathcal{U}_2^2 + \mathcal{U}_4^2] [[S^3] \mathcal{U}_4^2 + [S^4] \mathcal{U}_2^2]] \lambda_1^{\alpha_1+\alpha_3+6} \lambda_2^{\alpha_1+\alpha_3+2} \gamma^{2\alpha_1+2\alpha_3+4} R^{2\alpha_1+2\alpha_3+4} \\
 &\quad + \mu_3^* [\mathcal{U}_1 R^2 [\mathcal{U}_2^2 + \mathcal{U}_4^2] [[S^5] \mathcal{U}_4^2 + [S^6] \mathcal{U}_2^2]] \lambda_1^{\alpha_1+\alpha_2+6} \lambda_2^{\alpha_1+\alpha_2+2} \gamma^{2\alpha_1+2\alpha_2+4} R^{2\alpha_1+2\alpha_2+4},
 \end{aligned} \tag{40}$$

and

$$\begin{aligned}
 \mathcal{V}_1 &= \mu_1^* [\mathcal{V}^2] \mathcal{U}_1 \mathcal{U}_2 [\mathcal{U}_2^2 + \mathcal{U}_4^2]^2 \gamma R \sin \theta + [\mathcal{V}^7] [\mathcal{U}_2^2 + \mathcal{U}_4^2]^3 R^2 \lambda_1^{\alpha_2+\alpha_3+6} \lambda_2^{\alpha_2+\alpha_3+2} \gamma^{2\alpha_2+2\alpha_3+4} R^{2\alpha_2+2\alpha_3+4} \\
 &\quad - \mu_1^* [\mathcal{V}^1] \mathcal{U}_2 [\mathcal{U}_2^2 + \mathcal{U}_4^2]^2 \lambda_1^{\alpha_2+\alpha_3+6} \lambda_2^{\alpha_2+\alpha_3+2} \gamma^{2\alpha_2+2\alpha_3+4} R^{2\alpha_2+2\alpha_3+4} \\
 &\quad + \mu_2^* [\mathcal{V}^4] \mathcal{U}_1 \mathcal{U}_2 [\mathcal{U}_2^2 + \mathcal{U}_4^2]^2 \gamma R \sin \theta + [\mathcal{V}^8] [\mathcal{U}_2^2 + \mathcal{U}_4^2]^3 R^2 \lambda_1^{\alpha_1+\alpha_3+6} \lambda_2^{\alpha_1+\alpha_3+2} \gamma^{2\alpha_1+2\alpha_3+4} R^{2\alpha_1+2\alpha_3+4} \\
 &\quad - \mu_2^* [\mathcal{V}^3] \mathcal{U}_2 [\mathcal{U}_2^2 + \mathcal{U}_4^2]^2 \lambda_1^{\alpha_1+\alpha_3+6} \lambda_2^{\alpha_1+\alpha_3+2} \gamma^{2\alpha_1+2\alpha_3+4} R^{2\alpha_1+2\alpha_3+4}
 \end{aligned}$$

$$\begin{aligned}
& + \mu_3^* [\mathcal{V}^6] \mathcal{U}_1 \mathcal{U}_2 [\mathcal{U}_2^2 + \mathcal{U}_4^2]^2 \gamma R \sin \theta + [\mathcal{V}^9] [\mathcal{U}_2^2 + \mathcal{U}_4^2]^3 R^2 \lambda_1^{\alpha_1 + \alpha_2 + 6} \lambda_2^{\alpha_1 + \alpha_2 + 2} \gamma^{2\alpha_1 + 2\alpha_2 + 4} R^{2\alpha_1 + 2\alpha_2 + 4} \\
& - \mu_3^* [\mathcal{V}^5] \mathcal{U}_2 [\mathcal{U}_2^2 + \mathcal{U}_4^2]^2 \lambda_1^{\alpha_1 + \alpha_2 + 6} \lambda_2^{\alpha_1 + \alpha_2 + 2} \gamma^{2\alpha_1 + 2\alpha_2 + 4} R^{2\alpha_1 + 2\alpha_2 + 4} \\
& - \frac{1}{2} \mu_1^* P \mathcal{U}_1 \mathcal{U}_4 [\mathcal{U}_2^2 + \mathcal{U}_4^2]^3 \lambda_1^{\alpha_1 + \alpha_2 + \alpha_3 + 9} \lambda_2^{\alpha_1 + \alpha_2 + \alpha_3 + 3} \gamma^{2\alpha_1 + 2\alpha_2 + 2\alpha_3 + 6} R^{2\alpha_1 + 2\alpha_2 + 2\alpha_3 + 6}, \\
\mathcal{V}_2 = & \mu_1^* [\mathcal{V}^2] \mathcal{U}_1 \mathcal{U}_4 [\mathcal{U}_2^2 + \mathcal{U}_4^2]^2 \gamma R \sin \theta \lambda_1^{\alpha_2 + \alpha_3 + 6} \lambda_2^{\alpha_2 + \alpha_3 + 2} \gamma^{2\alpha_2 + 2\alpha_3 + 4} R^{2\alpha_2 + 2\alpha_3 + 4} \\
& - \mu_1^* [\mathcal{V}^1] \mathcal{U}_4 [\mathcal{U}_2^2 + \mathcal{U}_4^2]^2 \lambda_1^{\alpha_2 + \alpha_3 + 6} \lambda_2^{\alpha_2 + \alpha_3 + 2} \gamma^{2\alpha_2 + 2\alpha_3 + 4} R^{2\alpha_2 + 2\alpha_3 + 4} \\
& + \mu_2^* [\mathcal{V}^4] \mathcal{U}_1 \mathcal{U}_4 [\mathcal{U}_2^2 + \mathcal{U}_4^2]^2 \gamma R \sin \theta \lambda_1^{\alpha_1 + \alpha_3 + 6} \lambda_2^{\alpha_1 + \alpha_3 + 2} \gamma^{2\alpha_1 + 2\alpha_3 + 4} R^{2\alpha_1 + 2\alpha_3 + 4} \\
& - \mu_2^* [\mathcal{V}^3] \mathcal{U}_4 [\mathcal{U}_2^2 + \mathcal{U}_4^2]^2 \lambda_1^{\alpha_1 + \alpha_3 + 6} \lambda_2^{\alpha_1 + \alpha_3 + 2} \gamma^{2\alpha_1 + 2\alpha_3 + 4} R^{2\alpha_1 + 2\alpha_3 + 4} \\
& + \mu_3^* [\mathcal{V}^6] \mathcal{U}_1 \mathcal{U}_4 [\mathcal{U}_2^2 + \mathcal{U}_4^2]^2 \gamma R \sin \theta \lambda_1^{\alpha_1 + \alpha_2 + 6} \lambda_2^{\alpha_1 + \alpha_2 + 2} \gamma^{2\alpha_1 + 2\alpha_2 + 4} R^{2\alpha_1 + 2\alpha_2 + 4} \\
& - \mu_3^* [\mathcal{V}^5] \mathcal{U}_4 [\mathcal{U}_2^2 + \mathcal{U}_4^2]^2 \lambda_1^{\alpha_1 + \alpha_2 + 6} \lambda_2^{\alpha_1 + \alpha_2 + 2} \gamma^{2\alpha_1 + 2\alpha_2 + 4} R^{2\alpha_1 + 2\alpha_2 + 4} \\
& + \frac{1}{2} \mu_1^* P \mathcal{U}_1 \mathcal{U}_2 [\mathcal{U}_2^2 + \mathcal{U}_4^2]^3 \lambda_1^{\alpha_1 + \alpha_2 + \alpha_3 + 9} \lambda_2^{\alpha_1 + \alpha_2 + \alpha_3 + 3} \gamma^{2\alpha_1 + 2\alpha_2 + 2\alpha_3 + 6} R^{2\alpha_1 + 2\alpha_2 + 2\alpha_3 + 6}, \tag{41}
\end{aligned}$$

along with

$$\begin{aligned}
\mathcal{S}^1 &= [\alpha_1 - 1] [\mathcal{U}_2^2 + \mathcal{U}_4^2]^{\alpha_1} \mathcal{U}_1^{\alpha_1} R^{\alpha_1} + [\alpha_1 + 1] \gamma^{2\alpha_1} R^{2\alpha_1}, & \mathcal{S}^2 &= [\mathcal{U}_2^2 + \mathcal{U}_4^2]^{\alpha_1} \mathcal{U}_1^{\alpha_1} R^{\alpha_1} - \gamma^{2\alpha_1} R^{2\alpha_1}, \\
\mathcal{S}^3 &= [\alpha_2 - 1] [\mathcal{U}_2^2 + \mathcal{U}_4^2]^{\alpha_2} \mathcal{U}_1^{\alpha_2} R^{\alpha_2} + [\alpha_2 + 1] \gamma^{2\alpha_2} R^{2\alpha_2}, & \mathcal{S}^4 &= [\mathcal{U}_2^2 + \mathcal{U}_4^2]^{\alpha_2} \mathcal{U}_1^{\alpha_2} R^{\alpha_2} - \gamma^{2\alpha_2} R^{2\alpha_2}, \\
\mathcal{S}^5 &= [\alpha_3 - 1] [\mathcal{U}_2^2 + \mathcal{U}_4^2]^{\alpha_3} \mathcal{U}_1^{\alpha_3} R^{\alpha_3} + [\alpha_3 + 1] \gamma^{2\alpha_3} R^{2\alpha_3}, & \mathcal{S}^6 &= [\mathcal{U}_2^2 + \mathcal{U}_4^2]^{\alpha_3} \mathcal{U}_1^{\alpha_3} R^{\alpha_3} - \gamma^{2\alpha_3} R^{2\alpha_3}, \\
\mathcal{V}^1 &= \alpha_1 [\mathcal{U}_2 R + \mathcal{U}_1 \gamma \sin \theta] \gamma^{2\alpha_1} R^{2\alpha_1 + 1}, & \mathcal{V}^2 &= [\mathcal{U}_2^2 + \mathcal{U}_4^2]^{\alpha_1} \mathcal{U}_1^{\alpha_1} R^{\alpha_1} - \gamma^{2\alpha_1} R^{2\alpha_1}, \\
\mathcal{V}^3 &= \alpha_2 [\mathcal{U}_2 R + \mathcal{U}_1 \gamma \sin \theta] \gamma^{2\alpha_2} R^{2\alpha_2 + 1}, & \mathcal{V}^4 &= [\mathcal{U}_2^2 + \mathcal{U}_4^2]^{\alpha_2} \mathcal{U}_1^{\alpha_2} R^{\alpha_2} - \gamma^{2\alpha_2} R^{2\alpha_2}, \\
\mathcal{V}^5 &= \alpha_3 [\mathcal{U}_2 R + \mathcal{U}_1 \gamma \sin \theta] \gamma^{2\alpha_3} R^{2\alpha_3 + 1}, & \mathcal{V}^6 &= [\mathcal{U}_2^2 + \mathcal{U}_4^2]^{\alpha_3} \mathcal{U}_1^{\alpha_3} R^{\alpha_3} - \gamma^{2\alpha_3} R^{2\alpha_3}, \\
\mathcal{V}^7 &= [\mathcal{U}_2^2 + \mathcal{U}_4^2]^{\alpha_1/2} \mathcal{U}_1^{2\alpha_1} \gamma^{\alpha_1} - \gamma^{2\alpha_1} R^{2\alpha_1}, & \mathcal{V}^8 &= [\mathcal{U}_2^2 + \mathcal{U}_4^2]^{\alpha_2/2} \mathcal{U}_1^{2\alpha_2} \gamma^{\alpha_2} - \gamma^{2\alpha_2} R^{2\alpha_2}, \\
\mathcal{V}^9 &= [\mathcal{U}_2^2 + \mathcal{U}_4^2]^{\alpha_3/2} \mathcal{U}_1^{2\alpha_3} \gamma^{\alpha_3} - \gamma^{2\alpha_3} R^{2\alpha_3},
\end{aligned}$$

$$P = \frac{2\hat{P}R_b}{\mu_1 T}. \tag{42}$$

Nondimensional principal Cauchy stresses in the  $\theta$ - and  $\phi$ -directions are computed as

$$\sigma_{\theta\theta} = \left[ \frac{\lambda_3 \alpha_1}{\mu_1^*} \right] \left[ \sum_{j=1}^3 \mu_j^* \lambda_1^{\alpha_j} - \sum_{j=1}^3 \mu_j^* \lambda_3^{\alpha_j} \right], \quad \sigma_{\phi\phi} = \left[ \frac{\lambda_3 \alpha_1}{\mu_1^*} \right] \left[ \sum_{j=1}^3 \mu_j^* \lambda_2^{\alpha_j} - \sum_{j=1}^3 \mu_j^* \lambda_3^{\alpha_j} \right]. \tag{43}$$

**A.2. Coefficients for Mooney–Rivlin model.** The components of matrices in (14) for the Mooney–Rivlin energy density are given by

$$\begin{aligned}
\mathcal{S}_{22} &= [\mathcal{U}_1 R^2 [\mathcal{U}_2^2 + \mathcal{U}_4^2] [\mathcal{S}_m^1 \mathcal{U}_2^2 + [\mathcal{S}_m^2] \mathcal{U}_4^2]] \lambda_1^4 \\
&\quad - \mathfrak{M} [\mathcal{U}_1 R^2 [\mathcal{U}_2^2 + \mathcal{U}_4^2] [\mathcal{S}_m^3] \mathcal{U}_2^2 + [\mathcal{S}_m^4] \mathcal{U}_4^2]] \lambda_1^8 \lambda_2^4 \gamma^8 R^8, \\
\mathcal{S}_{24} &= [\mathcal{U}_1 R^2 [\mathcal{U}_2^2 + \mathcal{U}_4^2] [\mathcal{S}_m^1] \mathcal{U}_2 \mathcal{U}_4 - [\mathcal{S}_m^2] \mathcal{U}_2 \mathcal{U}_4]] \lambda_1^4 \\
&\quad - \mathfrak{M} [\mathcal{U}_1 R^2 [\mathcal{U}_2^2 + \mathcal{U}_4^2] [\mathcal{S}_m^3] \mathcal{U}_2 \mathcal{U}_4 - [\mathcal{S}_m^4] \mathcal{U}_2 \mathcal{U}_4]] \lambda_1^8 \lambda_2^4 \gamma^8 R^8,
\end{aligned}$$



$$\begin{aligned} \mathcal{S}_{42} = \mathcal{S}_{24}, \mathcal{S}_{44} = & [\mathcal{U}_1 R^2 [\mathcal{U}_2^2 + \mathcal{U}_4^2] [\mathcal{S}_m^1 \mathcal{U}_4^2 + \mathcal{S}_m^2 \mathcal{U}_2^2]] \lambda_1^4 \\ & - \mathfrak{M} [\mathcal{U}_1 R^2 [\mathcal{U}_2^2 + \mathcal{U}_4^2] [\mathcal{S}_m^3 \mathcal{U}_4^2 + \mathcal{S}_m^4 \mathcal{U}_2^2]] \lambda_1^8 \lambda_2^4 \gamma^8 R^8, \end{aligned} \quad (44)$$

and

$$\begin{aligned} \mathcal{V}_1 = & [\mathcal{V}_m^2] \mathcal{U}_1 \mathcal{U}_2 [\mathcal{U}_2^2 + \mathcal{U}_4^2]^2 \gamma R \sin \theta + [\mathcal{V}_m^5] [\mathcal{U}_2^2 + \mathcal{U}_4^2]^3 R^2 \lambda_1^4 - [\mathcal{V}_m^1] \mathcal{U}_2 [\mathcal{U}_2^2 + \mathcal{U}_4^2]^2 \lambda_1^4 \\ & - \mathfrak{M} [\mathcal{V}_m^4] \mathcal{U}_1 \mathcal{U}_2 [\mathcal{U}_2^2 + \mathcal{U}_4^2]^2 \gamma R \sin \theta + [\mathcal{V}_m^6] [\mathcal{U}_2^2 + \mathcal{U}_4^2]^3 R^2 \lambda_1^8 \lambda_2^4 \gamma^8 R^8 \\ & + \mathfrak{M} [\mathcal{V}_m^3] \mathcal{U}_2 [\mathcal{U}_2^2 + \mathcal{U}_4^2]^2 \lambda_1^8 \lambda_2^4 \gamma^8 R^8 - \frac{1}{2} P \mathcal{U}_1 \mathcal{U}_4 [\mathcal{U}_2^2 + \mathcal{U}_4^2]^{3/2} \lambda_1^9 \lambda_2^3 \gamma^6 R^6, \\ \mathcal{V}_2 = & [\mathcal{V}_m^2] \mathcal{U}_1 \mathcal{U}_4 [\mathcal{U}_2^2 + \mathcal{U}_4^2]^2 \gamma R \sin \theta \lambda_1^4 - [\mathcal{V}_m^1] \mathcal{U}_4 [\mathcal{U}_2^2 + \mathcal{U}_4^2]^2 \lambda_1^4 \\ & - \mathfrak{M} [\mathcal{V}_m^4] \mathcal{U}_1 \mathcal{U}_4 [\mathcal{U}_2^2 + \mathcal{U}_4^2]^2 \gamma R \sin \theta \lambda_1^8 \lambda_2^4 \gamma^8 R^8 \\ & + \mathfrak{M} [\mathcal{V}_m^3] \mathcal{U}_4 [\mathcal{U}_2^2 + \mathcal{U}_4^2]^2 \lambda_1^8 \lambda_2^4 \gamma^8 R^8 + \frac{1}{2} P \mathcal{U}_1 \mathcal{U}_2 [\mathcal{U}_2^2 + \mathcal{U}_4^2]^{3/2} \lambda_1^9 \lambda_2^3 \gamma^6 R^6, \end{aligned} \quad (45)$$

along with

$$\begin{aligned} \mathcal{S}_m^1 = & [\mathcal{U}_2^2 + \mathcal{U}_4^2]^2 \mathcal{U}_1^2 R^2 + 3\gamma^4 R^4, & \mathcal{S}_m^2 = & [\mathcal{U}_2^2 + \mathcal{U}_4^2]^2 \mathcal{U}_1^2 R^2 - \gamma^4 R^4, \\ \mathcal{S}_m^3 = & -3[\mathcal{U}_2^2 + \mathcal{U}_4^2]^{-2} \mathcal{U}_1^{-2} R^{-2} - \gamma^{-4} R^{-4}, & \mathcal{S}_m^4 = & [\mathcal{U}_2^2 + \mathcal{U}_4^2]^{-2} \mathcal{U}_1^{-2} R^{-2} - \gamma^{-4} R^{-4}, \end{aligned} \quad (46)$$

$$\begin{aligned} \mathcal{V}_m^1 = & 2[\mathcal{U}_2 R + \mathcal{U}_1 \gamma \sin \theta] \gamma^4 R^5, & \mathcal{V}_m^2 = & [\mathcal{U}_2^2 + \mathcal{U}_4^2]^2 \mathcal{U}_1^2 R^2 - \gamma^4 R^4, \\ \mathcal{V}_m^3 = & -2[\mathcal{U}_2 R + \mathcal{U}_1 \gamma \sin \theta] \gamma^{-4} R^{-3}, & \mathcal{V}_m^4 = & [\mathcal{U}_2^2 + \mathcal{U}_4^2]^{-2} \mathcal{U}_1^{-2} R^{-2} - \gamma^{-4} R^{-4}, \\ \mathcal{V}_m^5 = & [\mathcal{U}_2^2 + \mathcal{U}_4^2] \mathcal{U}_1^4 \gamma^2 - \gamma^4 R^4, & \mathcal{V}_m^6 = & [\mathcal{U}_2^2 + \mathcal{U}_4^2]^{-1} \mathcal{U}_1^{-4} \gamma^{-2} - \gamma^{-4} R^{-4}, \end{aligned} \quad (47)$$

$$P = \frac{\hat{P} R_b}{\frac{1}{2} \mu_1 T}, \quad \mathfrak{M} = -\frac{\mu_2}{\mu_1}. \quad (48)$$

Nondimensional principal Cauchy stresses in the  $\theta$ - and  $\phi$ -directions are computed as

$$\sigma_{\theta\theta} = 2 \left[ \frac{\lambda_1}{\lambda_2} - \frac{1}{\lambda_1^3 \lambda_2^3} \right] [1 + \mathfrak{M} \lambda_2^2], \quad \sigma_{\phi\phi} = 2 \left[ \frac{\lambda_2}{\lambda_1} - \frac{1}{\lambda_1^3 \lambda_2^3} \right] [1 + \mathfrak{M} \lambda_1^2]. \quad (49)$$

**A.3. Coefficients for neo-Hookean model.** The components of matrices in (14) for the neo-Hookean energy density are given by

$$\begin{aligned} \mathcal{S}_{22} = & [\mathcal{U}_1 R^2 [\mathcal{U}_2^2 + \mathcal{U}_4^2] [\mathcal{S}_n^1 \mathcal{U}_2^2 + \mathcal{S}_n^2 \mathcal{U}_4^2]] \lambda_1^6 \lambda_2^2 \gamma^4 R^4, \\ \mathcal{S}_{24} = & [\mathcal{U}_1 R^2 [\mathcal{U}_2^2 + \mathcal{U}_4^2] [\mathcal{S}_n^1 \mathcal{U}_2 \mathcal{U}_4 - \mathcal{S}_n^2 \mathcal{U}_2 \mathcal{U}_4]] \lambda_1^6 \lambda_2^2 \gamma^4 R^4, \\ \mathcal{S}_{42} = & \mathcal{S}_{24}, \\ \mathcal{S}_{44} = & [\mathcal{U}_1 R^2 [\mathcal{U}_2^2 + \mathcal{U}_4^2] [\mathcal{S}_n^1 \mathcal{U}_4^2 + \mathcal{S}_n^2 \mathcal{U}_2^2]] \lambda_1^6 \lambda_2^2 \gamma^4 R^4, \end{aligned} \quad (50)$$

and

$$\begin{aligned} \mathcal{V}_1 = & [\mathcal{V}_n^2] \mathcal{U}_1 \mathcal{U}_2 [\mathcal{U}_2^2 + \mathcal{U}_4^2]^2 \gamma R \sin \theta + [\mathcal{V}_n^3] [\mathcal{U}_2^2 + \mathcal{U}_4^2]^3 R^2 \lambda_1^6 \lambda_2^2 \gamma^4 R^4 \\ & - [\mathcal{V}_n^1] \mathcal{U}_2 [\mathcal{U}_2^2 + \mathcal{U}_4^2]^2 \lambda_1^6 \lambda_2^2 \gamma^4 R^4 - \frac{1}{2} P \mathcal{U}_1 \mathcal{U}_4 [\mathcal{U}_2^2 + \mathcal{U}_4^2]^{3/2} \lambda_1^{11} \lambda_2^5 \gamma^{10} R^{10}, \\ \mathcal{V}_2 = & [\mathcal{V}_n^2] \mathcal{U}_1 \mathcal{U}_4 [\mathcal{U}_2^2 + \mathcal{U}_4^2]^2 \gamma R \sin \theta \lambda_1^6 \lambda_2^2 \gamma^4 R^4 - [\mathcal{V}_n^1] \mathcal{U}_4 [\mathcal{U}_2^2 + \mathcal{U}_4^2]^2 \lambda_1^6 \lambda_2^2 \gamma^4 R^4 \\ & + \frac{1}{2} P \mathcal{U}_1 \mathcal{U}_2 [\mathcal{U}_2^2 + \mathcal{U}_4^2]^{3/2} \lambda_1^{11} \lambda_2^5 \gamma^{10} R^{10}, \end{aligned} \quad (51)$$

along with

$$\begin{aligned} S_n^1 &= [\mathcal{U}_2^2 + \mathcal{U}_4^2] \mathcal{U}_1^2 R^2 + 3\gamma^4 R^4, \quad S_n^2 = [\mathcal{U}_2^2 + \mathcal{U}_4^2] \mathcal{U}_1^2 R^2 - \gamma^4 R^4, \\ \mathcal{V}_n^1 &= 2[\mathcal{U}_2 R + \mathcal{U}_1 \gamma \sin \theta] \gamma^4 R^5, \quad \mathcal{V}_n^2 = [\mathcal{U}_2^2 + \mathcal{U}_4^2] \mathcal{U}_1^2 R^2 - \gamma^4 R^4, \quad \mathcal{V}_n^3 = [\mathcal{U}_2^2 + \mathcal{U}_4^2] \mathcal{U}_1^4 \gamma^2 - \gamma^4 R^4, \\ P &= \frac{\widehat{P} R_b}{\frac{1}{2} \mu_1 T}. \end{aligned} \quad (52)$$

Nondimensional principal Cauchy stresses in the  $\theta$ - and  $\phi$ -directions are computed as

$$\sigma_{\theta\theta} = 2 \left[ \frac{\lambda_1}{\lambda_2} - \frac{1}{\lambda_1^3 \lambda_2^3} \right], \quad \sigma_{\phi\phi} = 2 \left[ \frac{\lambda_2}{\lambda_1} - \frac{1}{\lambda_1^3 \lambda_2^3} \right]. \quad (53)$$

**A.4. Matrix coefficients for wrinkled region.** In the wrinkled region, using the relaxed energy density obtained by substituting  $\lambda_2 = 1/\sqrt{\lambda_1}$ , we find that the terms  $S_{22}$ ,  $S_{24}$ ,  $S_{42}$ ,  $S_{44}$ ,  $\mathcal{V}_1$ ,  $\mathcal{V}_2$  for each of the material models discussed above are modified as below.

For Ogden energy density, we get

$$\begin{aligned} S_{22} &= \mu_1^* R [\varrho_\theta^2 [\alpha_1 - 1] \lambda_1^{3\alpha_1/2} + [\tfrac{1}{2} \alpha_1 + 1]] + \eta_\theta^2 [\lambda_1^{3\alpha_1/2} - 1] \lambda_1^{(\alpha_2 + \alpha_3)/2 + 8} \\ &\quad + \mu_2^* R [\varrho_\theta^2 [\alpha_2 - 1] \lambda_1^{3\alpha_2/2} + [\tfrac{1}{2} \alpha_2 + 1]] + \eta_\theta^2 [\lambda_1^{3\alpha_2/2} - 1] \lambda_1^{(\alpha_1 + \alpha_3)/2 + 8} \\ &\quad + \mu_3^* R [\varrho_\theta^2 [\alpha_3 - 1] \lambda_1^{3\alpha_3/2} + [\tfrac{1}{2} \alpha_3 + 1]] + \eta_\theta^2 [\lambda_1^{3\alpha_3/2} - 1] \lambda_1^{(\alpha_1 + \alpha_2)/2 + 8}, \\ S_{24} &= \mu_1^* R [\varrho_\theta \eta_\theta [\alpha_1 - 2] \lambda_1^{3\alpha_1/2} + [\tfrac{1}{2} \alpha_1 + 2]] \lambda_1^{(\alpha_2 + \alpha_3)/2 + 8} \\ &\quad + \mu_2^* R [\varrho_\theta \eta_\theta [\alpha_2 - 2] \lambda_1^{3\alpha_2/2} + [\tfrac{1}{2} \alpha_2 + 2]] \lambda_1^{(\alpha_1 + \alpha_3)/2 + 8} \\ &\quad + \mu_3^* R [\varrho_\theta \eta_\theta [\alpha_3 - 2] \lambda_1^{3\alpha_3/2} + [\tfrac{1}{2} \alpha_3 + 2]] \lambda_1^{(\alpha_1 + \alpha_2)/2 + 8}, \\ S_{42} &= S_{24}, \\ S_{44} &= \mu_1^* R [\eta_\theta^2 [\alpha_1 - 1] \lambda_1^{3\alpha_1/2} + [\tfrac{1}{2} \alpha_1 + 1]] + \varrho_\theta^2 [\lambda_1^{3\alpha_1/2} - 1] \lambda_1^{(\alpha_2 + \alpha_3)/2 + 8} \\ &\quad + \mu_2^* R [\eta_\theta^2 [\alpha_2 - 1] \lambda_1^{3\alpha_2/2} + [\tfrac{1}{2} \alpha_2 + 1]] + \varrho_\theta^2 [\lambda_1^{3\alpha_2/2} - 1] \lambda_1^{(\alpha_1 + \alpha_3)/2 + 8} \\ &\quad + \mu_3^* R [\eta_\theta^2 [\alpha_3 - 1] \lambda_1^{3\alpha_3/2} + [\tfrac{1}{2} \alpha_3 + 1]] + \varrho_\theta^2 [\lambda_1^{3\alpha_3/2} - 1] \lambda_1^{(\alpha_1 + \alpha_2)/2 + 8}, \end{aligned} \quad (54)$$

along with

$$\begin{aligned} \mathcal{V}_1 &= [\mu_1^* [\lambda_1^{3\alpha_1/2} - 1] \lambda_1^{(\alpha_2 + \alpha_3)/2 + 10} + \mu_2^* [\lambda_1^{3\alpha_2/2} - 1] \lambda_1^{(\alpha_1 + \alpha_3)/2 + 10} \\ &\quad + \mu_3^* [\lambda_1^{3\alpha_3/2} - 1] \lambda_1^{(\alpha_1 + \alpha_2)/2 + 10}] \gamma^3 \mathcal{U}_2 \sin \theta \\ &\quad - \tfrac{1}{2} \mu_1^* P \mathcal{U}_1 \mathcal{U}_4 \lambda_1^{(\alpha_1 + \alpha_2 + \alpha_3)/2 + 12} \gamma^3, \\ \mathcal{V}_2 &= [\mu_1^* [\lambda_1^{3\alpha_1/2} - 1] \lambda_1^{(\alpha_2 + \alpha_3)/2 + 10} + \mu_2^* [\lambda_1^{3\alpha_2/2} - 1] \lambda_1^{(\alpha_1 + \alpha_3)/2 + 10} \\ &\quad + \mu_3^* [\lambda_1^{3\alpha_3/2} - 1] \lambda_1^{(\alpha_1 + \alpha_2)/2 + 10}] \gamma^3 \mathcal{U}_4 \sin \theta \\ &\quad + \tfrac{1}{2} \mu_1^* P \mathcal{U}_1 \mathcal{U}_2 \lambda_1^{(\alpha_1 + \alpha_2 + \alpha_3)/2 + 12} \gamma^3, \\ P &= \frac{2 \widehat{P} R_b}{\mu_1 T}. \end{aligned} \quad (55)$$

For Mooney–Rivlin energy density, we get

$$\begin{aligned} S_{22} &= R[\varrho_\theta^2[\lambda_1^4 + 2\lambda_1 + 3\mathfrak{M}] + \eta_\theta^2[\lambda_1^4 - \lambda_1 + \mathfrak{M}[\lambda_1^3 - 1]]], \\ S_{24} &= R[\varrho_\theta \eta_\theta [3\lambda_1 + 4\mathfrak{M} - \mathfrak{M}\lambda_1^3]], \\ S_{42} &= S_{24}, \\ S_{44} &= R[\eta_\theta^2[\lambda_1^4 + 2\lambda_1 + 3\mathfrak{M}] + \varrho_\theta^2[\lambda_1^4 - \lambda_1 + \mathfrak{M}[\lambda_1^3 - 1]]], \end{aligned} \quad (56)$$

along with

$$\begin{aligned} \nu_1 &= [\lambda_1^4 - \lambda_1 + \mathfrak{M}[\lambda_1^3 - 1]]\gamma^3 \lambda_1^2 \mathcal{U}_2 \sin \theta - \left[\left[\frac{1}{2}P\right]\mathcal{U}_1 \mathcal{U}_4 \lambda_1^6 \gamma^3\right], \\ \nu_2 &= [\lambda_1^4 - \lambda_1 + \mathfrak{M}[\lambda_1^3 - 1]]\gamma^3 \lambda_1^2 \mathcal{U}_4 \sin \theta + \left[\left[\frac{1}{2}P\right]\mathcal{U}_1 \mathcal{U}_2 \lambda_1^6 \gamma^3\right]. \end{aligned} \quad (57)$$

For neo-Hookean energy density, we get

$$\begin{aligned} S_{22} &= R[\varrho_\theta^2[\lambda_1^4 + 2\lambda_1] + \eta_\theta^2[\lambda_1^4 - \lambda_1]], & S_{24} &= R[\varrho_\theta \eta_\theta [3\lambda_1]], \\ S_{42} &= S_{24}, & S_{44} &= R[\eta_\theta^2[\lambda_1^4 + 2\lambda_1] + \varrho_\theta^2[\lambda_1^4 - \lambda_1]], \end{aligned} \quad (58)$$

and

$$\nu_1 = [\lambda_1^4 - \lambda_1]\gamma^3 \lambda_1^2 \mathcal{U}_2 \sin \theta - \left[\left[\frac{1}{2}P\right]\mathcal{U}_1 \mathcal{U}_4 \lambda_1^6 \gamma^3\right], \quad (59)$$

$$\nu_2 = [\lambda_1^4 - \lambda_1]\gamma^3 \lambda_1^2 \mathcal{U}_4 \sin \theta + \left[\left[\frac{1}{2}P\right]\mathcal{U}_1 \mathcal{U}_2 \lambda_1^6 \gamma^3\right]. \quad (60)$$

### Acknowledgements

Major portion of this work was conducted when both the authors were based at IIT Hyderabad. This work was financially supported by a research grant associated with the Ramanujan fellowship by the Science and Engineering Research Board (Sanction No: SB/S2/RJN-116/2015) awarded to Saxena.

### References

- [Başar and Itskov 1998] Y. Başar and M. Itskov, “Finite element formulation of the Ogden material model with application to rubber-like shells”, *Int. J. Numer. Methods Eng.* **42**:7 (1998), 1279–1305.
- [Barsotti 2015] R. Barsotti, “Approximated solutions for axisymmetric wrinkled inflated membranes”, *J. Appl. Mech. (ASME)* **82**:11 (2015), art. id. 111007.
- [Benedict et al. 1979] R. Benedict, A. Wineman, and W. H. Yang, “The determination of limiting pressure in simultaneous elongation and inflation of nonlinear elastic tubes”, *Int. J. Solids Struct.* **15**:3 (1979), 241–249.
- [Bonadies 1987] M. Bonadies, “Asymptotic behaviour of inflated toroidal elastic membranes”, *Rend. Sem. Mat. Univ. Politec. Torino* **45**:3 (1987), 63–74.
- [Budiansky 1974] B. Budiansky, “Theory of buckling and post-buckling behavior of elastic structures”, *Adv. Appl. Mech.* **14** (1974), 1–65.
- [Carroll 1987] M. M. Carroll, “Pressure maximum behavior in inflation of incompressible elastic hollow spheres and cylinders”, *Quart. Appl. Math.* **45**:1 (1987), 141–154.
- [Clark 1950] R. A. Clark, “On the theory of thin elastic toroidal shells”, *J. Math. Phys.* **29**:1-4 (1950), 146–178.
- [Dreyer et al. 1982] W. Dreyer, I. Müller, and P. Strehlow, “A study of equilibria of interconnected balloons”, *Quart. J. Mech. Appl. Math.* **35**:3 (1982), 419–440.
- [Epstein 1999] M. Epstein, “On the wrinkling of anisotropic elastic membranes”, *J. Elasticity* **55**:2 (1999), 99–109.

- [Gruttmann and Taylor 1992] F. Gruttmann and R. L. Taylor, “Theory and finite element formulation of rubberlike membrane shells using principal stretches”, *Int. J. Numer. Methods Eng.* **35**:5 (1992), 1111–1126.
- [Harold 1970] M. E. Harold, “Load transfer via a wrinkled membrane”, *Proc. R. Soc. Lond. A* **316**:1525 (1970), 269–289.
- [Haughton and McKay 1995] D. M. Haughton and B. A. McKay, “Wrinkling of annular discs subjected to radial displacements”, *Int. J. Eng. Sci.* **33**:3 (1995), 335–350.
- [Hill 1980] J. M. Hill, “The finite inflation of a thick-walled elastic torus”, *Quart. J. Mech. Appl. Math.* **33**:4 (1980), 471–490.
- [Holzapfel 2000] G. A. Holzapfel, *Nonlinear solid mechanics: a continuum approach for engineering*, Wiley, Chichester, UK, 2000.
- [Holzapfel et al. 1996] G. A. Holzapfel, R. Eberlein, P. Wriggers, and H. W. Weizsäcker, “A new axisymmetrical membrane element for anisotropic, finite strain analysis of arteries”, *Commun. Numer. Methods Eng.* **12**:8 (1996), 507–517.
- [Horný et al. 2006] L. Horný, R. Žitný, H. Chlup, and H. Macková, “Identification of the material parameters of an aortic wall”, *Bull. Appl. Mech.* **2**:8 (2006), 173–181.
- [Humphrey 1998] J. D. Humphrey, “Computer methods in membrane biomechanics”, *Comput. Methods Biomech. Biomed. Engin.* **1**:3 (1998), 171–210.
- [Jenkins et al. 1998] C. H. Jenkins, F. Haugen, and W. H. Spicher, “Experimental measurement of wrinkling in membranes undergoing planar deformation”, *Exp. Mech.* **38**:2 (1998), 147–152.
- [Jordan 1962] P. F. Jordan, “Stresses and deformations of the thin-walled pressurized torus”, *J. Aerosp. Sci.* **29**:2 (1962), 213–225.
- [Kanner and Horgan 2007] L. M. Kanner and C. O. Horgan, “Elastic instabilities for strain-stiffening rubber-like spherical and cylindrical thin shells under inflation”, *Int. J. Non-Linear Mech.* **42**:2 (2007), 204–215.
- [Khayat et al. 1992] R. E. Khayat, A. Derdorri, and A. Garcia-Réjon, “Inflation of an elastic cylindrical membrane: non-linear deformation and instability”, *Int. J. Solids Struct.* **29**:1 (1992), 69–87.
- [Koiter 1945] W. T. Koiter, *The stability of elastic equilibrium*, Ph.D. thesis, Technische Hooze School, 1945, Available at <https://tinyurl.com/koiterphd>.
- [Kydonieffs and Spencer 1965] A. D. Kydonieffs and A. J. M. Spencer, “The finite inflation of an elastic torus”, *Int. J. Eng. Sci.* **3**:2 (1965), 173–195.
- [Kydonieffs and Spencer 1967] A. D. Kydonieffs and A. J. M. Spencer, “The finite inflation of an elastic toroidal membrane of circular cross section”, *Int. J. Eng. Sci.* **5**:4 (1967), 367–391.
- [Li and Steigmann 1995a] X. Li and D. J. Steigmann, “Finite deformation of a pressurized toroidal membrane”, *Int. J. Non-Linear Mech.* **30**:4 (1995), 583–595.
- [Li and Steigmann 1995b] X. Li and D. J. Steigmann, “Point loads on a hemispherical elastic membrane”, *Int. J. Non-Linear Mech.* **30**:4 (1995), 569–581.
- [Liepins and Sanders 1963] A. Liepins and J. L. Sanders, “Toroidal membrane under internal pressure”, *AIAA J.* **1**:9 (1963), 2105–2110.
- [Mansfield 1981] E. H. Mansfield, “Gravity-induced wrinkle lines in vertical membranes”, *Proc. R. Soc. Lond. A* **375**:1762 (1981), 307–325.
- [Müller and Struchtrup 2002] I. Müller and H. Struchtrup, “Inflating a rubber balloon”, *Math. Mech. Solids* **7**:5 (2002), 569–577.
- [Nayyar et al. 2011] V. Nayyar, K. Ravi-Chandar, and R. Huang, “Stretch-induced stress patterns and wrinkles in hyperelastic thin sheets”, *Int. J. Solids Struct.* **48**:25–26 (2011), 3471–3483.
- [Ogden 1972] R. W. Ogden, “Large deformation isotropic elasticity: on the correlation of theory and experiment for incompressible rubberlike solids”, *Proc. R. Soc. Lond. A* **326**:1567 (1972), 565–584.
- [Papargyri 1995] S. Papargyri-Pegiou, “Stability of the axisymmetric analytical and numerical solutions in a thin-walled pressurized torus of compressible nonlinear elastic material”, *Int. J. Eng. Sci.* **33**:7 (1995), 1005–1025.
- [Papargyri 2005] S. Papargyri-Beskou, “Finite-element analysis of an axisymmetric, thin-walled, nonlinear elastic pressurized torus”, *Acta Mech.* **178**:1–2 (2005), 1–22.

- [Papargyri and Stavrakakis 2000] S. Papargyri-Pegiou and E. Stavrakakis, “Axisymmetric numerical solutions of a thin-walled pressurized torus of incompressible nonlinear elastic materials”, *Comput. Struct.* **77**:6 (2000), 747–757.
- [Patil et al. 2015] A. Patil, A. Nordmark, and A. Eriksson, “Wrinkling of cylindrical membranes with non-uniform thickness”, *Eur. J. Mech. A Solids* **54** (2015), 1–10.
- [Pipkin 1986] A. C. Pipkin, “The relaxed energy density for isotropic elastic membranes”, *IMA J. Appl. Math.* **36**:1 (1986), 85–99.
- [Reddy and Saxena 2017] N. H. Reddy and P. Saxena, “Limit points in the free inflation of a magnetoelastic toroidal membrane”, *Int. J. Non-Linear Mech.* **95** (2017), 248–263.
- [Reddy and Saxena 2018] N. H. Reddy and P. Saxena, “Instabilities in the axisymmetric magnetoelastic deformation of a cylindrical membrane”, *Int. J. Solids Struct.* **136-137** (2018), 203–219.
- [Roxburgh 1995] D. G. Roxburgh, “Inflation of nonlinearly deformed annular elastic membranes”, *Int. J. Solids Struct.* **32**:14 (1995), 2041–2052.
- [Roychowdhury and DasGupta 2015] S. Roychowdhury and A. DasGupta, “Inflating a flat toroidal membrane”, *Int. J. Solids Struct.* **67-68** (2015), 182–191.
- [Saxena et al. 2019] P. Saxena, N. H. Reddy, and S. P. Pradhan, “Magnetoelastic deformation of a circular membrane: wrinkling and limit point instabilities”, *Int. J. Non-Linear Mech.* **116** (2019), 250–261.
- [Shang and Cheng 1991] X.-c. Shang and C.-j. Cheng, “Instability of toroidal membrane with large tensile deformation”, *Appl. Math. Mech.* **12**:6 (1991), 557–564.
- [Steigmann 1990] D. J. Steigmann, “Tension-field theory”, *Proc. R. Soc. Lond. A* **429**:1876 (1990), 141–173.
- [Steigmann 2005] D. J. Steigmann, “Puncturing a thin elastic sheet”, *Int. J. Non-Linear Mech.* **40**:2-3 (2005), 255–270.
- [Stein and Hedgepeth 1961] M. Stein and J. M. Hedgepeth, “Analysis of partly wrinkled membranes”, technical note D-813, NASA, 1961.
- [Szyszkowski and Glockner 1987] W. Szyszkowski and P. G. Glockner, “Spherical membranes subjected to vertical concentrated loads: an experimental study”, *Eng. Struct.* **9**:3 (1987), 183–192.
- [Tamadapu and DasGupta 2012] G. Tamadapu and A. DasGupta, “In-plane surface modes of an elastic toroidal membrane”, *Int. J. Eng. Sci.* **60** (2012), 25–36.
- [Tamadapu and DasGupta 2014] G. Tamadapu and A. DasGupta, “Effect of curvature and anisotropy on the finite inflation of a hyperelastic toroidal membrane”, *Eur. J. Mech. A Solids* **46** (2014), 106–114.
- [Tamadapu et al. 2013] G. Tamadapu, N. N. Dhavale, and A. DasGupta, “Geometrical feature of the scaling behavior of the limit-point pressure of inflated hyperelastic membranes”, *Phys. Rev. E* **88**:5 (2013), art. id. 053201.
- [Wang et al. 2017] F. Wang, C. Yuan, T. Lu, and T. J. Wang, “Anomalous bulging behaviors of a dielectric elastomer balloon under internal pressure and electric actuation”, *J. Mech. Phys. Solids* **102** (2017), 1–16.
- [Wong and Pellegrino 2006] Y. W. Wong and S. Pellegrino, “Wrinkled membranes, II: Analytical models”, *J. Mech. Mater. Struct.* **1**:1 (2006), 27–61.
- [Wriggers and Taylor 1990] P. Wriggers and R. L. Taylor, “A fully non-linear axisymmetrical membrane element for rubber-like materials”, *Eng. Computation.* **7**:4 (1990), 303–310.
- [Wu 1974] C. H. Wu, “The wrinkled axisymmetric air bags made of inextensible membrane”, *J. Appl. Math. (ASME)* **41**:4 (1974), 963–968.
- [Wu 1978] C.-H. Wu, “Nonlinear wrinkling of nonlinear membranes of revolution”, *J. Appl. Mech. (ASME)* **45**:3 (1978), 533–538.
- [Wu and Canfield 1981] C. H. Wu and T. R. Canfield, “Wrinkling in finite plane-stress theory”, *Quart. Appl. Math.* **39**:2 (1981), 179–199.
- [Yang and Feng 1970] W. H. Yang and W. W. Feng, “On axisymmetrical deformations of nonlinear membranes”, *J. Appl. Mech. (ASME)* **37**:4 (1970), 1002–1011.
- [Zak 1982] M. Zak, “Statics of wrinkling films”, *J. Elasticity* **12**:1 (1982), 51–63.

Received 7 Jan 2019. Revised 1 Aug 2019. Accepted 7 Aug 2019.

SAIRAM PAMULAPARTHI VENKATA: [sairampv44@gmail.com](mailto:sairampv44@gmail.com)

*Department of Mechanical and Aerospace Engineering, Field of Theoretical and Applied Mechanics, Cornell University, Ithaca, NY, United States*

and

*Department of Mechanical and Aerospace Engineering, Indian Institute of Technology Hyderabad, Telangana, India*

PRASHANT SAXENA: [prashant.saxena@glasgow.ac.uk](mailto:prashant.saxena@glasgow.ac.uk)

*Glasgow Centre for Computational Engineering, James Watt School of Engineering, University of Glasgow, Glasgow, United Kingdom*

and

*Department of Mechanical and Aerospace Engineering, Indian Institute of Technology Hyderabad, Telangana, India*

## PLANE STRAIN POLAR ELASTICITY OF FIBRE-REINFORCED FUNCTIONALLY GRADED MATERIALS AND STRUCTURES

KONSTANTINOS P. SOLDATOS, METIN AYDOGDU AND UFAK GUL

This study investigates the flexural response of a linearly elastic rectangular strip reinforced in a functionally graded manner by a single family of straight fibres resistant in bending. Fibre bending resistance is associated with the thickness of fibres which, in turn, is considered measurable through use of some intrinsic material length parameter involved in the definition of a corresponding elastic modulus. Solution of the relevant set of governing differential equations is achieved computationally, with the use of a well-established semianalytical mathematical method. A connection of this solution with its homogeneous fibre-reinforced material counterpart enables the corresponding homogeneous fibrous composite to be regarded as a source of a set of equivalent functionally graded structures, each one of which is formed through inhomogeneous redistribution of the same volume of fibres within the same matrix material. A subsequent stress and couple-stress analysis provides details of the manner in which the flexural response of the polar structural component of interest is affected by certain types of inhomogeneous fibre distribution.

### 1. Introduction

Fibrous composites with either homogeneously or inhomogeneously distributed stiff fibres are increasingly attracting attention and interest, particularly after carbon nanotube fibres were found suitable for inclusion in their constituent phases (e.g., [Liew et al. 2015]). Despite their low density and nanometer thickness, carbon nanotubes are known to exhibit remarkably high strength and stiffness, as well as similarly high bending resistance.

Fibre bending stiffness of such a kind of stiff fibres is thus naturally required to be accounted for in modelling and studying the behaviour of relevant composites, regardless of whether fibre reinforcement is distributed in a homogeneous or in some inhomogeneous manner. This requirement becomes particularly important in cases of high fibre concentration (either global or local), where fibre bending resistance gives rise to a couple-stress field. The latter makes the stress field nonsymmetric, and endows the composite characteristics of a polar material. It is recalled in this context that the conventional theory of fibre-reinforced materials is built on the simplifying assumption of perfectly flexible fibres [Adkins and Rivlin 1955; Rivlin 1955; Spencer 1972], namely fibres that exhibit no bending resistance, and is therefore inherently a nonpolar elasticity theory.

The study of polar material behaviour is naturally associated with modelling features falling into the Cosserat theoretical framework [Cosserat and Cosserat 1909]. Linearly elastic behaviour of polar fibrous composites may accordingly be attempted through use of either the polar linear elasticity theory

---

*Keywords:* cylindrical bending, elastic beams, elastic plates, fibre bending stiffness, fibre-reinforced structures, functionally graded structures, plane strain elasticity, polar elasticity.

proposed in [Mindlin and Tiersten 1962] for generally anisotropic materials or the linearised version of the theory proposed in [Spencer and Soldatos 2007] for specific types of polar fibrous composites (see also [Soldatos 2015]). It is recalled in this connection that the type of appropriate material anisotropy that fits a relevant boundary value problem is dictated by the specific direction(s) that fibres are aligned to in a fibrous composite.

However, as is also pointed out in [Soldatos 2018], there exists no evidence suggesting that the anisotropic version of the Mindlin and Tiersten theory [Mindlin and Tiersten 1962] was motivated by potential applications referring to linearly elastic composites having embedded fibres resistant in bending. As a matter of fact, most of the polar linear elasticity analysis detailed in [Mindlin and Tiersten 1962] is devoted to the isotropic version of that theory.

Motivated by these observations, the analysis presented in [Soldatos 2018]:

- (i) underlined the principal equations of the Cosserat polar material framework (see also [Truesdell and Toupin 1960]) that provide common ground for the theories proposed in [Mindlin and Tiersten 1962] and [Spencer and Soldatos 2007];
- (ii) noted the manner in which the linear constitutive equation employed in [Mindlin and Tiersten 1962] was obtained through a suitable truncation of the energy expansion proposed in [Toupin 1962];
- (iii) enlarged and enriched the theoretical background through which both theories [Mindlin and Tiersten 1962; Spencer and Soldatos 2007] are valid and operate; and, within that enlarged background,
- (iv) identified their similarities and potential differences without having the intention to either bridge or eliminate the latter.

The principal relevant similarity recorded in [Soldatos 2018] refers to the fact that the governing equations of either theory are generally nonelliptic. As a result, the solution to any well-posed boundary value problem, attempted through use of either theory, may be not unique. There are basic historical reasons (see [Soldatos 2018]) that prevented Mindlin and Tiersten from noticing this fact [Mindlin and Tiersten 1962], where it is stated that such a potential solution, described by continuous displacements possessing continuous derivatives of all orders, is the unique solution of the implied boundary value problem.

However, reference [Soldatos 2018] has shown that such a solution, which will be termed as a “continuous solution” in what follows, is in fact the only possible solution described by continuous displacements possessing continuous derivatives of all orders. Due to the observed “lack of ellipticity” of polar elasticity equations, that continuous solution may be accompanied by a number of “weak discontinuity” solutions of the same boundary value problem and may thus be not unique. These are solutions described by continuous displacements that possess discontinuous derivatives, and may thus represent microscale (fibre-thickness) material failure modes (e.g., [Soldatos 2015; Merodio and Ogden 2002; Merodio and Ogden 2003]). Such kind of possible solutions are not observable in corresponding problems underpinned by nonpolar linear elasticity principles, which always lead to elliptic governing differential equations.

The outlined observations raise immediately a question of whether the prevailing solution of a polar elasticity boundary value problem is the continuous one or some of its possible weak discontinuity counterparts. The task of seeking for an answer to this question is of paramount practical importance in structural analysis applications.



Such a challenging task may well depend on the particular polar elasticity problem of interest. Moreover, it seemingly requires some analytical or numerical/computational comparison of all relevant weak discontinuity solutions among themselves, as well as against their common continuous counterpart. In fact an appropriate comparison may also be required of the stored energy levels reached by all possible solutions involved. The need becomes thus evident for the derivation of relevant continuous or weak discontinuity solutions to a number of relatively simple or more difficult boundary value problems, with the aim to reach afterwards a stage that makes the implied comparisons possible.

The present study is considered as an immediate continuation of an initial, relatively simple step made already in that direction [Farhat and Soldatos 2015], in the sense that it complements the latter in the search for continuous solutions to the plane strain bending problem of a simply supported, linearly elastic rectangular strip reinforced by a single family of straight fibres resistant in bending. While Farhat and Soldatos [2015] dealt with the case of either homogeneous or layer-wise inhomogeneous (laminated) strips, this communication considers the more general case of material inhomogeneity due to continuous through-thickness variation of the fibre-reinforcement.

The elastic strip of interest may be regarded as a rectangular beam made of functionally graded material (FGM) having unit width, or as the cross-section of a corresponding rectangular plate having infinite extent in the out-of-plane direction. The latter representation provides direct connection with the relevant, nonpolar elasticity problem considered and solved in [Pagano 1969] but, here, the implied bending stiffness of functionally graded fibres furnishes the strip with polar material properties. Moreover, material inhomogeneity features in the analysis through the variable form attained by the coefficients of the corresponding set of Navier-type partial differential equations.

With the help of Appendix A, Section 2 thus provides a proper mathematical description of the plane strain state of polar, linearly elastic structures reinforced in a functionally graded manner by a single family of straight fibres resistant in bending. For simplicity, this description is based on the restricted version of the polar elasticity theory presented in [Spencer and Soldatos 2007]. This version of the theory (see also [Soldatos 2015]) involves only a single elasticity modulus of fibre bending resistance and, as soon as certain additional conditions are met [Soldatos 2018], can establish connection with the theory of Mindlin and Tiersten [1962].

Section 3 formulates the aforementioned bending problem of a simply supported prismatic beam (or rectangular plate cross-section). Moreover, with use of Appendix B, it employs a suitable semianalytical mathematical method (e.g., [Soldatos and Hadjigeorgiou 1990; Soldatos and Ye 1994; Shuvalov and Soldatos 2003; Ye 2003; Dagher and Soldatos 2011; Brischetto 2019]), provides information that underpins its computational efficiency, and finalises the solution of the corresponding Navier-type equations. With the help of appendices C and D, Section 4 connects afterwards the present problem of interest with its homogeneous polar elasticity counterpart [Farhat and Soldatos 2015]. This connection enables a homogeneous fibre-reinforced component [Farhat and Soldatos 2015] to be regarded as the source of a set of equivalent functionally graded structures, each one of which is made through inhomogeneous redistribution of the same volume of fibres within the same matrix material.

Three different types of such inhomogeneous fibre redistribution are thus selected in Section 4, and are employed afterwards in Section 5, in the discussion of the numerical results presented there. The latter thus examines in detail the manner in which each of the employed types of inhomogeneous fibre distribution affects the flexural response of the composite structure. Finally, Section 6 summarises the

main conclusions drawn and outlines directions on the manner in which the search for identification of corresponding weak discontinuity solutions should be contacted.

## 2. Theoretical formulation

A linearly elastic fibre-reinforced plate has finite length,  $L$ , in the  $x$  direction, infinite extent in the  $y$  direction, and finite thickness,  $h$ , in the  $z$  direction of a Cartesian coordinate system  $Oxyz$  ( $0 \leq x \leq L$ ,  $-\infty \leq y \leq +\infty$ ,  $-h/2 \leq z \leq h/2$ ). The plate material has embedded a single family of fibres which are parallel to the  $x$ -axis, can resist bending, and are distributed in the  $z$ -axis direction in a continuous, functionally graded manner. The plate is subjected to external loading that justifies plane strain response, in the sense that the displacement component in the  $y$  direction is zero while the other two displacement components, as well as all remaining physical quantities, are independent of the coordinate parameter  $y$ . In the usual manner, the plate cross-section can thus be considered as a two-dimensional elastic strip or as a prismatic beam having length  $L$ , thickness  $h$  and unit width (Figure 1). In this context, relevant terminology of prismatic beams is also employed in what follows.

The through-thickness inhomogeneous distribution of the fibres is regulated by controlling their volume fraction,  $V^f(z)$ , which requires from the material properties of the structural component to be known functions of the  $z$  coordinate parameter. Every material property,  $P(z)$  say, of such a functionally graded fibrous composite is usually expected to obey the mixture law

$$P(z) = V^f(z)P^f + V^m(z)P^m, \quad V^f(z) + V^m(z) = 1 \quad (0 \leq V^f(z), V^m(z) \leq 1), \quad (1)$$

where  $V^m(z)$  is the volume fraction of the matrix phase, while  $P^f$  and  $P^m$  represent the corresponding constant material property of the fibre and the matrix phase, respectively.

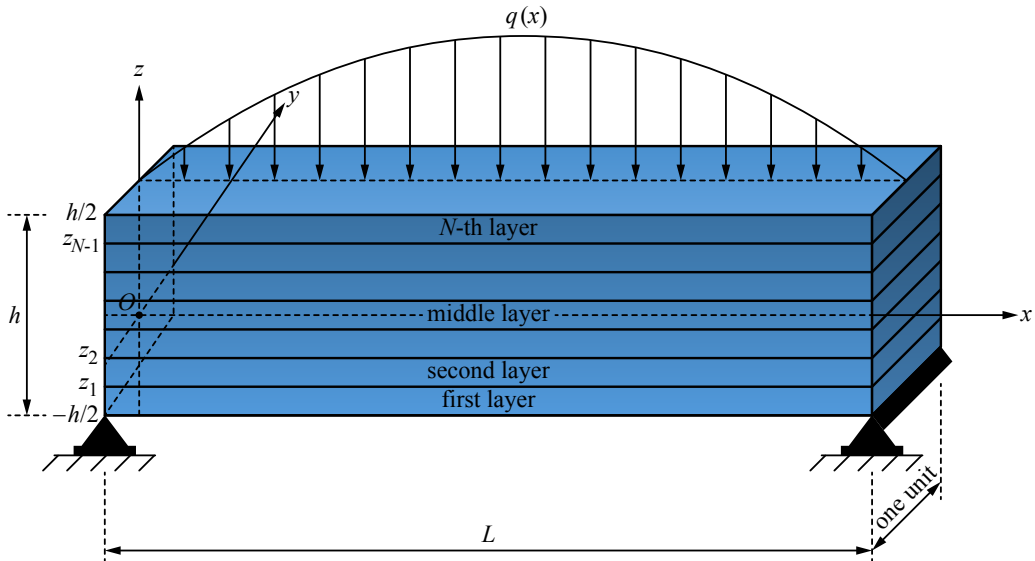


**Figure 1.** Geometrical features and nomenclature of a prismatic beam.

It is pointed out that the inequality conditions noted in (1) are imposed on the ground of evident theoretical arguments that hold true regardless of the particular form of  $V^f(z)$  or, equivalently,  $V^m(z)$ . In this context, the denoted upper limit of the fibre volume fraction, namely  $V^f(z) = 1$ , is in principle possible only in cases that fibres are assumed perfectly flexible and, having no thickness, can therefore fill in completely the entire volume of the composite. However, fibres do have thickness in practice and, due to the structural architecture of the fibrous composite, leave gaps among them which are filled in with matrix material even in parts of the composite that fibres are distributed very densely.

A more realistic approach thus requires introduction of a maximum fibre volume parameter,  $V_{\max}^f$  say, such that

$$0 \leq V^f(z) \leq V_{\max}^f < 1. \quad (2)$$

This additional condition does not need to be discussed further at these early stages of the problem formulation. However, it is reconsidered and discussed later, in sections 4 and 5, where determination of a value for  $V_{\max}^f$  becomes part of some specific applications.

In the implied plane strain state, the average fibre and matrix concentrations of the composite are defined as

$$\langle V^f \rangle = \frac{1}{h} \int_{-h/2}^{h/2} V^f(z) dz, \quad \langle V^m \rangle = \frac{1}{h} \int_{-h/2}^{h/2} V^m(z) dz, \quad \langle V^f \rangle + \langle V^m \rangle = 1. \quad (3)$$

The particular case of a homogeneous fibrous composite, where the fibre volume fraction is constant, is thus characterised by the relationship  $V^f(z) = \langle V^f \rangle$  for all  $z$ . If the fibres resist bending and  $\langle V^f \rangle$  is adequately high, say 40% to 60%, then the fibre response to mechanical loading generates considerable couple-stress and nonsymmetric stress (e.g., [Spencer and Soldatos 2007; Soldatos 2015; 2018; Farhat and Soldatos 2015]). In the case of FG fibrous composites with relatively low  $\langle V^f \rangle$ , creation of a couple-stress field is still possible locally, namely in specific parts of the composite where  $V^f(z)$  anticipates high fibre concentration.

The stress and couple-stress components that contribute actively in plane strain equilibrium are shown schematically in Figure 2 (see also [Spencer and Soldatos 2007; Farhat and Soldatos 2015; Soldatos 2009]). The symmetric part of the stress tensor is given by the standard form of the generalised Hooke's law, which in the present, plane strain case acquires the form

$$\begin{bmatrix} \sigma_x \\ \sigma_z \\ \tau_{(xy)} \end{bmatrix} = \begin{bmatrix} C_{11} & C_{13} & 0 \\ C_{13} & C_{33} & 0 \\ 0 & 0 & C_{55} \end{bmatrix} \begin{bmatrix} e_x \\ e_z \\ 2e_{xz} \end{bmatrix}, \quad (4)$$

where the appearing linear strain components are

$$e_x = U_{,x}, \quad 2e_{xz} = U_{,z} + W_{,x}, \quad e_z = W_{,z}. \quad (5)$$

Here,  $U(x, z)$  and  $W(x, z)$  are the displacement components along the axial and transverse coordinate direction, respectively, and a comma denotes partial differentiation with respect to the indicated coordinate parameter(s).

The elastic moduli appearing in (4) vary in the transverse direction in accordance with the mixture law (1), namely

$$C_{ij}(z) = V^f(z) C_{ij}^f + V^m(z) C_{ij}^m. \quad (6)$$

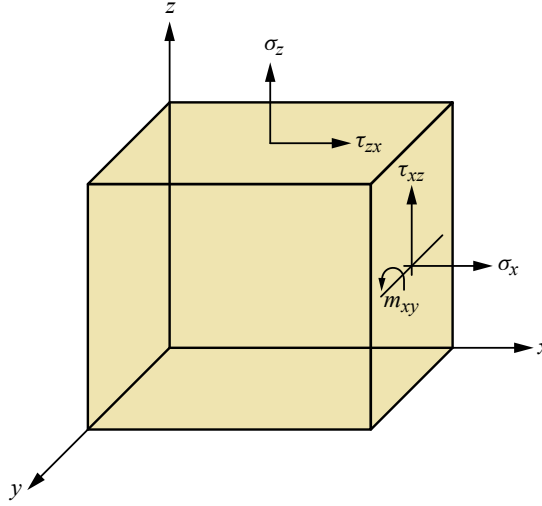


**Figure 2.** Schematic representation of the active stress and couple-stress components.

As the matrix phase is naturally considered isotropic, the following relationships are assumed valid:

$$C_{11}^m = C_{33}^m = \lambda + 2\mu, \quad C_{13}^m = \lambda, \quad C_{55}^m = (C_{11}^m - C_{13}^m)/2 = \mu. \quad (7)$$

where  $\lambda$  and  $\mu$  are the constant Lamé moduli of the matrix material. In this context, [Appendix A](#) describes an alternative manner in which the elastic moduli of the matrix and the fibre phases can be related, and thus lead to the determination of their  $C_{ij}$  counterparts appearing in (4).

The antisymmetric part of the stress tensor is defined as

$$\tau_{[xz]} = \frac{1}{2} m_{xy,x}, \quad (8)$$

where the only nonzero couple-stress component met in this plane strain problem (e.g., [\[Spencer and Soldatos 2007; Farhat and Soldatos 2015\]](#)), namely

$$m_{xy} = d^f K_z^f = -d^f W_{,xx}, \quad (9)$$

acts in the manner shown in [Figure 2](#), and  $K_z^f$  represents the fibre curvature. Unlike  $C_{ij}$ , which have dimensions of stress, the fibre bending modulus  $d^f$  has dimensions of force. Like  $C_{ij}$  though, this is also expected to obey the mixture law (1).

However, unlike the fibre phase, the isotropic matrix phase does not contribute to the bending stiffness of the fibrous composite, and, as a result, the second term in the right-hand side of the corresponding expression (1)<sub>1</sub> is zero. Hence, in line with previous relevant studies [\[Farhat and Soldatos 2015; Soldatos 2009\]](#), where material homogeneity enabled the relevant constant value of  $d^f$  to be considered as a product of the form  $C_{11}lL$ , the fibre bending modulus attains here the through-thickness variable form

$$d^f(z) = V^f(z) C_{11}^f lL, \quad (10)$$

where the intrinsic material length parameter  $l$  is connected with the fibre thickness. In this manner,  $l = 0$  represents cases of nonpolar material behaviour, where fibres are perfectly flexible and the subsequent

absence of couple-stress ( $m_{xy,x} = \tau_{[xz]} = 0$ ) enables the stress tensor to attain its conventional symmetric form (4).

When  $l$  is nonzero, the nonzero shear stresses are unequal, so that

$$\tau_{xz} = \tau_{(xz)} + \tau_{[xz]}, \quad \tau_{zx} = \tau_{(xz)} - \tau_{[xz]}. \quad (11)$$

In the absence of body forces, the equilibrium equations thus acquire the form

$$\sigma_{x,x} + \tau_{(xz),z} - \tau_{[xz],z} = 0, \quad \tau_{(xz),x} + \tau_{[xz],x} + \sigma_{z,z} = 0, \quad (12)$$

which, after appropriate use of equations (4)–(9), lead to the Navier-type equations:

$$\begin{aligned} C_{11}U_{,xx} + (C_{13} + C_{55})W_{,xz} + C_{55}U_{,zz} + C_{55,z}(U_{,z} + W_{,x}) + \frac{1}{2}lL C_{11}^f V^f W_{,xxxz} \\ + \frac{1}{2}lL C_{11}^f V_{,z}^f l W_{,xxx} = 0, \\ C_{55}W_{,xx} + (C_{13} + C_{55})U_{,xz} + C_{13,z}U_{,x} + C_{33,z}W_{,z} + C_{33}W_{,zz} - \frac{1}{2}lL C_{11}^f V^f W_{,xxx} = 0. \end{aligned} \quad (13)$$

The outlined polar elasticity formulation is general, in the sense that it applies to all cases that a relevant FGM fibrous composite exhibits plane strain behaviour. For analytical purposes, it is found convenient to rearrange equations (13) into the following matrix form

$$\mathbf{A}\mathbf{X} = \mathbf{0}, \quad (14)$$

where

$$\mathbf{A} = \begin{bmatrix} C_{11}\frac{\partial^2}{\partial x^2} + C_{55}\frac{\partial^2}{\partial z^2} + C_{55,z}\frac{\partial}{\partial z} & (C_{13} + C_{55})\frac{\partial^2}{\partial x\partial z} + C_{55,z}\frac{\partial}{\partial x} + \frac{1}{2}LC_{11}^f V_{,z}^f l\frac{\partial^3}{\partial x^3} + \frac{1}{2}LC_{11}^f V^f l\frac{\partial^4}{\partial x^3\partial z} \\ (C_{13} + C_{55})\frac{\partial^2}{\partial x\partial z} + C_{13,z}\frac{\partial}{\partial x} & C_{55}\frac{\partial^2}{\partial x^2} + C_{33}\frac{\partial^2}{\partial z^2} + C_{33,z}\frac{\partial}{\partial z} - \frac{1}{2}LC_{11}^f V^f l\frac{\partial^4}{\partial x^4} \end{bmatrix},$$

$$\mathbf{X} = [U \ W]^T,$$

### 3. Cylindrical bending of a simply supported plate

Attention is now confined into the particular case that deformation is due to external application of the lateral boundary tractions:

$$\sigma_z(x, h/2) = q(x), \quad \sigma_z(x, -h/2) = 0, \quad \tau_{zx}(x, h/2) = 0, \quad \tau_{zx}(x, -h/2) = 0. \quad (15)$$

The externally applied transverse load,  $q(x)$ , is considered known and can, therefore, be represented in the following Fourier-type sine-series form

$$q(x) = \sum_{m=1}^{\infty} q_m \sin(Mx), \quad M = m\pi/L \quad (m = 1, 2, \dots). \quad (16)$$

It is further assumed that the longitudinal ends of the plate cross-section or prismatic beam ( $x = 0, L$ ) are subjected to the following set of homogeneous boundary conditions:

$$\sigma_x(0, z) = \sigma_x(L, z) = 0, \quad W(0, z) = W(L, z) = 0, \quad m_{xy}(0, z) = m_{xy}(L, z) = 0, \quad (17)$$

which is consistent with the symmetries of simply supported boundaries. In the particular case of a homogeneous fibrous composite, where  $V^f$  and  $V^m$  are both known constants, the problem of present interest thus reduces naturally to its polar elasticity counterpart studied in [Farhat and Soldatos 2015].

The simple support boundary conditions (17) are satisfied exactly by the following choice of a displacement field:

$$U = hf(z) \cos(m\pi x/L), \quad W = hg(z) \sin(m\pi x/L) \quad (m = 1, 2, \dots), \quad (18)$$

where the functions  $f(z)$  and  $g(z)$  are to be determined. The expressions in (18) represent a potential solution to the described boundary value problem when the external loading is identical with a single term of the series expansion (16), namely

$$q(x) = q_m \sin(Mx), \quad M = \frac{m\pi}{L}. \quad (19)$$

The linearity of the described boundary value problem, combined with the superposition principle of relevant solutions, makes it then sufficient for someone to look only for a solution of the particular case in which the external load is given according to (19), with  $m$  being an arbitrary positive integer.

Upon inserting (18) into (14), the latter equation is transformed into a fourth-order set of simultaneous ordinary differential equations (ODEs) with variable coefficients. This can be expressed as

$$\mathbf{G}(z, D)\mathbf{B} = \mathbf{0}, \quad (20)$$

where

$$\mathbf{G}(z, D) = \begin{bmatrix} d_1 + d_2 D^2 + d_3 D & (d_4 + d_{11})D + d_5 \\ -d_4 D^2 + d_7 & d_6 D + d_8 + d_9 D^2 + d_{12} \end{bmatrix}, \quad (21)$$

$$D = d/dz, \quad \mathbf{B} = [f(z) \ g(z)]^T.$$

Due to the variable form of  $V^f(z)$ , the appearing coefficients, namely

$$\begin{aligned} d_1 &= -h^2 M^2, & d_2 &= C_{55}/C_{11}, & d_3 &= C_{55,z}/C_{11}, \\ d_4 &= hM(C_{13} + C_{55})/C_{11}, & d_5 &= (Mh/L)(C_{11}^f DV^f/C_{11}), & d_6 &= DC_{33}/C_{11}, \\ d_7 &= \left(\frac{Mh}{L}\right)DC_{13}/C_{11}, & d_8 &= -(C_{55}h^2 M^2)/C_{11}, \\ d_9 &= C_{33}/C_{11}, & d_{11} &= -\frac{1}{2}hM^3 lL(C_{11}^f V^f/C_{11}), & d_{12} &= -\frac{1}{2}hM^4 lL(C_{11}^f V^f/C_{11}), \end{aligned} \quad (22)$$

are, in general, functions of  $z$ .

Solution of (20) is here achieved with the use of a semianalytical method, which considers that the inhomogeneous polar material strip of interest is essentially made of an infinite number of fictitious layers having infinitesimally small thickness and constant material properties. As computational practice requires use of a finite number of such fictitious layers (see Figure 1), the larger the number of those fictitious layers considered the nearer the obtained numerical results approach their exact elasticity counterparts.

The implied “fictitious layers method” was initially introduced for the solution of nonpolar linear elasticity problems dealing with the dynamic response of isotropic cylindrical components [Soldatos and Hadjigeorgiou 1990]. In such problems, it is the geometry rather than the material inhomogeneity of

the structure that spreads variable coefficients into the governing differential equations. The method has since been applied successfully to both static and dynamic studies of homogeneous and laminated composite components of cylindrical geometry (e.g., [Soldatos and Hadjigeorgiou 1990; Soldatos and Ye 1994; Shuvalov and Soldatos 2003; Ye 2003; Dagher and Soldatos 2011] and relevant references therein), and is proven capable to provide asymptotically identical results to those based on potential or existing exact elasticity solutions.

Moreover, the numerical stability and the rate of convergence of the method are found in practice superior to those of corresponding analytical solutions based on power-series methods (e.g., [Dagher and Soldatos 2011]), where computational practice still requires some suitable finite term truncation of ultimately infinite series solutions, and, hence, does not avoid the concept of an approximation. More recently, the applicability of this fictitious layer method has successfully been extended towards solution of relevant structural mechanics problems that involve even doubly curved functionally graded structural components [Brischetto 2019].

Description of the solution thus obtained is facilitated by initially converting (20) into the following, equivalent set of four first-order linear ODEs with variable coefficients:

$$D\mathbf{F} = \mathbf{T}(z)\mathbf{F}, \quad (23)$$

where

$$\mathbf{F} = [Df, f, Dg, g]^T, \quad (24)$$

$$\mathbf{T}(z) = \begin{bmatrix} -d_3/d_2 & -d_1/d_2 & -(d_4 + d_{11})/d_2 & -d_5/d_2 \\ 1 & 0 & 0 & 0 \\ d_4/d_9 & -d_7/d_9 & -d_6/d_9 & (-d_8 + d_{12})/d_9 \\ 0 & 0 & 1 & 0 \end{bmatrix}.$$

The implied solution then continues by resembling its counterparts described in [Soldatos and Hadjigeorgiou 1990; Soldatos and Ye 1994; Shuvalov and Soldatos 2003; Ye 2003; Dagher and Soldatos 2011]. For self-sufficiency of this communication, further details are briefly presented in Appendix B.

#### 4. Application for selected forms of the fibre volume fraction

As pointed out in Section 2, even in parts of the composite where fibres are distributed very densely, the fibre structural architecture leaves gaps which are naturally filled in with matrix material. The inequality conditions noted in (1) should accordingly be refined through use of the more realistic inequality (2), provided that proper consideration of the fibre-scale structure can enable determination of the refined upper bound parameter  $V_{\max}^f$ . This may be achieved with use of some appropriate representative volume, or area elements (RVE) of the fibre distribution pattern [Gibson 1994]. Nevertheless, any  $V_{\max}^f$ -value thus obtained depends on the chosen RVE discretisation, and may therefore be not unique.

Appendix C thus demonstrates the manner in which rectangular or triangular RVEs of the kind implied in Figure 3 (bottom) can be used as reasonably simple examples in the present problem of interest, where the direction of the considered uniaxial family of fibres is normal to the depicted  $yz$ -plane (see also Figure 1). The two different values of maximum fibre volume fraction thus determined in (C.5)

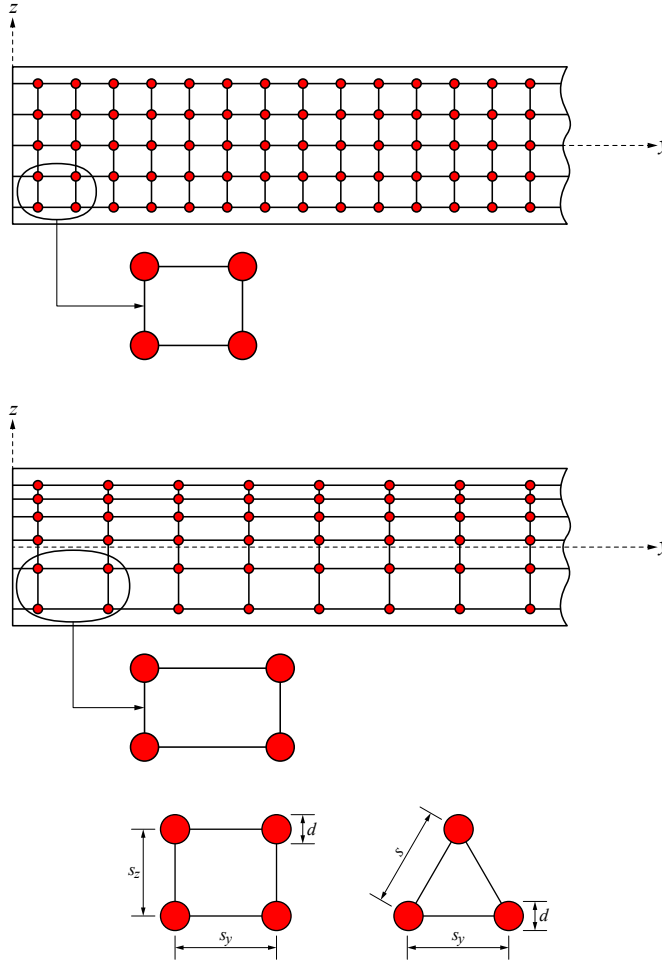


**Figure 3.** Discretization of fibre representative elements: homogeneous composite,  $S_z = \text{constant}$  (top), inhomogeneous composite,  $S_z = \text{variable}$  (middle), and rectangular and triangular fibre representative elements (bottom).

and (C.6) are here conjoined as

$$V_{\max}^f = \begin{cases} \pi/4 \cong 0.785, & \text{for rectangular RVEs,} \\ \pi/2\sqrt{3} \cong 0.907, & \text{for triangular RVEs.} \end{cases} \quad (25)$$

**4.1. Particular case: homogeneous composites [Farhat and Soldatos 2015].** In order to deal with applications of the outlined analysis, connection is initially established with the corresponding study detailed in [Farhat and Soldatos 2015] for corresponding homogeneous fibrous composites. It is recalled in this context that the effective material properties of the homogeneous fibrous composite employed in [Farhat and Soldatos 2015] are

$$E_L/E_T = 40, \quad G_{LT}/E_T = 0.5, \quad \nu_{LT} = \nu_{TT} = 0.25. \quad (26)$$



The analysis is evidently capable to consider homogeneous fibre distributions by using appropriate constant values of the fibre volume fraction  $V^f$  and, upon taking (2) and (3) into consideration, it thus requires

$$\langle V^f \rangle = V^f \leq V_{\max}^f, \quad \langle V^m \rangle = V^m = V_{\max}^f - V^f. \quad (27)$$

Let us, for instance, consider the choice

$$V^f(z) = \langle V^f \rangle = \frac{1}{2}, \quad (28)$$

which refers to a homogeneous fibrous composite whose volume consists 50% homogeneously distributed fibres and 50% matrix material. Upon inserting

$$\alpha_1 = 79, \quad \alpha_3 = 1.5, \quad \alpha_2 = \alpha_4 = \alpha_5 = 1, \quad \nu = 0.25, \quad (29)$$

into (A.3), and making use of (3), the mixture law (1) reveals that the effective material properties of the corresponding homogeneous composite are those detailed in (26). With use of (A.2), the holding relationships between the elastic moduli of the corresponding fibre and matrix phases are then found to be

$$E_T^f/E = 1, \quad E_L^f/E_T^f = 79, \quad G_{LT}^f/E_T^f = \frac{3}{5}, \quad \nu_{LT}^f = \nu_{TT}^f = \nu = 0.25, \quad G_{TT}^f/E_T^f = \frac{2}{5}. \quad (30)$$

It can then readily be verified that, in this particular case that the fibrous composite of interest is homogeneous and possesses effective material properties of the kind described in (26), the present analysis produces identical displacement and stress distributions to those detailed in [Farhat and Soldatos 2015] with its first iteration ( $N = 1$ ). Further iterations are unnecessary in that case, as they naturally return the same numerical results.

It is emphasised that the outlined verification of the present analysis is still possible for constant choices of  $V^f$  that differ from (28), as soon as the values of the constants (29) and, subsequently, of the ratios (30) are modified in a manner that enables the mixture law (1) to yield again to the effective elastic moduli (26). A couple of specific, additional relevant cases are in fact identified in Section 4.3 below, in connection with the form (35) of possible inhomogeneous fibre distribution.

**4.2. Functionally graded, linear redistribution of the fibres.** The connection established with the homogeneous fibrous composite considered in [Farhat and Soldatos 2015] is now exploited by considering the following pair of linearly inhomogeneous fibre distributions:

$$V^f(z) = 0.5 + \varepsilon(z/h) \quad (0 < \varepsilon \leq \varepsilon_{\max} \leq 1), \quad (31)$$

$$V^f(z) = 0.5 - \varepsilon(z/h) \quad (0 < \varepsilon \leq \varepsilon_{\max} \leq 1). \quad (32)$$

As either of these return

$$\langle V^f \rangle = \frac{1}{2}, \quad (33)$$

they both represent corresponding inhomogeneous composites consisting of 50% fibre and 50% matrix material.

A schematic representation of the volume fraction of these inhomogeneous fibre distributions is depicted in Figure 4, along with their counterparts that represent the homogenous composite described already in Section 4.1 (Figure 4, left). Both (31) and (32) are evidently fibre distributions which vary

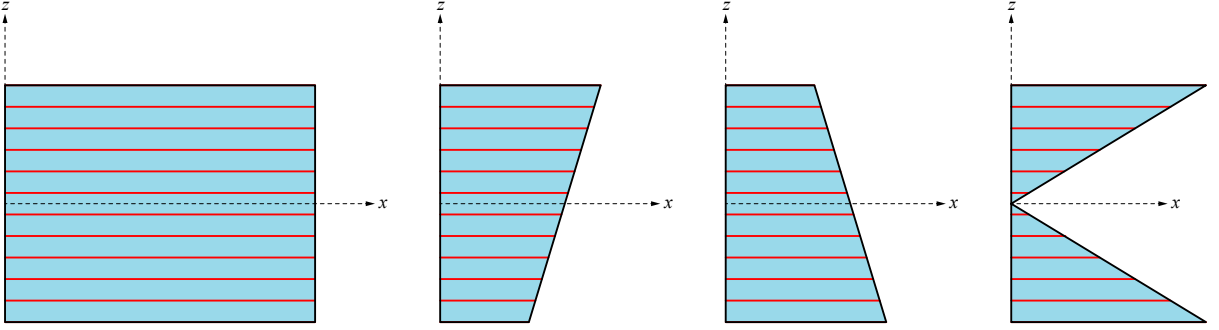


**Figure 4.** Schematic representation of fibre volume fractions of the type (28) (left), (31) (second), (32) (third) and (35) (right).

linearly through the thickness, and are nonsymmetric with respect to the middle plane of the composite beam. It is evident that (31) represents a top-stiff fibrous composite while (32) corresponds to a bottom-stiff such.

When inserted into (31), the value  $\varepsilon = \varepsilon_{\max}$  refers to an inhomogeneous fibrous composite with maximum fibre volume fraction at the top ( $V^f(h/2) = (1 + \varepsilon_{\max})/2$ ) and minimum at the bottom ( $V^f(-h/2) = (1 - \varepsilon_{\max})/2$ ) lateral plane of the composite. The situation is evidently reversed ( $V^f(h/2) = (1 - \varepsilon_{\max})/2$ ,  $V^f(-h/2) = (1 + \varepsilon_{\max})/2$ ) when  $\varepsilon = \varepsilon_{\max}$  is inserted into (32). In principle,  $\varepsilon_{\max}$  may be as high as  $\varepsilon_{\max} = 1$  but the fibre-scale structure of a composite relates this parameter with  $V_{\max}^f$ . Hence, by virtue of (25), the second part of Appendix C shows that

$$\varepsilon_{\max} = 2V_{\max}^f - 2 \cong \begin{cases} 0.5708, & \text{for rectangular RVEs,} \\ 0.812, & \text{for triangular RVEs.} \end{cases} \quad (34)$$

The relevant numerical results presented in Section 5 below refer to inhomogeneous composites whose effective material properties are evaluated with use of the mixture law (1), after each of (31) and (32) is inserted into (A.3). This process requires also use of (29) and (30), so that the resulting inhomogeneous composite is thought of as formed by a relevant redistribution into the same matrix of a same volume of fibres (50%) possessing the material properties (30). It can indeed be readily verified that, in both cases, the obtained through thickness average elastic moduli are still in exact agreement with the effective material properties (26) of the homogeneous fibrous composite employed in [Farhat and Soldatos 2015].

**4.3. Symmetric, piecewise linear redistribution of the fibres.** The last fibre distribution of present interest is associated with a class of inhomogeneous fibrous composites whose volume fraction varies symmetrically with respect to the middle plane of the composite (see Appendix D). This class is described as

$$V^f(z) = \alpha |z/h|, \quad (35)$$

where  $\alpha$  is some real positive constant.

In this case, the fibre volume fraction increases in a piecewise linear manner with the increasing distance from the middle plane (see Figure 4, right). As  $V^f(0) = 0$  and  $V^f(h/2) = V^f(-h/2) = \alpha/2$ , equation (35) refers to a fibrous composite graded in a manner that maximum fibre volume fraction

is attained at both lateral planes. As also noted in [Appendix D](#), equation (35) yields the average fibre volume fraction (33) when  $\alpha = 2$ .

However, as shown next with the help of [Appendix C](#), the types of fibre-scale structure considered there make (33) incompatible with the fibre distribution (35). This is because the connection of (35) with maximum volume fractions noted in (25) gives, respectively, the following maximum value of the positive constant  $\alpha$ :

$$\alpha_{\max} = 2V_{\max}^f \cong \begin{cases} 1.571, & \text{for rectangular RVEs,} \\ 1.814, & \text{for triangular RVEs,} \end{cases} \quad (36)$$

which, in either case is smaller than 2.

Indeed, the corresponding average volume fractions, namely

$$\langle V^f \rangle \cong \begin{cases} 0.39, & \text{for rectangular RVEs,} \\ 0.45, & \text{for triangular RVEs,} \end{cases} \quad (37)$$

verify that neither of the values of  $\alpha$  noted in (36) enables consideration of an average fibre volume fraction which is as high as its 0.5 counterpart assumed by the top- and bottom-stiff fibre distributions (31) and (32).

Nevertheless, as also pointed out in [Appendix C](#), a relevant inhomogeneous fibrous composite having average volume fraction  $\langle V^f \rangle = 0.45$  and effective properties (26), is obtained by replacing all material constants and moduli appearing in (A.3) and (30) with

$$\begin{aligned} \alpha_1 &= 87.667, \quad \alpha_3 = 1.55575, \quad \alpha_2 = \alpha_4 = \alpha_5 = 1, \quad \nu = 0.25, \\ E_T^f/E &= 1, \quad E_L^f/E_T^f = 87.667, \quad G_{LT}^f/E_T^f = 0.6223, \\ \nu_{LT}^f &= \nu_{TT}^f = \nu = 0.25, \quad G_{TT}^f/E_T^f = \frac{2}{5}. \end{aligned} \quad (38)$$

A considerable part of the numerical results presented in the next section thus refers to the polar mechanical response of this inhomogeneous fibre-reinforced composite which, along with employing the material properties (38), implies further that  $\alpha = 1.814$  in (35).

## 5. Numerical results and discussion

All numerical results presented and discussed in this section are obtained by setting  $m = 1$  in (19). These results are presented in a nondimensional form, through use of the following dimensionless displacement and stress parameters:

$$\begin{aligned} \bar{W} &= \frac{\langle E_T \rangle W}{Lq_1}, \quad \bar{U} = \frac{\langle E_T \rangle U}{Lq_1}, \quad \bar{\sigma}_x = \frac{\sigma_x}{q_1}, \quad \bar{\sigma}_z = \frac{\sigma_z}{q_1}, \\ \bar{\tau}_{zx} &= \frac{\tau_{zx}}{q_1}, \quad \bar{\tau}_{xz} = \frac{\tau_{xz}}{q_1}, \quad \bar{m}_{xy} = \frac{m_{xy}}{Lq_1}. \end{aligned} \quad (39)$$

By virtue of (33), these are seen equivalent to their counterparts employed for the corresponding case of a homogenous fibrous composite in [\[Farhat and Soldatos 2015\]](#), where, however, an evident typographical error is noticed in the couple-stress nondimensionalisation. The evident symmetries that (19) imposes along the  $x$ -direction imply that the magnitude of displacements, stresses, and couple-stress have identical

through-thickness distribution at  $x/L$  and  $1 - x/L$ . Numerical results are accordingly presented for the left half of the beam only.

All rectangular beams considered for the results shown next possess the same span ratio with their homogeneous counterpart studied in [Farhat and Soldatos 2015], namely

$$h/L = 0.25. \quad (40)$$

For a natural connection with [Farhat and Soldatos 2015], the same notation, namely

$$\lambda = l/h \leq 1, \quad (41)$$

is used for the nondimensional intrinsic material parameter that refers to fibre thickness. In this regard, a note is made of the fact that this parameter should not be misinterpreted as denoting the Lamé modulus employed in (7) and (A.1).

As  $l$  is connected with the fibre thickness and, hence, cannot exceed the beam thickness,  $\lambda$  acquires naturally the upper bound value noted in (41) only if  $l = h$ . However, connection of  $l$  with the fibre thickness is here refereed to only as an example of the manner in which one can handle the aforementioned dimensions difference between the fibre bending modulus,  $d^f$ , and the conventional elastic moduli met in nonpolar elasticity.

If, for instance, one accepts that fibres are approximately arranged through the beam thickness in the form of representative volume elements described in Appendix C, the estimated upper bound of  $\lambda$  may further be reduced considerably, or even be related to the  $V_{\max}^f$ -values noted there. All numerical results shown in what follows take this observation into careful consideration by using reasonably low values of  $\lambda$ .

However, in view of (10), equation (41) leads essentially to the following reparametrisation of the fibre bending stiffness modulus:

$$d^f(z) = \lambda h L V^f(z) C_{11}^f. \quad (42)$$

This relationship shows that, although useful on physical grounds,  $\lambda$  is not necessarily the most influential parameter for a proper determination of  $d^f$ . In fact, determination of  $d^f$  in a structural component should still be based on potential experimental work and observation, precisely as happens with the determination of conventional elastic moduli.

By setting  $\varepsilon = 0$  in (31) or (32), it is thus made initially sure that the present analysis gives identical numerical results, and is thus in complete agreement with its counterpart presented in [Farhat and Soldatos 2015]. This confirmation then enables the next consideration and study of corresponding numerical results that refer to inhomogeneous relevant composites having fibre volume fraction of the type (31) and (32) with  $\varepsilon \neq 0$ , or (35) with  $\alpha = 1.814$ .

**5.1. Through-thickness displacements distributions.** For several different values of the fibre inhomogeneity and the fibre bending stiffness parameters, Tables 1 and 2 present the nondimensional value of the in-plane and the transverse (flexural) displacement, respectively, obtained at selected points through the thickness of a top-stiff beam. To a considerable extent, these results are susceptible to comparison with their counterparts presented in Table 1 and Table 2 of [Farhat and Soldatos 2015], respectively, for corresponding homogeneous fibrous composites.

$z/h$	$\lambda = 0$	$\lambda = 0.004$	$\lambda = 0.01$
$\varepsilon = 0.01$			
0.50	0.011225	-0.025557	-0.047459
0.25	-0.097383	-0.063687	-0.044853
0	-0.114490	-0.067416	-0.041244
-0.25	-0.131141	-0.071387	-0.038791
-0.50	-0.228791	-0.104571	-0.038351
$\varepsilon = 0.05$			
0.50	-0.427908	-0.292289	-0.219078
0.25	-0.522101	-0.318635	-0.205783
0	-0.522724	-0.308312	-0.189578
-0.25	-0.527046	-0.302616	-0.178970
-0.50	-0.609684	-0.329450	-0.176406
$\varepsilon = 0.1$			
0.50	-0.874707	-0.575411	-0.405471
0.25	-0.945979	-0.585632	-0.378715
0	-0.922377	-0.556283	-0.346454
-0.25	-0.907455	-0.536790	-0.325080
-0.50	-0.962171	-0.554231	-0.319076
$\varepsilon = \varepsilon_{\max} = 0.812$			
0.50	-0.643334	-0.619429	-0.587989
0.25	-0.497675	-0.470583	-0.434870
0	-0.287050	-0.269299	-0.245997
-0.25	-0.141990	-0.132669	-0.120484
-0.50	-0.086794	-0.080983	-0.073505

**Table 1.** Through-thickness in-plane displacement distributions  $\bar{U}(0, z)$  of a top-stiff beam with volume fraction  $V_f = 0.5 + \varepsilon(z/h)$ .

In line with the relevant trend noted in [Farhat and Soldatos 2015], Table 2 thus confirms that the magnitude of the flexural displacement decreases with increasing fibre bending stiffness parameter,  $\lambda$ , due to the additional flexural stiffness provided by the fibre bending resistance. However, it is seen here further that the magnitude of the flexural displacement decreases further with the increase in inhomogeneity parameter,  $\varepsilon$ . This is because, by increasing  $\varepsilon$ , the bending stiffness of the beam is increasing near the top lateral boundary where the external load is applied.

It is recalled on the other hand that the results presented in Table 1 and Table 2 of [Farhat and Soldatos 2015] show that, in the case of a homogeneous beam ( $\varepsilon = 0$ ), the in-plane displacement is always at least an order of magnitude smaller than its flexural counterpart. However, upon increasing the nonzero value of  $\varepsilon$ , the increasing material inhomogeneity affects the existing local coupling between bending and extension to such an extent that the magnitude of  $\bar{U}$  becomes comparable to that of  $\bar{W}$ .

$z/h$	$\lambda = 0$	$\lambda = 0.004$	$\lambda = 0.01$
$\varepsilon = 0.01$			
0.50	-1.206993	-0.739809	-0.484421
0.25	-1.149196	-0.685004	-0.431542
0	-1.104615	-0.645031	-0.394655
-0.25	-1.078050	-0.620907	-0.372337
-0.50	-1.063969	-0.610125	-0.363511
$\varepsilon = 0.05$			
0.50	-1.180509	-0.728882	-0.478972
0.25	-1.096412	-0.658369	-0.416258
0	-1.027262	-0.604367	-0.371167
-0.25	-0.976980	-0.567067	-0.341455
-0.50	-0.939239	-0.543660	-0.324820
$\varepsilon = 0.1$			
0.50	-1.111774	-0.702100	-0.466968
0.25	-1.001214	-0.615004	-0.393610
0	-0.907888	-0.546501	-0.339828
-0.25	-0.834697	-0.495854	-0.302449
-0.50	-0.776832	-0.458180	-0.277773
$\varepsilon = \varepsilon_{\max} = 0.812$			
0.50	-0.171586	-0.164078	-0.154164
0.25	-0.083960	-0.079280	-0.073117
0	-0.030777	-0.028854	-0.026333
-0.25	-0.006525	-0.006087	-0.005518
-0.50	0.002057	0.001928	0.001574

**Table 2.** Through-thickness deflection distributions  $\bar{W}(L/2, z)$  of a top-stiff beam with volume fraction  $V_f = 0.5 + \varepsilon(z/h)$ .

It is then not surprising that the values of  $\bar{U}$  shown in Table 1 differ from those of their counterparts presented in [Farhat and Soldatos 2015] even for  $\varepsilon = 0.01$ . In fact, for  $\varepsilon = 0.05$  the values of  $\bar{U}$  are already comparable with their  $\bar{W}$  counterparts (Table 2). Moreover, for  $\varepsilon = \varepsilon_{\max} = 0.812$ , which is the maximum value assigned to  $\varepsilon$  when fibre scale structure is designed with use of triangular RVEs, the magnitude of the in-plane displacement parameter exceeds that of  $\bar{W}$ , at least within the adopted region of the  $\lambda$ -variation. It is pointed out that, as all numerical results shown in this study refer to the left half of the beam, the minus sign associated with almost all numerical values shown in Table 1 implies that the beam deformation creates a predominantly tensile in-plane displacement.

Analogous conclusions may be drawn by observing and comparing the numerical results tabulated in Tables 3 and 4 for corresponding  $\bar{U}$ - and  $\bar{W}$ -values of a bottom-stiff inhomogeneous beam. The magnitude of displacements is again decreasing with increasing the value of the fibre bending stiffness parameter,  $\lambda$ . However, the sign of almost all numerical values shown in Table 3 reveals that the beam

$z/h$	$\lambda = 0$	$\lambda = 0.004$	$\lambda = 0.01$
$\varepsilon = 0.01$			
0.50	0.250340	0.118811	0.045144
0.25	0.136190	0.075284	0.042483
0	0.112192	0.065065	0.039931
-0.25	0.090771	0.056854	0.038507
-0.50	-0.013041	0.021001	0.038125
$\varepsilon = 0.05$			
0.50	0.748837	0.423789	0.242223
0.25	0.627284	0.370636	0.229269
0	0.592660	0.348727	0.214766
-0.25	0.564908	0.333408	0.206064
-0.50	0.452050	0.293394	0.204560
$\varepsilon = 0.1$			
0.50	1.368695	0.821958	0.506558
0.25	1.244704	0.759189	0.481362
0	1.202953	0.725370	0.452783
-0.25	1.173460	0.703956	0.435998
-0.50	1.055960	0.661147	0.434126
$\varepsilon = \varepsilon_{\max} = 0.812$			
0.50	2.811083	2.737809	2.637961
0.25	2.775249	2.680974	2.554224
0	2.784161	2.645146	2.461564
-0.25	2.854059	2.671874	2.433894
-0.50	2.877000	2.705601	2.480754

**Table 3.** Through-thickness in-plane displacement distributions  $\bar{U}(0, z)$  of a bottom-stiff beam with volume fraction  $V_f = 0.5 - \varepsilon(z/h)$ .

deformation creates now a predominantly compressive in-plane displacement.

Strong local inhomogeneity effects, of the type observed previously in Tables 1 and 2, have now emerged mainly at the bottom part of the beam. It is instructive for someone to observe that for  $\varepsilon = 0.05$  the magnitude of the in-plane displacement (Table 3) is again comparable with its flexural displacement counterpart (Table 4). Moreover, for  $\varepsilon = \varepsilon_{\max} = 0.812$ , the former parameter exceeds the latter to such a substantial degree, that the deformation seems in this case to take mainly place through in-plane extension rather than flexure. Nevertheless, Tables 1–4 suggest that, in general, top-stiff beams suffer smaller flexure and, therefore, may generally be considered stronger than their bottom-stiff counterparts at the same value of the inhomogeneity parameter,  $\varepsilon$ .

The observed in-plane deformation dominance seems to increase with increasing  $\varepsilon$  to an extent that affects substantially the detailed features of relevant stress distributions. This discussed later in Section 5.3,

$z/h$	$\lambda = 0$	$\lambda = 0.004$	$\lambda = 0.01$
$\varepsilon = 0.01$			
0.50	-1.209372	-0.741459	-0.485668
0.25	-1.165977	-0.695181	-0.438107
0	-1.135000	-0.662904	-0.405705
-0.25	-1.121685	-0.646083	-0.387473
-0.50	-1.120934	-0.642795	-0.382980
$\varepsilon = 0.05$			
0.50	-1.192043	-0.736960	-0.485114
0.25	-1.178822	-0.708742	-0.448893
0	-1.176597	-0.692904	-0.426143
-0.25	-1.191500	-0.691817	-0.416782
-0.50	-1.219350	-0.704768	-0.421728
$\varepsilon = 0.1$			
0.50	-1.132737	-0.717222	-0.478691
0.25	-1.157282	-0.712660	-0.457720
0	-1.191433	-0.718584	-0.448099
-0.25	-1.242375	-0.738541	-0.450930
-0.50	-1.307130	-0.773375	-0.467856
$\varepsilon = \varepsilon_{\max} = 0.812$			
0.50	-0.077214	-0.077423	-0.077602
0.25	-0.203017	-0.197384	-0.189706
0	-0.337329	-0.321135	-0.299640
-0.25	-0.486706	-0.454688	-0.412841
-0.50	-0.657611	-0.609844	-0.547717

**Table 4.** Through-thickness deflection distributions  $\bar{W}(L/2, z)$  of a bottom-stiff beam with volume fraction  $V_f = 0.5 - \varepsilon(z/h)$ .

which illustrates the influence that the increasing value of  $\varepsilon$  exerts on the bending stress distribution observed within both top- and bottom-stiff beams.

Under these considerations, the corresponding nondimensional displacement results shown in Tables 5 and 6 suggest that beams with through-thickness symmetric fibre distribution are similarly strong. Indeed, the magnitude of the flexural displacements shown in Table 6 are comparable with their counterparts shown in Table 2 for the largest value of the fibre inhomogeneity parameter,  $\varepsilon = \varepsilon_{\max} = 0.812$ , at least within the top half of the beam. Moreover, while the top-stiff beam has higher average fibre volume fraction, the difference observed between corresponding numerical results shown in Tables 2 and 6 is decreasing at the top part of the beam with the increase in fibre bending stiffness parameter.

**5.2. Through-thickness couple-stress and shear stress distributions.** As transition from nonpolar to polar material behaviour is caused by the emerging couple-stress field, immediate attention is next directed



$z/h$	$\lambda = 0$	$\lambda = 0.004$	$\lambda = 0.01$
0.50	-1.986187	-1.829115	-1.642851
0.25	-1.609659	-1.460507	-1.283656
0	-1.304430	-1.172045	-1.015665
-0.25	-1.330097	-1.185678	-1.015671
-0.50	-1.394719	-1.242775	-1.063927

**Table 5.** Through-thickness in-plane displacement distributions  $\bar{U}(0, z)$  of a beam with volume fraction  $V^f = 1.814|z/h|$ .

$z/h$	$\lambda = 0$	$\lambda = 0.004$	$\lambda = 0.01$
0.50	-0.227618	-0.209966	-0.188966
0.25	-0.073957	-0.066799	-0.058321
0	0.003799	0.003735	0.003642
-0.25	0.064515	0.057539	0.049324
-0.50	0.144491	0.127854	0.108322

**Table 6.** Through-thickness deflection distributions  $\bar{W}(L/2, z)$  of a beam with volume fraction  $V^f = 1.814|z/h|$ .

towards the influence that couple-stress creation exerts on the shear stress components, giving thus rise to nonsymmetric stress. Corresponding numerical results that show the manner in which normal stresses are affected are also presented and discussed afterwards, in [Section 5.3](#).

In this context, [Figures 5 and 6](#) depict the through-thickness distribution of the nondimensional couple-stress parameter  $\bar{m}_{xy}$  measured at selected axial positions of a top-stiff and a bottom-stiff beam, respectively, when  $\lambda = 0.006$  and  $\varepsilon = 0.1$ . The sinusoidal form that  $\bar{m}_{xy}$  acquires in the axial direction enables the couple-stress to satisfy the homogeneous boundary conditions [\(17\)<sub>3</sub>](#) imposed at the beam ends. These figures thus demonstrate the manner in which nonzero couple-stress distribution is created away from those ends, as well as the manner in which the  $\bar{m}_{xy}$ -magnitude increases with increasing distance from the left end of the beam. As expected, the figures also show that, regardless of the value of  $x/L$ , the magnitude of  $\bar{m}_{xy}$  attains a maximum on the top or on the bottom lateral plane of a top-stiff or a bottom-stiff beam, respectively.

For different values of the fibre bending stiffness parameter,  $\lambda$ , [Figures 7 and 8](#) illustrate next the through-thickness distribution of the shear stress  $\bar{\tau}_{zx}$  at the left end of a top- and a bottom-stiff beam, respectively. In line with [\[Farhat and Soldatos 2015\]](#), all depicted distributions satisfy the zero shear traction boundary conditions imposed on the upper and lower surface of the beam. Due to the relatively small value of the material inhomogeneity parameter ( $\varepsilon = 0.1$ ), the depicted curves do not diverge substantially from their counterparts shown in [Figure 6](#) of [\[Farhat and Soldatos 2015\]](#). However, they have all lost their largely symmetric form observed in [\[Farhat and Soldatos 2015\]](#) with respect to the beam middle axis, while their highest magnitude is moved towards the direction of increased fibre reinforcement; namely, upwards for the top-stiff and downwards for the bottom-stiff beam. As the beam

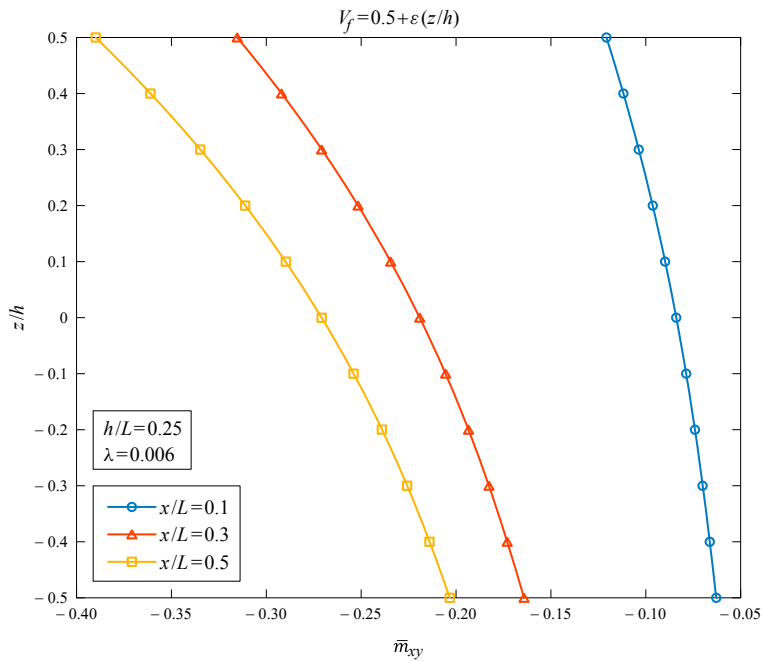


**Figure 5.** Through-thickness distribution of the couple-stress,  $\bar{m}_{xy}$ , at different axial positions of a top-stiff beam ( $\epsilon = 0.1$ ).

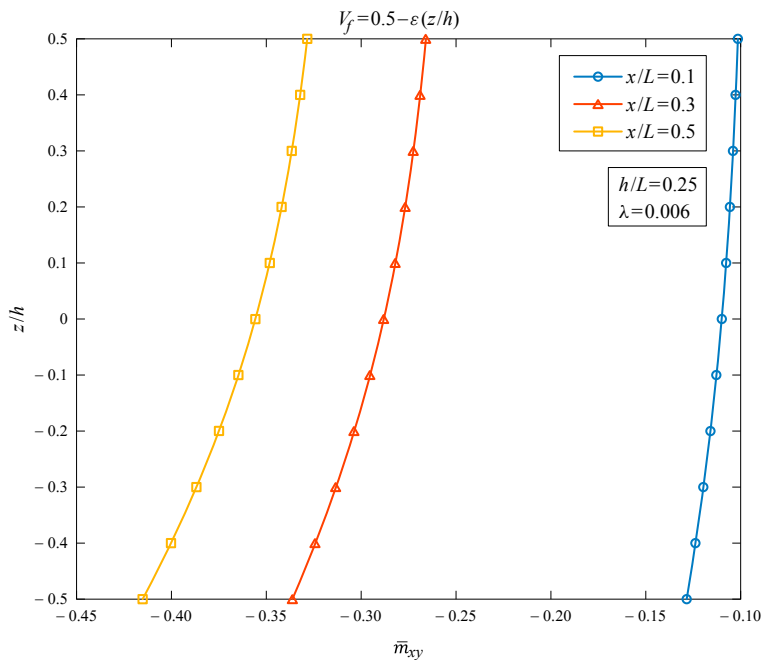


**Figure 6.** Through-thickness distribution of the couple-stress,  $\bar{m}_{xy}$ , at different axial positions of a bottom-stiff beam ( $\epsilon = 0.1$ ).

becomes stiffer with increasing  $\lambda$ , that highest magnitude of  $\bar{\tau}_{zx}$  decreases and moves naturally towards zero. It comes, however, a little as a surprise that, in the case of the bottom-stiff beam (Figure 8) and for the relatively large value  $\lambda = 0.009$  of the fibre thickness parameter, the relatively small value of that highest  $\bar{\tau}_{zx}$ -magnitude changes sign, along with the sign of the whole  $\bar{\tau}_{zx}$ -distribution.

Figures 9 and 10 show next the through-thickness distributions of the stresses  $\bar{\tau}_{xz}$  that correspond to  $\bar{\tau}_{zx}$ -distributions illustrated in Figures 7 and 8, respectively. Due to the symmetry of the stress tensor when  $\lambda = 0$ , the distributions drawn for  $\lambda = 0$  in Figures 7 and 8 are identical to their counterparts shown in Figures 9 and 10, respectively. However, as generation of nonzero couple-stress destroys stress symmetry, all  $\bar{\tau}_{xz}$  distributions associated with  $\lambda \neq 0$  in Figures 9 and 10 acquire nonzero values on the lateral beam boundaries.

Due to the relatively small value of the fibre inhomogeneity parameter ( $\varepsilon = 0.1$ ) the depicted  $\bar{\tau}_{xz}$ -distributions present again similarities with their counterparts shown in Figure 5 of [Farhat and Soldatos 2015]. Nevertheless, in almost all cases, the highest magnitude of the  $\bar{\tau}_{xz}$ -value moves again towards the stiffest part of the inhomogeneous structural component. An exception to this trend is again observed in the case of the bottom-stiff beam (Figure 10) where, for the relatively large value  $\lambda = 0.09$  of the fibre thickness parameter, the  $\bar{\tau}_{xz}$ -distribution reverses hollows and attains highest magnitude on the bottom lateral boundary.

Another remarkable observation relates to the fact that, like their counterparts depicted in Figure 6 of [Farhat and Soldatos 2015], all  $\bar{\tau}_{xz}$ -distributions shown in Figures 9 and 10 intersect at a certain pair of material points located at the vicinity of  $z/h = \pm 0.3$ . At those points, the value of  $\bar{\tau}_{xz}$  thus

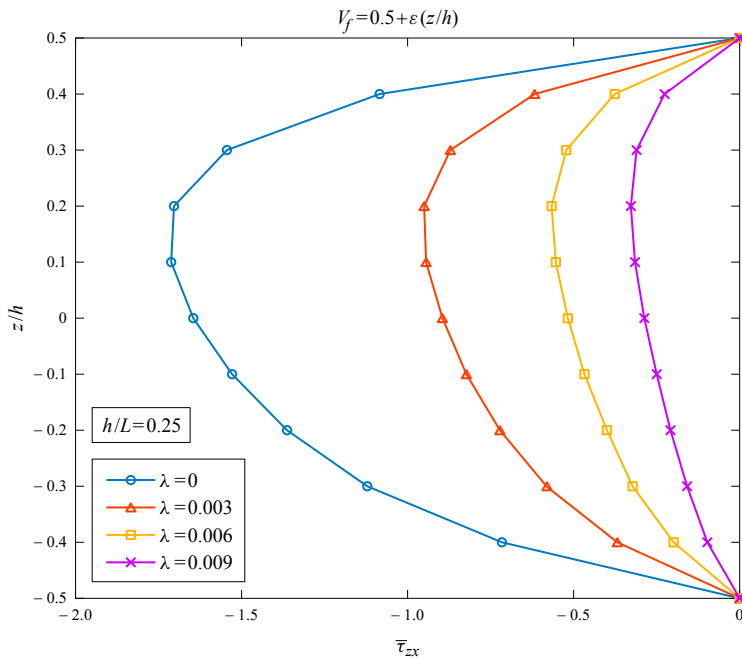


**Figure 7.** Through-thickness distribution of the shear stress  $\bar{\tau}_{zx}$  at the left end of a top-stiff beam ( $\varepsilon = 0.1$ ).

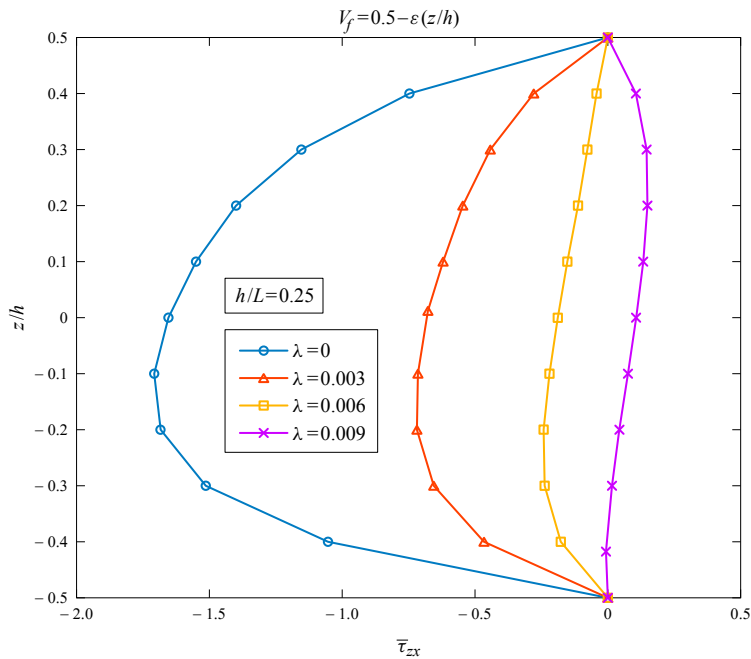


**Figure 8.** Through-thickness distribution of the shear stress  $\bar{\tau}_{zx}$  at the left end of a bottom-stiff beam ( $\epsilon = 0.1$ ).

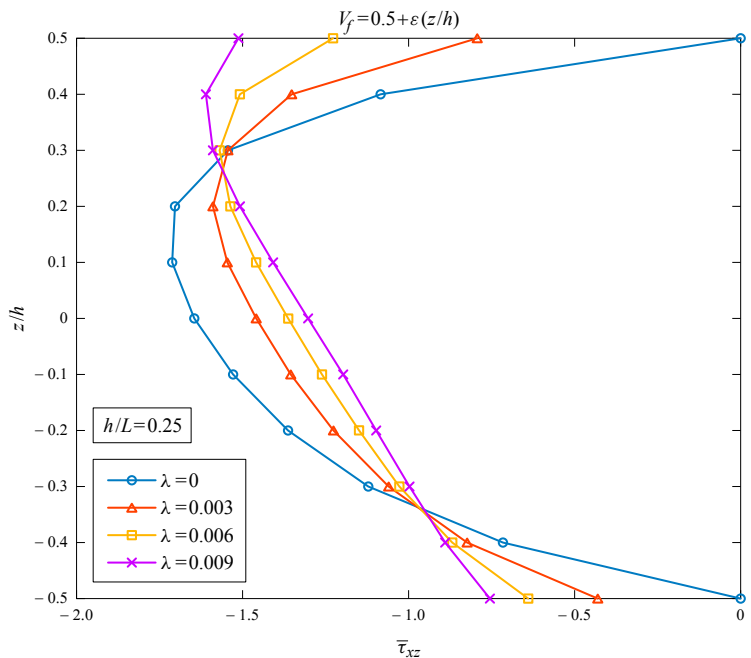


**Figure 9.** Through-thickness distribution of the shear stress  $\bar{\tau}_{xz}$  at the left end of a top-stiff beam ( $\epsilon = 0.1$ ).

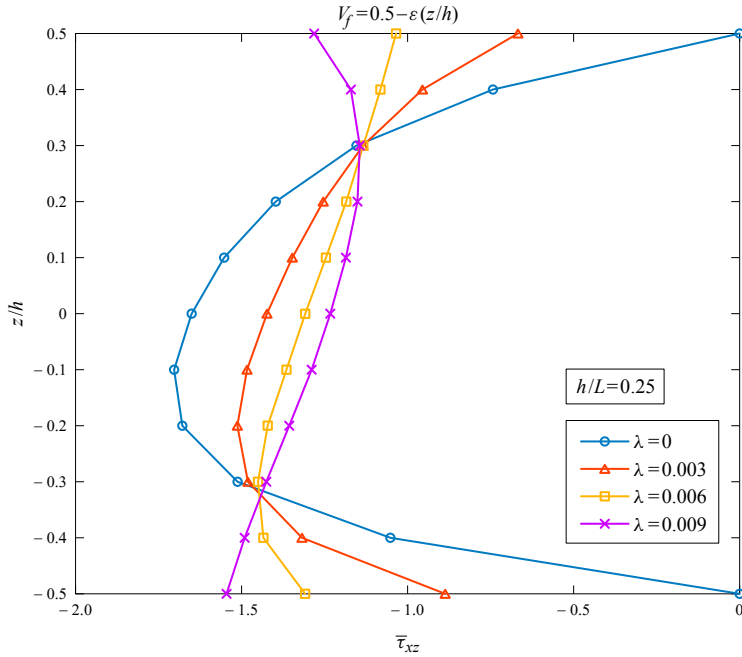


**Figure 10.** Through-thickness distribution of the shear stress  $\bar{\tau}_{xz}$  at the left end of a top-stiff beam ( $\varepsilon = 0.1$ ).

seems independent of the fibre thickness parameter,  $\lambda$ , although it evidently still depends on the fibre inhomogeneity parameter,  $\varepsilon$ . At present, there seems no obvious explanation to this effect, which is apparently due to the manner in which the couple-stress influences the values of  $\bar{\tau}_{xz}$ .

Under these considerations, Figures 11 and 12 depict the through-thickness  $\bar{\tau}_{zx}$ - and  $\bar{\tau}_{xz}$ -distributions, respectively, predicted at the left end of a beam reinforced in the symmetric, piecewise linear manner (35). Remarkably, changes of the fibre bending stiffness parameter,  $\lambda$ , do not seem to influence notably either of these shear stress distributions. The considerable similarity observed between the  $\bar{\tau}_{zx}$ -distributions depicted in Figure 11 and their  $\bar{\tau}_{xz}$  counterparts shown in Figure 12 is thus not surprising.

In fact, the principal difference between corresponding results demonstrated in those figures is that all  $\bar{\tau}_{zx}$ -distributions (Figure 11) attain, naturally, a zero value at the top and bottom lateral plane. Like their counterparts depicted previously in Figures 9 and 10, all different  $\bar{\tau}_{xz}$ -curves shown in Figure 12 pass again through a certain pair of material points, which are now moved at the vicinity of  $z/h = \pm 0.4$ . Moreover, the lack of fibre-reinforcement on the middle-axis has apparently made  $z/h = 0$  a third point of intersection for all  $\bar{\tau}_{xz}$ - and  $\bar{\tau}_{zx}$ -curves depicted in Figures 11 and 12. It is thus observed that, due to low local fibre-reinforcement, the stress state is nearly symmetric within a certain material band that surrounds the beam middle-axis.

**5.3. Through-thickness normal stress distributions.** Figures 13 and 14 depict the through-thickness distribution of the nondimensional normal stresses  $\bar{\sigma}_z$  and  $\bar{\sigma}_x$ , respectively, at the mid-span of a homogeneous fibre-reinforced beam ( $\varepsilon = 0$ ). Both figures depict in blue ( $\lambda = 0$ ) the known distribution of the implied normal stress when fibres are perfectly flexible [Soldatos and Watson 1997]. The remaining

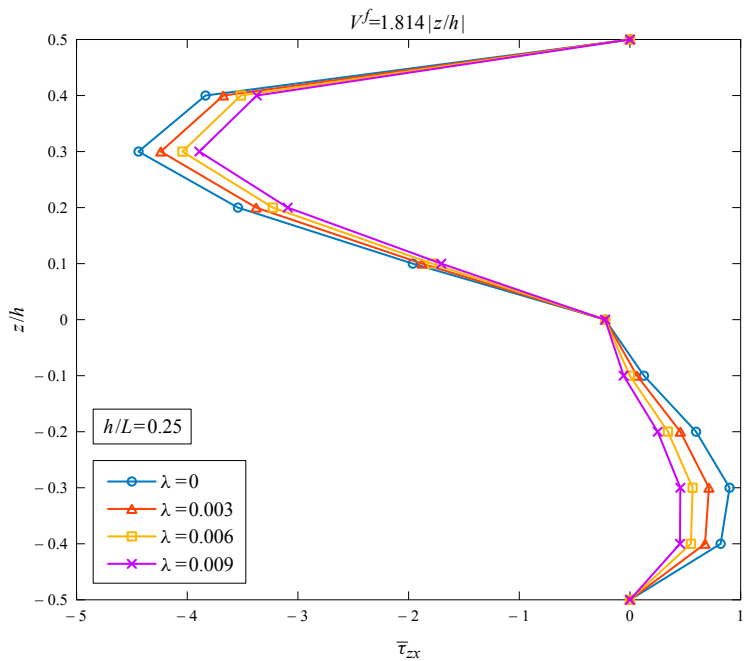


**Figure 11.** Through-thickness distribution of the shear stress  $\bar{\tau}_{zx}$  at the left end of a beam subjected to the symmetric, piecewise linear fibre reinforcement (35).

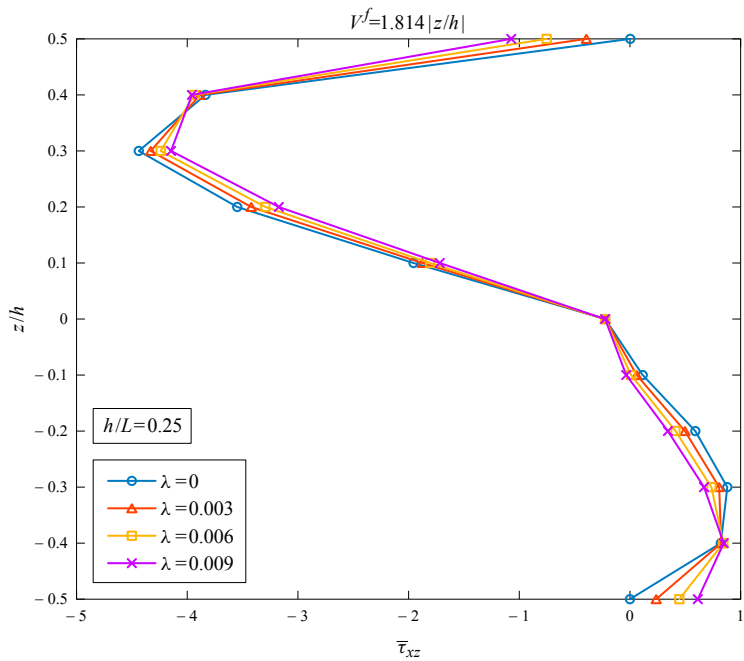


**Figure 12.** Through-thickness distribution of the shear stress  $\bar{\tau}_{xz}$  at the left end of a beam subjected to the symmetric, piecewise linear fibre reinforcement (32).

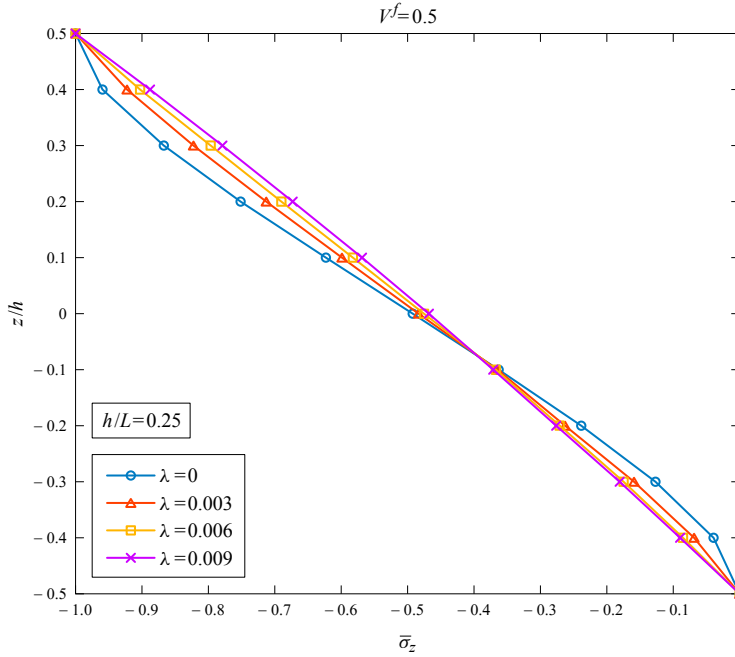


**Figure 13.** Distribution of the normal stress  $\bar{\sigma}_z$  at the mid-span ( $x/L = 0.5$ ) of a homogeneous beam ( $\epsilon = 0$ ).

curves then show the influence that fibre bending stiffness exerts on those known distributions upon gradually increasing the value of  $\lambda$ . Figure 13 thus makes it clear that fibre bending stiffness has marginal effect on the transverse normal stress distribution.

However, Figure 14 reveals that, upon increasing  $\lambda$ , the increasing resistance of the beam lowers the magnitude of  $\bar{\sigma}_x$  and, hence, decreases the influence that the depicted, well-known boundary layer effect of the  $\bar{\sigma}_x$ -distribution exerts on the strength of the structure. In fact, for  $\lambda$  as small as 0.009, the influence is decreased to such an extent that the value of the axial normal stress might be felt notable only within a particularly narrow layer near the beam lateral boundary. Still though, every curve shown in Figure 14 evolves about a pivotal point, located at the vicinity of  $(\bar{\sigma}_x, z) = (0, 0)$ , in a manner that divides the corresponding bending stress distribution into a compressive and a tensile part (top and bottom half of the beam, respectively).

In the light of these observations, Figures 15 and 16 present next evidence of the fact that the combined action of fibre bending stiffness and material inhomogeneity ( $\epsilon = 0.1$ ) has still marginal effect on the  $\bar{\sigma}_z$ -distribution of a top- and a bottom-stiff beam, respectively. However, the same is not true for the corresponding  $\bar{\sigma}_x$ -distributions.

A search for the effect that combined action of fibre bending stiffness and material inhomogeneity has on the  $\bar{\sigma}_x$ -distribution is facilitated by initially considering that fibres are perfectly flexible ( $\lambda = 0$ ) and varying only the value of the inhomogeneity parameter  $\epsilon$ . In this context, Figures 17 and 18 demonstrate the manner in which the “blue”  $\bar{\sigma}_x$ -distribution associated in Figure 14 with  $\lambda = 0$  evolves with increasing inhomogeneity in a top- and a bottom-stiff beam, respectively. A thorough study of the results presented

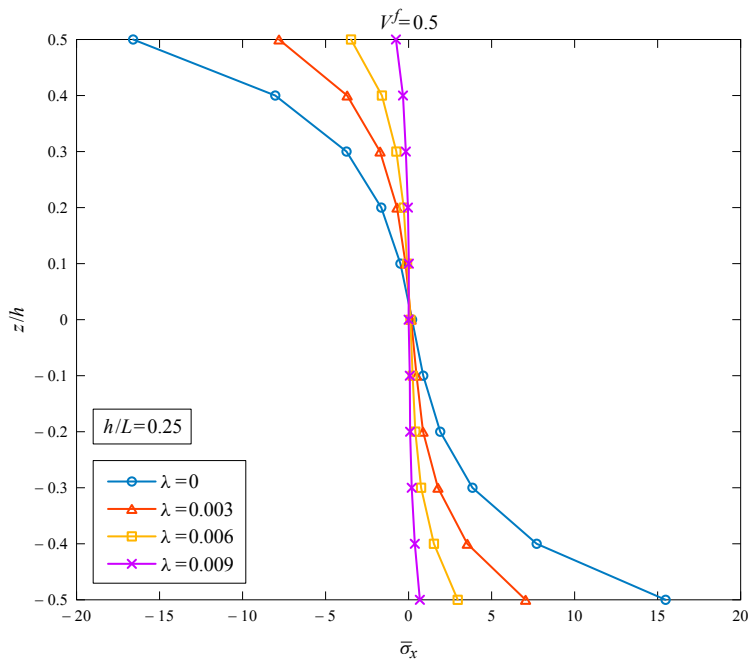


**Figure 14.** Distribution of the bending stress,  $\bar{\sigma}_x$ , at the mid-span ( $x/L = 0.5$ ) of a homogeneous beam ( $\epsilon = 0$ ).

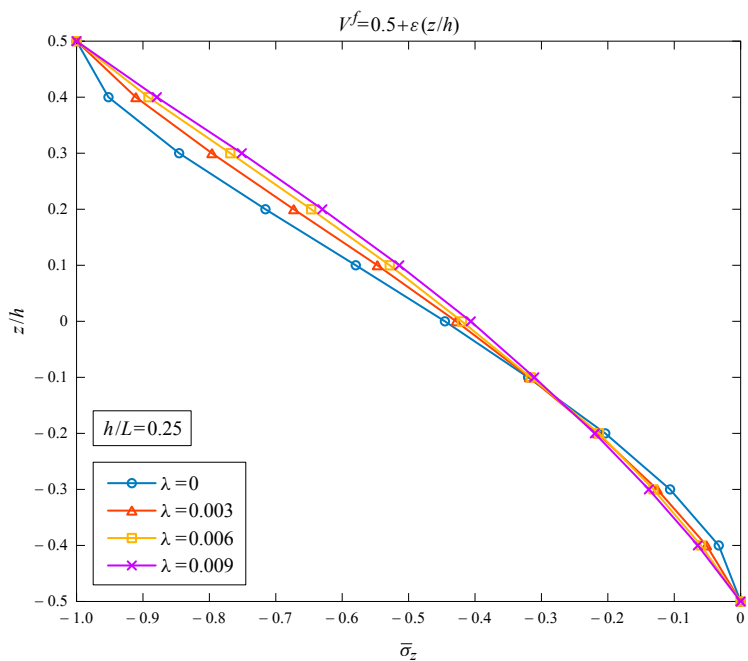


**Figure 15.** Distribution of the normal stress  $\bar{\sigma}_z$  at the mid-span ( $x/L = 0.5$ ) of a top-stiff beam ( $\epsilon = 0.1$ ).



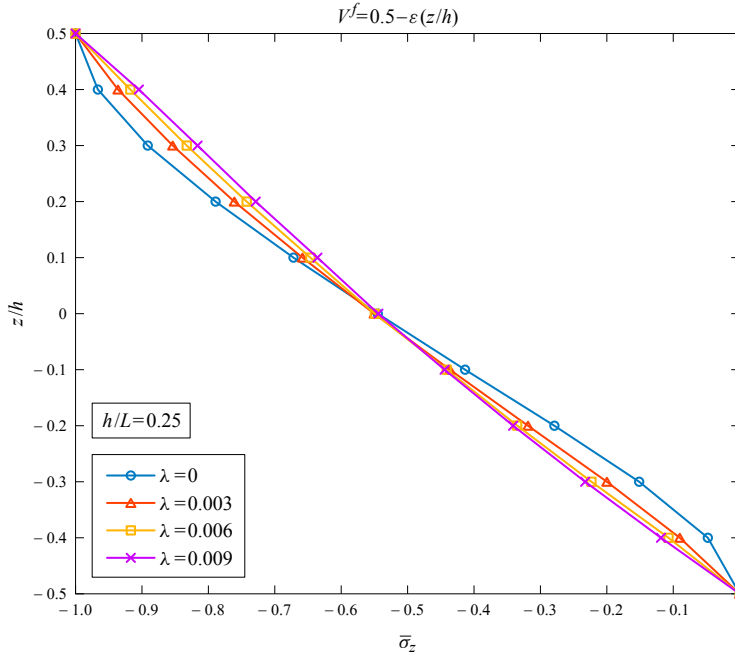
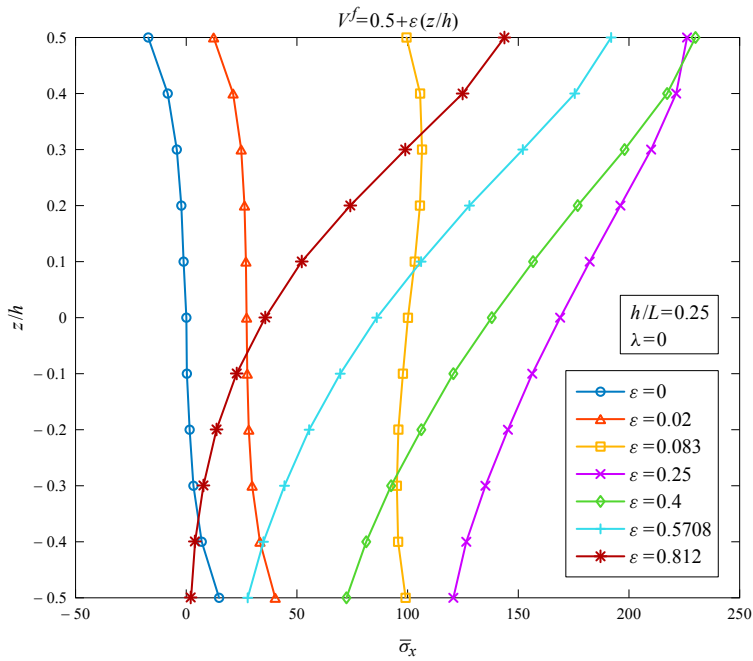


**Figure 16.** Distribution of the normal stress  $\bar{\sigma}_z$  at the mid-span ( $x/L = 0.5$ ) of a bottom-stiff beam ( $\varepsilon = 0.1$ ).

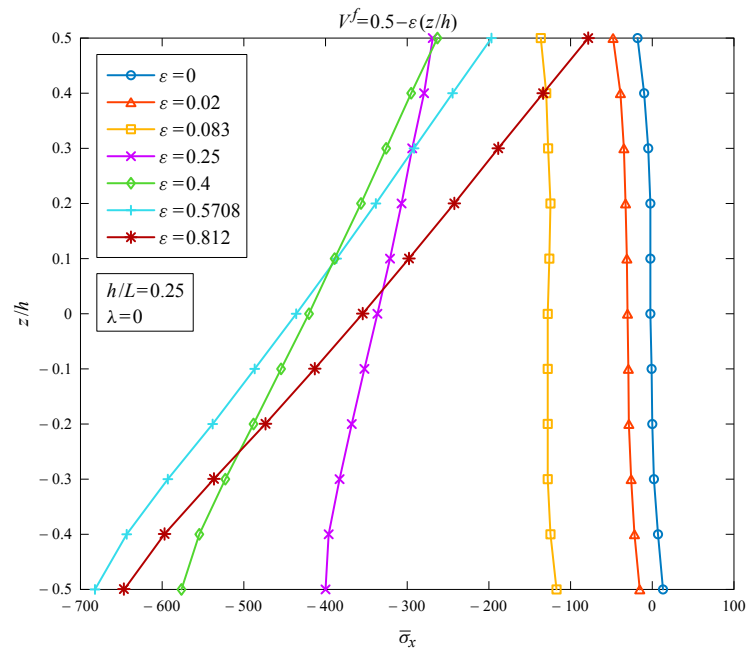
in Figures 17 and 18 makes afterwards clearer the corresponding results depicted in Figures 19 and 20 for corresponding inhomogeneous beams with embedded fibres resistant in bending ( $\lambda = 0.06$ ).

Figure 17 thus reveals that, upon increasing  $\varepsilon$ , the observed  $\bar{\sigma}_x$ -distribution curve is initially transposed to the right. This is due to the dominance the  $\varepsilon$  exerts on its linearly dependent elastic moduli for small amounts of inhomogeneity. Hence, upon increasing  $\varepsilon$  within a narrow interval of relatively small values, the corresponding change of the elastic moduli suffices to “push” the depicted curve to the right, to an extent that soon turns the whole  $\bar{\sigma}_x$ -distribution completely tensile. Nevertheless, beyond the value  $\varepsilon = 0.083$ , which is still relatively small, the inhomogeneity difference between the top and the bottom parts of the beam becomes very dominant. Upon increasing  $\varepsilon$  further, the  $\bar{\sigma}_x$ -curve thus changes shape and, while still moves to the right and hence stays tensile, reveals that it is the upper, rather than the bottom part of the top-stiff beam that bares most of the externally applied loading.

Eventually, at about  $\varepsilon = 0.25$ , the top part of the beam becomes so stiff that, while the value of the tensile bending stresses start to decrease at the lower part of the beam, the value of  $\bar{\sigma}_x$  approaches a maximum on the top lateral plane. Further increase of the  $\varepsilon$ -value and, hence, of the stiffness of top part of the beam lowers the observed tensile bending stresses throughout the beam thickness. It is instructive in this regard to note that the  $\bar{\sigma}_x$ -curve in Figure 17 for  $\varepsilon = 0.4$  is essentially transposed to the left when the inhomogeneity parameter is increased up to  $\varepsilon = 0.5708$ , or further up to  $\varepsilon = 0.812$ . It is recalled that (34) associates 0.5708 or 0.812 with the maximum value that  $\varepsilon$  may attain when the fibre-scale structure is modelled with rectangular or triangular RVEs, respectively. It is thus observed that, upon increasing  $\varepsilon$  towards its maximum value, the decreasing tensile value of  $\bar{\sigma}_x$  observed near the bottom boundary of the top-stiff beam is naturally moving towards zero.



**Figure 17.** Variation of the bending stress distribution at the mid-span ( $x/L = 0.5$ ) with increasing inhomogeneity of a top-stiff beam reinforced by perfectly flexible fibres ( $\lambda = 0$ ).



**Figure 18.** Variation of the bending stress distribution at the mid-span ( $x/L = 0.5$ ) with increasing inhomogeneity of a bottom-stiff beam reinforced by perfectly flexible fibres ( $\lambda = 0$ ).

Figure 18 demonstrates that the bending stress distribution of a bottom-stiff beam with embedded perfectly flexible fibres responds in an analogous manner. One of the evident principal differences with the trends observed in Figure 17 is the fact that, upon increasing material inhomogeneity, the  $\bar{\sigma}_x$ -distribution curve that corresponds to  $\lambda = 0$  in Figure 14 moves towards the left, and thus soon turns completely compressive. Moreover, the change of shape that the  $\bar{\sigma}_x$ -curve observes for higher values of  $\varepsilon$  suggests that, naturally, it is now the bottom, rather than the upper part of the bottom-stiff beam that bares most of the loading. Finally, the aforementioned observations, associated in Figure 17 with the top and the bottom plane of a top-stiff beam, are naturally seen in Figure 18 associated with the bottom and the top plane, respectively, of a bottom-stiff beam.

In the light of these observations, Figures 19 and 20 illustrate next the manner in which the “yellow”  $\bar{\sigma}_x$ -distribution curve, formed in Figure 14 by setting  $\lambda = 0.006$ , evolves with increasing inhomogeneity of a top- and a bottom-stiff beam, respectively. To a considerable extent, these results show substantial quantitative similarity with their counterparts depicted in Figures 17 and 18 for corresponding beams having embedded perfectly flexible fibres. However, and in close agreement with all previously observed trends, the extra bending stiffness added now on the functional graded beam lowers significantly the magnitude of the observed bending stresses.

Figures 21 and 22 depict the distribution of the normal stresses  $\bar{\sigma}_x$  and  $\bar{\sigma}_z$ , respectively, at the mid-span of a fibre-reinforced beam subjected to the symmetric, piecewise linear fibre reinforcement (35). In line with the results depicted in Figures 11 and 12 for corresponding shear stress distributions, both stress distributions attain a nearly symmetric form, with respect to the middle axis, within a narrow band of weak local fibre-reinforcement. Regardless of the value of the fibre bending stiffness parameter, that symmetry gradually fades outside that band around the middle axis.

The value of the bending stress at the top boundary of the beam, where the external load is applied, thus becomes naturally bigger from its bottom boundary counterpart (see Figure 21). However, like the top-stiff beam (see Figures 17 and 19 for  $\varepsilon \neq 0$ ), the bending stress is always tensile throughout the beam thickness. Unlike the corresponding results shown in Figures 17 and 19 though, the imposed lack of local fibre-reinforcement at  $z/h = 0$  enables the beam middle axis to remain almost free of bending stress. It is also noticeable in this regard that, regardless of the value of the fibre bending stiffness parameter, the through-thickness shape of the  $\bar{\sigma}_x$ -distribution resembles closely the form (35) of the corresponding fibre volume fraction.

On the other hand, Figure 22 reveals that the weak reinforcement observed around the beam middle axis and, hence, practically the negligible influence of  $\bar{\sigma}_x$  is locally compensated by a sharp jump of the transverse normal stress,  $\bar{\sigma}_z$ . The latter is seen positive and, therefore, tensile within the aforementioned narrow band, as well as within the bottom part of the beam. Unlike its top- and bottom-stiff counterparts, which are negative and therefore compressive throughout the beam thickness (see Figures 15 and 16), the distribution of  $\bar{\sigma}_z$  depicted in Figure 22 is compressive at and near the top beam boundary, where the external load is applied, but turns tensile within the aforementioned band of weak fibre-reinforcement. It then remains tensile in the bottom part of the beam, where it decreases and becomes finally zero on the unstressed bottom beam boundary.

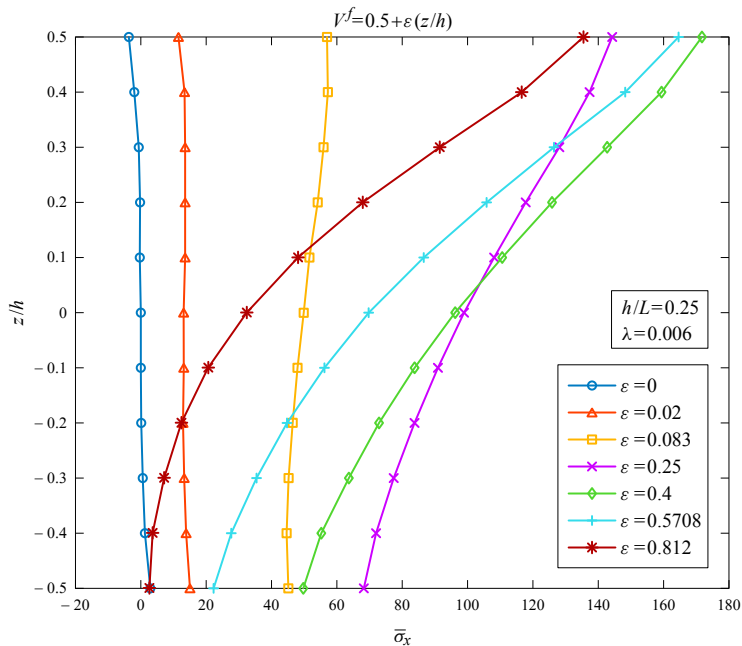


**Figure 19.** Variation of the bending stress distribution at the mid-span ( $x/L = 0.5$ ) with increasing inhomogeneity of a top-stiff beam reinforced by fibres resistant in bending ( $\lambda = 0.006$ ).

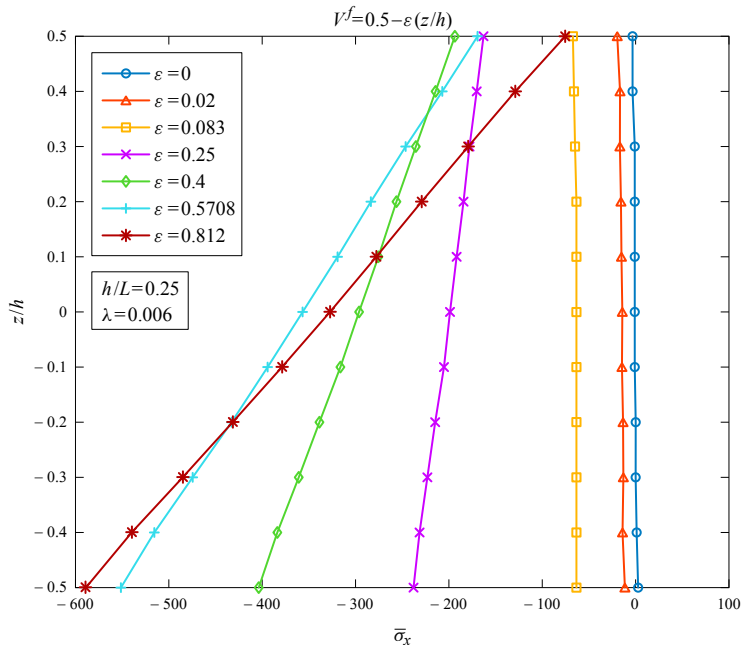


**Figure 20.** Variation of the bending stress distribution at the mid-span ( $x/L = 0.5$ ) with increasing inhomogeneity of a bottom-stiff beam reinforced by fibres resistant in bending ( $\lambda = 0.006$ ).

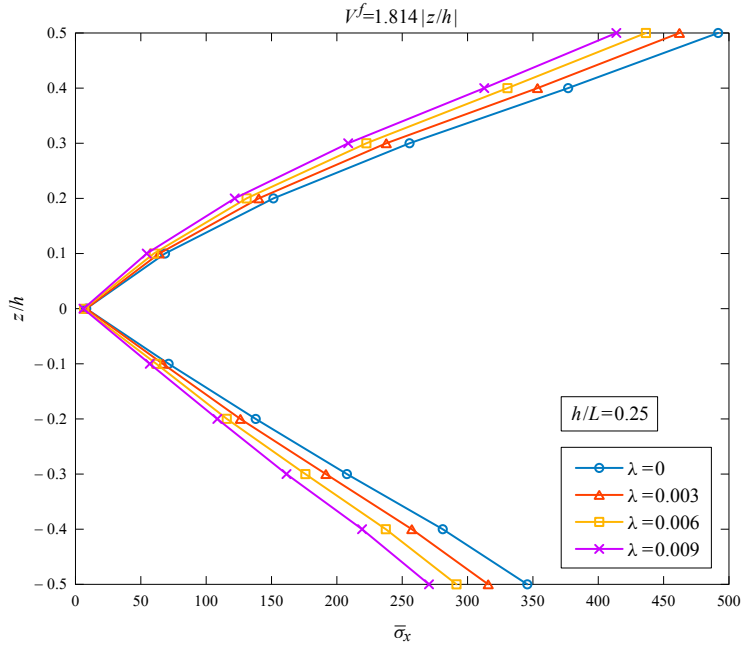


**Figure 21.** Variation of the bending stress distribution at the mid-span ( $x/L = 0.5$ ) with increasing fibre bending stiffness of a beam subjected to the symmetric, piecewise linear fibre reinforcement (35).

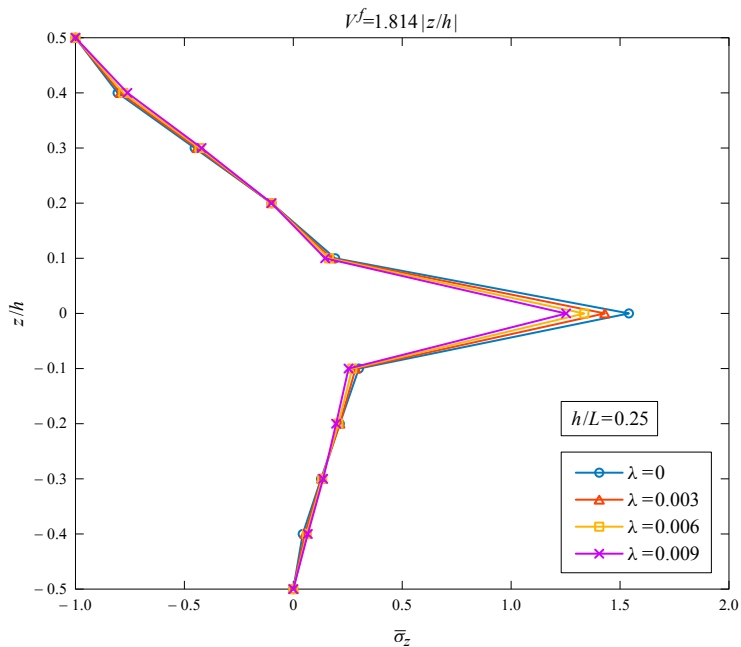


**Figure 22.** Variation of the distribution of the transverse normal stress,  $\bar{\sigma}_z$ , at the mid-span ( $x/L = 0.5$ ) of a beam subjected to the symmetric, piecewise linear fibre reinforcement (35).

## 6. Conclusions

This study aims initially to promote the need for extension into the regime of polar material response of fibrous composites of relevant nonpolar linear elasticity solutions. Namely, existing solutions of well-posed boundary value problems represented by continuous displacements having continuous derivatives of all orders. As nonpolar elasticity of fibre-reinforced materials assumes that fibres embedded in a structural component are perfectly flexible, the implied solution extensions will offer substantially better understanding of the behaviour of composites reinforced by stiff fibres, such as carbon nanotubes, that exhibit considerable bending resistance.

In serving the first of these aims, this study continued an initial relevant extension [Farhat and Soldatos 2015] of the well-known Pagano's nonpolar plane strain elasticity solution [Pagano 1969], by considering that the implied stiff fibres are redistributed within their matrix in an inhomogeneous, functionally graded manner. Like in [Farhat and Soldatos 2015], the implied solution extension was based on the restricted version of the polar elasticity theory presented in [Spencer and Soldatos 2007], namely a theory that involves only a single elasticity modulus of fibre bending resistance. That extra elasticity modulus is associated with the global response of the fibrous composite, rather than with the response of individual fibres, but its involvement enables the theory to make use of an intrinsic length parameter that relates to an average fibre thickness.

By setting that intrinsic length parameter and, therefore, the fibre thickness equal to zero, our theory and analysis reduce naturally to their conventional, nonpolar elasticity counterparts. Thus content and results of this article are useful even in cases of nonpolar material response, where the fibres embedded in a relevant functionally graded fibrous composite are perfectly flexible. In this context, the parametric studies performed in Section 5, along with their counterparts presented in [Farhat and Soldatos 2015], enable better understanding of the influence that fibre bending resistance exerts on the plane strain behaviour of the implied class of fibrous composites, provided that the obtained, continuous solution of the boundary value problem (Section 3) prevails over potential weak discontinuity solutions.

In this connection, it is reemphasised that this communication aims further to make it wider known that, unlike its nonpolar linear elasticity counterpart, a corresponding fully continuous polar linear elasticity solution is not necessarily the unique solution of the respective boundary value problem. Due to the lack of ellipticity that linear elasticity equations suffer outside their nonpolar material regime, the implied polar elasticity extension of a continuous solution may instead be accompanied by a number of additional "weak discontinuity" solutions. Namely, solutions of the same boundary value problem that may represent fibre-scale failure modes.

It is recalled in this context that a preliminary theoretical analysis that enables determination of weak discontinuity surfaces in linearly elastic structural components reinforced by fibres resistant in bending is already available in [Soldatos 2014; 2015]. Reference [Soldatos 2015], in particular, makes use of precisely the same, restricted theoretical background employed in the present study, but applies its findings to three-dimensional study of composites reinforced by two families of straight uniaxial fibres. Specialization of that analysis [Soldatos 2015] to the case of a single fibre family is currently under way. This is expected to lead to weak discontinuity solutions that accompany potential three-dimensional extensions of the continuous solution as detailed in Section 3. Identifications of weak discontinuity solutions associated with the plane strain solution (Section 3) may then follow as particular cases.

### Appendix A: Determination of the elastic moduli appearing in (4)

The Young's modulus and the Poisson's ratio of the isotropic matrix phase are respectively given, in terms of the Lamé moduli appearing in (7), by the standard formulas

$$E \equiv E_L^m = E_T^m = \frac{\mu(3\lambda + 2\mu)}{\lambda + \mu}, \quad \nu \equiv \nu^m = \frac{\lambda}{2(\lambda + \mu)}. \quad (\text{A.1})$$

The fibre phase of the composite can be either isotropic or anisotropic. For the purpose of the present study, this is considered as transversely isotropic.

The elastic moduli of the fibre phase are accordingly considered to relate with their matrix phase counterparts as

$$\begin{aligned} (E_L^f, E_T^f) &= (\alpha_1, \alpha_2) E, & G_{LT}^f &= \alpha_3 \mu = \alpha_3 \frac{E}{2(1 + \nu)}, \\ (\nu_{LT}^f, \nu_{TT}^f) &= (\alpha_4, \alpha_5) \nu, & G_{TT}^f &= \frac{E}{2(1 + \nu_{TT}^f)}, \end{aligned} \quad (\text{A.2})$$

where  $\alpha_1, \alpha_2, \dots, \alpha_5$  are considered as known dimensionless constants, and a subscript “ $L$ ” or “ $T$ ” indicates the axis or the plane of transverse isotropy, respectively.

With use of the mixture law (1), the effective elastic moduli of the functionally graded fibrous composite are obtained in the following form:

$$\begin{aligned} E_L &= [1 + (\alpha_1 - 1)V^f(z)]E, & E_T &= [1 + (\alpha_2 - 1)V^f(z)]E, \\ G_{LT} &= [1 + (\alpha_3 - 1)V^f(z)] \frac{E}{2(1 + \nu)}, \\ \nu_{LT} &= [1 + (\alpha_4 - 1)V^f(z)]\nu, & \nu_{TT} &= [1 + (\alpha_5 - 1)V^f(z)]\nu, \end{aligned} \quad (\text{A.3})$$

while it is still (e.g., [Jones 1998])

$$G_{TT} = \frac{E_T}{2(1 + \nu_{TT})}. \quad (\text{A.4})$$

The elastic moduli appearing in (4) can then be obtained by inserting (A.3) and (A.4) into the standard relevant formulas (e.g., [Jones 1998]), after aligning the longitudinal direction of transverse isotropy,  $L$ , with the  $x$ -axis of the adopted Cartesian coordinate system.

### Appendix B: Implementation of the fictitious layers method

For a sufficiently thin plate or beam ( $h/L \ll 1$ ), an approximate solution of (23) is obtained by replacing the variable  $z$  appearing in (6) and, hence, in (22) with its middle-plane value, namely its value at  $z = 0$ . In this manner, (23) is replaced by the following system of approximate linear ODEs:

$$D\mathbf{F} = \mathbf{T}(0)\mathbf{F}, \quad \mathbf{F} = [Df, f, Dg, g]^T. \quad (\text{B.1})$$

As this ODE system has constant coefficients, the exact form of its general solution can be expressed as

$$\mathbf{F}(z) = \mathbf{S}(z)\mathbf{F}(-\tfrac{1}{2}h), \quad \mathbf{S}(z) = \exp\left[(z + \tfrac{1}{2}h)\mathbf{T}(0)\right] \quad (-\tfrac{1}{2}h \leq z \leq \tfrac{1}{2}h), \quad (\text{B.2})$$

where the elements of the appearing exponential matrix  $\mathbf{S}(z)$  are determined in the manner detailed in [Ye 2003]. It is thus anticipated that the thinner is the inhomogeneous structural component of interest the nearer (B.2) approximates the exact solution of (23) or, equivalently, (20).

When the thickness is not sufficiently small, the exact solution of (20) is approached computationally very closely by dividing the structure into  $N$  successive fictitious layers (see Figure 1) having the same constant thickness,  $h^{(j)} = h/N$  ( $j = 1, 2, \dots, N$ ). Each individual fictitious layer is associated with a local transverse coordinate parameter,  $z^{(j)} = z - (j - 1)h/N + h/2$ , and, due to the FGM nature of the plate, is itself materially inhomogeneous in the region  $h^{(j)}/2 \leq z^{(j)} \leq h^{(j)}/2$ .

However, by choosing a suitably large value of  $N$ , each fictitious layer is itself regarded as a sufficiently thin plate or beam whose mechanical response and behaviour are described satisfactorily by an approximate solution of the form (B.2). The approximate solutions thus obtained for all  $N$  fictitious layers are then suitably connected together by means of appropriate continuity conditions imposed on the displacement and interlayer stress components. Upon increasing the value of  $N$ , this process provides a sufficiently close solution to that of the exact governing equations (20) (see also [Shuvalov and Soldatos 2003]).

In more detail, the continuity conditions imposed on a generic  $j$ -th material interface (denoted by  $z_j$  in Figure 1) are as ( $j = 1, 2, \dots, N - 1$ ):

$$\begin{aligned} U(-h^{(j+1)}/2) &= U(h^{(j)}/2), & W(-h^{(j+1)}/2) &= W(h^{(j)}/2), \\ \sigma_z(-h^{(j+1)}/2) &= \sigma_z(h^{(j)}/2), & \tau_{zx}(-h^{(j+1)}/2) &= \tau_{zx}(h^{(j)}/2). \end{aligned} \quad (\text{B.3})$$

In matrix form, these are transformed into

$$\mathbf{F}^{(j+1)}(-h^{(j+1)}/2) = \mathbf{R}^{(j)} \mathbf{F}^{(j)}(h^{(j)}/2), \quad (\text{B.4})$$

where

$$\mathbf{R}^{(j)} = \begin{bmatrix} \frac{C_{55}^{(j-1)}}{C_{55}^{(j)}} & 0 & 0 & \frac{C_{55}^{(j-1)} + d^{f(j-1)}/4}{C_{55}^{(j)}} - \frac{C_{55}^{(j)} + d^{f(j)}/4}{C_{55}^{(j)}} \\ 0 & 1 & 0 & 0 \\ 0 & \frac{C_{13}^{(j-1)}}{C_{33}^{(j)}} - \frac{C_{13}^{(j)}}{C_{33}^{(j)}} & \frac{C_{33}^{(j-1)}}{C_{33}^{(j)}} & 0 \\ 0 & 0 & 0 & 1 \end{bmatrix}, \quad (\text{B.5})$$

and  $C_{55}^{(j)}$ ,  $C_{13}^{(j)}$ ,  $\dots$ , etc., signify the constant values that the implied elastic moduli acquire on the middle plane,  $z^{(j)} = 0$ , of the  $j$ -th fictitious layer ( $j = 1, 2, \dots, N$ ). Application of the same notation is extended to include the appearing fibre bending stiffness parameter,  $d^{f(j)}$ , where, however, it is also implied that the previous use is made of (10).

Upon using successively (B.1), (B.2) and (B.4), one builds up the solution of the problem considered



in a recursive manner. Hence, for the  $i$ -th layer, it is

$$\begin{aligned}
 \mathbf{F}(z) \equiv \mathbf{F}^{(i)}(z^{(i)}) &= \mathbf{S}^{(i)}(z^{(i)}) \mathbf{F}^{(i)}\left(\frac{-h^{(i)}}{2}\right) = \mathbf{S}^{(i)}(z^{(i)}) \mathbf{R}^{(i-1)} \mathbf{F}^{(i-1)}\left(\frac{h^{(i-1)}}{2}\right) \\
 &= \mathbf{S}^{(i)}(z^{(i)}) \mathbf{R}^{(i-1)} \mathbf{S}^{(i-1)}\left(\frac{h^{(i-1)}}{2}\right) \mathbf{F}^{(i-1)}\left(\frac{-h^{(i-1)}}{2}\right) \\
 &= \mathbf{S}^{(i)}(z^{(i)}) (\mathbf{H}^{(i)}) \mathbf{F}^{(1)}\left(\frac{-h^{(1)}}{2}\right),
 \end{aligned} \tag{B.6}$$

where

$$\mathbf{H}^{(i)} = \prod_{k=i-1}^1 \mathbf{R}^{(k)} \mathbf{S}^{(k)}\left(\frac{h^{(k)}}{2}\right). \tag{B.7}$$

The value of  $\mathbf{F}(z)$  on the outer lateral surface is then obtained as

$$\mathbf{F}^{(N)}(h^{(N)}/2) = \mathbf{H} \mathbf{F}^{(1)}(-h^{(1)}/2), \quad \mathbf{H} = \mathbf{S}^{(N)}(h^{(N)}/2) \mathbf{H}^{(N)}. \tag{B.8}$$

If this is connected with the lateral boundary conditions (15), then (B.6) yields a linear system of four simultaneous algebraic equations for the four unknown components of the vector  $\mathbf{F}(-h^{(1)}/2) \equiv \mathbf{F}(-h/2)$ . Solution of that system of algebraic equations is then substituted back into (B.6) and it provides a semi-analytical solution of the governing differential equations (23).

In the case of homogeneous fibrous composites, the first iteration of the outlined solution ( $N = 1$ ) provides naturally the exact elasticity results obtained in [Farhat and Soldatos 2015]. For inhomogeneous composites, the number of iterations ( $N > 1$ ) required for accurate prediction of displacement and stress distributions depends on the degree of the assumed material inhomogeneity. As already mentioned, the convergence behaviour and success of this fictitious layer method has been verified repeatedly in the past (e.g., [Soldatos and Hadjigeorgiou 1990; Soldatos and Ye 1994; Shuvalov and Soldatos 2003; Ye 2003; Dagher and Soldatos 2011]) as well as most recently in [Brischetto 2019]. It accordingly suffices here to note that the value of  $\lambda$  does not seem to exert significant influence on the observed convergence characteristics of the method, which thus remain essentially unchanged, regardless of whether the plate is made of polar ( $\lambda \neq 0$ ) or nonpolar material ( $\lambda = 0$ ).

All numerical results shown in this communication were obtained by setting  $N = 100$ . In general, the maximum difference observed between corresponding results obtained on the basis of  $N = 100$  and  $N = 70$  iterations never exceeded 0.3%. It is worth noting that each iteration requires multiplication of  $4 \times 4$  matrices only. As a result, the implied hundreds of iterations involved in computations do not require noticeable use of excessive computer time.

### Appendix C: Consideration of the fibre-scale structure

It is assumed that fibres have circular cross-section of diameter  $d$  and, in the case of a homogeneous plate [Farhat and Soldatos 2015] are distributed along the  $z$ -direction in a regular form of  $N$  equidistant rows. The possible types of rectangular or triangular types RVEs depicted in Figure 3 consider that each vertex of an element is the centre of a fibre cross-section. In either case,  $S_y$  represents the distance of two neighbouring fibres in the  $y$ -direction.

Similarly,  $S_z$  represents the aforementioned constant distance between two neighbouring fibre rows. In this manner,  $S_z$  is the distance of neighbouring fibres in the  $z$ -direction of the rectangular element while, for a triangular RVE, it represents the height of the depicted isosceles triangle. In the particular case that the depicted triangle is considered equilateral ( $S = S_y$ ), it is  $S_z = \sqrt{3} S_y/2$ .

It becomes then readily understood that, necessarily, the following conditions always hold:

$$S_y \geq d, \quad S_z \geq d, \quad (\text{C.1})$$

for the rectangular element. For the triangular element, these are modified as

$$S_y \geq d, \quad S \geq d. \quad (\text{C.2})$$

For the purposes of the present study,  $d$  may be considered identical with the intrinsic parameter  $l$  introduced in (9). However, the adopted notation distinction of those two parameters is retained here, in order to signify that (i) the shape of the fibre cross-section may be considered noncircular in different applications, and (ii) the intrinsic length parameter  $l$  can acquire some different meaning in the theory of polar elasticity for fibre-reinforced materials [Spencer and Soldatos 2007], such as the fibre spacing for example.

Under these considerations, the fibre volume fraction of the RVE is defined as

$$V^f = \frac{\text{area of fibers within the RVE}}{\text{area of rectangle or triangle}}. \quad (\text{C.3})$$

For a rectangular RVE, this definition leads directly to

$$V^f = \frac{\pi d^2}{4S_y S_z}, \quad (\text{C.4})$$

but this result still holds true in the case a equilateral triangular RVE ( $S = S_y$ ,  $S_z = \sqrt{3} S_y/2$ ). It is thus seen that the plane strain assumption which underpins the principal problem of present interest is adequately and properly served by considering  $S_y = d$  in (C.4), regardless of whether the implied element is a rectangular or a triangular one.

It follows that the maximum fibre volume fraction in a rectangular RVE is achieved by setting  $S_y = S_z = d$  in (C.4), thus leading to

$$V_{\max}^f = \frac{\pi}{4} \cong 0.785. \quad (\text{C.5})$$

This value of  $V_{\max}^f$  necessarily coincides with the maximum possible value of  $V^f$  that the homogeneous counterpart of the present problem [Farhat and Soldatos 2015] is associated with when the fibre-scale structure is simulated with rectangular RVEs.

Similarly, maximum fibre volume fraction in a triangular RVE is achieved when  $S = S_y = d$ . In that case, (C.4) yields

$$V_{\max}^f = \frac{\pi}{2\sqrt{3}} \cong 0.907, \quad (\text{C.6})$$

which coincides with the maximum  $V^f$ -value that the homogeneous version of the problem is associated with if the fibre structure is simulated with equilateral triangular elements.

The values of  $V_{\max}^f$  shown in either (C.5) or (C.6) thus also consist of their corresponding upper limits such that the  $V^f$ -value can attain in the present inhomogeneous version of the problem, where

fibres are assumed redistributed in the manner described by (31), (32) or (35) within the same matrix material. However, such an upper limit of  $V^f$  can here be associated only with the densest fibre part of the inhomogeneous beam. Namely, the part located at the neighbourhood of  $z/h = 1/2$  or  $z/h = -1/2$  in top-stiff (31) or a bottom-stiff (32) beam, respectively, and the neighbourhood of both lateral planes ( $z/h = \pm 1/2$ ) in the case of a beam reinforced in the symmetric manner (35). This is achievable by considering that  $S_z$  is a suitable function of  $z$  which takes its lowest value (namely  $S_z = d$  or  $S_z = \sqrt{3}d/2$  for rectangular or triangular elements, respectively), in those densest fibre parts of the composite.

Hence, by associating  $V_{\max}^f$  with the top ( $z/h = 1/2$ ) or the bottom plane ( $z/h = -1/2$ ) of a top- or bottom-stiff beam, respectively, either of (31) or (32) yields the maximum value of the parameter  $\varepsilon_{\max}$  provided in (34). The inhomogeneous fibre distributions proposed in (31) and (32) are accordingly connected naturally with the present analysis when the fibre-scale structure is accurately simulated with rectangular or triangular RVEs, as soon as the  $\varepsilon_{\max}$ -value shown in (34) replaces the noted theoretical upper bound  $\varepsilon = 1$ . It is recalled that, by virtue of (3)<sub>1</sub>, both (31) and (32) will thus still return  $\langle V^f \rangle = 1/2$ .

However, in the case of the symmetric fibre distribution (35), association of  $V_{\max}^f$  with the densest fibre part of the beam,  $z/h = \pm 1/2$ , yields  $V_{\max}^f = \alpha/2$ . By virtue of (C.5) and (C.6) (alternatively (25)), one thus obtain the maximum values of  $\alpha$  shown in (36). The corresponding average volume fractions noted in (37) are then obtained by inserting each of those maximum  $\alpha$ -values into (35) and, then, performing the integration noted in (3).

Consideration of a fibrous composite having the effective properties (26) is still possible for  $\langle V^f \rangle = 0.39$  in this case, after replacing (A.3) with

$$\alpha_1 = 101, \quad \alpha_3 = 1.64165, \quad \alpha_2 = \alpha_4 = \alpha_5 = 1, \quad \nu = 0.25, \quad (\text{C.7})$$

and simultaneously modifying (30) as

$$E_T^f/E = 1, \quad E_L^f/E_T^f = 101, \quad G_{LT}^f/E_T^f = 0.6566, \quad \nu_{LT}^f = \nu_{TT}^f = \nu = 0.25, \quad G_{TT}^f/E_T^f = \frac{2}{3}. \quad (\text{C.8})$$

In a similar manner, a fibrous composite with effective properties (26) is obtained for  $\langle V^f \rangle = 0.45$  when all quantities appearing in (C.7) and (C.8) are replaced by their counterparts shown in (38).

#### Appendix D: A class of through-thickness symmetric fibre volume fractions

Consider a class of fibre volume fractions represented by the following even function of  $z$ :

$$V^f(z) = \alpha_n |z/h|^n \leq 1 \quad (-h/2 \leq z \leq h/2). \quad (\text{D.1})$$

Regardless of the value of the positive integer  $n$ , this form of  $V^f(z)$  is evidently symmetric with respect to the middle axis,  $z = 0$ , of the composite. Consider further that

$$\langle V^f(z) \rangle = k_1/k_2 \quad (k_2 \geq k_1 \geq 0, \quad k_2 \neq 0), \quad (\text{D.2})$$

so that the known integers  $n$ ,  $k_1$  and  $k_2$  are such that the inequalities noted in (1) are satisfied regardless of the value of the variable  $z$ .

It is observed in this regard that the maximum value of the fibre volume fraction, namely

$$V_{\max}^f = V^f(\pm h/2) = \alpha_n/2^n \leq 1, \quad (\text{D.3})$$

is attained at the lateral planes of the functionally graded fibrous composite. It follows that satisfaction of the inequalities noted in (1) restricts the value of the coefficient  $\alpha_n$  as

$$0 < \alpha_n \leq 2^n. \quad (\text{D.4})$$

By introducing (D.1) into (3)<sub>1</sub> and performing the denoted integration, one obtains

$$\alpha_n = 2^n(n+1)k_1/k_2, \quad (\text{D.5})$$

so that

$$V^f(z) = \frac{2^n(n+1)k_1}{k_2}|z/h|^n \quad (-h/2 \leq z \leq h/2). \quad (\text{D.6})$$

However, connection of (D.5) with (D.4) makes it clear that a fibre volume fraction of the form (D.6) is admissible for all values of  $z$  only if

$$n \leq (k_2/k_1) - 1 \quad (k_2 \geq k_1 > 0). \quad (\text{D.7})$$

For instance, in the particular case met in Section 4.2, where the composite contains 50% fibre and 50% matrix material, a combination of (D.2) with (33) suggests that

$$k_1 = 1, \quad k_2 = 2. \quad (\text{D.8})$$

Use of (D.7) makes it then further understood that, in that case, the only admissible value of the positive integer  $n$  is

$$n = 1, \quad (\text{D.9})$$

thus leading to  $\alpha_1 = 2$  and, hence, to the fibre volume fraction (35) with  $\alpha = 2$ .

It becomes also understood that, in cases when the fibre volume fraction is such that  $k_2/k_1 \geq 3$ , (D.7) returns multiple admissible values of  $n$  and, therefore, multiple admissible forms of (D.1). However, cases of volume fractions that admit multiple values of  $n$  are not considered in this investigation.

### Acknowledgement

KPS acknowledges support from the University of Nottingham, via the International Collaboration Fund, which enabled him to visit Trakya University, Edirne, Turkey, in August 2018. He also acknowledges the splendid hospitality of Trakya University.

### References

- [Adkins and Rivlin 1955] J. E. Adkins and R. S. Rivlin, “Large elastic deformations of isotropic materials X. Reinforcement by inextensible cords”, *Phil. Trans. R. Soc. A* **248**:944 (1955), 201–223.
- [Brischetto 2019] S. Brischetto, “Exponential matrix method for the solution of exact 3D equilibrium equations for free vibrations of functionally graded plates and shells”, *J. Sandw. Struct. Mater.* **21**:1 (2019), 77–114.
- [Cosserat and Cosserat 1909] E. Cosserat and F. Cosserat, *Théorie des corps déformables*, Hermann, Paris, 1909.
- [Dagher and Soldatos 2011] M. A. Dagher and K. P. Soldatos, “On small azimuthal shear deformation of fibre-reinforced cylindrical tubes”, *J. Mech. Mater. Struct.* **6**:1-4 (2011), 141–168.
- [Farhat and Soldatos 2015] A. F. Farhat and K. P. Soldatos, “Cylindrical bending and vibration of polar material laminates”, *Mech. Adv. Mater. Struct.* **22** (2015), 885–896.
- [Gibson 1994] R. F. Gibson, *Principles of composite material mechanics*, McGraw-Hill, 1994.

- [Jones 1998] R. M. Jones, *Mechanics of composite materials*, 2nd ed., Taylor & Francis, Washington, 1998.
- [Liew et al. 2015] K. M. Liew, Z. X. Lei, and L. W. Zhang, “Mechanical analysis of functionally graded carbon nanotube reinforced composites: a review”, *Compos. Struct.* **120** (2015), 90–97.
- [Merodio and Ogden 2002] J. Merodio and R. W. Ogden, “Material instabilities in fiber-reinforced nonlinearly elastic solids under plane deformation”, *Arch. Mech.* **54**:5-6 (2002), 525–552.
- [Merodio and Ogden 2003] J. Merodio and R. W. Ogden, “Instabilities and loss of ellipticity in fiber-reinforced compressible non-linearly elastic solids under plane deformation”, *Int. J. Solids Struct.* **40**:18 (2003), 4707–4727.
- [Mindlin and Tiersten 1962] R. D. Mindlin and H. F. Tiersten, “Effects of couple-stresses in linear elasticity”, *Arch. Ration. Mech. Anal.* **11**:1 (1962), 415–448.
- [Pagano 1969] N. J. Pagano, “Exact solutions for composite laminates in cylindrical bending”, *J. Compos. Mater.* **3**:3 (1969), 398–411.
- [Rivlin 1955] R. S. Rivlin, “Plane strain of a net formed by inextensible cords”, *J. Ration. Mech. Anal.* **4** (1955), 951–974.
- [Shuvalov and Soldatos 2003] A. L. Shuvalov and K. P. Soldatos, “On the successive approximation method for three-dimensional analysis of radially inhomogeneous tubes with an arbitrary cylindrical anisotropy”, *J. Sound Vib.* **259**:1 (2003), 233–239.
- [Soldatos 2009] K. P. Soldatos, “Towards a new generation of 2D mathematical models in the mechanics of thin-walled fibre-reinforced structural components”, *Int. J. Eng. Sci.* **47**:11-12 (2009), 1346–1356.
- [Soldatos 2014] K. P. Soldatos, “Foundation of polar linear elasticity for fibre-reinforced materials”, *J. Elasticity* **114**:2 (2014), 155–178.
- [Soldatos 2015] K. P. Soldatos, “Foundation of polar linear elasticity for fibre-reinforced materials II: advanced anisotropy”, *J. Elasticity* **118**:2 (2015), 223–242.
- [Soldatos 2018] K. P. Soldatos, “On the characterisation of polar fibrous composites when fibres resist bending — part II: connection with anisotropic polar linear elasticity”, *Int. J. Solids Struct.* **152-153** (2018), 1–11.
- [Soldatos and Hadjigeorgiou 1990] K. P. Soldatos and V. P. Hadjigeorgiou, “Three-dimensional solution of the free vibration problem of homogeneous isotropic cylindrical shells and panels”, *J. Sound Vib.* **137**:3 (1990), 369–384.
- [Soldatos and Watson 1997] K. P. Soldatos and P. Watson, “A method for improving the stress analysis performance of one- and two-dimensional theories for laminated composites”, *Acta Mech.* **123**:1-4 (1997), 163–186.
- [Soldatos and Ye 1994] K. P. Soldatos and J.-Q. Ye, “Three-dimensional static, dynamic, thermoelastic and buckling analysis of homogeneous and laminated composite cylinders”, *Compos. Struct.* **29**:2 (1994), 131–143.
- [Spencer 1972] A. J. M. Spencer, *Deformations of fibre-reinforced materials*, Clarendon Press, Oxford, 1972.
- [Spencer and Soldatos 2007] A. J. M. Spencer and K. P. Soldatos, “Finite deformations of fibre-reinforced elastic solids with fibre bending stiffness”, *Int. J. Non-Linear Mech.* **42**:2 (2007), 355–368.
- [Toupin 1962] R. A. Toupin, “Elastic materials with couple-stresses”, *Arch. Ration. Mech. Anal.* **11**:1 (1962), 385–414.
- [Truesdell and Toupin 1960] C. Truesdell and R. Toupin, “The classical field theories”, pp. 226–858 in *Principles of classical mechanics and field theory*, edited by S. Flügge, Springer, Berlin, 1960.
- [Ye 2003] J. Ye, *Laminated composite plates and shells: 3D modelling*, Springer, 2003.

Received 20 Feb 2019. Revised 11 Sep 2019. Accepted 30 Sep 2019.

KONSTANTINOS P. SOLDATOS: [kostas.soldatos@nottingham.ac.uk](mailto:kostas.soldatos@nottingham.ac.uk)

University of Nottingham, School of Mathematical Sciences, University Park, Nottingham, NG7 2RD, United Kingdom

METIN AYDOĞDU: [metina@trakya.edu.tr](mailto:metina@trakya.edu.tr)

Mechanical Engineering, Trakya University, 22030 Edirne, Turkey

UFUK GUL: [ufukgul@trakya.edu.tr](mailto:ufukgul@trakya.edu.tr)

Mechanical Engineering, Trakya University, 22030 Edirne, Turkey



# INTEGRATED MODELLING OF TOOL WEAR AND MICROSTRUCTURAL EVOLUTION INTERNAL RELATIONS IN FRICTION STIR WELDING WITH WORN PIN PROFILES

ZHAO ZHANG AND ZHIJUN TAN

An adaptive remeshing model was coupled with the Archard equation to calculate the tool wear in friction stir welding (FSW). The Monte Carlo method was used to simulate recrystallization in FSW with worn tools. In addition, experiments were used to validate the predicted temperatures and microstructures. As indicated by the results, appropriate tool wear can lead to self-optimization of the tool in FSW. This wear mechanism is controlled by the change in the average strain rate during the FSW process. The average strain rate first increases and then decreases with tool wear, which is the key factor when determining the final grains. An appropriate amount of tool wear can lead to smaller grains in the stirring zone of FSW whereas excess tool wear can lead to larger grains.

## 1. Introduction

Friction stir welding (FSW) has emerged in recent decades and has quickly been applied in various industries due to its advantages, including no melting, no pollution, and low residual distortions. Furthermore, FSW is suitable for light alloys, such as aluminum and magnesium alloys. Optimization of the process parameters can lead to high-quality friction stir welds without defects [Yang et al. 2018; He et al. 2017; Zhang and Zhang 2007; Ebrahimpour et al. 2019].

In FSW, the tool plays the key role for the final weld quality. De et al. [2014] tested the durability of a FSW welding tool of mild steel and found that the higher temperature, caused by increasing the tool rotation speed or the tool diameter, can lead to an increase of the tool durability. Sahlot et al. [2018] studied the tool wear in FSW of the CuCrZr alloy and found that the pin profile changes due to wear, resulting in root defects for a long weld distance. Suresha et al. [2011] studied the tool profile effects on the tensile properties of friction stir welded AA7075-T6. Moreover, Chen and Nakata [2009] studied the effect of tool geometry on microstructural changes as well as the mechanical properties in friction stir lap welding. Mehta et al. [2011] studied the influence of tool geometry in FSW and optimized the tool shoulder diameter. Zhang and Wu [2015] studied the tool diameter effect in FSW and correlated the changes of strain rates and temperatures with the grain sizes. The tool size effect on the grains was also studied by Zhang et al. [2014], as well as the effect on temperatures and material deformations [Zhang et al. 2009]. Mastanaiah et al. [2018] investigated the role of a hybrid tool pin profile compared with the conventional pin profile. Shindo et al. [2002] and Prado et al. [2003] found that there is self-optimization for tool wear in FSW. The wear rate decreases with the increase of the tool wear in FSW.

Sahlot and Arora [2018] established a numerical model based on Modified Archard's wear equation to investigate the tool wear in FSW with experimental validations, finding that the wear amount is more

*Keywords:* friction stir welding, wear, Monte Carlo.

obvious near the pin tip. The wear is more at the beginning and becomes less at long traverse. Tool wear can lead to the changes of pin profiles in FSW. In turn, the change in the pin profile can lead to a change in material flow, as indicated by Beygi et al. [2018], affecting the microstructures in welding zones. The relationship between microstructure and tool wear is very important when conducting a detailed investigation of the FSW mechanism.

The microstructural evolution can also be altered owing to the profile changes caused by tool wear. A numerical scheme for the microstructures provides an insight into the FSW process. Meanwhile, the recrystallization and grain growth in the stirring zone (SZ) and the grain coarsening in the heat-affected zone are usually simulated by a Monte Carlo method and cellular automaton method, respectively. Zhang et al. [2016] proposed a Monte Carlo method to simulate the microstructural changes in FSW, then further considered the effect of precipitate, as indicated in [Wu and Zhang 2017]. The evolution of the precipitates was determined by a numerical model, as displayed in [Zhang et al. 2017]. The Monte Carlo method was further extended to a 3D case in [Zhang and Hu 2018]. Another method to predict the grain sizes in FSW is cellular automaton. Earlier work for cellular automata coupled with a finite element method (FEM) was conducted by Saluja et al. [2012], then Song et al. [2014] to predict the grain sizes in FSW. Akbari et al. [2016] established a cellular automaton model to predict the grain sizes in the FSW of a magnesium alloy. Meanwhile, Valvi et al. [2016] combined the cellular automata method and a FEM to predict the grain sizes in the FSW of aluminum alloys.

Although the tool wear is not serious in the FSW of AA6061, there is evidence to show that it can be found for long-term use, i.e., for the FSW of AA6061. Thus, it is interesting to study how the worn tool affects the key phenomena, including the temperatures and recrystallizations in FSW. To understand the mechanism of tool wear and the wear-induced self-optimization in FSW, it is important to conduct theoretical and numerical analyses on the internal relationships among the internal parameters. Experiments must be used to validate the numerical models, then the internal relationships between the tool wear and microstructures can be established. In the current work, tool wear was calculated with validation from literatures. A Monte Carlo method was used to simulate the grain evolutions in the SZ. In addition, an experiment was performed to validate the grain sizes. Then, the correlation between the tool wear and the microstructures could be established. The systematic work was used for the investigation on the self-optimization mechanism of the tool in FSW.

## 2. Experimental procedure

The FSW machine and the instruments used in the experiment are shown in Figure 1. AA6061-T6 was selected as the welding material. The rotating speed was 1000 rpm and the transverse speed was 1 mm/s. The tool material was H13 steel. In addition, a scanning electron microscope (SEM) system was used to validate the grain morphologies and sizes predicted by the Monte Carlo method with a worn tool. An infrared radiation thermometer was used to validate the predicted temperature field.

A microstructure analysis was performed on the cross-section of the weld by field-emission scanning electron microscopy (FE-SEM, Supra-55, Carl Zeiss Sigma NTS GmbH, Germany). The SEM samples were ground and polished with a diamond paste of  $0.5\ \mu\text{m}$ . To investigate the grain size distribution of the weld zone, the samples were etched in the Keller's reagent for 200 s. The average grain size was then calculated using the linear intercept method:  $d = 1.56L$ , where  $L$  is the intercept length.



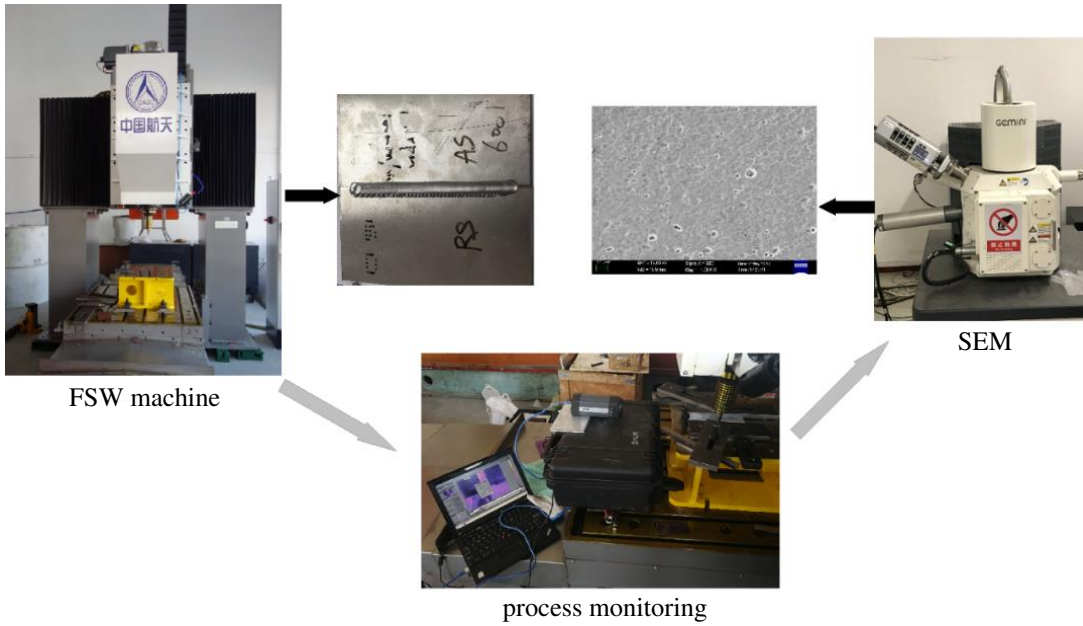


**Figure 1.** FSW machine and the used instruments.

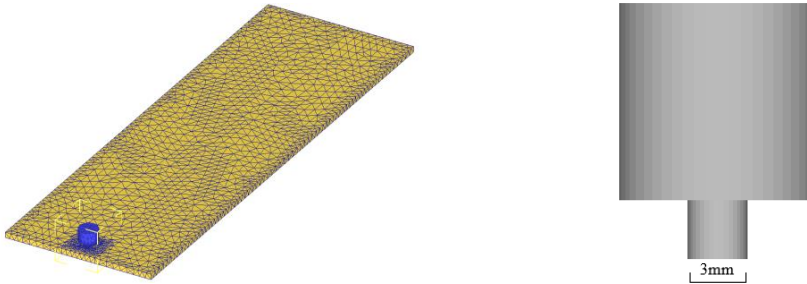


**Figure 2.** FSW model and welding tool before wear: FEM model (left) and welding tool (right).

### 3. Numerical models

An adaptive remeshing model was used to simulate the FSW process based on DEFORM<sup>3D</sup>, as shown in Figure 2 (left). The initial mesh sizes ranged from 2 mm–5.4 mm. Then, the mesh sizes ranged from 0.4 mm–1 mm in the remeshing region in the SZ. The used initial tool before wear is shown in Figure 2 (right). The shoulder diameter is 10 mm and the pin diameter is 3 mm. The pin is slightly shorter than the thickness of the welding plate, which is of the same length as that used in the experiment. The rotating speed was 1000 rpm while the transverse speed was 1 mm/s.

The shear friction model was used for the contact behaviors on the tool-plate interface:

$$\tau = mk, \quad (1)$$

where  $k$  is the yield shear stress and  $m$  is the frictional factor, which is selected as 0.6 according to [Wan et al. 2016].

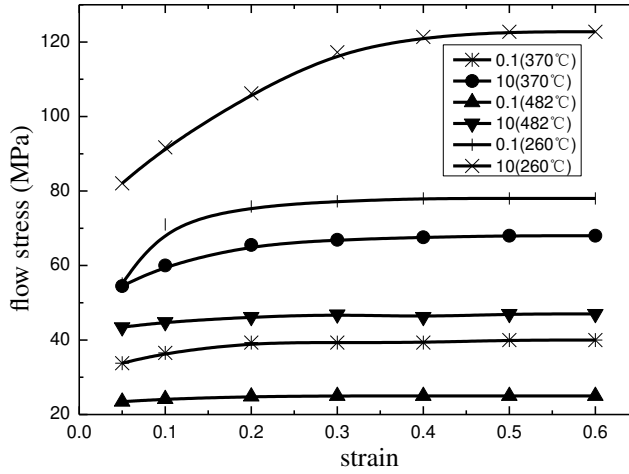


**Figure 3.** Mechanical properties of AA6061-T6.

The yield shear stress can be determined by the shear failure criteria:

$$k = \sigma_s / \sqrt{3}, \quad (2)$$

where  $\sigma_s$  is the yield strength. The tabulated flow stress was used as functions of the strain rates and temperatures:

$$\sigma_y = \sigma_y(\bar{\epsilon}^P, \dot{\bar{\epsilon}}^P, T), \quad (3)$$

where  $\bar{\epsilon}^P$  is the equivalent plastic strain and  $\dot{\bar{\epsilon}}^P$  is the equivalent plastic strain rate.

The relations between the flow stresses and the strain rates and temperatures are shown in [Figure 3](#) (data from DEFORM<sup>3D</sup>). Heat is generated by both friction and plastic deformation, with friction being the main contributor. A detailed description on the adaptive remeshing model can be found in [\[Zhang and Wan 2012\]](#).

The Archard equation was used to calculate the tool wear in FSW [\[Lee and Jou 2003\]](#):

$$W = \int K \frac{p^a \cdot v^b}{H^c} dt, \quad (4)$$

where  $W$  is the total wear depth of the tool,  $p$  is the pressure on the welding tool,  $v$  is the sliding velocity, and  $H$  is the hardness of the welding tool, taken as 62HRC. Additionally,  $K = 2 \cdot 10^{-5}$  for AA6061+20%Al<sub>2</sub>O<sub>3</sub> and  $K = 2 \cdot 10^{-8}$  for AA6061-T6;  $a$  and  $b$  are commonly taken as 1, and  $c = 1.75$  for the welding tool.

The simulation was divided into two steps. In the first step, the FSW process was simulated in DEFORM<sup>3D</sup>. The obtained data was combined with the Archard equation to simulate the tool wear. In the following step, the worn tools obtained at different instances were used in numerical models to connect the worn shapes with the FSW temperature histories. The obtained temperatures were then combined with the developed Monte Carlo method to correlate the tool wear with the microstructural evolutions in FSW with worn pin profiles.

physical property	value
average number per unit area ( $Z$ )	$4.31 \cdot 10^{20} \text{ atom/m}^2$
Planck constant ( $h$ )	$6.624 \cdot 10^{-34} \text{ J s}$
accommodation probability ( $A$ )	1
Avogadro's number ( $N_a$ )	$6.02 \cdot 10^{23} \text{ mol}^{-1}$
atom molar volume ( $V_m$ )	$1.0 \cdot 10^{-5} \text{ m}^3/\text{mol}$
fusion entropy ( $\Delta S_f$ )	11.5
activation enthalpy ( $Q$ )	156 kJ/mol
boundary energy ( $\gamma$ )	$0.5 \text{ J/m}^2$
gas constant ( $R$ )	$8.31 \text{ J mol}^{-1} \text{ K}^{-1}$
DRX constant ( $N_0$ )	$10^{24} \text{ m}^{-3}$

**Table 1.** Material parameters.

A Monte Carlo method was used to simulate the recrystallization and the following grain growth in FSW. In the previous work by Zhang et al. [2016], a relation between the Monte Carlo step and the real temperature was established as

$$(MCS)^{(n+1)n_1} = \left(\frac{L_0}{K_1 l}\right)^{n+1} + \frac{(n+1)\alpha C_1^n}{(K_1 l)^{n+1}} \sum \left[ \exp^n \left( -\frac{Q}{RT_i} \right) t_i \right], \quad (5)$$

where  $C_1$  can be described by

$$C_1 = \frac{2A\gamma Z V_m^2}{N_a^2 h} \exp\left(\frac{\Delta S_f}{R}\right), \quad (6)$$

where  $A$ ,  $Z$ ,  $V_m$ ,  $\Delta S_f$ ,  $R$ ,  $N_a$ ,  $\gamma$ ,  $Q$ , and  $h$  are summarized in Table 1. A detailed description on the Monte Carlo method can be found in [Zhang et al. 2016].

The nucleation rate is a function of the strain rate  $\dot{\varepsilon}$  [Grujicic et al. 2015]:

$$\dot{n} = N_0 \dot{\varepsilon} \exp(-Q/RT), \quad (7)$$

where  $N_0$  is a constant and  $\dot{\varepsilon}$  is the equivalent strain rate in the SZ, which is obtained using the FEM.

#### 4. Results and discussion

To validate the tool wear predictions, AA6061+20%Al<sub>2</sub>O<sub>3</sub> was used. The tool wear rate decreased with the increase of the wear depth. Furthermore, the numerical model fitted well with the experimental observation by Prado et al. [2003], as shown in Figure 4 (left). When AA6061-T6 was used, the tool wear obviously decreased. For the short welding distance for the FSW of AA6061-T6, the tool wear is difficult to observe. This phenomenon was also noticed in the experiment by Prado et al. [2001]. In comparison with the experiments, the current model on tool wear can be validated.

Figure 4 (right) shows the variation of the wear depth with the welding distance in the FSW of AA6061-T6. With the increase of the wear depth, the wear rate becomes smaller. This indicates a self-optimization for the welding tool in FSW. The wear mainly occurs near the tip of the welding pin. However, the material near the root of the pin is hardly worn.

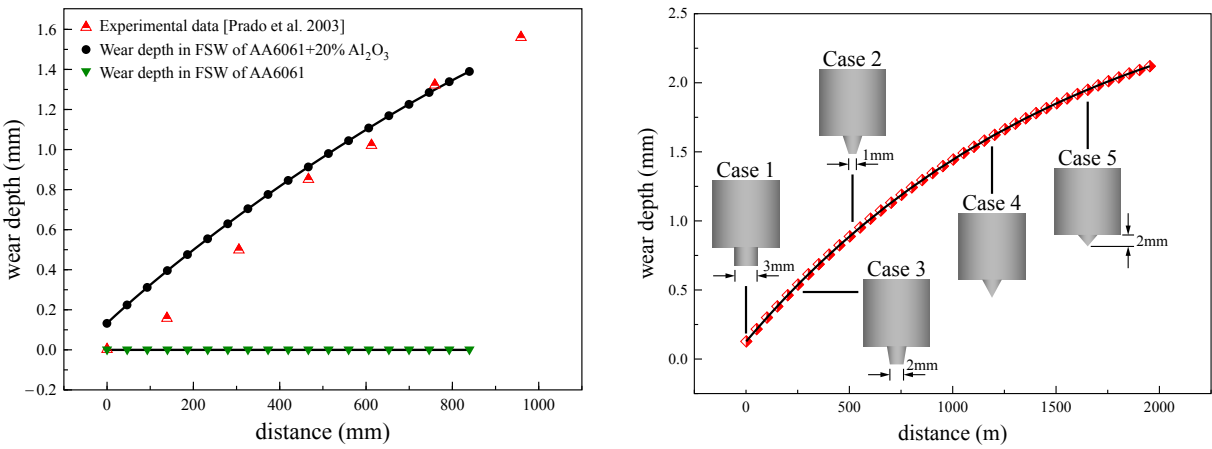


**Figure 4.** Left: comparison of tool wear with experimental data. Right: tool wear in FSW of AA6061-T6.

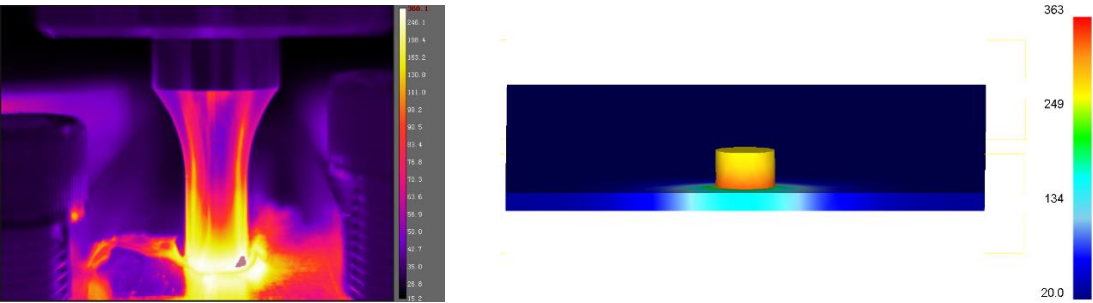


**Figure 5.** Comparison of predicted and experimental temperature: predicted temperature in Case 2 (left) and temperature image observed by Infrared Radiation Thermometer (right).

This phenomenon is clearly observed in the experiment performed by Sahlot and Arora [2018]. The change in the pin profile due to wear can lead to changes in the temperatures and microstructural evolutions in FSW. Determining how the tool wear affects the temperatures and deformations in the FSW process is key for investigations on the microstructural evolutions in FSW with worn tools. Therefore, four different worn tools were selected for further simulations. Case 1 represents the initial cylindrical tool without wear. Cases 2–4 represent the worn tools with worn distances ranging from 225 m–1425.5 m, as shown in Figure 4 (right).

Figure 5 shows a comparison of the predicted temperature from the adaptive remeshing model and the experimental temperature observed by the infrared radiation thermometer, showing that the results agree well with each other. However, the temperature field under the shoulder cannot be directly observed by the infrared radiation thermometer. Therefore, the maximum welding temperature extracted under the shoulder in the numerical model is usually higher than that observed, as can be seen in Figure 6.

Figure 6 shows the predicted temperature histories in FSW processes with different worn tools. With the increase of the wear depth, the maximum welding temperature decreases. The temperature during

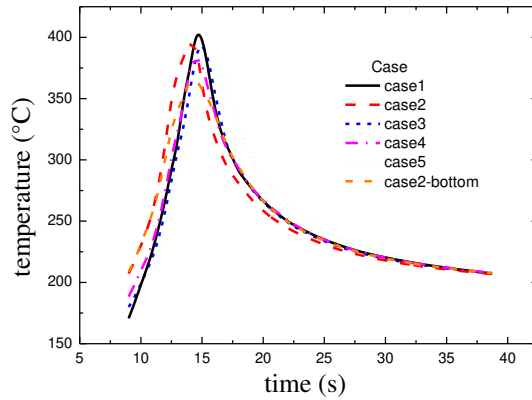


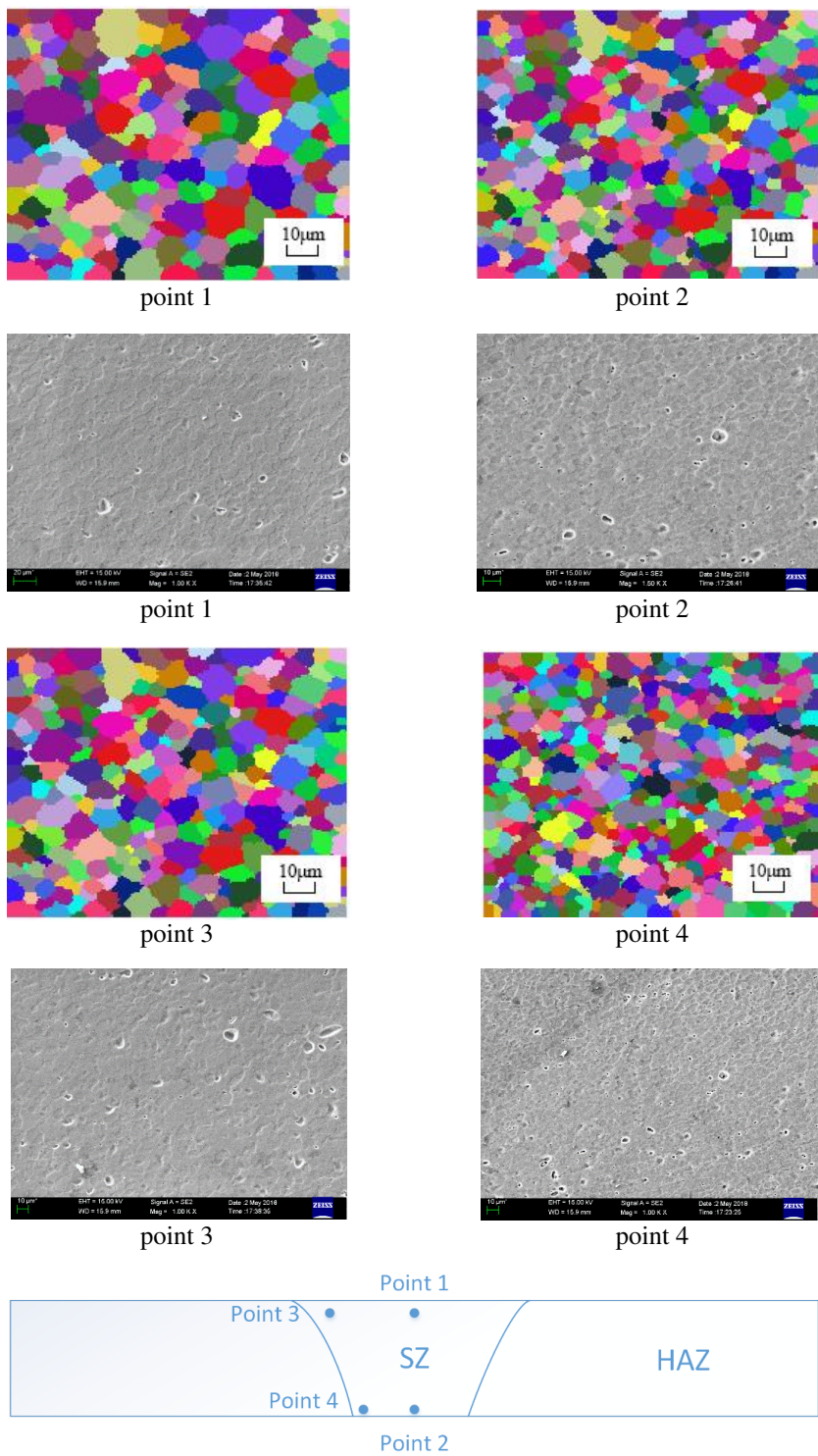
**Figure 6.** Temperature histories in FSW with different worn tools.

FSW is determined by the frictional and plastic dissipations, as indicated in [Zhang and Zhang 2009], with friction being the main contributor. Compared with Case 1, the pin-plate bottom contact surface decreased by 55.6% in Case 2, 88.9% in Case 3, and becomes zero in Cases 4 and 5. The decrease of the pin-plate bottom contact surface leads to the decrease of the welding temperature with the increase of tool wear.

Additionally, the change in the tool profile due to wear can lead to different grain evolutions in FSW. A Monte Carlo method was used to simulate the nucleation in dynamic recrystallization and the following grain growth. To validate the Monte Carlo method, an experiment was performed using the machine shown in Figure 1. The worn tool in Case 2 was used for the comparison of the numerical and experimental results, as shown in Figure 7. The grain sizes near the top and bottom surfaces are different. Due to the higher temperature near the top surface, the grain size near this area is larger than that near the bottom surface. This observation was also made in the 3D Monte Carlo simulation in the previous work by Zhang and Hu [2018]. The average grain size was  $12.1\ \mu\text{m}$  on point 1 and  $11\ \mu\text{m}$  on point 2 in the experiment. The predicted values on point 1 and point 2 in the numerical model were  $12.7\ \mu\text{m}$  and  $11.4\ \mu\text{m}$ , respectively. In addition, the average grain size was  $11.5\ \mu\text{m}$  on point 3 and  $10.8\ \mu\text{m}$  on point 4 in the experiment. Meanwhile, the predicted values on point 3 and point 4 in the numerical model were  $12.3\ \mu\text{m}$  and  $10.9\ \mu\text{m}$ , respectively. This shows that the numerical model fitted well with the experimental measurements.

The nine points shown in Figure 8 (left) were selected to calculate the average strain rates in different FSW processes with different worn tools. Figure 8 (right) shows the calculated strain rates in FSW with different worn tools. It indicates that the appropriate tool wear can increase the strain rates in FSW whereas excess tool wear can lead to a decrease of the strain rates. The strain rate is a key factor for determining the nucleation in recrystallization. The increase of the strain rate can lead to an increase of the nucleation rate, and vice versa, according to (7).

The calculated nucleation rate histories in FSW with different worn tools are shown in Figure 9. The point 1.5 mm away from the top surface was selected for comparison. For Case 2, the maximum nucleation rate increased to  $8.58 \cdot 10^{12}\ \text{s}^{-1}\ \text{m}^{-3}$  from  $7.98 \cdot 10^{12}\ \text{s}^{-1}\ \text{m}^{-3}$  in Case 1. In Cases 3–5, the maximum nucleation rates decreased to  $4.42 \cdot 10^{12}\ \text{s}^{-1}\ \text{m}^{-3}$ ,  $3.02 \cdot 10^{12}\ \text{s}^{-1}\ \text{m}^{-3}$ , and  $2 \cdot 10^{12}\ \text{s}^{-1}\ \text{m}^{-3}$ , respectively.



The location of selected point in experiment

**Figure 7.** Comparison of predicted grains with experiment in Case 2.



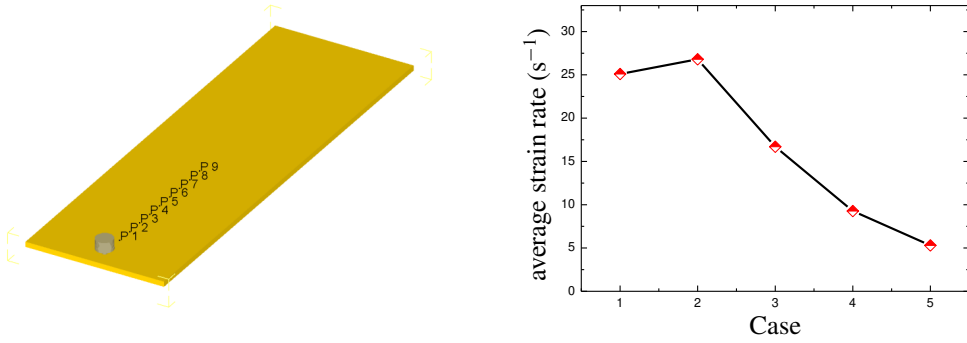


**Figure 8.** Effect of tool wear on strain rates: nine points selected for computation (left) and calculated strain rates (right).

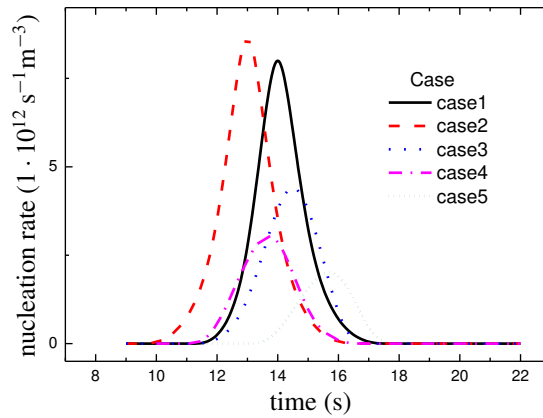


**Figure 9.** Nucleation rates in different worn tools.

Using the calculated nucleation rates shown in Figure 9, the grain sizes in the FSW with different worn tools could be predicted, as shown in Figure 10. In the FSW with the initial tool without wear (Case 1), the average grain size was  $13.2 \mu\text{m}$ . For Case 2, the average grain size decreased to  $12.7 \mu\text{m}$ . While for Cases 3–5, the average grain sizes increased to  $14.1 \mu\text{m}$ ,  $15.2 \mu\text{m}$ , and  $16.7 \mu\text{m}$ , respectively. Appropriate tool wear can lead to smaller grains in the SZ and lead to improvement of the welding quality. However, excess tool wear can lead to the coarsening of the grains in the SZ. This indicates that self-optimization exists in FSW, but the control of the tool wear remains important for the control of the final welding quality in FSW.

The variations of the grain sizes with time in different FSW processes with different worn tools are summarized in Figure 11. The tool wear can obviously affect the grain growth in FSW. The differences between the numerical model and the experiment are 4.96% for point 1, 3.63% for point 2, 6.96% for point 3 and 0.9% for point 4. The error for point 3 is higher than the other points. This is caused by the generation of flash in this region [Kumar et al. 2013]. This can lead to errors on the prediction of strain rates and then affect the predictions of microstructural evolutions. But the comparison shows the proposed models are successful in almost all the regions in the stirring zone. With validation from the experiment, the Monte Carlo method becomes an efficient tool for the design of an appropriate tool pin profile for the optimal welding quality.

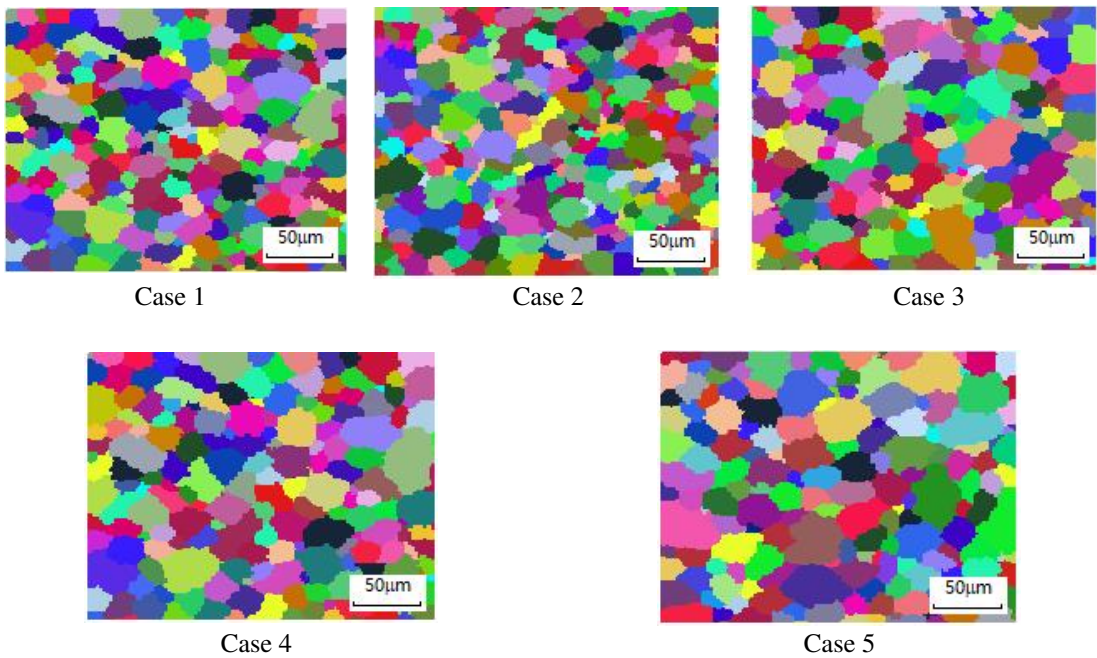


**Figure 10.** Predicted grain morphologies in FSW with worn tools.

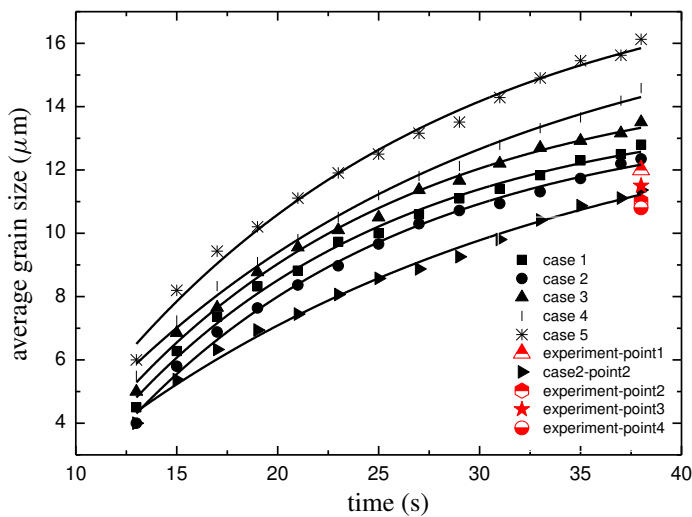


**Figure 11.** Variations of average grain sizes in FSW with worn tools.

### 5. Conclusions

- (1) Tool wear can lead to a decrease of the wear rate in FSW.
- (2) Appropriate tool wear can lead to the formation of smaller equiaxed grains in the SZ. However, excess tool wear can lead to the coarsening of grains in the SZ in FSW.
- (3) Strain rate is a key factor for controlling the self-optimization of the tool in FSW.



## Acknowledgement

This study was funded by the National Natural Science Foundation of China (No. 11572074).

The authors declare that they have no conflict of interest.

## References

- [Akbari et al. 2016] M. Akbari, P. Asadi, M. B. Givi, and P. Zolghadr, “A cellular automaton model for microstructural simulation of friction stir welded AZ91 magnesium alloy”, *Model. Simul. Mater. Sci. Eng.* **24**:3 (2016), 035012.
- [Beygi et al. 2018] R. Beygi, M. Z. Mehrizi, D. Verdera, and A. Loureiro, “Influence of tool geometry on material flow and mechanical properties of friction stir welded Al-Cu bimetals”, *J. Mater. Process. Technol.* **255** (2018), 739–748.
- [Chen and Nakata 2009] Y. C. Chen and K. Nakata, “Effect of tool geometry on microstructure and mechanical properties of friction stir lap welded magnesium alloy and steel”, *Mater. Des.* **30**:9 (2009), 3913–3919.
- [De et al. 2014] A. De, H. K. D. H. Bhadeshia, and T. DebRoy, “Friction stir welding of mild steel: tool durability and steel microstructure”, *Mater. Sci. Technol.* **30**:9 (2014), 1050–1056.
- [Ebrahimpour et al. 2019] A. Ebrahimpour, A. Mostafapour, and K. Samadian, “Finite element and experimental investigation on the effects of temperature, strain and strain rate on microstructure and mechanical properties of FSSWed TRIP steel joints”, *Mater. Res. Express* **6**:1 (2019), 016559.
- [Grujicic et al. 2015] M. Grujicic, S. Ramaswami, J. S. Snipes, V. Avuthu, R. Galgalikar, and Z. Zhang, “Prediction of the grain-microstructure evolution within a Friction Stir Welding (FSW) joint via the use of the Monte Carlo simulation method”, *J. Mater. Eng. Perform.* **24**:9 (2015), 3471–3486.
- [He et al. 2017] W. J. He, L. Zheng, R. L. Xin, and Q. Liu, “Microstructure-based modeling of tensile deformation of a friction stir welded AZ31 Mg alloy”, *Mater. Sci. Eng. A* **687** (2017), 63–72.
- [Kumar et al. 2013] M. Kumar, S. V. Kailas, and R. G. Narayanan, “Influence of external weld flash on the in-plane plane-strain formability of friction stir welded sheets”, *J. Strain Anal. Eng. Des.* **48**:6 (2013), 376–385.
- [Lee and Jou 2003] R. S. Lee and J. L. Jou, “Application of numerical simulation for wear analysis of warm forging die”, *J. Mater. Process. Technol.* **140**:1-3 (2003), 43–48.
- [Mastanaiah et al. 2018] P. Mastanaiah, A. Sharma, and G. M. Reddy, “Role of hybrid tool pin profile on enhancing welding speed and mechanical properties of AA2219-T6 friction stir welds”, *J. Mater. Process. Technol.* **257** (2018), 257–269.
- [Mehta et al. 2011] M. Mehta, A. Arora, A. De, and T. DebRoy, “Tool geometry for friction stir welding — optimum shoulder diameter”, *Metall. Mater. Trans. A* **42**:9 (2011), 2716–2722.
- [Prado et al. 2001] R. A. Prado, L. E. Murr, D. J. Shindo, and K. F. Soto, “Tool wear in the friction-stir welding of aluminum alloy 6061+20% Al<sub>2</sub>O<sub>3</sub>: a preliminary study”, *Scr. Mater.* **45**:1 (2001), 75–80.
- [Prado et al. 2003] R. A. Prado, L. E. Murr, K. F. Soto, and J. C. McClure, “Self-optimization in tool wear for friction-stir welding of Al 6061+20% Al<sub>2</sub>O<sub>3</sub> MMC”, *Mater. Sci. Eng. A* **349**:1-2 (2003), 156–165.
- [Sahlot and Arora 2018] P. Sahlot and A. Arora, “Numerical model for prediction of tool wear and worn-out pin profile during friction stir welding”, *Wear* **408-409** (2018), 96–107.
- [Sahlot et al. 2018] P. Sahlot, K. Jha, G. K. Dey, and A. Arora, “Wear-induced changes in FSW tool pin profile: effect of process parameters”, *Metall. Mater. Trans. A* **49**:6 (2018), 2139–2150.
- [Saluja et al. 2012] R. S. Saluja, R. G. Narayanan, and S. Das, “Cellular automata finite element (CAFE) model to predict the forming of friction stir welded blanks”, *Comput. Mater. Sci.* **58** (2012), 87–100.
- [Shindo et al. 2002] D. J. Shindo, A. R. Rivera, and L. E. Murr, “Shape optimization for tool wear in the friction-stir welding of cast Al359-20% SiC MMC”, *J. Mater. Sci.* **37**:23 (2002), 4999–5005.
- [Song et al. 2014] K. J. Song, Z. B. Dong, K. Fang, X. H. Zhan, and Y. H. Wei, “Cellular automaton modelling of dynamic recrystallisation microstructure evolution during friction stir welding of titanium alloy”, *Mater. Sci. Technol.* **30**:6 (2014), 700–711.

- [Suresha et al. 2011] C. N. Suresha, B. M. Rajaprakash, and S. Upadhya, “A study of the effect of tool pin profiles on tensile strength of welded joints produced using friction stir welding process”, *Mater. Manuf. Process.* **26**:9 (2011), 1111–1116.
- [Valvi et al. 2016] S. R. Valvi, A. Krishnan, S. Das, and N. R. G., “Prediction of microstructural features and forming of friction stir welded sheets using cellular automata finite element (CAFE) approach”, *Int. J. Mater. Form.* **9**:1 (2016), 115–129.
- [Wan et al. 2016] Z. Y. Wan, Z. Zhang, and X. Zhou, “Finite element modeling of grain growth by point tracking method in friction stir welding of AA6082-T6”, *Int. J. Adv. Manuf. Technol.* **90**:9-12 (2016), 3567–3574.
- [Wu and Zhang 2017] Q. Wu and Z. Zhang, “Precipitation-induced grain growth simulation of friction-stir-welded AA6082-T6”, *J. Mater. Eng. Perform.* **26**:5 (2017), 2179–2189.
- [Yang et al. 2018] C. Yang, D. R. Ni, P. Xue, B. L. Xiao, W. Wang, K. S. Wang, and Z. Y. Ma, “A comparative research on bobbin tool and conventional friction stir welding of Al-Mg-Si alloy plates”, *Mater. Charact.* **145** (2018), 20–28.
- [Zhang and Hu 2018] Z. Zhang and C. P. Hu, “3D Monte Carlo simulation of grain growth in friction stir welding”, *J. Mech. Sci. Technol.* **32**:3 (2018), 1287–1296.
- [Zhang and Wan 2012] Z. Zhang and Z. Y. Wan, “Predictions of tool forces in friction stir welding of AZ91 magnesium alloy”, *Sci. Technol. Weld. Join.* **17**:6 (2012), 495–500.
- [Zhang and Wu 2015] Z. Zhang and Q. Wu, “Numerical studies of tool diameter on strain rates, temperature rises and grain sizes in friction stir welding”, *J. Mech. Sci. Technol.* **29**:10 (2015), 4121–4128.
- [Zhang and Zhang 2007] Z. Zhang and H. W. Zhang, “The simulation of residual stresses in friction stir welds”, *J. Mech. Mater. Struct.* **2**:5 (2007), 951–964.
- [Zhang and Zhang 2009] Z. Zhang and H. W. Zhang, “Numerical studies on controlling of process parameters in friction stir welding”, *J. Mater. Process. Technol.* **209**:1 (2009), 241–270.
- [Zhang et al. 2009] Z. Zhang, Y. L. Liu, and J. T. Chen, “Effect of shoulder size on the temperature rise and the material deformation in friction stir welding”, *Int. J. Adv. Manuf. Technol.* **45**:9 (2009), 889–895.
- [Zhang et al. 2014] Z. Zhang, Q. Wu, and H.-W. Zhang, “Numerical studies of effect of tool sizes and pin shapes on friction stir welding of AA2024-T3 alloy”, *Trans. Nonferr. Met. Soc. China* **24**:10 (2014), 3293–3301.
- [Zhang et al. 2016] Z. Zhang, Q. Wu, M. Grujicic, and Z. Y. Wan, “Monte Carlo simulation of grain growth and welding zones in friction stir welding of AA6082-T6”, *J. Mater. Sci.* **51**:4 (2016), 1882–1895.
- [Zhang et al. 2017] Z. Zhang, Z. Y. Wan, L.-E. Lindgren, Z. J. Tan, and X. Zhou, “The simulation of precipitation evolutions and mechanical properties in friction stir welding with post-weld heat treatments”, *J. Mater. Eng. Perform.* **26**:12 (2017), 5731–5740.

Received 2 Mar 2019. Revised 30 Jul 2019. Accepted 15 Aug 2019.

ZHAO ZHANG: [zhangz@dlut.edu.cn](mailto:zhangz@dlut.edu.cn)

Department of Engineering Mechanics, Dalian University of Technology, No. 2 Linggong Road, Dalian, 116024, China

ZHIJUN TAN: [742046605@qq.com](mailto:742046605@qq.com)

Department of Engineering Mechanics, Dalian University of Technology, No. 2 Linggong Road, Dalian, 116024, China

# LOCAL GRADIENT THEORY FOR THERMOELASTIC DIELECTRICS: ACCOUNTING FOR MASS AND ELECTRIC CHARGE TRANSFER DUE TO MICROSTRUCTURE CHANGES

OLHA HRYTSYNA AND VASYL KONDRAT

In this paper a complete set of nonlinear field equations of a gradient-type continuum theory for thermoelastic nonferromagnetic dielectrics is obtained. The specification of the mentioned set of equations is based on the application of electrothermomechanical balance laws and takes into consideration the polarization electric current and mass flux (of nondiffusive and nonconvective nature) associated with microstructure changes. The electric current is caused by a change of both dipole and quadrupole electric moments over time, whilst the mass flux is caused by a change of the vector of the local mass displacement over time. The obtained set of equations accounts for the electromechanical coupling for isotropic materials and describes the near-surface, size, flexoelectric and thermopolarization effects. The classical theory of piezoelectrics is incapable of describing the mentioned phenomena. For isothermal linear approximation, the proposed theory is used to investigate the effect of thin-film thickness as well as of the diameter and surface curvature of a thin fiber and a cylindrical hole in elastic dielectrics on their stationary stress-strain state, bound surface electric charge, surface energy of deformation and polarization, etc. It is shown that a disjoining pressure emerges in thin films. This pressure can affect the strength and stability of nanoscale dielectric films. The results obtained in this paper are general and can be used for designing new nanocomposite materials and devices utilizing the micro/nanoscale films, fibers, etc.

*A list of symbols including the notations used in this paper can be found on page 566. In general, bold symbols stand for vector quantities and bold symbols with caps denote second-order tensor quantities.*

## 1. Introduction

The generalized theories of dielectrics have attracted the attention of many investigators. Extension of the classical field theory was stimulated by intensive development of new technologies, in particular, nanotechnologies, as well as by the availability of a number of inconsistencies in classical (local) theories. For example, classical theories predict a singular solution in problems with concentrated sources, cracks, and defects. Some experimental results (namely, polarization of a material with centrosymmetry under nonuniform mechanical loads or temperature gradients [Kholkin et al. 1982; Zholudev 1966], nonlinear dependence of capacitance of thin dielectric film on its thickness, known as Mead's anomaly [Mead 1961], size effects [Axe et al. 1970; Nam et al. 2006; Tang and Alici 2011] etc.) are outside the scope of classical theories of dielectrics.

There are several different ways of constructing extended theories of elastic dielectrics. One group of theories considers the additional degrees of freedom (i.e., microrotations, microdeformations, etc.) for

---

*Keywords:* local gradient theory, electric quadrupole moment, local mass displacement, surface and size effects.

material points in order to model the contribution of the microstructure changes to the macroscopic behavior of the body. In such a way there were developed more general theories, in particular, micromorphic, microstretch, micropolar continua, etc. [Eringen 1966; 1999; Eringen and Suhubi 1964]. The nonlocal and gradient theories form another group of extended theories of dielectrics. The nonlocal field theory for piezoelectricity with functional constitutive relations was proposed in [Eringen 1984; 2002]. The gradient-type theories were mainly formulated using the variation methods or methods of nonequilibrium thermodynamics [Kalpakidis and Massalas 1993; Maugin 1980; Nowacki 1983; Papenfuss and Forest 2006; Ván 2003]. Such theories were developed by allowing the stored energy density to depend on the gradient of some physical quantities, namely, the strain tensor gradient [Mindlin 1965], the polarization gradient [Mindlin 1968], or the electric field gradient [Kafadar 1971; Kalpakides and Agiasofitou 2002; Kalpakidis and Massalas 1993; Maugin 1988]. Note that the electric field gradient is a thermodynamic conjugate of the electric quadrupole [Kafadar 1971]. For a more detailed description of these theories, see monographs [Burak et al. 2011; Eringen 1999; 2002; Erofeyev 2003; Maugin 1988; Nowacki 1983; 1986] and reviews [Kondrat and Hrytsyna 2009; Yang 2006].

Burak et al. [2007; 2008] proposed a continuum-thermodynamical approach to the construction of a gradient-type theory of electrothermoelasticity of polarized solids (local gradient electrothermomechanics of dielectrics, in the author's terminology). The mentioned approach is based on accounting for nondiffusive and nonconvective mass fluxes associated with changes in the material microstructure. These fluxes are related to the process of local mass displacement [Burak et al. 2007; 2008].

The objective of this paper is to develop this approach and to construct the local gradient theory of nonferromagnetic dielectrics that accounts for the above mass fluxes as well as for the polarization currents. Here, we will consider the contribution of electric dipole and quadrupole moments to the polarization current. The developed theory will be used for describing near-surface and size effects, in particular, to investigate the surface energy of deformation and polarization, a disjoining pressure in thin solid films, etc.

## 2. Investigation object and notations

We consider an electrically polarizable nonferromagnetic heat-conducting elastic body which occupies the domain  $(V_*)$  of three-dimensional Euclidean space with a smooth surface  $(\Sigma_*)$ . In view of the action of external forces, electromagnetic field and heating of the body, mechanical, thermal, and electromagnetic processes can occur within the solid. These processes may be accompanied by changes in the microstructure of a small body element  $(dV)$  (representative volume). We characterize these changes by an electric flux  $\mathbf{J}_{es}$  (polarization current) and a nonconvective and nondiffusive mass flux  $\mathbf{J}_{ms}$ . It should be noted that Marchenko et al. [2009] observed the mentioned nondiffusive mass flux within the near-surface domains of thin films during their formation. We relate the mass flux  $\mathbf{J}_{ms}$  to the process of the local mass displacement [Burak et al. 2007; 2008].

All fields that characterize the processes occurring in the solid should obey the fundamental laws of continuum physics, namely, the Maxwell equations and the corresponding balance laws (balances of energy, mass, linear momentum, angular momentum, and entropy).

### 3. Conservation laws of mass and induced mass

We separate from the body a fixed small volume ( $V$ ) bounded by closed surface ( $\Sigma$ ). The interaction of the microparticles of the considered volume ( $V$ ) with the exterior microparticles occurs through the surface ( $\Sigma$ ). The integral form of the mass balance equation for the considered volume can be written as

$$\frac{d}{dt} \int_{(V)} \rho dV = - \oint_{(\Sigma)} \mathbf{J}_{m*} \cdot \mathbf{n} d\Sigma. \quad (1)$$

Here,  $\rho$  is the mass density,  $\mathbf{J}_{m*}$  is the density of mass flux,  $\mathbf{n}$  is the outward unit normal to the surface ( $\Sigma$ ), and the dot denotes the scalar product.

We take into consideration that the mass-center displacement of the representative volume may be induced not only by its convective displacement as a rigid entity (i.e., translational displacement of the element geometric center) but also by the changes of the relative positions of microparticles within this element, that is, the change of its microstructure (see [Figure 1](#)). In view of this, we represent the mass flux  $\mathbf{J}_{m*}$  as the sum of the convective component  $\rho \mathbf{v}_*$  and component  $\mathbf{J}_{ms}$  related to the ordering of microstructure of the representative volume, that is  $\mathbf{J}_{m*} = \rho \mathbf{v}_* + \mathbf{J}_{ms}$ . Here,  $\mathbf{v}_* = \dot{\mathbf{u}}_*$  is the velocity vector of convective displacement of the representative volume,  $\mathbf{u}_* = \mathbf{r}_* - \mathbf{r}_0$  ([Figure 1](#)). Hence, equation (1) in the local form can be written as

$$\frac{\partial \rho}{\partial t} + \nabla \cdot (\rho \mathbf{v}_* + \mathbf{J}_{ms}) = 0, \quad (2)$$

where  $\nabla$  is the Hamilton operator.

We introduce the velocity vector  $\mathbf{v}$  of the center of mass by the formula [[Burak et al. 2007; 2008](#)]

$$\mathbf{v} = \frac{1}{\rho} (\rho \mathbf{v}_* + \mathbf{J}_{ms}). \quad (3)$$

In view of formula (3), the equation of mass balance (2) can be written in the standard form

$$\frac{\partial \rho}{\partial t} + \nabla \cdot (\rho \mathbf{v}) = 0. \quad (4)$$

Following Burak et al. [[2007; 2008](#)], assume that the mass flux  $\mathbf{J}_{ms}$  is caused by a change over time of the mass dipole moment  $\mathbf{\Pi}_m$  (i.e., the vector of local mass displacement):

$$\mathbf{J}_{ms} = \partial \mathbf{\Pi}_m / \partial t. \quad (5)$$

To describe the local mass displacement by the formula

$$\int_{(V_*)} \mathbf{\Pi}_m dV = \int_{(V_*)} \rho_{m\pi} \mathbf{r} dV, \quad (6)$$

we also introduce the density of induced mass  $\rho_{m\pi}$  [[Burak et al. 2008](#)]. In (6), we integrate over the volume ( $V_*$ ) of the solid body. Note that from the integral equation (6) the following useful relations can be easily obtained:

$$\int_{(V_*)} \rho_{m\pi} dV = 0, \quad (7)$$

$$\rho_{m\pi} = -\nabla \cdot \mathbf{\Pi}_m. \quad (8)$$

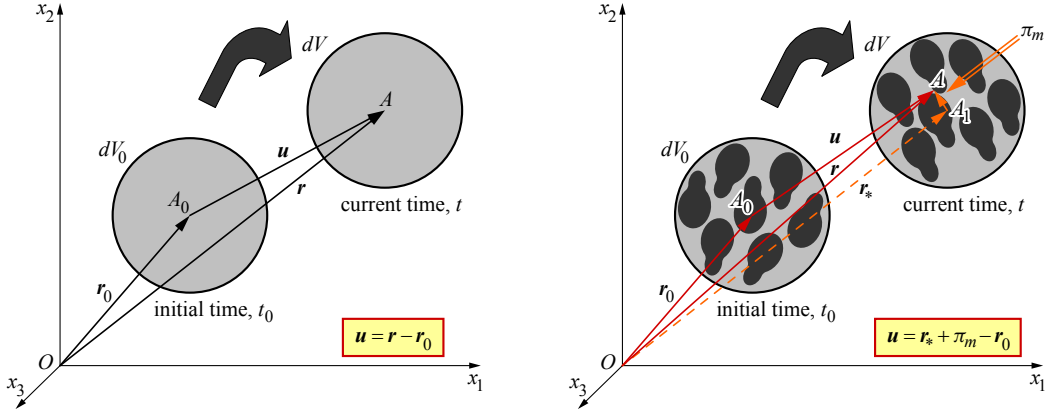


**Figure 1.** Changing the center of mass of a small body element within the classical theory ( $\mathbf{u} = \mathbf{r} - \mathbf{r}_0$ ) (left), and local gradient theory taking the local mass displacement into account ( $\mathbf{u} = \mathbf{r}_* + \boldsymbol{\pi}_m - \mathbf{r}_0$ , where  $\boldsymbol{\pi}_m = \boldsymbol{\Pi}_m / \rho$ ) (right).

Let's derive the formula (8). To this end, we multiply the lefthand and righthand sides of the relation (6) by an arbitrary constant vector  $\mathbf{a}$  and use the identity  $\mathbf{a} \cdot \boldsymbol{\Pi}_m = (\boldsymbol{\Pi}_m \cdot \nabla)(\mathbf{a} \cdot \mathbf{r})$ . As a result, after some algebra, we obtain

$$\int_{(V_*)} (\mathbf{a} \cdot \mathbf{r}) \rho_{m\pi} dV = \int_{(V_*)} (\boldsymbol{\Pi}_m \cdot \nabla)(\mathbf{a} \cdot \mathbf{r}) dV = - \int_{(V_*)} \nabla \cdot [\boldsymbol{\Pi}_m (\mathbf{a} \cdot \mathbf{r})] dV - \int_{(V_*)} (\mathbf{a} \cdot \mathbf{r})(\nabla \cdot \boldsymbol{\Pi}_m) dV. \quad (9)$$

Assume that the body comes in contact with vacuum. Since vector  $\boldsymbol{\Pi}_m$  is equal to zero outside the body, then

$$\int_{(V_*)} \nabla \cdot [\boldsymbol{\Pi}_m (\mathbf{a} \cdot \mathbf{r})] dV = 0. \quad (10)$$

Because vector  $\mathbf{a}$  is arbitrary, from the expression (9) we get formula (8). Similarly, formula (7) can be obtained [Burak et al. 2011].

By differentiating formula (8) with respect to time and taking relation (5) into account, one can obtain a conservation law of an induced mass:

$$\frac{\partial \rho_{m\pi}}{\partial t} + \nabla \cdot \mathbf{J}_{ms} = 0. \quad (11)$$

#### 4. Electrodynamics equations

The Maxwell equations in the local form are given by [Landau and Lifshitz 1982]

$$\nabla \times \mathbf{E} = -\frac{\partial \mathbf{B}}{\partial t}, \quad \nabla \times \mathbf{H} = \mathbf{J}_{ef}, \quad (12)$$

$$\nabla \cdot \mathbf{B} = 0, \quad \nabla \cdot \mathbf{D} = \rho_e. \quad (13)$$

Here  $\mathbf{J}_{ef} = \mathbf{J}_e + \mathbf{J}_{ed} + \mathbf{J}_{es}$ , where  $\mathbf{J}_e$  is the density of the electric current (convection and conduction currents),  $\mathbf{J}_{es}$  is the polarization current, and  $\mathbf{J}_{ed} = \varepsilon_0(\partial \mathbf{E} / \partial t)$ ,  $\varepsilon_0$  is the electric permittivity of a vacuum.

Assume that the polarization current  $\mathbf{J}_{es}$  is caused by a change over time of both the dipole  $\mathbf{P}$  and the quadrupole  $\hat{\mathbf{Q}}$  electric moments [Kondrat and Hrytsyna 2019], namely

$$\mathbf{J}_{es} = \frac{\partial \mathbf{\Pi}_e}{\partial t}, \quad \mathbf{\Pi}_e = \mathbf{P} - \frac{1}{6} \nabla \cdot \hat{\mathbf{Q}}. \quad (14)$$

Here,  $\mathbf{\Pi}_e$  is the polarization vector, which can be thought of as a vector of the local displacement of electric charges. Thus, using (14), one can write

$$\mathbf{J}_{ef} = \mathbf{J}_e + \varepsilon_0 \frac{\partial \mathbf{E}}{\partial t} + \frac{\partial \mathbf{\Pi}_e}{\partial t}. \quad (15)$$

For nonferromagnetic dielectrics, the constitutive equations for the vectors of magnetic  $\mathbf{B}$  and electric  $\mathbf{D}$  inductions look like

$$\mathbf{B} = \mu_0 \mathbf{H}, \quad \mathbf{D} = \varepsilon_0 \mathbf{E} + \mathbf{P} - \frac{1}{6} \nabla \cdot \hat{\mathbf{Q}}. \quad (16)$$

Here,  $\mu_0$  is the magnetic permeability in vacuum. We also introduce the density of an induced charge  $\rho_{e\pi}$  [Bredov et al. 1985]

$$\int_{(V_*)} \mathbf{\Pi}_e dV = \int_{(V_*)} \rho_{e\pi} \mathbf{r} dV. \quad (17)$$

From (17) it follows that [Bredov et al. 1985]

$$\int_{(V_*)} \rho_{e\pi} dV = 0, \quad \rho_{e\pi} = -\nabla \cdot \mathbf{\Pi}_e. \quad (18)$$

The conservation law of induced electric charges looks like [Bredov et al. 1985]

$$\frac{\partial \rho_{e\pi}}{\partial t} + \nabla \cdot \mathbf{J}_{es} = 0. \quad (19)$$

Equations (12), (13), (15), and (16) yield the following balance law for the energy  $U_e$  of the electromagnetic field [Burak et al. 2011]:

$$\frac{\partial U_e}{\partial t} + \nabla \cdot \mathbf{S}_e + \left( \mathbf{J}_e + \frac{\partial \mathbf{\Pi}_e}{\partial t} \right) \cdot \mathbf{E} = 0. \quad (20)$$

Here,  $U_e = (\varepsilon_0 \mathbf{E}^2 + \mu_0^{-1} \mathbf{B}^2)/2$ ,  $\mathbf{S}_e = \mu_0^{-1} \mathbf{E} \times \mathbf{B}$ . Note that the last term in (20) describes the effect of the electromagnetic field on a substance. Let us rewrite the above term in such a way that it contains the quadrupole  $\hat{\mathbf{Q}}_*$  and dipole  $\mathbf{P}_*$  electric moments, the electric field vector  $\mathbf{E}_*$ , and the density of the electric current  $\mathbf{J}_{e*}$  in the reference frame of the mass centers moving with a velocity  $\mathbf{v}$  relative to the laboratory reference frame. In this co-moving frame, the vectors  $\mathbf{E}$ ,  $\mathbf{P}$ ,  $\mathbf{J}_e$  and the tensor  $\hat{\mathbf{Q}}$  are transformed according to the relations:  $\mathbf{E} = \mathbf{E}_* - \mathbf{v} \times \mathbf{B}$ ,  $\mathbf{P} = \mathbf{P}_*$ ,  $\mathbf{J}_e = \mathbf{J}_{e*} + \rho_e \mathbf{v}$ ,  $\hat{\mathbf{Q}} = \hat{\mathbf{Q}}_*$ . Here, the vector  $\mathbf{J}_{e*}$  is the conduction current density. Substituting these equations into (20) and using the mass conservation law (4), the balance equation for the energy of the electromagnetic field can be reduced to



the following form:

$$\begin{aligned} \frac{\partial U_e}{\partial t} + \nabla \cdot \mathbf{S}_e + \mathbf{J}_{e*} \cdot \mathbf{E}_* + \rho \frac{D\mathbf{p}}{Dt} \cdot \mathbf{E}_* + \rho \frac{D\hat{\mathbf{q}}}{Dt} : (\nabla \otimes \mathbf{E}_*) \\ + \mathbf{v} \cdot \left[ \rho_e \mathbf{E}_* + \left( \mathbf{J}_{e*} + \frac{\partial \Pi_e}{\partial t} \right) \times \mathbf{B} + \rho (\nabla \otimes \mathbf{E}_*) \cdot \mathbf{p} - \rho (\nabla \otimes \nabla \otimes \mathbf{E}_*) : \hat{\mathbf{q}} \right] \\ - \nabla \cdot \{ [\mathbf{p} \cdot \mathbf{E}_* + \hat{\mathbf{q}} : (\nabla \otimes \mathbf{E}_*)] \rho \mathbf{v} \} = 0. \quad (21) \end{aligned}$$

Here,  $\mathbf{p} = \mathbf{P}/\rho$  and  $\hat{\mathbf{q}} = \hat{\mathbf{Q}}/6\rho$ ,  $\otimes$  is the tensor product, and  $\frac{D\cdots}{Dt} = \frac{\partial \cdots}{\partial t} + \mathbf{v} \cdot \nabla \dots$  denotes the material time derivative.

### 5. Equation of entropy balance

We used the approaches of classical nonequilibrium thermodynamics. Within the nonequilibrium thermodynamics, the entropy balance equation may be expressed in the local form as [de Groot and Mazur 1962]

$$\rho \frac{Ds}{Dt} = -\nabla \cdot \left( \frac{\mathbf{J}_q}{T} \right) + \eta + \rho \frac{\mathfrak{R}}{T}. \quad (22)$$

Here,  $s$  is the specific entropy,  $\mathbf{J}_q$  is the density of the heat flux,  $T$  is the absolute temperature,  $\mathfrak{R}$  denotes the distributed heat source, and  $\eta$  is the entropy production per unit of volume and time.

### 6. Energy balance law for system “solid-electromagnetic field”

We assume that the total energy  $\mathcal{E}$  is the sum of internal energy  $\rho u$  ( $u$  is the specific internal energy), kinetic energy  $\rho \mathbf{v}^2/2$ , and the energy  $U_e$  of the electromagnetic field:  $\mathcal{E} = \rho u + \frac{1}{2}\rho \mathbf{v}^2 + U_e$ . We also assume that the change in the total energy is caused (i) by the convective energy transport  $\rho(u + \mathbf{v}^2/2)$  through the body surface, (ii) by the energy flux  $\hat{\sigma} \cdot \mathbf{v}$  due to the power of surface forces, (iii) by the heat flux  $\mathbf{J}_q$ , (iv) by the electromagnetic energy flux  $\mathbf{S}_e$ , (v) by the energy flux  $\mu \mathbf{J}_m$  linked with the mass transport relative to the centre of mass of the small body element, (vi) by the energy flux  $\mu_\pi \mathbf{J}_{ms}$  related to the material microstructure ordering (i.e., local mass displacement), as well as (vii) by the action of mass forces  $\mathbf{F}$  and (viii) by the action of distributed heat sources  $\mathfrak{R}$ . Thus, the law of the energy balance can be written as

$$\frac{d}{dt} \int_{(V)} \mathcal{E} dV = - \oint_{(\Sigma)} \left[ \rho \left( u + \frac{1}{2} \mathbf{v}^2 \right) \mathbf{v} - \hat{\sigma} \cdot \mathbf{v} + \mathbf{S}_e + \mathbf{J}_q + \mu \mathbf{J}_m + \mu_\pi \mathbf{J}_{ms} \right] \cdot \mathbf{n} d\Sigma + \int_{(V)} (\rho \mathbf{F} \cdot \mathbf{v} + \rho \mathfrak{R}) dV, \quad (23)$$

where  $\hat{\sigma}$  is the Cauchy stress tensor,  $\mu$  is chemical potential,  $\mu_\pi$  is an energy measure of the effect of the local mass displacement on the internal energy and  $\mathbf{J}_m = \rho(\mathbf{v}_* - \mathbf{v})$  [Burak et al. 2008].

By the use of (4), (5), (8), (21), and (22), taking a time derivative of the righthand side of (23) and by means of the divergence theorem, after some lengthy algebraic manipulations, we obtain the following local form of the balance equation for the internal energy  $u$ :

$$\begin{aligned} \rho \frac{Du}{Dt} = \rho T \frac{Ds}{Dt} + \hat{\sigma}_* : \frac{D\hat{\sigma}}{Dt} + \rho \mathbf{E}_* \cdot \frac{D\mathbf{p}}{Dt} + \rho \nabla \otimes \mathbf{E}_* : \frac{D\hat{\mathbf{q}}}{Dt} + \rho \mu'_\pi \frac{D\rho_m}{Dt} - \rho \nabla \mu'_\pi \cdot \frac{D\boldsymbol{\pi}_m}{Dt} \\ + \mathbf{J}_{e*} \cdot \mathbf{E}_* - \mathbf{J}_q \cdot \frac{\nabla T}{T} - T\eta + \mathbf{v} \cdot \left[ -\rho \frac{D\mathbf{v}}{Dt} + \nabla \cdot \hat{\sigma}_* + \mathbf{F}_e + \rho(\mathbf{F} + \mathbf{F}_m) \right], \quad (24) \end{aligned}$$



where  $\boldsymbol{\pi}_m = \boldsymbol{\Pi}_m/\rho$ ;  $\rho_m = \rho_{m\pi}/\rho$ ;  $\mu'_\pi = \mu_\pi - \mu$ . Here,  $\hat{\mathbf{e}}$ ,  $\mathbf{F}_e$ ,  $\mathbf{F}_m$ , and  $\hat{\sigma}_*$  are the infinitesimal strain tensor, ponderomotive force, additional mass force, and modified stress tensor that are defined by

$$\hat{\mathbf{e}} = [\nabla \otimes \mathbf{u} + (\nabla \otimes \mathbf{u})^T]/2, \quad (25)$$

$$\mathbf{F}_e = \rho_e \mathbf{E}_* + \rho(\nabla \otimes \mathbf{E}_*) \cdot \mathbf{p} + \left( \mathbf{J}_{e*} + \frac{\partial \boldsymbol{\Pi}_e}{\partial t} \right) \times \mathbf{B} + \rho(\nabla \otimes \nabla \otimes \mathbf{E}_*)^{T(2,3)} : \hat{\mathbf{q}}, \quad (26)$$

$$\mathbf{F}_m = \rho_m \nabla \mu'_\pi - (\nabla \otimes \nabla \mu'_\pi) \cdot \boldsymbol{\pi}_m, \quad (27)$$

$$\hat{\sigma}_* = \hat{\sigma} - \rho[\mathbf{p} \cdot \mathbf{E}_* + \hat{\mathbf{q}} : (\nabla \otimes \mathbf{E}_*) + \rho_m \mu'_\pi - \boldsymbol{\pi}_m \cdot \nabla \mu'_\pi] \hat{\mathbf{I}}, \quad (28)$$

where superscript  $\langle T \rangle$  denotes a transposed tensor and  $\hat{\mathbf{I}}$  is the unit tensor.

Applying the principle of frame indifference in a rigid translation, from (21) we obtain the balance of momentum in the form

$$\rho(D\mathbf{v}/Dt) = \nabla \cdot \hat{\sigma}_* + \mathbf{F}_e + \rho(\mathbf{F} + \mathbf{F}_m). \quad (29)$$

It is evident from (29), that the electric quadrupole and mass dipole moments induce nonlinear body forces  $\mathbf{F}'_e = -\rho(\nabla \otimes \nabla \otimes \mathbf{E}_*) : \hat{\mathbf{q}}$  and  $\mathbf{F}_m$  and couple stresses  $\hat{\sigma}'_* = -\rho[\hat{\mathbf{q}} : (\nabla \otimes \mathbf{E}_*) + \rho_m \mu'_\pi - \boldsymbol{\pi}_m \cdot \nabla \mu'_\pi] \hat{\mathbf{I}}$  within the body. Note that as evident from relation (25), we confined ourselves to linear strain-displacement relations (i.e., geometric nonlinearity is neglected within the framework of constructed mathematical model) whereas the balance equations (4), (11), (22), and (29) are nonlinear (the model takes physical nonlinearity into account).

By means of the Legendre transformation  $f = u - Ts - \mathbf{E}_* \cdot \mathbf{p} - \hat{\mathbf{q}} : (\nabla \otimes \mathbf{E}_*) + \nabla \mu'_\pi \cdot \boldsymbol{\pi}_m$  we define the generalized Helmholtz free energy. Using this new thermodynamic function and the balance of linear momentum (29), from (24) we obtain

$$\begin{aligned} \rho \frac{Df}{Dt} = & -\rho s \frac{DT}{Dt} + \hat{\sigma}_* : \frac{D\hat{\mathbf{e}}}{Dt} - \rho \mathbf{p} \cdot \frac{D\mathbf{E}_*}{Dt} - \rho \hat{\mathbf{q}} : \frac{D(\nabla \otimes \mathbf{E}_*)}{Dt} + \rho \mu'_\pi \frac{D\rho_m}{Dt} + \rho \boldsymbol{\pi}_m \cdot \frac{D\nabla \mu'_\pi}{Dt} \\ & + \mathbf{J}_{e*} \cdot \mathbf{E}_* - \mathbf{J}_q \cdot \frac{\nabla T}{T} - T\eta. \end{aligned} \quad (30)$$

While inspecting (30), we assume that the Helmholtz free energy is a function of  $T$ ,  $\hat{\mathbf{e}}$ ,  $\mathbf{E}_*$ ,  $\nabla \otimes \mathbf{E}_*$ ,  $\rho_m$ , and  $\nabla \mu'_\pi$  that is  $f = f(T, \hat{\mathbf{e}}, \mathbf{E}_*, \nabla \otimes \mathbf{E}_*, \rho_m, \nabla \mu'_\pi)$ . Note that the density of free energy depends not only on temperature  $T$ , strain tensor  $\hat{\mathbf{e}}$ , and electric field vector  $\mathbf{E}_*$ , as it follows from the classical theories, but also on the parameters  $\nabla \otimes \mathbf{E}_*$ ,  $\rho_m = -\nabla \cdot (\rho \boldsymbol{\pi}_m)/\rho$ , and  $\nabla \mu'_\pi$ , related to the electric quadrupole and mass dipole moments. Using (30), we get the expression

$$\begin{aligned} \rho \left( \frac{\partial f}{\partial T} + s \right) \frac{DT}{Dt} + \left( \rho \frac{\partial f}{\partial \hat{\mathbf{e}}} - \hat{\sigma}_* \right) : \frac{D\hat{\mathbf{e}}}{Dt} + \rho \left( \frac{\partial f}{\partial \mathbf{E}_*} + \mathbf{p} \right) \cdot \frac{D\mathbf{E}_*}{Dt} + \rho \left( \frac{\partial f}{\partial (\nabla \otimes \mathbf{E}_*)} + \hat{\mathbf{q}} \right) : \frac{D(\nabla \otimes \mathbf{E}_*)}{Dt} \\ + \rho \left( \frac{\partial f}{\partial \rho_m} - \mu'_\pi \right) \frac{D\rho_m}{Dt} + \rho \left( \frac{\partial f}{\partial \nabla \mu'_\pi} - \boldsymbol{\pi}_m \right) \cdot \frac{D\nabla \mu'_\pi}{Dt} = 0, \end{aligned} \quad (31)$$

and the following relation for entropy production

$$\eta = \mathbf{J}_{e*} \cdot \mathbf{E}_* - \mathbf{J}_q \cdot (\nabla T/T). \quad (32)$$

Note that in relation (32) for entropy production, the terms caused by polarization and the local mass displacement are absent because we describe these processes as reversible.

## 7. Constitutive equations

Since parameters  $T$ ,  $\hat{\mathbf{e}}$ ,  $\mathbf{E}_*$ ,  $\nabla \otimes \mathbf{E}_*$ ,  $\rho_m$ , and  $\nabla \mu'_\pi$  are independent, we obtain the following constitutive equations from relation (31):

$$\hat{\sigma}_* = \rho \frac{\partial f}{\partial \hat{\mathbf{e}}} \Big|_{T, \mathbf{E}_*, \nabla \otimes \mathbf{E}_*, \rho_m, \nabla \mu'_\pi}, \quad s = -\frac{\partial f}{\partial T} \Big|_{\hat{\mathbf{e}}, \mathbf{E}_*, \nabla \otimes \mathbf{E}_*, \rho_m, \nabla \mu'_\pi}, \quad \mathbf{p} = -\frac{\partial f}{\partial \mathbf{E}_*} \Big|_{\hat{\mathbf{e}}, T, \nabla \otimes \mathbf{E}_*, \rho_m, \nabla \mu'_\pi}, \quad (33)$$

$$\hat{\mathbf{q}} = -\frac{\partial f}{\partial (\nabla \otimes \mathbf{E}_*)} \Big|_{\hat{\mathbf{e}}, T, \mathbf{E}_*, \rho_m, \nabla \mu'_\pi}, \quad \mu'_\pi = \frac{\partial f}{\partial \rho_m} \Big|_{\hat{\mathbf{e}}, T, \mathbf{E}_*, \nabla \otimes \mathbf{E}_*, \nabla \mu'_\pi}, \quad \boldsymbol{\pi}_m = \frac{\partial f}{\partial (\nabla \mu'_\pi)} \Big|_{\hat{\mathbf{e}}, T, \mathbf{E}_*, \nabla \otimes \mathbf{E}_*, \rho_m}. \quad (34)$$

The specific electric quadrupole  $\hat{\mathbf{q}}$ , the potential  $\mu'_\pi$ , and the local mass displacement vector  $\boldsymbol{\pi}_m$  are the thermodynamic conjugates of the electric field gradient, the specific induced mass, and the gradient of modified chemical potential.

We can write (33) and (34) in an explicit form. In order to obtain the linear constitutive relations, we expand  $f$  into a Taylor series about  $\hat{\mathbf{e}} = 0$ ,  $T = T_0$ ,  $\mathbf{E}_* = 0$ ,  $\nabla \otimes \mathbf{E}_* = 0$ ,  $\rho_m = 0$ ,  $\mu'_\pi = \mu'_{\pi 0}$ , and  $\nabla \mu'_\pi = 0$ , where  $T_0$  is a reference temperature and  $\mu'_{\pi 0}$  is the potential  $\mu'_\pi$  of an infinite medium. Denoting  $\theta = T - T_0$ ,  $I_{e1} = \hat{\mathbf{e}} : \hat{\mathbf{I}} = e$ ,  $I_{e2} = \hat{\mathbf{e}} : \hat{\mathbf{e}}$ ,  $I_{E1} = (\nabla \otimes \mathbf{E}_*) : \hat{\mathbf{I}} = \nabla \otimes \mathbf{E}_*$ ,  $I_{E2} = (\nabla \otimes \mathbf{E}_*) : (\nabla \otimes \mathbf{E}_*)$  and keeping linear and quadratic terms only, we can write the following for isotropic materials

$$\begin{aligned} f = f_0 - s_0 \theta + \mu'_{\pi 0} \rho_m + \frac{1}{2\rho_0} \left( K - \frac{2}{3}G \right) I_{e1}^2 + \frac{G}{\rho_0} I_{e2} - \frac{C_V}{2T_0} \theta^2 + \frac{d_\rho}{2} \rho_m^2 \\ - \frac{\chi_m}{2} (\nabla \mu'_\pi)^2 - \frac{\chi_E}{2} \mathbf{E}_*^2 + \frac{\chi_{q1}}{2} I_{E1}^2 - \chi_{q2} I_{E2} - \frac{K\alpha_T}{\rho_0} I_{e1} \theta - \frac{K\alpha_\rho}{\rho} I_{e1} \rho_m \\ - \frac{K\alpha_{E1}}{\rho_0} I_{e1} I_{E1} - \beta_{T\rho} \rho_m \theta + \beta_{TE} I_{E1} \theta + \beta_{E\rho} I_{E1} \rho_m \\ + \chi_{Em} \mathbf{E}_* \cdot \nabla \mu'_\pi + 2G \frac{\alpha_{E2}}{\rho_0} \hat{\mathbf{e}} : (\nabla \otimes \mathbf{E}_*). \end{aligned} \quad (35)$$

Here  $K$ ,  $G$ ,  $C_V$ ,  $d_\rho$ ,  $\alpha_T$ ,  $\alpha_\rho$ ,  $\alpha_{E1}$ ,  $\alpha_{E2}$ ,  $\chi_E$ ,  $\chi_m$ ,  $\chi_{Em}$ ,  $\chi_{q1}$ ,  $\chi_{q2}$ ,  $\beta_{T\rho}$ ,  $\beta_{TE}$ ,  $\beta_{E\rho}$  are material characteristics.

Using the formulas (33), (34) and (35) we obtain the following constitutive relations for isotropic dielectric materials

$$\hat{\sigma} = 2G\hat{\mathbf{e}} + 2G\alpha_{E2}\nabla \otimes \mathbf{E} + \left[ \left( K - \frac{2}{3}G \right) e - K\alpha_T\theta - K\alpha_\rho\rho_m - K\alpha_{E1}\nabla \cdot \mathbf{E} \right] \hat{\mathbf{I}}, \quad (36a)$$

$$s = s_0 + \frac{C_V}{T_0} \theta + \frac{K\alpha_T}{\rho_0} e + \beta_{T\rho} \rho_m - \beta_{TE} \nabla \cdot \mathbf{E}, \quad (36b)$$

$$\mu'_\pi = \mu'_{\pi 0} + d_\rho \rho_m - \frac{K\alpha_\rho}{\rho_0} e - \beta_{T\rho} \theta + \beta_{E\rho} \nabla \cdot \mathbf{E}, \quad (36c)$$

$$\mathbf{p} = \chi_E \mathbf{E} - \chi_{Em} \nabla \mu'_\pi, \quad (36d)$$

$$\boldsymbol{\pi}_m = -\chi_m \nabla \mu'_\pi + \chi_{Em} \mathbf{E}, \quad (36e)$$

$$\hat{\mathbf{q}} = 2\chi_{q2} \nabla \otimes \mathbf{E} - 2G\alpha_{E2} \hat{\mathbf{e}} - \left( \chi_{q1} \nabla \cdot \mathbf{E} - \frac{K\alpha_{E1}}{\rho_0} e + \beta_{TE} \theta + \beta_{E\rho} \rho_m \right) \hat{\mathbf{I}}. \quad (36f)$$

The constitutive equations describe an electromechanical interaction in isotropic (centrosymmetric) materials. In the framework of the proposed theory, the body polarization is caused not only by the electric field but also by the spatial nonhomogeneity of the field, as well as by the gradients of the strain, and the temperature and density of induced mass. Hence, the constitutive equations (36) for isotropic materials make it possible to describe both the flexoelectric and thermopolarization effects. Note that the classical theories of dielectrics cannot describe these effects.

Now we shall specify the expressions for fluxes. We represent (32) for entropy production as follows:  $\eta = \frac{1}{T} \sum_{k=1}^2 \mathbf{j}_k \cdot \mathbf{X}_k$ , where  $\mathbf{J}_1 = \mathbf{J}_e^*$ ,  $\mathbf{J}_2 = \mathbf{J}_q$ ,  $\mathbf{X}_1 = \mathbf{E}_*$ , and  $\mathbf{X}_2 = -\nabla T/T$  are thermodynamic fluxes and forces. Assuming that thermodynamic forces are the cause of the thermodynamic fluxes  $\mathbf{j}_1$  and  $\mathbf{j}_2$ , we can write  $\mathbf{j}_i = \mathbf{j}_i(\mathbf{X}_1, \mathbf{X}_2)$ ,  $i = 1, 2$ . In a linear approximation, we obtain the following equations for fluxes

$$\mathbf{J}_e = \zeta_E \mathbf{E} - \zeta \nabla T, \quad \mathbf{J}_q = -\lambda \nabla T + \zeta_T \mathbf{J}_e, \quad (37)$$

where  $\zeta_E$  and  $\lambda$  are electric and thermal conductivity, respectively, and the coefficients  $\zeta_T$  and  $\zeta$  characterize thermoelectric phenomena. Note that the Second Law of thermodynamics states that entropy production is positive definite, i.e.,  $\eta \geq 0$ . In order to ensure the positive character of entropy production, the coefficients  $\lambda$ ,  $\zeta_E$ ,  $\zeta$ , and  $\zeta_T$  should be positive defined.

## 8. Key equations for isothermal approximation

Balance equations (11), (19), (22), (29), Maxwell's equations (12), (13), constitutive relations (16), (36), (37), and formulas (5), (14), (15), (25) form a complete set of field equations for the coupled problems of local gradient electrothermoelasticity for nonferromagnetic dielectric solids.

In what follows, we shall consider an isothermal approximation. We obtain the final form of the key equations by substituting the constitutive equations (16), (36), (37), geometric relations (25), and formulas (5), (14), and (15) into the balance of momentum (29), the conservation laws of induced mass (11), and Maxwell's equations (12), (13). The fundamental field equations for ideal dielectrics expressed in terms of the displacement vector  $\mathbf{u}$ , induced mass  $\rho_m$ , electric field  $\mathbf{E}$  and magnetic induction  $\mathbf{B}$  can be written as

$$\rho_0 \frac{\partial^2 \mathbf{u}}{\partial t^2} = \left( K + \frac{1}{3} G \right) \nabla (\nabla \cdot \mathbf{u}) + G \Delta \mathbf{u} - K \alpha_{E1} \nabla (\nabla \cdot \mathbf{E}) + 2G \alpha_{E2} \Delta \mathbf{E} - K \alpha_\rho \nabla \rho_m + \rho_0 \mathbf{F}, \quad (38)$$

$$\Delta \rho_m - \frac{1}{\chi_m d_\rho} \rho_m = \frac{K \alpha_\rho}{\rho_0 d_\rho} \Delta (\nabla \cdot \mathbf{u}) - \frac{\beta_{E\rho}}{d_\rho} \Delta (\nabla \cdot \mathbf{E}) + \frac{\chi_{Em}}{\chi_m d_\rho} \nabla \cdot \mathbf{E}, \quad (39)$$

$$\nabla \times \mathbf{E} = -\frac{\partial \mathbf{B}}{\partial t}, \quad \nabla \cdot \mathbf{B} = 0, \quad (40)$$

$$\begin{aligned} \frac{1}{\mu_0} \nabla \times \mathbf{B} = \sigma_e \mathbf{E} + \varepsilon \frac{\partial \mathbf{E}}{\partial t} + \rho (\chi_{q1} - \beta_{E\rho} \chi_{Em}) \frac{\partial \nabla (\nabla \cdot \mathbf{E})}{\partial t} - 2\rho_0 \chi_{q2} \frac{\partial \Delta \mathbf{E}}{\partial t} + \rho_0 (\beta_{E\rho} - d_\rho \chi_{Em}) \frac{\partial \nabla \rho_m}{\partial t} \\ + (K \alpha_\rho \chi_{Em} + \rho_0 G \alpha_{E2} - K \alpha_{E1}) \frac{\partial (\nabla \nabla \cdot \mathbf{u})}{\partial t} + \rho_0 G \alpha_{E2} \frac{\partial \Delta \mathbf{u}}{\partial t}, \end{aligned} \quad (41)$$

$$\begin{aligned} \varepsilon \nabla \cdot \mathbf{E} + \rho_0 (\chi_{q1} - 2\chi_{q2} - \chi_{Em} \beta_{E\rho}) \Delta (\nabla \cdot \mathbf{E}) + (2\rho_0 G \alpha_{E2} - K \alpha_{E1} + K \alpha_\rho \chi_{Em}) \Delta (\nabla \cdot \mathbf{u}) \\ + \rho_0 (\beta_{E\rho} - d_\rho \chi_{Em}) \Delta \rho_m = \rho_e. \end{aligned} \quad (42)$$

Here,  $\varepsilon = \varepsilon_0 + \rho_0 \chi_E$ .

Note that the ponderomotive  $\mathbf{F}_e$  and additional mass  $\mathbf{F}_m$  forces are absent in (38) because these forces are nonlinear functions of the perturbations fields. Accounting for the local mass displacement yields an additional equation (39) in the key set and suggests modifications of (38), (41) and (42), all of which contain certain terms related to this process. Equation (39) is stationary because we consider the local mass displacement as a reversible process. Its solution depends on the sign of the coefficient  $(d_\rho \chi_m)^{-1}$ . From the estimation of coefficients  $d_\rho$  and  $\chi_m$  it follows that these quantities are positive [Burak et al. 2011], thus,  $(d_\rho \chi_m)^{-1} = \lambda_\mu^2$ . Here,  $\lambda_\mu^{-1}$  is the intrinsic length scale parameter (a material constant which dimension is length). The emergence of such a constant is typical of the gradient-type theories [Mindlin 1972], while an intrinsic length scale is absent from classical theories. As a result of accounting for the electric quadrupole, summands proportional to a second-order space partial derivative of the electric field vector  $\mathbf{E}$  appear in the balance of momentum (38). Equations (41) and (42) change too. Now they contain summands proportional to a third-order mixed partial derivative of the electric field vector.

### 9. Surface energy of deformation and polarization

We apply the above relations to determine the surface energy of deformation and polarization. The notion of surface energy of deformation and polarization was originally introduced in [Mindlin 1965; 1968].

Using the constitutive equations (36), we modify expression (35) as

$$f - f_0 = \frac{1}{2\rho_0} \hat{\sigma} : \hat{\epsilon} + \frac{1}{2} \mu'_{\pi 0} \rho_m + \frac{1}{2} \mu'_\pi \rho_m + \frac{1}{2} \boldsymbol{\pi}_m \cdot \nabla \mu'_\pi - \frac{1}{2} \mathbf{E} \cdot \mathbf{p} - \frac{1}{2} \hat{\mathbf{q}} : (\nabla \otimes \mathbf{E}). \quad (43)$$

Let us consider an equilibrium state of ideal dielectrics for which  $\mathbf{E} = -\nabla \varphi_e$ , where  $\varphi_e$  is electric potential. Using this formula, the equilibrium equation  $\nabla \hat{\sigma} + \rho_0 \mathbf{F} = 0$ , the geometrical relation (25), Gauss's law (13)<sub>2</sub>, as well as the formulas (8) and (16), and after applying some algebra to (43), we can express the perturbation of the total energy  $\mathcal{E}$  as

$$\mathcal{E} = \frac{1}{2} \rho_0 \mu'_{\pi 0} \rho_m + \frac{1}{2} \rho_0 \mathbf{F} \cdot \mathbf{u} + \frac{1}{2} \nabla \cdot (\hat{\sigma} \cdot \mathbf{u}) - \frac{1}{2} \rho_0 \nabla \cdot (\boldsymbol{\pi}_m \tilde{\mu}'_\pi) - \frac{1}{2} \nabla \cdot (\varphi_e \mathbf{D}) + \frac{1}{12} \nabla \cdot (\mathbf{E} \cdot \hat{\mathbf{Q}}). \quad (44)$$

Here,  $\tilde{\mu}'_\pi = \mu'_\pi - \mu'_{\pi 0}$ .

We integrate both parts of (44) over the region  $(V') = (V) \cup (V_v)$  occupied by the body (region  $(V)$ ) and vacuum (region  $(V_v)$ ). Finally, using the divergence theorem, we obtain

$$\int_{(V')} \mathcal{E} dV = \frac{1}{2} \rho_0 \mu'_{\pi 0} \int_{(V)} \rho_m dV + \frac{1}{2} \rho_0 \int_{(V)} \mathbf{F} \cdot \mathbf{u} dV + \frac{1}{2} \int_{(\Sigma)} \left( \hat{\sigma} \cdot \mathbf{u} - \rho_0 \boldsymbol{\pi}_m \tilde{\mu}'_\pi - \varphi_e [\mathbf{D}] + \frac{1}{6} \mathbf{E} \cdot \hat{\mathbf{Q}} \right) \cdot \mathbf{n} d\Sigma. \quad (45)$$

Here,  $[\mathbf{D}]$  denotes the finite jump of the electric induction over the surface  $(\Sigma)$ .

Consider the solids with traction-free surfaces and in the absence of external forces ( $\mathbf{F} = 0$ ). Then, we have  $\forall \mathbf{r} \in (\Sigma) : \hat{\sigma} \cdot \mathbf{n} = 0$ , and  $[\mathbf{D}] = 0$ . Hence, using formula (7), we get

$$\int_{(V)} \mathcal{E} dV = \frac{1}{2} \rho_0 \int_{(\Sigma)} (\mathbf{E} \cdot \hat{\mathbf{q}} - \boldsymbol{\pi}_m \tilde{\mu}'_\pi) \cdot \mathbf{n} d\Sigma. \quad (46)$$

The righthand side of the above equality defines the surface energy of deformation and polarization  $U_\Sigma$ , for which in the framework of the proposed theory we obtain

$$U_\Sigma = \frac{1}{2} \rho_0 (\mathbf{E} \cdot \hat{\mathbf{q}} - \boldsymbol{\pi}_m \tilde{\mu}'_\pi) \cdot \mathbf{n} \Big|_{r \in \Sigma}. \quad (47)$$

Thus, the specific surface energy of deformation and polarization is defined by the electric field vector  $\mathbf{E}$ , the quadrupole moment  $\hat{\mathbf{q}}$ , the local mass displacement vector  $\boldsymbol{\pi}_m$  and a perturbation of the modified chemical potential  $\tilde{\mu}'_\pi$ .

## 10. Surface and size effects

The linear relations of the local gradient theory of dielectrics are tested on some simple problems. In this section, they are used to study the effect of a free surface on the stress-strain state and polarization of elastic bodies having plane and cylindrical surfaces.

We apply the key set of equations (38)–(42) to investigate the near-surface inhomogeneity of electromechanical fields (i) in an infinite layer (region  $|x| \leq l$ ), (ii) in a cylinder (region  $r \leq R$ ), and (iii) in an elastic dielectric medium with a cylindrical hole (region  $r \geq R$ ). Let as these bodies are in contact with vacuum. The body force is assumed to be zero. If we neglect the effect of electric quadrupole moments, the key set of equations can be written as

$$\left(\bar{K} + \frac{1}{3}G\right)\nabla(\nabla \cdot \mathbf{u}) + G\Delta \mathbf{u} - K\frac{\alpha_\rho}{d_\rho}\nabla\tilde{\mu}'_\pi = 0, \quad (48)$$

$$\Delta\tilde{\mu}'_\pi - \lambda_\mu^2\tilde{\mu}'_\pi = \lambda_\mu^2\frac{K\alpha_\rho}{\rho_0}\nabla \cdot \mathbf{u} + \frac{\chi_{Em}}{\chi_m}\nabla \cdot \mathbf{E}, \quad (49)$$

$$\nabla \cdot \mathbf{E} - \kappa_E\Delta\tilde{\mu}'_\pi = 0. \quad (50)$$

Since the body surfaces are traction-free, the boundary conditions on  $(\Sigma)$  ( $x = \pm l$  for a layer and  $r = R$  for solids of a cylindrical geometry) are

$$\hat{\boldsymbol{\sigma}} \cdot \mathbf{n} = 0, \quad \mu'_\pi = 0, \quad \text{and } [\mathbf{D}] = 0. \quad (51)$$

Here  $\bar{K} = K - K^2\alpha_\rho^2/(\rho_0 d_\rho)$ , and  $\kappa_E = \rho_0\chi_{Em}/\varepsilon$ .

To determine the displacement field and density of induced mass, we formulate a stationary boundary value problem, while the problem of electrodynamics is formulated as a contact problem. Therefore, the Maxwell equations in vacuum as well as the radiation conditions [Bredov et al. 1985; Nowacki 1983] should be considered together with (48)–(50).

We find analytical solutions to the problems formulated above. These solutions enable us (i) to determine the surface stresses and the surface energy of deformation and polarization in solid dielectric films and fibers, (ii) to investigate the effect of surface curvature on these values, (iii) to describe the size effects, and (iv) to justify the occurrence of a bound charge on a free surface of dielectric bodies as well as the emergence of disjoining pressure in thin solid films.

**10.1. Layer with free boundaries.** An analysis of the results obtained reveals that the near-surface regions of the layer are characterized by an inhomogeneous distribution of the stresses  $\sigma_{yy} = \sigma_{zz} \equiv \sigma$  (Figure 2), polarization  $\mathbf{p} = (p(x), 0, 0)$ , electric field  $\mathbf{E} = (E(x), 0, 0)$  and modified chemical  $\tilde{\mu}'_\pi$

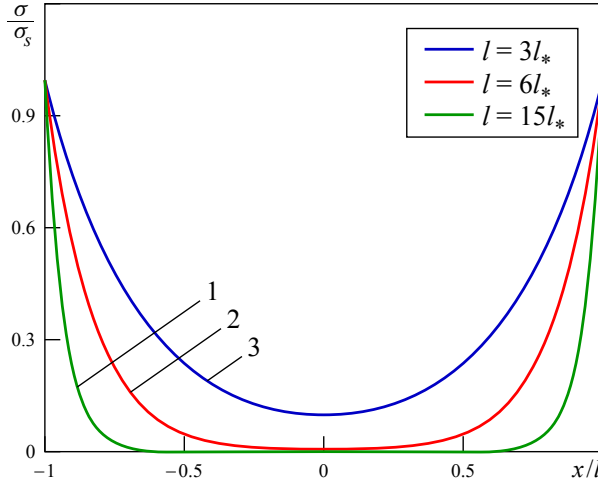


**Figure 2.** The distribution of the stresses  $\sigma_{yy}/\sigma_s$  in films of different thicknesses:  $l = 15l_*$  (curve 1),  $l = 6l_*$  (curve 2),  $l = 3l_*$  (curve 3).

potentials [Burak et al. 2008]:

$$\sigma(x) = \frac{2G\rho_0 \mathfrak{M} \mu'_{\pi 0}}{K\alpha_\rho} \frac{\text{ch}(\check{\lambda}x)}{\text{ch}(\check{\lambda}l)}, \quad p(x) = \kappa_E \check{\lambda} \mu'_{\pi 0} \frac{\varepsilon_0 \text{sh}(\check{\lambda}x)}{\rho_0 \text{ch}(\check{\lambda}l)}, \quad (52)$$

$$\tilde{\mu}'_\pi(x) = -\mu'_{\pi 0} \frac{\text{ch}(\check{\lambda}x)}{\text{ch}(\check{\lambda}l)}, \quad E(x) = -\kappa_E \check{\lambda} \mu'_{\pi 0} \frac{\text{sh}(\check{\lambda}x)}{\text{ch}(\check{\lambda}l)}. \quad (53)$$

Here,

$$\check{\lambda} = \lambda_\mu \left| \sqrt{\frac{1 + \mathfrak{M}}{(1 - \kappa_E \chi_{Em}/\chi_m)}} \right|, \quad \mathfrak{M} = \frac{K^2 \alpha_\rho^2}{\rho_0 d_\rho (\bar{K} + 4G/3)}.$$

In this case, a bound electrical charge of density  $\vartheta_{se}(\pm l) = \pm \varepsilon_0 \kappa_E \mu'_{\pi 0} \text{th}(l/l_*)/l_*$  is induced on the surfaces of the layer  $x = \pm l$  (see Figure 3, where  $\vartheta_* = \varepsilon_0 \kappa_E \mu'_{\pi 0}$ ,  $l_* = \check{\lambda}^{-1}$ ). The factors  $\mathfrak{M}$  and  $\kappa_E$  describe the coupling between the local mass displacement and the process of deformation and the electric field, respectively [Burak et al. 2011]. Note that  $\mathfrak{M}$  and  $\kappa_E$  are small parameters. The analysis of the results obtained also shows that layer thickness does not affect the value of surface stresses  $\sigma_s = 2G\rho_0 \mathfrak{M} \mu'_{\pi 0}/(K\alpha_\rho)$ , but it does affect the distribution of stresses within the body [Burak et al. 2008].

The interior regions of thick layer (line 1 in Figure 2) are stress-free, while the interior regions of thin film (line 3 in Figure 2) are stressed:  $\sigma(0) = \sigma_s / \text{ch}(l/l_*)$  describes middle surface stresses. Here, we define thin films as layers with the thickness of several characteristic lengths  $l_*$ . For such films, overlaps of the regions of the near-surface inhomogeneity of fields are typical. One can see that a reduction in the film thickness leads to an increase in the stress level in the film's cross section. The dependence of the stress distribution (Figure 2) and the bound electric charge (Figure 3) on the film thickness displays their size effect.

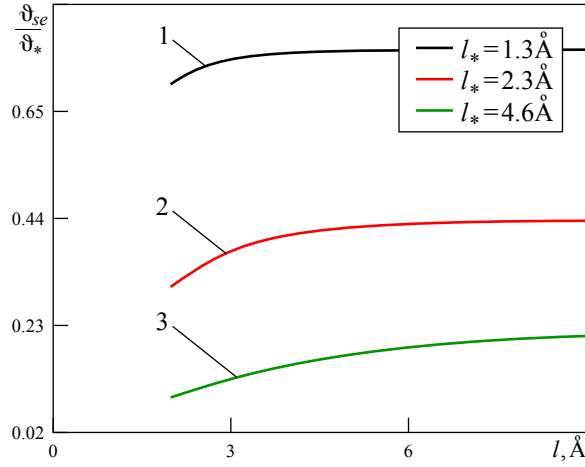


**Figure 3.** The dependence of the bound surface electric charge  $\vartheta_{se}(l)$  on the film thickness for different materials:  $l_* = 1.3 \text{ \AA}$  (curve 1),  $l = 2.3 \text{ \AA}$  (curve 2),  $l = 4.6 \text{ \AA}$  (curve 3).

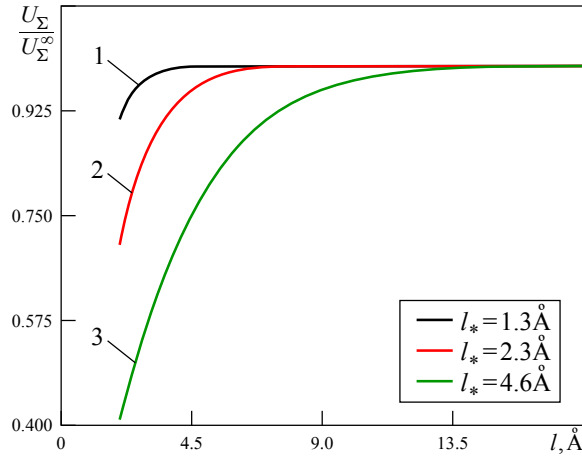


**Figure 4.** The dependence of the surface energy of deformation and polarization on the film thickness for different materials:  $l_* = 1.3 \text{ \AA}$  (curve 1),  $l = 2.3 \text{ \AA}$  (curve 2),  $l = 4.6 \text{ \AA}$  (curve 3).

Using (36e), (47), and (53) we obtain the formula  $U_\Sigma(l) = U_\Sigma^\infty \text{th}(\tilde{\lambda}l)$  that describes the size effect of surface energy of deformation and polarization in thin dielectric films. Here,

$$U_\Sigma^\infty = -\rho_0 \mu_{\pi 0}'^2 \frac{\chi_m - {}^K E \chi_{Em}}{2l_*},$$

is the surface energy of deformation and polarization in the half-space of the same material. The absolute value of  $U_\Sigma$  decreases with a decrease in the thickness of the thin film (Figure 4).

**10.2. Solids of cylindrical geometry.** In this subsection, the effect of surface curvature on the equilibrium stress distribution, polarization, surface energy of deformation and polarization, and bond surface

electric charge is studied for dielectric bodies free from external loads. To this end, the solutions to the problems for a cylindrical fiber (region  $r \leq R$ ) and an infinite medium containing a thin cylindrical hole (region  $r \geq R$ ) with traction-free surfaces at  $r = R$  are used. The axes of the fiber and cylindrical hole coincide with the  $z$  axis. In this case the key functions  $\mathbf{u} = (u_r(r), 0, 0)$ ,  $\mathbf{E} = (E_r(r), 0, 0)$  and  $\tilde{\mu}'_\pi(r)$  are functions of the space coordinate  $r$  only. Thus, the solution of boundary problem (48)–(51) is given by

$$u_r(r) = \mu'_{\pi 0} \frac{K \alpha_\rho}{\check{\lambda} d_\rho (\bar{K} + \frac{4}{3}G)} \left[ \frac{1}{2} Q \check{\lambda} r - (1 - \mathfrak{M} Q) \frac{I_1(\check{\lambda} r)}{I_0(\check{\lambda} R)} \right], \quad (54)$$

$$\tilde{\mu}'_\pi(r) = -\mu'_{\pi 0} \left[ (1 - \mathfrak{M} Q) \frac{I_0(\check{\lambda} r)}{I_0(\check{\lambda} R)} + \mathfrak{M} Q \right], \quad (55)$$

$$E_r(r) = -\kappa_E \mu'_{\pi 0} \check{\lambda} (1 - \mathfrak{M} Q) \frac{I_1(\check{\lambda} r)}{I_0(\check{\lambda} R)}, \quad (56)$$

for cylindrical fiber ( $r \leq R$ ), and

$$u_r(r) = \mu'_{\pi 0} \frac{K \alpha_\rho}{\check{\lambda} d_\rho (\bar{K} + \frac{4}{3}G)} \frac{K_1(\check{\lambda} R)}{K_0(\check{\lambda} R)} \left( \frac{K_1(\check{\lambda} r)}{K_1(\check{\lambda} R)} - \frac{R}{r} \right), \quad (57)$$

$$\tilde{\mu}'_\pi(r) = -\mu'_{\pi 0} \frac{K_0(\check{\lambda} r)}{K_0(\check{\lambda} R)}, \quad (58)$$

$$E_r(r) = \mu'_{\pi 0} \kappa_E \check{\lambda} \frac{K_1(\check{\lambda} r)}{K_0(\check{\lambda} R)}, \quad (59)$$

for infinite medium with cylindrical hole ( $r \geq R$ ). Here,  $I_j$  and  $K_j$  are the first- and second-kind modified Bessel functions of the order  $j$  (Macdonald functions), and

$$Q = - \frac{2GI_1(\check{\lambda} R)}{(K + G/3)\check{\lambda} R I_0(\check{\lambda} R) - 2G\mathfrak{M} I_1(\check{\lambda} R)}. \quad (60)$$

The analysis of the obtained solutions shows that the surface curvature has important effects on thin fibers. An increase in the surface curvature of thin fibers leads to a reduction in the density of the surface bound charge:

$$\vartheta_{se}(R) = \kappa_E \check{\lambda} \varepsilon_0 \mu'_{\pi 0} \frac{(K + G/3)\check{\lambda} R I_1(\check{\lambda} R)}{(K + G/3)\check{\lambda} R I_0(\check{\lambda} R) - 2G\mathfrak{M} I_1(\check{\lambda} R)}, \quad (61)$$

as well as to an increase of the levels of absolute value of the corresponding stresses (see Figure 5, where  $\mathfrak{M} = 3 \cdot 10^{-3}$ ,  $K/G = 2.79$ ).

A formula that describes the influence of surface curvature on the density of the surface energy of deformation and polarization is given by

$$\frac{U_\Sigma^c}{U_\Sigma^\infty} = \begin{cases} \frac{K_1(-1/\kappa)}{K_0(-1/\kappa)}, & \kappa < 0, \\ 1, & \kappa = 0, \\ \frac{I_1(1/\kappa)}{I_0(1/\kappa) - 2G\mathfrak{M}(K + G/3)^{-1}I_1(1/\kappa)}, & \kappa > 0. \end{cases} \quad (62)$$



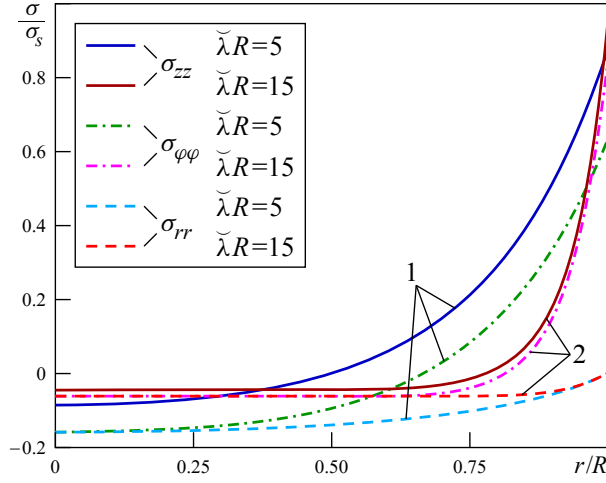


**Figure 5.** The effect of surface curvature on the stresses in fiber for  $\check{\lambda}R = 5$  (curve 1) and  $\check{\lambda}R = 15$  (curve 2).

Here,  $\kappa = -(\check{\lambda}R)^{-1}$  for a dielectric medium with a cylindrical hole,  $\kappa = (\check{\lambda}R)^{-1}$  for a fiber, and  $\kappa = 0$  for solids with plane surfaces. An increased surface curvature of a free cylinder leads to a decrease in the absolute value of the surface energy compared to the body with a plane surface (Figure 6). By contrast, in the infinite medium with a thin cylindrical hole, an increased curvature of the surface results in an increased surface energy. Note that the characteristic lengths  $l_* = 1.3 \text{ \AA}$  and  $l_* = 1.89 \text{ \AA}$  correspond to crystals NaCl and KCl [Askar et al. 1971; Mindlin 1972]. Thus, the value of the surface energy of deformation and polarization for the body with a plane surface ( $\kappa = 0$ ) is not the minimum of the surface energy  $U_\Sigma$  as a function of surface curvature.

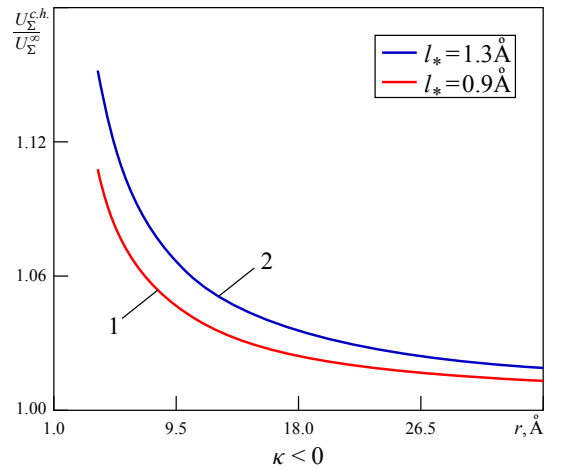
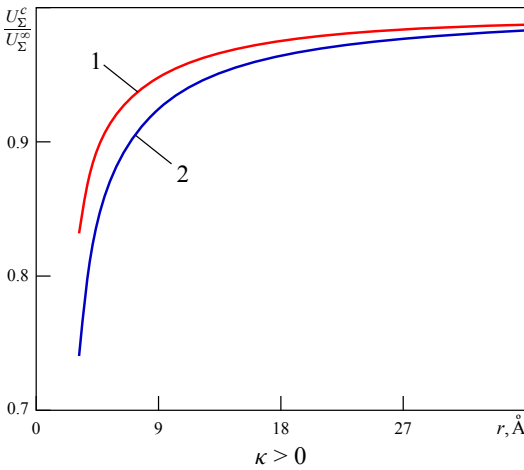


**Figure 6.** The effect of surface curvature on the surface energy of deformation and polarization for  $l_* = 0.9 \text{ \AA}$  (curve 1) and  $l_* = 1.3 \text{ \AA}$  (curve 2).

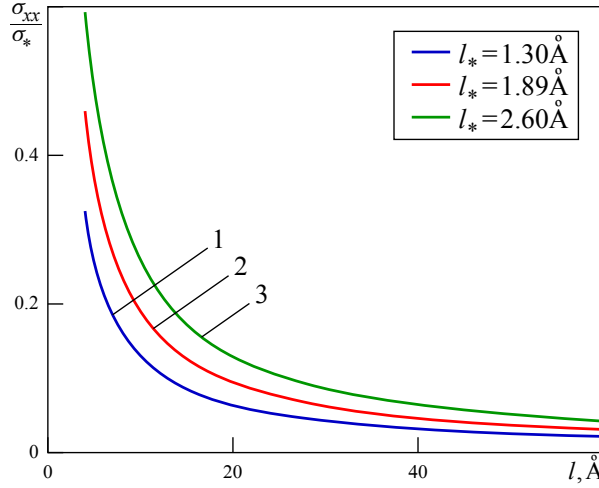


**Figure 7.** The dependence of the disjoining pressure on the film thickness for different materials:  $l_* = 1.3 \text{ \AA}$  (curve 1),  $l_* = 1.89 \text{ \AA}$  (curve 2),  $l_* = 2.6 \text{ \AA}$  (curve 3).

**10.3. Layer with clamped boundaries.** Deryagin et al. [1985] show that a disjoining pressure emerges in thin liquid films. We show that such a pressure can be present in thin solid films as well. Within the framework of the developed theory, the emergence of the disjoining pressure is associated with changes in the structure of the near-surface regions of the thin body (with the local mass displacement). To demonstrate this, within this section, we study the near-surface inhomogeneity of electromechanical fields in an infinite isotropic dielectric layer ( $|x| \leq l$ ) with clamped boundaries. Using the solutions to (48)–(50) that satisfy the boundary conditions  $\mathbf{u} = 0$ ,  $\mu'_\pi = 0$ , and  $[\mathbf{D}] = 0$  on the surfaces  $x = \pm l$  of the layer, we investigate the stress-strain state, polarization, as well as electric and modified chemical potentials in dielectric films. In particular, for the components  $\sigma_{xx}$ ,  $\sigma_{yy} = \sigma_{zz} \equiv \sigma$  of the stress tensor we obtain

$$\sigma_{xx} = \frac{\sigma_*(1 + \mathfrak{M})}{\check{\lambda}l \operatorname{cth}(\check{\lambda}l) + \mathfrak{M}}, \quad \sigma_{yy} = \sigma_{zz} = \sigma_* \frac{\check{\lambda}l \operatorname{ch}(\check{\lambda}x) + (3K - 2G) \operatorname{sh}(\check{\lambda}l)/6G}{\check{\lambda}l \operatorname{ch}(\check{\lambda}l) + \mathfrak{M} \operatorname{sh}(\check{\lambda}l)}. \quad (63)$$

Here,  $\sigma_* = \mu'_{\pi 0} K \alpha_\rho / d_\rho$ .

One can see that in films with clamped boundaries the constant normal stresses  $\sigma_{xx}$  appear in addition to the stresses  $\sigma_{yy}$  and  $\sigma_{zz}$ . In thick films, the stresses  $\sigma_{xx}$  are negligibly small, but a decreasing thickness of thin films leads to an increase of the absolute value of these stresses (Figure 7). These stresses cause a disjoining pressure in thin solid films:

$$p_{\text{dis}} = \frac{1}{2l} \int_{-l}^l \sigma_{xx} dx.$$

Note also that a positive disjoining pressure can prevent the reduction of the film thickness under the effect of external forces, whereas a negative pressure can reduce the thickness of the film and thus may lead to its destruction.

## 11. Conclusions

It is shown that a local gradient theory of electrothermoelasticity for nonferromagnetic dielectric continua can be formulated by considering the contribution of the electric charge and mass fluxes caused by changes in material microstructure. These fluxes are (i) the nondiffusive and nonconvective mass flux, caused by a change over time of the vector of the local mass displacement (the mass dipole moment) and (ii) the electric polarization current, caused by the change over time of both the dipole and quadrupole electric moments. The result of accounting for the mentioned fluxes is an extension of the phase space of thermodynamic constitutive parameters by three additional pairs of conjugate parameters. Compared to the classical theory of dielectrics, the space of constitutive variables additionally includes: (i) the specific electric quadrupole moment  $\hat{q}$  and the gradient of the electric field vector  $\nabla \otimes \mathbf{E}_*$ ; (ii) the specific density of induced mass  $\rho_m$  and the modified chemical potential  $\mu'_\pi$ ; (iii) the specific vector of the local mass displacement  $\boldsymbol{\pi}_m$  and the gradient of the modified chemical potential  $\nabla \mu'_\pi$ . Moreover, accounting for the mentioned fluxes results in a modification of the stress tensor  $\hat{\sigma}_*$  and in the emergence of a nonlinear mass force  $\mathbf{F}_m$ , in addition to the ponderomotive force  $\mathbf{F}_e$  in the momentum equation. The effect of the force  $\mathbf{F}_m$  can be important for investigating nonlinear effects in nanoscale films, fibers, and wires, since all of them are characterized by high gradients of physical and mechanical fields.

Within the classical linear theory of elastic dielectrics, there is no interaction between the mechanical and electromagnetic fields if the material is isotropic. Hence, flexoelectric and thermopolarization effects can occur in anisotropic materials only. Within the framework of the local gradient theory of dielectrics, the electric and thermomechanical fields are coupled. Therefore, the constitutive equations describe the polarization of the high symmetry dielectric materials (isotropic materials) caused by nonuniform deformation or by the temperature gradient (i.e., flexoelectric and thermopolarization effects).

The near-surface effects in nonferromagnetic isotropic dielectric solids are investigated to illustrate the efficiency of constructed theory. To this end, the equilibrium steady state of infinite bodies with plane-parallel and cylindrical surfaces (film, fiber, and infinite medium with a cylindrical hole) is studied within an isothermal approximation. The solutions to the formulated stationary problems allow us to describe the experimental data reported in the literature, namely, the near-surface inhomogeneity of electromechanical fields, the emergence of a bound electric charge on the free surfaces of the dielectric bodies, as well as the size effects of the stresses, bound electric charge, surface energy of deformation and polarization. It is established that the absolute value of the surface charge density decreases and mechanical stresses increases when thin film thickness decreases. This effect became more significant when the film thickness became comparable to the internal material length scale parameters.

As the curvature of the surface increases, its impact on the stressed state of thin fibers and on the value of the bound charge on their surfaces becomes more significant. An increase in the surface curvature of thin cylindrical fiber leads to increased levels of stresses and to a reduced density of the surface bound charge. The influence of the curvature on the surface energy of deformation and polarization depends on the curvature sign. Namely, an increase in the absolute value of a positive curvature leads to a decrease in the absolute value of this energy. For a negative curvature, this dependence is reversed.

The theory also implies the emergence of disjoining pressure in thin solid films. The existence of such pressure was previously anticipated in liquid films [Deryagin et al. 1985]. It is shown that in thin solid films, whose thickness is comparable to the internal material length scale parameters, the disjoining

pressure can appear. This pressure is proportional to the coefficient of volume dilatation caused by the local mass displacement. The absolute value of disjoining pressure increases if the mentioned coefficient increases. In light of this finding, during an investigation of the stiffness and strength of nanoscale thin films, the effect of the disjoining pressure on the abovementioned parameters should be considered.

The results obtained in the paper are general and can be useful for the design of the devices utilizing the micro/nanofilm elements.

### List of symbols

$\rho$	mass density	$J_{ef}$	density of total electric current
$\rho_{m\pi}$	density of induced mass	$J_e$	density of electric current (convection and conduction currents)
$\rho_m$	specific density of induced mass	$J_{es}$	polarization current
$\rho_{e\pi}$	density of induced charge	$J_{m*}$	density of mass flux
$\rho_e$	density of free charges	$J_{ms}$	nonconvective and nondiffusive mass flux related to local mass displacement
$T$	absolute temperature	$S_e$	flux of electromagnetic energy
$t$	time variable	$\Pi_m$	vector of local mass displacement (mass dipole moment)
$s$	specific entropy	$\Pi_e$	polarization vector
$\mathfrak{R}$	distributed heat source	$P, \hat{Q}$	dipole and quadrupole electric moments
$\eta$	entropy production	$E, H$	electric and magnetic fields
$\mathcal{E}$	total energy	$D, B$	electric and magnetic inductions
$u$	specific internal energy	$v_*$	velocity vector of convective displacement of the fixed body element
$U_e$	electromagnetic field energy	$v$	velocity vector of the center of mass
$U_\Sigma$	surface energy of deformation and polarization	$r$	position vector
$f$	Helmholtz free energy	$F$	mass forces
$\mu$	chemical potential	$F_e$	ponderomotive force
$\mu_\pi$	energy measure of the effect of the local mass displacement on the internal energy	$\hat{\sigma}$	Cauchy stress tensor
$\varphi_e$	electric potential	$\hat{e}$	infinitesimal strain tensor
$\vartheta_{se}$	density of bound electrical charge		
$J_q$	density of heat flux		

### Funding

Hrytsyna acknowledges support from the Slovak Science and Technology Assistance Agency registered under number SK-CN-RD-18-0005 and National Academy of Sciences of Ukraine (grant number 0117U004156).

### References

- [Askar et al. 1971] A. Askar, P. C. Y. Lee, and A. S. Cakmak, “The effect of surface curvature and discontinuity on the surface energy density and other induced fields in elastic dielectrics with polarization gradient”, *Int. J. Solids Struct.* **7**:5 (1971), 523–537.

- [Axe et al. 1970] J. D. Axe, J. Harada, and G. Shirane, “Anomalous acoustic dispersion in centrosymmetric crystals with soft optic phonons”, *Phys. Rev. B* **1**:3 (1970), 1227–1234.
- [Bredov et al. 1985] M. M. Bredov, V. V. Rumjantsev, and I. N. Toptyhin, *Классическая электродинамика*, Nauka, Moscow, 1985.
- [Burak et al. 2007] Y. I. Burak, V. F. Kondrat, and O. R. Hrytsyna, “Subsurface mechanoelectromagnetic phenomena in thermoelastic polarized bodies in the case of local displacements of mass”, *Mater. Sci. (Ukraine)* **43**:4 (2007), 449–463.
- [Burak et al. 2008] Y. Burak, V. Kondrat, and O. Hrytsyna, “An introduction of the local displacements of mass and electric charge phenomena into the model of the mechanics of polarized electromagnetic solids”, *J. Mech. Mater. Struct.* **3**:6 (2008), 1037–1046.
- [Burak et al. 2011] Y. Burak, V. Kondrat, and O. Hrytsyna, *Fundamentals of the local gradient theory of dielectrics*, Lira, Uzhgorod, 2011. in Ukrainian.
- [de Groot and Mazur 1962] S. R. de Groot and P. Mazur, *Non-equilibrium thermodynamics*, North-Holland, Amsterdam, 1962.
- [Deryagin et al. 1985] B. V. Deryagin, N. V. Churayev, and V. M. Muller, *Surface forces*, Nauka, Moscow, 1985. in Russian.
- [Eringen 1966] A. C. Eringen, “Linear theory of micropolar elasticity”, *J. Math. Mech.* **15**:6 (1966), 909–923.
- [Eringen 1984] A. C. Eringen, “Theory of nonlocal piezoelectricity”, *J. Math. Phys.* **25**:3 (1984), 717–727.
- [Eringen 1999] A. C. Eringen, *Microcontinuum field theories: foundations and solids*, Springer, New York, 1999.
- [Eringen 2002] A. C. Eringen, *Nonlocal continuum field theories*, Springer, New York, 2002.
- [Eringen and Suhubi 1964] A. C. Eringen and E. S. Suhubi, “Nonlinear theory of simple micro-elastic solids — I”, *Int. J. Eng. Sci.* **2**:2 (1964), 189–203.
- [Erofeyev 2003] V. I. Erofeyev, *Wave processes in solids with microstructure*, World Scientific, Singapore, 2003.
- [Kafadar 1971] C. B. Kafadar, “The theory of multipoles in classical electromagnetism”, *Int. J. Eng. Sci.* **9**:9 (1971), 831–853.
- [Kalpakides and Agiasofitou 2002] V. K. Kalpakides and E. K. Agiasofitou, “On material equations in second order gradient electroelasticity”, *J. Elasticity* **67**:3 (2002), 205–227.
- [Kalpakidis and Massalas 1993] V. K. Kalpakidis and C. V. Massalas, “Tiersten’s theory of thermoelectroelasticity: an extension”, *Int. J. Eng. Sci.* **31**:1 (1993), 157–164.
- [Kholkin et al. 1982] A. L. Kholkin, V. A. Trepakov, and G. A. Smolenskii, “Thermopolarization currents in dielectrics”, *J. Exp. Theor. Phys. Lett.* **35**:3 (1982), 103–106.
- [Kondrat and Hrytsyna 2009] V. Kondrat and O. Hrytsyna, “Linear theories of electromagnetomechanics of dielectrics”, *Phys.-Math. Model. Inf. Technol.* **9** (2009), 7–46.
- [Kondrat and Hrytsyna 2019] V. F. Kondrat and O. R. Hrytsyna, “Equations of the local gradient electromagnetothermomechanics of polarizable nonferromagnetic bodies with regard for electric quadrupole moments”, *J. Math. Sci.* **238**:2 (2019), 129–138.
- [Landau and Lifshitz 1982] L. D. Landau and E. M. Lifshitz, *Электродинамика сплошных сред*, 2nd ed., Nauka, Moscow, 1982. Translated as *Course of Theoretical Physics 8: Electrodynamics of continuous media*, Pergamon, Oxford, 1984.
- [Marchenko et al. 2009] I. G. Marchenko, I. M. Neklyudov, and I. I. Marchenko, “Collective atomic ordering processes during the low-temperature film deposition”, *Proc. Nat. Acad. Sci. of Ukraine* **10** (2009), 97–103. in Russian.
- [Maugin 1980] G. A. Maugin, “The method of virtual power in continuum mechanics: application to coupled fields”, *Acta Mech.* **35**:1-2 (1980), 1–70.
- [Maugin 1988] G. A. Maugin, *Continuum mechanics of electromagnetic solids*, vol. 33, North-Holland Series in Applied Mathematics and Mechanics, North-Holland, 1988.
- [Mead 1961] C. A. Mead, “Anomalous capacitance of thin dielectric structures”, *Phys. Rev. Lett.* **6**:10 (1961), 545–546.
- [Mindlin 1965] R. D. Mindlin, “Second gradient of strain and surface-tension in linear elasticity”, *Int. J. Solids Struct.* **1**:4 (1965), 417–438.
- [Mindlin 1968] R. D. Mindlin, “Polarization gradient in elastic dielectrics”, *Int. J. Solids Struct.* **4**:6 (1968), 637–642.

- [Mindlin 1972] R. D. Mindlin, “Elasticity, piezoelectricity and crystal lattice dynamics”, *J. Elasticity* **2**:4 (1972), 217–282.
- [Nam et al. 2006] C.-Y. Nam, P. Jaroenapibal, D. Tham, D. E. Luzzi, S. Evoy, and J. E. Fischer, “Diameter-dependent electromechanical properties of GaN nanowires”, *Nano Lett.* **6**:2 (2006), 153–158.
- [Nowacki 1983] W. Nowacki, *Efekty elektromagnetyczne w stałych ciałach odkształcalnych*, Państwowe Wydawnictwo Naukowe, Warszawa, 1983.
- [Nowacki 1986] W. Nowacki, *Theory of asymmetric elasticity*, Pergamon Press, Oxford, New York, 1986.
- [Papenfuss and Forest 2006] C. Papenfuss and S. Forest, “Thermodynamical frameworks for higher grade material theories with internal variables or additional degrees of freedom”, *J. Non Equilib. Thermodyn.* **31**:4 (2006), 319–353.
- [Tang and Alici 2011] C. Tang and G. Alici, “Evaluation of length-scale effects for mechanical behaviour of micro- and nanocantilevers: I—experimental determination of length-scale factors”, *J. Phys. D Appl. Phys.* **44**:33 (2011), 335501.
- [Ván 2003] P. Ván, “Weakly nonlocal irreversible thermodynamics”, *Ann. Phys.* **12**:3 (2003), 146–173.
- [Yang 2006] J. S. Yang, “A review of a few topics in piezoelectricity”, *Appl. Mech. Rev. (ASME)* **59**:6 (2006), 335–345.
- [Zholudev 1966] E. S. Zholudev, “Symmetry and piezoelectric properties of crystals”, *Czech. J. Phys.* **16**:5 (1966), 368–381. in Russian.

Received 1 Apr 2019. Revised 20 Aug 2019. Accepted 26 Aug 2019.

OLHA HRYTSYNA: [hrytsyna.olha@gmail.com](mailto:hrytsyna.olha@gmail.com)

*Institute of Construction and Architecture, Slovak Academy of Sciences, 9 Dúbravská cesta, 84503 Bratislava 45, Slovakia,*  
*Center of Mathematical Modelling of Pidstryhach Institute for Applied Problems of Mechanics and Mathematics,*  
*National Academy of Sciences of Ukraine, 15 D. Dudajeva St. 15, 79005 Lviv, Ukraine*

VASYL KONDRAT: [vasyl.kondrat@gmail.com](mailto:vasyl.kondrat@gmail.com)

*Center of Mathematical Modeling of the Institute of Applied Mathematics and Mechanics, National Academy of Sciences of Ukraine, 15 D. Dudajeva St. 15, 79005 Lviv, Ukraine*

## THE EFFECT OF BOUNDARY CONDITIONS ON THE LOWEST VIBRATION MODES OF STRONGLY INHOMOGENEOUS BEAMS

ONUR ŞAHİN

This paper investigates the influence of the boundary conditions on the lowest vibration modes of strongly inhomogeneous beams. It is observed that the softer component of the composite beams asymptotically contributes to an almost rigid-body motion of the stiffer parts and gives rise to one or two nonzero eigenfrequencies contrary to a single beam with free end conditions. An asymptotic procedure is employed to derive the eigenfrequencies as well as the eigenforms in the case of global low frequency regime. The developed model is adapted for two and three-component beams with different end conditions. It is also shown that all eigenforms corresponding to the stiffer components of the beams perform almost rigid body motions. Comparisons of exact and approximate solutions are presented, demonstrating the validity of the proposed approach.

### 1. Introduction

Low-frequency vibrations of inhomogeneous structural elements have been actively studied in recent years due to their numerous applications in modern engineering; see, e.g., [Le 1999; Horgan and Chan 1999]. Among the latest technological developments, composite materials, each part of which possesses high contrast mechanical and geometrical properties, have received an increased amount of attention in various fields of civil and mechanical engineering; see [Milton 2002; Elishakoff 2005]. As typical examples we refer to sandwich structures (see, e.g., [Vinson 1999; Reddy 2003; Zenkert 1995]), which are widely used in aerospace, automation, naval architecture, etc., because of their conveniently combined light weight and relatively large flexural stiffness properties; see [Kaplunov et al. 2017; Sorokin 2004]. The composite materials are also highly utilized in smart periodic structures [Ruzzene and Baz 2000]; laminated glass beams and plates [Viverge et al. 2016; Schulze et al. 2012] and photovoltaic panels [Aßmus et al. 2017]. We also mention related problem of homogenisation of periodic media [Cherednichenko et al. 2006; Smyshlyaev 2009] and multiparametric asymptotic approach for inhomogeneous layered plate; see [Kaplunov et al. 2017; Prikazchikova et al. 2018]. Metamaterials, which are employed considerably in engineering with recent technological developments, may be given as another example for multilayered structures; see [Martin et al. 2012]. Another promising application area of composite beam structures is connected with soft robotics using deformable materials to construct compliant systems; see, e.g., [Rus and Tolley 2015; Majidi 2014].

The high frequency vibrations in the multilayered structures are very inviting because they contain high energy. However, the low-frequency vibrations are more attractive due to their omnipresent character [Kudaibergenov et al. 2016]. This paper is devoted to analysis of low frequency vibrations of strongly

*Keywords:* composite beam, low frequency vibration, contrast, perturbation, rigid body motion.



piecewise inhomogeneous beams. The analysis shows that the low eigenfrequencies of the considered composite beam may be observed only when certain restrictions are imposed on the material properties such as Young moduli, densities and lengths; see [Kaplunov et al. 2016; 2019]. It can also be observed that the lowest natural frequencies tend to zero at high contrast of the material properties. An asymptotic approach relying on the concept of “almost rigid body motion” was also developed in [Kaplunov et al. 2016] for strongly inhomogeneous elastic rods. Unlike a rod that has one rigid body motion, the multicomponent beams may have two rigid body motions including translation and rotation.

The paper is organized as follows. In Section 2, a general concept for rigid body motions of a beam with different end conditions is presented. Then, the governing equations of two and three component beams with four types of end condition are introduced. The exact displacements for each problem and exact natural frequencies of two component beams are also derived. In Section 3, an asymptotic procedure is established with the help of a small parameter emerging due to high contrast of the material properties. The restrictions on the material parameters, allowing low natural frequencies, are determined. Then, the established perturbation procedure is applied to the aforementioned problems and approximate eigenfrequencies and eigenforms are obtained. Section 4 contains numerical illustrations of the approximate solutions and their comparison with the exact solutions. Conclusions are presented in the final section.

## 2. Statement of the problem

Consider a homogeneous beam with free ends. It is well known that such a beam possesses only double zero eigenfrequencies, corresponding to rigid body translation and rotation; see Figure 1a. Changing one of the free end condition of the beam with simply supported or dashed end condition results in only one nonzero small eigenfrequency corresponding rotation or translation; see Figures 1b and 1c. In the case of contact of stiff and soft components, it may be expected that the stiff component with free ends has two small eigenfrequencies arising from perturbation of zero eigenfrequencies corresponding to the limiting rigid body translation and rotation. A similar interpretation can be made for simply supported and dashed end conditions and three component beam composed of two stiff and one soft parts.

The main purpose of the paper is to investigate the effect of the end conditions on the lowest vibration modes of strongly inhomogeneous beams with the use of an asymptotic approach relying on the concept of almost rigid body motion established in [Kaplunov et al. 2016]. In order to extract the effect of boundary conditions two and three component beams with different boundary conditions will be studied.

Consider time harmonic vibrations of two and three component beams composed of alternating soft and stiff parts of arbitrary lengths with different end conditions. For each problem considered, the beams are supposed to be finite, having conventional continuity conditions between the components and have local coordinates; see Figure 2.

The governing equations for each component of the beam are written as

$$d^4 y_i / dx_i^4 - \omega^2 / a_k y_i = 0, \quad i = 1, 2, 3 \quad \text{and} \quad k = st, sf, \quad (2-1)$$

where  $y_i$  are displacements,  $\omega$  is angular frequency,  $a_k = a_{st}$  and  $a_k = a_{sf}$  correspond to stiff and soft components, respectively, with  $a_k = \sqrt{D_k / M_k}$ . Here  $D_k = E_k I$  is the flexural rigidity and  $M_k = \rho_k A$  is linear mass density with  $I$  denoting the moment of inertia and  $A$  the cross-sectional area. It is clear that all the soft components have the same Young's modulus and density.



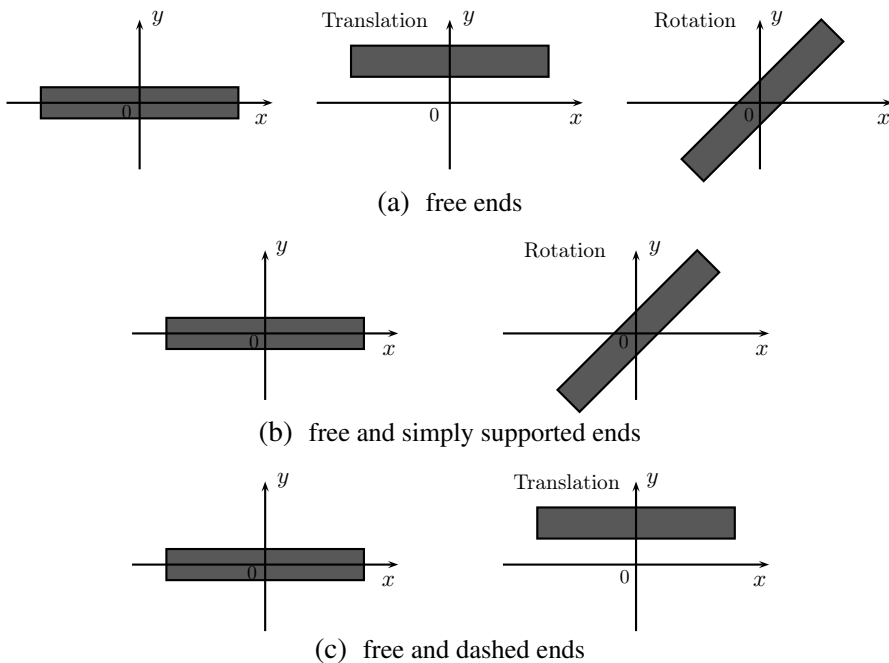


**Figure 1.** Rigid body motion of beam.

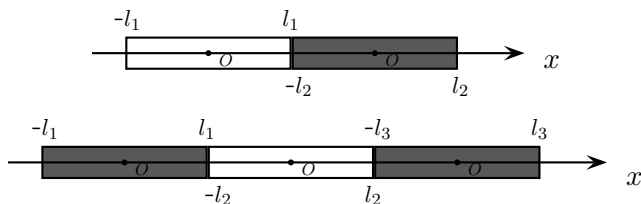


**Figure 2.** Two and three-component beams. Each 0 represents the origin of its local coordinates.

Let us first the define local dimensionless coordinates and scaled frequencies by

$$\xi_i = x_i/l_i \quad \text{and} \quad \Omega_i = l_i \sqrt{\omega/a_k}, \quad i = 1, 2, 3, \quad k = st, sf. \quad (2-2)$$

The equations of motion and the continuity conditions along the interfaces are expressed in terms of the new variables as

$$d^4 y_i / d\xi_i^4 - \Omega_i^4 y_i = 0, \quad -1 \leq \xi_i \leq 1, \quad i = 1, 2, 3, \quad (2-3)$$

and

$$y_1(1) = y_2(-1), \quad y_3(-1) = y_2(1), \quad (2-4)$$

$$y_1'(1) = (l_1/l_2)y_2'(-1), \quad y_3'(-1) = (l_3/l_2)y_2'(1), \quad (2-5)$$

$$D_{st}y_1''(1) = (l_1/l_2)^2 D_{sf}y_2''(-1), \quad D_{st}y_3''(-1) = (l_3/l_2)^2 D_{sf}y_2''(1), \quad (2-6)$$

$$D_{st}y_1'''(1) = (l_1/l_2)^3 D_{sf}y_2'''(-1), \quad D_{st}y_3'''(-1) = (l_3/l_2)^3 D_{sf}y_2'''(1). \quad (2-7)$$

In addition, we introduce the dimensionless quantities

$$D = D_{sf}/D_{st}, \quad M = M_{sf}/M_{st}, \quad a = a_{sf}/a_{st}. \quad (2-8)$$

The displacements for each component of the beam can be written from (2-3) as

$$y_i(\xi_i) = A_i \cos(\Omega_i \xi_i) + B_i \sin(\Omega_i \xi_i) + C_i \cosh(\Omega_i \xi_i) + D_i \sinh(\Omega_i \xi_i), \quad i = 1, 2, 3. \quad (2-9)$$

In the following, we will consider combinations of four types of boundary conditions, namely clamped, free, simply supported and dashed, for the two and three component beams.

In view of the development of new materials including soft robotics, the old problems for multispan beams may take another flavour because of low frequency resonances related to almost rigid body motions which are most harmful for the structures; see [Kaplunov et al. 2016; 2019; Rus and Tolley 2015; Majidi 2014]. In this context, throughout the paper, we assume that Young modulus of the stiff parts is much greater than of the soft part, i.e.,

$$\varepsilon = D_{sf}/D_{st} \ll 1 \quad (2-10)$$

is a small parameter signifying the high contrast material properties.

### 3. Asymptotic approach

In this section, an asymptotic approach is established for two and three-component beams in case of different boundary conditions. As may be seen from the previous section analytical solutions for the frequency and displacement of such problems cannot be obtained effortlessly. Therefore developing a perturbation scheme which reduces the problem to a simple boundary value problem having solutions in terms of elementary functions is highly important for analysing the frequencies and displacements. In this framework, we develop an asymptotic approach leading to the estimation of the lowest eigenfrequencies and eigenforms of the aforementioned problems.

Let us start by expanding the frequencies and displacements in the asymptotic series on using the small parameter (2-10);

$$\Omega_i^4 = \varepsilon(\Omega_{i,0}^4 + \varepsilon\Omega_{i,1}^4 + \varepsilon^2\Omega_{i,2}^4 + \cdots), \quad y_i = y_{i,0} + \varepsilon y_{i,1} + \varepsilon^2 y_{i,2} + \cdots, \quad i = 1, 2, 3. \quad (3-1)$$

which may also correspond to the low frequency regimes of the problems mentioned at the end of Section 2. Since we consider the global low frequency behaviour, i.e.,  $\Omega_1^4 \sim \Omega_2^4 \sim \Omega_3^4 \sim \varepsilon$ , the ratio of the masses and lengths have the following asymptotic equality

$$\varepsilon \frac{M_{st}}{M_{sf}} = M_*, \quad M_* \sim 1, \quad (3-2)$$

and

$$(l_1/l_2)^4 = \delta_1^4 \sim 1, \quad (l_3/l_2)^4 = \delta_3^4 \sim 1. \quad (3-3)$$

In case there are no considerable changes in the cross-sectional area  $A$ , the assumed contrast in Young's moduli and densities given in (2-10) and (3-2) occurs for photovoltaic panels; see, e.g., [Aßmus et al. 2017; Kaplunov et al. 2017; Schulze et al. 2012]. It can easily be observed from (3-1) that the scaled frequencies are also related to each other by

$$\Omega_1^4 = \Omega_2^4 \delta_1^4 M_*, \quad \Omega_3^4 = \Omega_2^4 \delta_3^4 M_*. \quad (3-4)$$

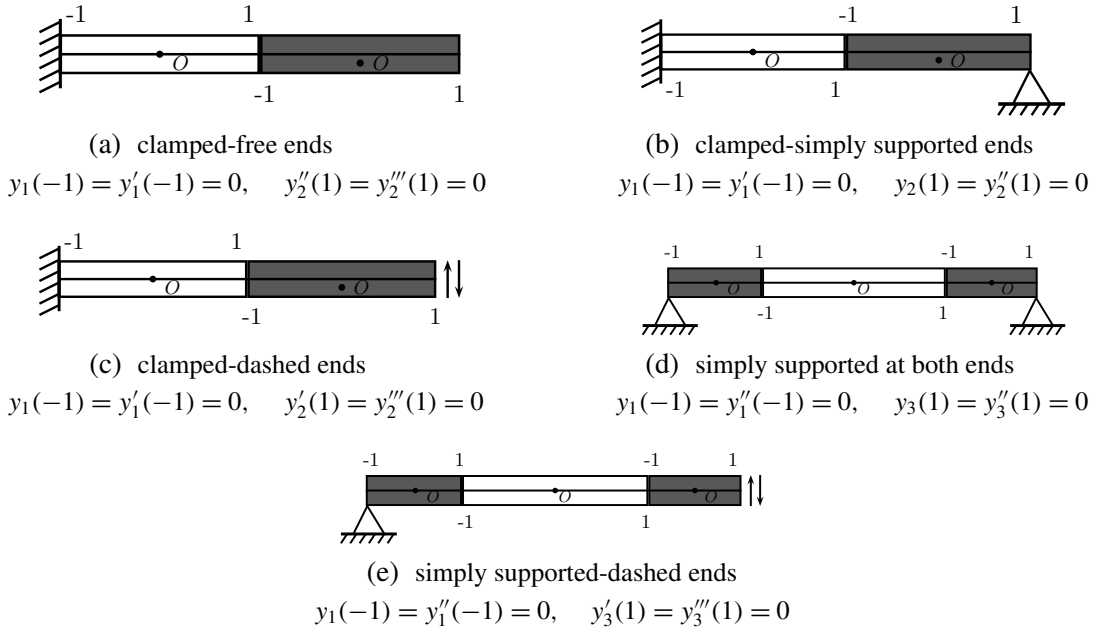


**Figure 3.** Types of boundary conditions.

**3A. Perturbation scheme for a two component beam with clamped and free ends.** We first consider the two component beam with one end clamped and other free as depicted in Figure 3a. Bearing in mind the definition of the small parameter and the relations between the lengths, see (3-3), the continuity conditions at the interfaces and the boundary conditions take, respectively, form

$$y_1(1) = y_2(-1), \quad y_1'(1) = \delta_1 y_2'(-1), \quad \varepsilon y_1''(1) = \delta_1^2 y_2''(-1), \quad \varepsilon y_1'''(1) = \delta_1^3 y_2'''(-1), \quad (3-5)$$

$$y_1(-1) = 0, \quad y_1'(-1) = 0, \quad y_2''(1) = 0, \quad y_2'''(1) = 0. \quad (3-6)$$

On substituting the asymptotic expansions (3-1) into (2-3), the equations of motion, at the leading order, become

$$\frac{d^4 y_{i,0}}{d\xi_i^4} = 0, \quad i = 1, 2. \quad (3-7)$$

Applying the asymptotic expansion for the displacements in (3-1) into equations (3-5) results in the boundary conditions

$$y_{2,0}''(\pm 1) = y_{2,0}'''(\pm 1) = 0 \quad (3-8)$$

for the stiff component. The solution of the boundary value problem (3-7) and (3-8) for the stiff component may be written as

$$y_{2,0} = A_2 \xi_2 + B_2, \quad (3-9)$$

which corresponds to the rigid body translation and rotation; see Figure 1a.

The soft part of the beam has governing equation (3-7) subject to the boundary condition

$$y_{1,0}(1) = y_{2,0}(-1), \quad y_{1,0}'(1) = \delta_1 y_{2,0}'(-1), \quad (3-10)$$

and

$$y_{1,0}(-1) = y'_{1,0}(-1) = 0. \quad (3-11)$$

Therefore, it can be easily shown from the solution of the boundary value problem (3-7) and (3-10), (3-11) that the soft component, unlike the stiff component, undergoes an inhomogeneous deformation given by

$$y_{1,0} = (\xi_1^3 - 3\xi_1 - 2)A_1 + (\xi_1^2 + 2\xi_1 + 1)B_1. \quad (3-12)$$

Using equations (3-10), (3-11) and displacements (3-9), (3-12) the coefficients of the soft and stiff displacements are related by

$$A_1 = \frac{1}{4}((1 + \delta_1)A_2 - B_2), \quad B_1 = \frac{1}{4}A_2\delta_1. \quad (3-13)$$

At next order, the problem for the stiff component of the beam is formulated as

$$\frac{d^4 y_{2,1}}{d\xi_2^4} - \Omega_{2,0}^4 y_{2,0} = 0, \quad (3-14)$$

with the boundary conditions

$$\left. \frac{d^2 y_{2,1}}{d\xi_2^2} \right|_{\xi_2=-1} = \frac{1}{\delta_1^2} \left. \frac{d^2 y_{1,0}}{d\xi_1^2} \right|_{\xi_1=1}, \quad \left. \frac{d^3 y_{2,1}}{d\xi_2^3} \right|_{\xi_2=-1} = \frac{1}{\delta_1^3} \left. \frac{d^3 y_{1,0}}{d\xi_1^3} \right|_{\xi_1=1}, \quad (3-15)$$

and

$$\left. \frac{d^2 y_{2,1}}{d\xi_2^2} \right|_{\xi_2=1} = 0, \quad \left. \frac{d^3 y_{2,1}}{d\xi_2^3} \right|_{\xi_2=1} = 0. \quad (3-16)$$

Integrating (3-14) over  $\xi_2$  ( $-1 \leq \xi_2 \leq 1$ ) results in

$$3A_1 + \Omega_{2,0}^4 \delta_1^3 B_2 = 0. \quad (3-17)$$

Next, multiplying (3-14) by  $\xi_2$  and integrating over the length of the right component gives

$$9A_1 + 3\delta_1(3A_1 + B_1) - \Omega_{2,0}^4 \delta_1^3 A_2 = 0. \quad (3-18)$$

Using the relations between the coefficients (3-13), equations (3-17) and (3-18) give the linear system of equations in  $A_2$  and  $B_2$  as

$$\begin{aligned} \frac{1}{4}(3 + \delta_1)A_2 + \frac{1}{4}(4\delta_1^3\Omega_{2,0}^4 - 3)B_2 &= 0, \\ \frac{1}{4}(9 + 2(9 + 6\delta_1 - 2\delta_1^2\Omega_{2,0}^4))A_2 - \frac{9}{4}(1 + \delta_1)B_2 &= 0. \end{aligned} \quad (3-19)$$

Simultaneous equations possess nontrivial solutions provided that the associated determinant vanishes, i.e.,

$$\frac{9}{16}\delta_1^2 - \frac{3}{2}\delta_1^3(2 + \delta_1(3 + 2\delta_1))\Omega_{2,0}^4 + \delta_1^6\Omega_{2,0}^8 = 0. \quad (3-20)$$

The frequency equation (3-20), corresponding to the second component of the beam, has two nonzero eigenfrequencies given by

$$\begin{aligned}\Omega_{2,0}^4 &= \frac{3(2\delta_1^2 + 3\delta_1 + 2 - 2(\delta_1 + 1)\sqrt{\delta_1^2 + \delta_1 + 1})}{4\delta_1^3}, \\ \Omega_{2,0}^4 &= \frac{3(2\delta_1^2 + 3\delta_1 + 2 + 2(\delta_1 + 1)\sqrt{\delta_1^2 + \delta_1 + 1})}{4\delta_1^3}.\end{aligned}\quad (3-21)$$

As might be expected, the contact of a stiff component with a soft one perturbs the double zero eigenfrequencies to two lowest eigenfrequencies associated with the almost rigid translation and rotation.

**3B. Perturbation scheme for a two component beam with clamped and simply supported ends.** Let us now study two component beam having clamped and simply supported ends. The continuity conditions (2-4)–(2-7) assume the same forms given by (3-5) and the boundary conditions are as given in Figure 3b.

In this case, the leading order boundary conditions for the stiff component are

$$y_{2,0}''(-1) = y_{2,0}'''(-1) = 0, \quad y_{2,0}(1) = y_{2,0}''(1) = 0. \quad (3-22)$$

whereas the soft component has, as boundary conditions, (3-10) and (3-11). Therefore, the leading order displacements for the considered problem are written from (3-7) as

$$y_{1,0} = (\xi_1^3 - 3\xi_1 - 2)A_1 + (\xi_1^2 + 2\xi_1 + 1)B_1, \quad y_{2,0} = A_2(\xi_2 - 1). \quad (3-23)$$

The displacements (3-23) together with (3-10) and (3-11) imply

$$A_1 = \frac{1}{4}(\delta_1 + 2)A_2, \quad B_1 = \frac{1}{4}\delta_1 A_2. \quad (3-24)$$

At next order, the problem is formulated, once again, through equations (3-14), (3-15), and end conditions

$$y_{2,1}(1) = 0, \quad \left. \frac{d^2 y_{2,1}}{d\xi_2^2} \right|_{\xi_2=1} = 0. \quad (3-25)$$

Integrating (3-14) and using the end conditions (3-15) and (3-25) together with (3-24) result in

$$4\delta_1^3 \Omega_{2,0}^4 - 3(\delta_1^2 + 3\delta_1 + 3) = 0. \quad (3-26)$$

**3C. Perturbation scheme for a two component beam with clamped and dashed ends.** We now carry our dispersion analysis on to a beam with clamped and dashed ends. Similar to the previous two cases, the boundary value problem for the stiff component at the leading order is formulated by (3-7) and

$$y_{2,0}''(-1) = y_{2,0}'''(-1) = 0, \quad y_{2,0}'(1) = y_{2,0}''(1) = 0, \quad (3-27)$$

from which displacements are obtained as

$$y_{1,0} = (\xi_1^3 - 3\xi_1 - 2)A_1, \quad y_{2,0} = A_2, \quad (3-28)$$

with relation

$$A_1 = -\frac{1}{4}A_2. \quad (3-29)$$

The next order problem for the stiff component is again formulated by equations (3-14), (3-15) and

$$\left. \frac{dy_{2,1}}{d\xi_2} \right|_{\xi_2=1} = 0, \quad \left. \frac{d^3 y_{2,1}}{d\xi_2^3} \right|_{\xi_2=1} = 0. \quad (3-30)$$

the solution of which yields

$$\delta_1^3 \Omega_{2,0}^4 - \frac{3}{4} = 0. \quad (3-31)$$

**3D. Perturbation scheme for a three component simply supported beam.** We will now present asymptotic formulas for the displacements and frequencies for a three component beam with two stiff outer components simply supported at both ends, shown in Figure 3d. Taking into account the definitions of the small parameter (2-10) and the ratios of the lengths,  $\delta_1$  and  $\delta_2$ , the continuity conditions may be rewritten from equations (2-4)-(2-7) as

$$\begin{aligned} y_1(1) &= y_2(-1), & y_3(-1) &= y_2(1), \\ y_1'(1) &= \delta_1 y_2'(-1), & y_3'(-1) &= \delta_3 y_2'(1), \\ y_1''(1) &= \varepsilon \delta_1^2 y_2''(-1), & y_3''(-1) &= \varepsilon \delta_3^2 y_2''(1), \\ y_1'''(1) &= \varepsilon \delta_1^3 y_2'''(-1), & y_3'''(-1) &= \varepsilon \delta_3^3 y_2'''(1), \end{aligned} \quad (3-32)$$

and simply supported boundary conditions at both ends are, also, as presented in Figure 3d.

On substituting the asymptotic expansions (3-1) into equations of motion (2-3) we once again arrive at the leading order (3-7). In this case, the stiff and soft components have leading order boundary conditions given by

$$\begin{aligned} y_{1,0}(-1) &= y_{1,0}'(-1) = 0, & y_{1,0}''(1) &= y_{1,0}'''(1) = 0, \\ y_{3,0}(-1) &= y_{3,0}'(-1) = 0, & y_{3,0}''(1) &= y_{3,0}'''(1) = 0, \end{aligned} \quad (3-33)$$

and

$$\begin{aligned} y_{2,0}(-1) &= y_{1,0}(1), & \delta_1 y_{2,0}'(-1) &= y_{1,0}'(1), \\ y_{2,0}(1) &= y_{3,0}(-1), & \delta_3 y_{2,0}'(1) &= y_{3,0}'(-1), \end{aligned} \quad (3-34)$$

respectively. Thus, the leading order displacements can be written as

$$y_{1,0} = A_1(\xi_1 + 1), \quad y_{2,0} = A_2 \xi_2^3 + B_2 \xi_2^2 + C_2 \xi_2 + D_2, \quad y_{3,0} = A_3(\xi_3 - 1), \quad (3-35)$$

in which the coefficients are related as

$$\begin{aligned} A_2 &= \frac{1}{4}(A_1(2 + 1/\delta_1) + A_3(2 + 1/\delta_3)), & B_2 &= \frac{1}{4}(-A_1/\delta_1 + A_3/\delta_3), \\ C_2 &= -\frac{1}{4}(A_1(6 + 1/\delta_1) + A_3(6 + 1/\delta_3)), & D_2 &= A_1(1 + 1/(4\delta_1)) - A_3(1 + 1/(4\delta_3)). \end{aligned} \quad (3-36)$$

Let us now proceed to the next order problem. For the first stiff component we have

$$\frac{d^4 y_{1,1}}{d\xi_1^4} - \Omega_{1,0}^4 y_{1,0} = 0, \quad (3-37)$$

with the boundary conditions

$$\left. \frac{d^2 y_{1,1}}{d\xi_1^2} \right|_{\xi_1=1} = \delta_1^2 \left. \frac{d^2 y_{2,0}}{d\xi_2^2} \right|_{\xi_2=-1}, \quad \left. \frac{d^3 y_{1,1}}{d\xi_1^3} \right|_{\xi_1=1} = \delta_1^3 \left. \frac{d^3 y_{2,0}}{d\xi_2^3} \right|_{\xi_2=-1}, \quad (3-38)$$

and

$$y_{1,1}(-1) = \frac{d^2 y_{1,1}}{d\xi_1^2} \Big|_{\xi_1=-1} = 0. \quad (3-39)$$

Multiplying (3-37) by  $\xi_1$  and integrating over  $-1 \leq \xi_1 \leq 1$ , taking into account equations (3-38) and (3-39), we arrive at

$$\frac{d^3 y_{1,1}}{d\xi_1^3} \Big|_{\xi_1=-1} = -6\delta_1^3 A_2 - \delta_1^2 (6A_2 - 2B_2) + \frac{2}{3} A_1 \Omega_{1,0}^4. \quad (3-40)$$

Integrating (3-38) over  $-1 \leq \xi_1 \leq 1$  and using (3-40) results in

$$9\delta_1^2 (2\delta_1 + 1) A_2 - 3\delta_1^2 B_2 - 4\Omega_{1,0}^4 A_1 = 0. \quad (3-41)$$

Similarly, we derive for the second stiff component,  $y_{3,1}$ ,

$$9\delta_3^2 (2\delta_3 + 1) A_2 + 3\delta_3^2 B_2 - 4\Omega_{3,0}^4 A_1 = 0. \quad (3-42)$$

Equations (3-41) and (3-42) with the relations between the coefficients (3-36) lead to a frequency equation given by

$$27\delta_1\delta_3(1 + \delta_1 + \delta_3)^2 - 48\delta_3(3\delta_3^2 + 3\delta_3 + 1)\Omega_{1,0}^4 - 16(3\delta_1(3\delta_1^2 + 3\delta_1 + 1) - 4\Omega_{1,0}^4)\Omega_{3,0}^4 = 0. \quad (3-43)$$

Since the frequencies are related together as

$$\Omega_{3,0}^4 / \Omega_{1,0}^4 = \delta_3^4 / \delta_1^4, \quad (3-44)$$

see (3-4),  $\Omega_{1,0}$  may be written as the roots of the frequency equation (3-43), that is

$$\Omega_{1,0}^4 = \frac{3\delta_1}{8\delta_3^3} (\delta_3^3 + 3\delta_1\delta_3^3 + 3\delta_1^2\delta_3^3 + \delta_1^3(1 + 3\delta_3(1 + \delta_3))) - \sqrt{(\delta_3^3(1 + 3\delta_1(1 + \delta_1)) + \delta_1^3(1 + 3\delta_3(1 + \delta_3)))^2 - 3\delta_1^3\delta_3^3(1 + \delta_1 + \delta_3)^2}, \quad (3-45)$$

and

$$\Omega_{1,0}^4 = \frac{3\delta_1}{8\delta_3^3} (\delta_3^3 + 3\delta_1\delta_3^3 + 3\delta_1^2\delta_3^3 + \delta_1^3(1 + 3\delta_3(1 + \delta_3))) + \sqrt{(\delta_3^3(1 + 3\delta_1(1 + \delta_1)) + \delta_1^3(1 + 3\delta_3(1 + \delta_3)))^2 - 3\delta_1^3\delta_3^3(1 + \delta_1 + \delta_3)^2}. \quad (3-46)$$

It can easily be seen that the simply supported end conditions for a three component beam do not support pure rigid body motion with zero eigenfrequencies.

**3E. Perturbation scheme for three component beam with simply supported and dashed ends.** Finally, consider a three component beam having two stiff outer and one soft central parts. Contrary to the previous problem, in this case we have simply supported and dashed end conditions, stated in Figure 3e. The continuity conditions at the interface given by (3-32) are still valid for this problem. The leading order displacements may be written as

$$y_{1,0} = A_1(\xi_1 + 1), \quad y_{2,0} = A_2\xi_2^3 + B_2\xi_2^2 + C_2\xi_2 + D_2, \quad y_{3,0} = A_3, \quad (3-47)$$

with

$$\begin{aligned} A_2 &= \frac{1}{4\delta_1} (A_1(1 + 2\delta_1) - A_3\delta_1), & B_2 &= -\frac{A_1}{4\delta_1}, \\ C_2 &= -\frac{1}{4\delta_1} (A_1(1 + 6\delta_1) - 3A_3\delta_1), & D_2 &= A_1\left(1 + \frac{1}{4\delta_1}\right) + \frac{1}{2}A_3. \end{aligned} \quad (3-48)$$

The next order problem for the first component of the beam is formulated with the equations (3-37), (3-38) and (3-39), which gives (3-41). For the next order problem of the third component of the beam we have boundary conditions (3-38) and

$$\left. \frac{dy_{3,1}}{d\xi_3} \right|_{\xi_3=1} = \left. \frac{d^3 y_{3,1}}{d\xi_3^3} \right|_{\xi_3=1} = 0. \quad (3-49)$$

Integrating the next order governing equation for  $y_{3,1}$  over  $-1 \leq \xi_3 \leq 1$  and using the boundary conditions given by (3-38) and (3-49), we get

$$3\delta_3^3 A_2 + \Omega_{3,0}^4 A_3 = 0. \quad (3-50)$$

The equations (3-41) and (3-50) together with relations (3-48) imply the following frequencies

$$\Omega_{3,0}^4 (4\Omega_{1,0}^4 - 3\delta_1(1 + 3\delta_1(1 + \delta_1))) - 3\delta_3^3 \Omega_{1,0}^4 + \frac{9}{16} \delta_1 \delta_3^3 = 0, \quad (3-51)$$

resulting in

$$\Omega_{1,0}^4 = \frac{3\delta_1}{8\delta_3} (\delta_1^3 + \delta_3 + 3\delta_1\delta_3 + 3\delta_1^2\delta_3 - \sqrt{(\delta_1^3 + \delta_3 + 3\delta_1\delta_3(1 + \delta_1))^2 - \delta_1^3\delta_3}), \quad (3-52)$$

and

$$\Omega_{1,0}^4 = \frac{3\delta_1}{8\delta_3} (\delta_1^3 + \delta_3 + 3\delta_1\delta_3 + 3\delta_1^2\delta_3 + \sqrt{(\delta_1^3 + \delta_3 + 3\delta_1\delta_3(1 + \delta_1))^2 - \delta_1^3\delta_3}). \quad (3-53)$$

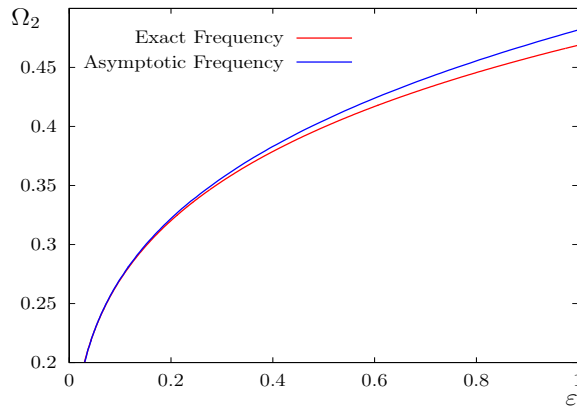
#### 4. Numerical results

In this section, we illustrate numerically the comparisons of exact and asymptotic results for all of the considered problems. Since all asymptotic estimates for the frequencies and displacements are valid in case of the global low frequency regime, the numerical comparisons are presented when the parameters are asymptotically related as  $D_{sf}/D_{st} \sim M_{sf}/M_{st} \sim \varepsilon$  and  $\delta_1 \sim \delta_2 \sim 1$ , see (3-2) and (3-3). which is a requirement for the global low frequency regime,

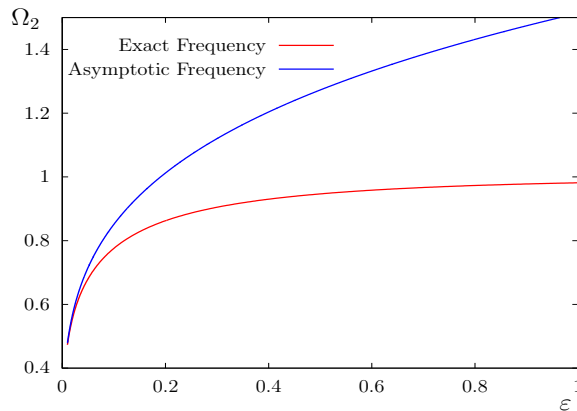
Figures 4, 5 and 6 show the exact and asymptotic curves of the frequency equation for two component beams with clamped-free, clamped-simply supported and clamped-dashed ends. In these figures in order to display more clearly the extent of the validity region of the approximation full agreement regions are chopped off. It can be easily seen from these figures that as the small parameter  $\varepsilon$  becomes smaller, which corresponds a great contrast between the stiff and soft components, the curves corresponding to the asymptotic solutions become highly compatible with the exact one. In Fig. different length components of the beam are considered, i.e.,  $l_1 = l$  and  $l_2 = 2l$  which gives  $\delta_1 = 0.5$ .

Figure 7 demonstrates the comparison of asymptotic curves of the frequency equations of two component beams given by (3-20), (3-26) and (3-31). Thus, it can be observed how the eigenfrequencies of a single beam are affected by the different boundary conditions. It is clear that the clamped-free end condition causes lowest and highest eigenfrequencies compared to other boundary conditions by perturbing the zero eigenfrequency of a beam with free-free end.





**Figure 4.** Comparison of asymptotic (3-20) and exact (6-1) frequency equations for two component beam with clamped and free ends at  $\delta_1 = 0.99$ .



**Figure 5.** Comparison of asymptotic (3-26) and exact (6-2) frequency equations for two component beam with clamped and simply supported ends at  $\delta_1 = 0.99$ .

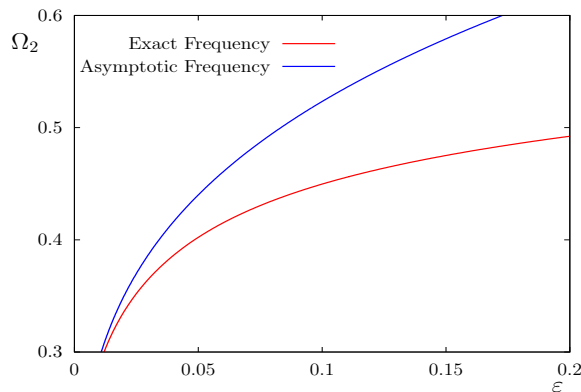


**Figure 6.** Comparison of asymptotic (3-31) and exact (6-3) frequency equations for two component beam with clamped and dashed ends at  $\delta_1 = 0.99$ .

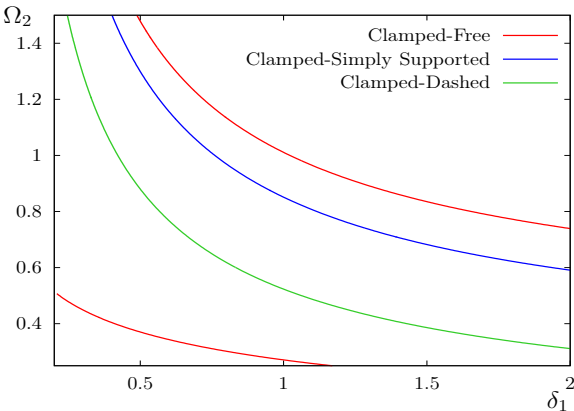


**Figure 7.** Comparison of asymptotic curves of frequency equations (3-20), (3-26) and (3-31) at  $\varepsilon = 0.1$ .

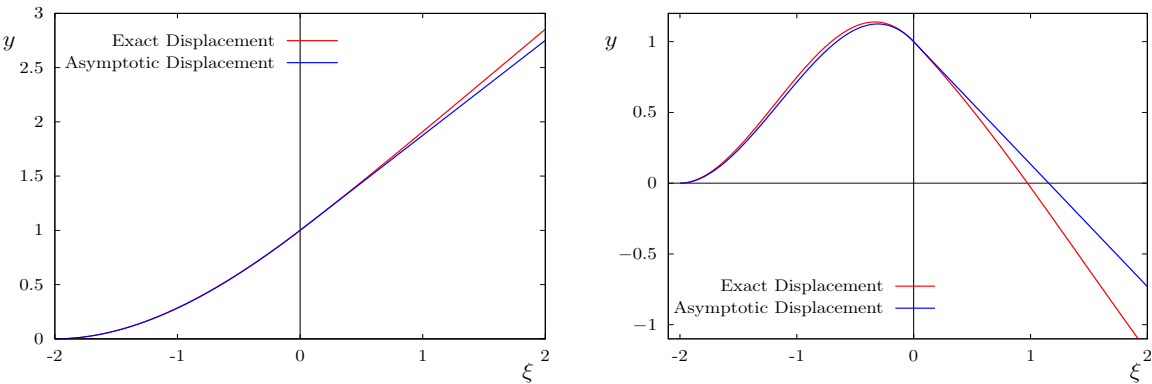


**Figure 8.** Comparison of exact (2-9), with  $i = 2$ , and asymptotic (3-9), (3-12) displacements at  $\varepsilon = 0.1$ ,  $\delta_1 = 0.99$ . Left: eigenfrequency (3-21)<sub>1</sub>. Right: eigenfrequency (3-21)<sub>2</sub>.

The exact and asymptotic scaled displacements corresponding to eigenfrequencies (3-21); (3-26) and (3-31) for the associated problems are demonstrated in Figures 8, 9 and 10. It can be observed from all these figures that even for not very small value of  $\varepsilon = 0.1$ , the asymptotic formula (3-9), (3-12); (3-23) and (3-28) present an excellent approximation to the exact displacements (2-9) with  $i = 2$ .

In Figure 11 comparisons of exact and asymptotic displacements of three component beam with simply supported at both ends are presented when the length of the components are not equal to each other, e.g.,  $\delta_1 = 1.5$  and  $\delta_2 = 1.25$ . As can be easily seen from this figure that the approximate displacement (3-35) is, again, in quite a good agreement with the exact one (2-9), with  $i = 3$ , for  $\varepsilon = 0.01$ . Similar results follow for three component beam with simply supported and dashed ends illustrated in Figure 12.

5. Concluding remarks

The low-frequency vibrations in two and three-component beams with high contrast properties have been studied. It is known that a stiff single component beam with free ends has double zero eigenfrequencies

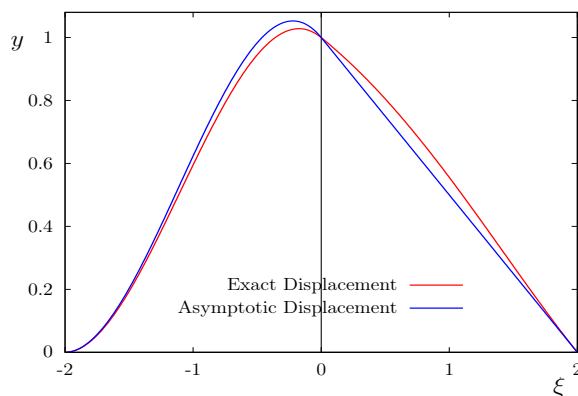


**Figure 9.** Comparison of exact (2-9), with  $i = 2$ , and asymptotic (3-23) displacements at  $\varepsilon = 0.1$ ,  $\delta_1 = 0.99$ .

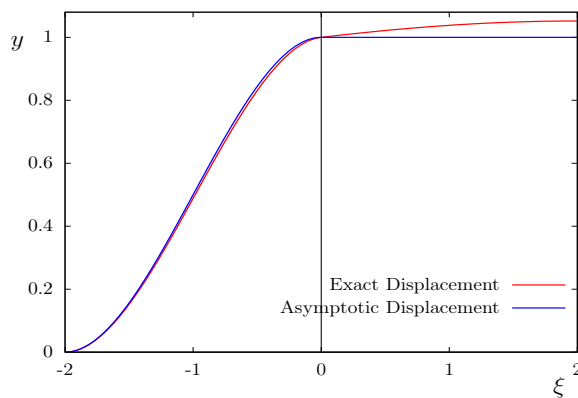


**Figure 10.** Comparison of exact (2-9), with  $i = 2$ , and asymptotic (3-28) displacements at  $\varepsilon = 0.1$ ,  $\delta_1 = 0.99$ .

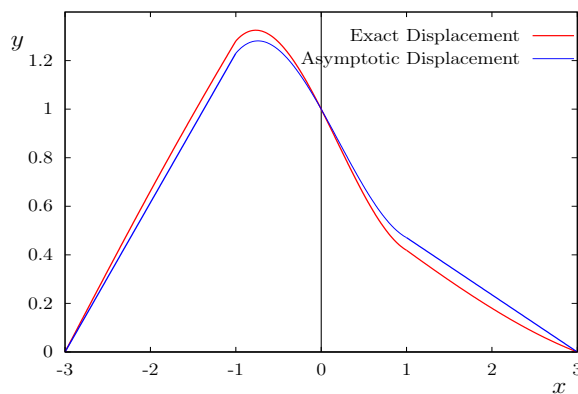


**Figure 11.** Comparison of exact (2-9), with  $i = 3$ , and asymptotic (3-35) displacements for the eigenfrequency (3-45) at  $\varepsilon = 0.01$ ,  $\delta_1 = 1.5$  and  $\delta_2 = 1.25$ .

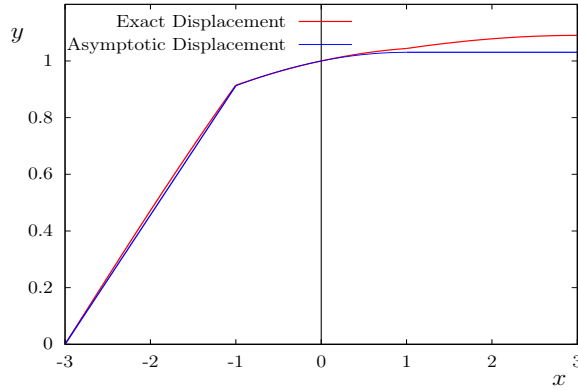


**Figure 12.** Comparison of exact (2-9), with  $i = 3$ , and asymptotic (3-47) displacements for the eigenfrequency (3-51) at  $\varepsilon = 0.01$ ,  $\delta_1 = 4$  and  $\delta_2 = 2$ .

corresponding to limiting rigid body translation and rotation. It is seen that the contact of a soft component with a stiffer one and change in the other end condition cause one or two small eigenfrequencies. It is shown that if the stiff component has a free end condition the beam possesses two nonzero lowest eigenfrequencies corresponding to almost rigid body translation and rotation of the stiff part. On the other hand, if the end condition of the stiff component is simply supported or dashed then the beam has only one lowest eigenfrequency arising from perturbation of zero eigenfrequencies, which correspond to rotation or translation. It is also demonstrated that among these three end conditions, free end condition gives the lowest and highest eigenfrequencies.

The exact formulation of eigenfrequencies and eigenforms of such problems are generally given by a sophisticated transcendental relation. Therefore an asymptotic procedure is established in order to investigate near zero frequencies and corresponding displacements. The derived asymptotic formulae are valid for certain conditions on the ratios of material and geometrical properties, which reveal the low frequency vibrations. It may also be emphasized that the approximate formulation for the leading order displacements of the stiffer parts carry out almost rigid body motion whereas the softer parts undergo almost homogeneous deformation. Another point to note is that eigenfrequencies and eigenmodes might have been calculated through a numerical procedure (such as FE method) however, in this case there is a limited potential for physical insight. In particular, there is a risk to miss low frequency eigenforms with polynomial but not expected sinusoidal behaviour.

The proposed perturbation approach may be generalised to multicomponent high-contrast structures with different end conditions including an  $n$  component strongly inhomogeneous beam. The approach may also be adapted for 2D and 3D eigenvalue problems for multilayered, high-contrast structures such as plates and shells. Multiparametric structures, in which material parameters are dependent on coordinate axis, are another promising research area which the established model can be applied.

## 6. Acknowledgement

The author gratefully acknowledges the support of Tübitak 2219 Postdoctoral Research Grant (number 1059B191700810). Fruitful discussions and insightful comments of J. Kaplunov, B. Erbaş and D. Prikazchikov are also gratefully acknowledged.

### Appendix

The frequency equations for two component beams with end conditions given in Figures 3a, 3b and 3c is given, respectively, by

$$\begin{aligned}
 & \cosh^2(\Omega_1) \left( -4 \sinh^2(\Omega_2) (\sqrt{a} \sin(\Omega_1) \cos(\Omega_2) + D \sin(\Omega_2) \cos(\Omega_1)) \right. \\
 & \quad \times (a^{3/2} \sin(\Omega_1) \cos(\Omega_2) + D \sin(\Omega_2) \cos(\Omega_1)) \\
 & \quad + 4 \cosh^2(\Omega_2) (D \cos(\Omega_1) \cos(\Omega_2) - \sqrt{a} \sin(\Omega_1) \sin(\Omega_2)) \\
 & \quad \times (D \cos(\Omega_1) \cos(\Omega_2) - a^{3/2} \sin(\Omega_1) \sin(\Omega_2)) \\
 & \quad \left. - (a-1) \sqrt{a} D \sin(2\Omega_1) \cos(2\Omega_2) \sinh(2\Omega_2) \right) \\
 & + \sinh^2(\Omega_1) \left( 4 \sinh^2(\Omega_2) (\sqrt{a} \cos(\Omega_1) \cos(\Omega_2) - D \sin(\Omega_1) \sin(\Omega_2)) \right. \\
 & \quad \times (a^{3/2} \cos(\Omega_1) \cos(\Omega_2) - D \sin(\Omega_1) \sin(\Omega_2)) \\
 & \quad - 4 \cosh^2(\Omega_2) (\sqrt{a} \sin(\Omega_2) \cos(\Omega_1) + D \sin(\Omega_1) \cos(\Omega_2)) \\
 & \quad \times (a^{3/2} \sin(\Omega_2) \cos(\Omega_1) + D \sin(\Omega_1) \cos(\Omega_2)) \\
 & \quad \left. - (a-1) \sqrt{a} D \sin(2\Omega_1) \cos(2\Omega_2) \sinh(2\Omega_2) \right) \\
 & + \sqrt{a} D \sinh(2\Omega_1) \left( \sinh(2\Omega_2) ((a+1) \cos(2\Omega_1) \cos(2\Omega_2) - 2\sqrt{a} \sin(2\Omega_1) \sin(2\Omega_2)) \right. \\
 & \quad \left. + (a-1) \sin(2\Omega_2) \cos(2\Omega_1) \cosh(2\Omega_2) \right) = 0, \quad (6-1) \\
 & \sinh(2\Omega_2) \left( \cosh(2\Omega_1) ((-a^2 - D^2) \cos(2\Omega_1) \cos(2\Omega_2) + 2\sqrt{a} D \sin(2\Omega_1) \sin(2\Omega_2)) \right. \\
 & \quad + (a-D)(a+D) \cos(2\Omega_2) \\
 & \quad + 2 \sinh(2\Omega_1) (aD \sin(2\Omega_1) \cos(2\Omega_2) + \sqrt{a} D \sin(2\Omega_2) \cos(2\Omega_1)) \\
 & \quad + 2 \cosh(2\Omega_2) \left( \sinh^2(\Omega_1) (a^{3/2} D \sin(2\Omega_1) \cos(2\Omega_2) \right. \\
 & \quad \left. + \sin(2\Omega_2) (a^2 \cos^2(\Omega_1) - D^2 \sin^2(\Omega_1))) \right. \\
 & \quad + \cosh^2(\Omega_1) (a^{3/2} D \sin(2\Omega_1) \cos(2\Omega_2) \\
 & \quad \left. + \sin(2\Omega_2) (D^2 \cos^2(\Omega_1) - a^2 \sin^2(\Omega_1))) \right. \\
 & \quad \left. + aD \sinh(2\Omega_1) (\sin(2\Omega_1) \sin(2\Omega_2) - \sqrt{a} \cos(2\Omega_1) \cos(2\Omega_2)) \right) = 0 \quad (6-2)
 \end{aligned}$$

and

$$\begin{aligned}
 & 2 \cosh^2(\Omega_1) \cosh^2(\Omega_2) \left( 2 \sin(\Omega_2) \cos(\Omega_2) (D^2 \cos^2(\Omega_1) - a^2 \sin^2(\Omega_1)) \right. \\
 & \quad \left. + \sqrt{a} D \sin(2\Omega_1) \cos(2\Omega_2) \right) \\
 & + 2 \sinh^2(\Omega_1) \cosh^2(\Omega_2) \left( 2 \sin(\Omega_2) \cos(\Omega_2) (a^2 \cos^2(\Omega_1) - D^2 \sin^2(\Omega_1)) \right. \\
 & \quad \left. + \sqrt{a} D \sin(2\Omega_1) \cos(2\Omega_2) \right) \\
 & + \sinh(\Omega_2) \left( (a^2 + D^2) \cos(2\Omega_1) \cosh(2\Omega_1) (\sin(2\Omega_2) \sinh(\Omega_2) + 2 \cos(2\Omega_2) \cosh(\Omega_2)) \right. \\
 & \quad + 2 \sqrt{a} D \sin(2\Omega_1) \cosh(2\Omega_1) (\cos(2\Omega_2) \sinh(\Omega_2) - 2a \sin(2\Omega_2) \cosh(\Omega_2)) \\
 & \quad \left. - (a-D)(a+D) (\sin(2\Omega_2) \sinh(\Omega_2) + 2 \cos(2\Omega_2) \cosh(\Omega_2)) \right)
 \end{aligned}$$

$$\begin{aligned}
& + \sqrt{a}D \sinh(2\Omega_1) (-2\sqrt{a} \sin(2\Omega_1) \sin(2\Omega_2) \cosh(2\Omega_2) \\
& \quad + 2a \sin(2\Omega_2) \cos(2\Omega_1) \sinh(2\Omega_2) \\
& \quad + 2 \cos(2\Omega_2) (\sqrt{a} \sin(2\Omega_1) \sinh(2\Omega_2) + \cos(2\Omega_1) \cosh(2\Omega_2))) = 0. \quad (6-3)
\end{aligned}$$

The related frequency equation for three component beam with simply supported both ends can be obtained from the determinant of the following  $12 \times 12$  matrix which can be obtained by applying the continuity, (2-4)–(2-7), and boundary conditions Figure 3d into the displacements (2-9).

$$\begin{pmatrix}
-c_1 & -s_1 & -ch_1 & -sh_1 & c_2 & -s_2 & ch_2 & sh_2 & 0 & 0 & 0 & 0 \\
\sqrt{a}s_1 & -\sqrt{a}c_1 & -\sqrt{a}sh_1 & -\sqrt{a}ch_1 & s_2 & c_2 & -sh_2 & ch_2 & 0 & 0 & 0 & 0 \\
ac_1 & as_1 & -ach_1 & -ash_1 & -\varepsilon c_2 & \varepsilon s_2 & \varepsilon ch_2 & -\varepsilon sh_2 & 0 & 0 & 0 & 0 \\
-a^{3/2}s_1 & a^{3/2}c_1 & -a^{3/2}sh_1 & -a^{3/2}ch_1 & -\varepsilon s_2 & -\varepsilon c_2 & -\varepsilon sh_2 & \varepsilon ch_2 & 0 & 0 & 0 & 0 \\
c_1 & -s_1 & ch_1 & -sh_1 & 0 & 0 & 0 & 0 & 0 & 0 & 0 & 0 \\
-c_1 & s_1 & ch_1 & -sh_1 & 0 & 0 & 0 & 0 & 0 & 0 & 0 & 0 \\
0 & 0 & 0 & 0 & c_2 & s_2 & ch_2 & sh_2 & -c_3 & s_3 & -ch_3 & sh_3 \\
0 & 0 & 0 & 0 & -s_2 & c_2 & sh_2 & ch_2 & -\sqrt{a}s_3 & -\sqrt{a}c_3 & \sqrt{a}sh_3 & -\sqrt{a}ch_3 \\
0 & 0 & 0 & 0 & -\varepsilon c_2 & -\varepsilon s_2 & \varepsilon ch_2 & \varepsilon sh_2 & ac_3 & -as_3 & -ach_3 & ash_3 \\
0 & 0 & 0 & 0 & \varepsilon s_2 & -\varepsilon c_2 & \varepsilon sh_2 & \varepsilon ch_2 & a^{3/2}s_3 & a^{3/2}c_3 & a^{3/2}sh_3 & -a^{3/2}ch_3 \\
0 & 0 & 0 & 0 & 0 & 0 & 0 & 0 & c_3 & s_3 & ch_3 & sh_3 \\
0 & 0 & 0 & 0 & 0 & 0 & 0 & 0 & -c_3 & -s_3 & ch_3 & sh_3
\end{pmatrix} \quad (6-4)$$

where

$$c_i = \cos(\Omega_i), \quad s_i = \sin(\Omega_i), \quad ch_i = \cosh(\Omega_i), \quad sh_i = \sinh(\Omega_i), \quad i = 1, 2, 3.$$

Since the result of the determinant is quite messy an explicit expression of the frequency equation is not presented.

The frequency equation of three component beam with simply supported and dashed ends, again, can be expressed via the determinant of the coefficient matrix, which cannot be presented straightforwardly.

## References

- [Aßmus et al. 2017] M. Aßmus, K. Naumenko, and H. Altenbach, “Mechanical behaviour of photovoltaic composite structures: influence of geometric dimensions and material properties on the eigenfrequencies of mechanical vibrations”, *Compos. Commun.* **6** (2017), 59–62.
- [Cherednichenko et al. 2006] K. D. Cherednichenko, V. P. Smyshlyaev, and V. V. Zhikov, “Non-local homogenized limits for composite media with highly anisotropic periodic fibres”, *Proc. R. Soc. Edinburgh Sect. A* **136**:1 (2006), 87–114.
- [Elishakoff 2005] I. Elishakoff, *Eigenvalues of inhomogeneous structures: unusual closed-form solutions*, CRC Press, Boca Raton, FL, 2005.
- [Horgan and Chan 1999] C. O. Horgan and A. M. Chan, “Vibration of inhomogeneous strings, rods and membranes”, *J. Sound Vib.* **225**:3 (1999), 503–513.
- [Kaplunov et al. 2016] J. Kaplunov, D. Prikazchikov, and O. Sergushova, “Multi-parametric analysis of the lowest natural frequencies of strongly inhomogeneous elastic rods”, *J. Sound Vib.* **366** (2016), 264–276.
- [Kaplunov et al. 2017] J. Kaplunov, D. A. Prikazchikov, and L. A. Prikazchikova, “Dispersion of elastic waves in a strongly inhomogeneous three-layered plate”, *Int. J. Solids Struct.* **113-114** (2017), 169–179.
- [Kaplunov et al. 2019] J. Kaplunov, D. A. Prikazchikov, L. A. Prikazchikova, and O. Sergushova, “The lowest vibration spectra of multi-component structures with contrast material properties”, *J. Sound Vib.* **445** (2019), 132–147.

- [Kudaibergenov et al. 2016] A. Kudaibergenov, A. Nobili, and L. Prikazchikova, “On low-frequency vibrations of a composite string with contrast properties for energy scavenging fabric devices”, *J. Mech. Mater. Struct.* **11**:3 (2016), 231–243.
- [Le 1999] K. C. Le, *Vibrations of shells and rods*, Springer, 1999.
- [Majidi 2014] C. Majidi, “Soft robotics, a perspective: current trends and prospects for the future”, *Soft Robot.* **1**:1 (2014), 5–11.
- [Martin et al. 2012] T. P. Martin, C. N. Layman, K. M. Moore, and G. J. Orris, “Elastic shells with high-contrast material properties as acoustic metamaterial components”, *Phys. Rev. B* **85**:16 (2012), art. id. 161103.
- [Milton 2002] G. W. Milton, *The theory of composites*, Cambridge Monogr. Appl. Comput. Math. **6**, Cambridge Univ. Press, 2002.
- [Prikazchikova et al. 2018] L. Prikazchikova, Y. E. Aydiin, B. Erbaş, and J. Kaplunov, “Asymptotic analysis of an anti-plane dynamic problem for a three-layered strongly inhomogeneous laminate”, *Math. Mech. Solids* (online publication August 2018).
- [Reddy 2003] J. N. Reddy, *Mechanics of laminated composite plates and shells: theory and analysis*, 2nd ed., CRC Press, Boca Raton, FL, 2003.
- [Rus and Tolley 2015] D. Rus and M. T. Tolley, “Design, fabrication and control of soft robots”, *Nature* **521** (2015), 467–475.
- [Ruzzene and Baz 2000] M. Ruzzene and A. Baz, “Attenuation and localization of wave propagation in periodic rods using shape memory inserts”, *Smart Mater. Struct.* **9**:6 (2000), 805–816.
- [Schulze et al. 2012] S.-H. Schulze, M. Pander, K. Naumenko, and H. Altenbach, “Analysis of laminated glass beams for photovoltaic applications”, *Int. J. Solids Struct.* **49**:15-16 (2012), 2027–2036.
- [Smyshlyaev 2009] V. P. Smyshlyaev, “Propagation and localization of elastic waves in highly anisotropic periodic composites via two-scale homogenization”, *Mech. Mater.* **41**:4 (2009), 434–447.
- [Sorokin 2004] S. V. Sorokin, “Analysis of wave propagation in sandwich plates with and without heavy fluid loading”, *J. Sound Vib.* **271**:3-5 (2004), 1039–1062.
- [Vinson 1999] J. R. Vinson, *The behavior of sandwich structures of isotropic and composite materials*, CRC Press, Boca Raton, FL, 1999.
- [Viverge et al. 2016] K. Viverge, C. Boutin, and F. Sallet, “Model of highly contrasted plates versus experiments on laminated glass”, *Int. J. Solids Struct.* **102-103** (2016), 238–258.
- [Zenkert 1995] D. Zenkert, *An introduction to sandwich construction*, EMAS, London, 1995.

Received 18 Jul 2019. Revised 13 Sep 2019. Accepted 28 Oct 2019.

ONUR ŞAHİN: [onur.sahin@giresun.edu.tr](mailto:onur.sahin@giresun.edu.tr)

Department of Mathematics, Giresun University, Güre Campus, Giresun, Turkey





# THERMAL STRESS AROUND AN ARBITRARILY SHAPED NANO HOLE WITH SURFACE ELASTICITY IN A THERMOELECTRIC MATERIAL

KUN SONG, HAO-PENG SONG, PETER SCHIAVONE AND CUN-FA GAO

In response to the significance of the role of surface mechanics in continuum models of deformation at the nanoscale, we consider the thermal stress distribution in the vicinity of an arbitrarily shaped nanohole in a thermoelectric material by incorporating the contribution of surface elasticity. Accordingly, we develop specific solutions describing the corresponding electric, temperature and elastic fields in the material. Our results indicate that the contribution of surface elasticity is to generate considerable normal and shear stress and to significantly influence hoop stress on the boundary of the nanohole. By controlling the electric current applied to the material, the normal and shear stresses induced by surface elasticity can be enhanced or decreased for various shaped nanoholes. It is also worth noting that the incorporation of surface elasticity allows for the ability to suppress the maximum value of the von Mises stress on the boundary of an arbitrarily shaped nanohole, particularly in the case of a triangular-shaped hole in which case the maximum von Mises stress can be suppressed by up to 35% thereby dramatically improving the reliability of the corresponding thermoelectric device. Our investigations provide an important theoretical basis for the design and manufacture of thermoelectric materials.

## 1. Introduction

Thermoelectric materials have the distinct capability of direct conversion between thermal and electrical energy. This particular property makes them attractive for use in a variety of fields of application including waste heat recovery [Yu et al. 2015], solid-state refrigeration [He and Tritt 2017] and solar energy harvesting [Özdemir et al. 2015]. Furthermore, thermoelectric systems are environmentally friendly in that they emit no gases, contain no pollutants, have no moving parts and operate quietly. One of the major drawbacks in the use of thermoelectric materials and the main factor in preventing thermoelectric devices from replacing traditional heat engines, however, is a low energy conversion efficiency.

The thermoelectric figure of merit  $ZT$  was introduced to characterize the conversion efficiency of thermoelectric materials and much effort has been devoted recently towards its improvement. The most effective and widely used method to improve the  $ZT$  value of a thermoelectric material involves the introduction of nanosized holes or inclusions into the thermoelectric medium. This method has achieved remarkable results in many mainstream thermoelectric materials [Yang et al. 2015; Xu et al. 2017; Kim et al. 2006] but suffers from the fact that the operation of inserting an inhomogeneity (here taken to represent a hole or inclusion) into thermoelectric materials generates an uneven temperature distribution which leads to considerable thermal stress in the vicinity of the inhomogeneity [Kim et al. 2016].

---

*Keywords:* thermoelectric material, thermal stress, arbitrarily shaped hole, surface elasticity.

The theoretical modelling of the behavior of thermoelectric materials presents formidable challenges over the modeling of simple electric conduction or heat transfer processes mainly due to the coupled transport of heat and electricity which results in nonlinear governing equations. Using complex variable methods, Song et al. [2015] have succeeded in deriving the general solution of the two-dimensional problem of a thermoelectric material containing a crack and discussed the field intensity factors at the crack tip. Soon after, Wang and Wang [2017] used the same methods to construct a theoretical model for the thermal stress distribution around an inclined elliptic hole in a thermoelectric material. Subsequently, the model of a thin infinite plate containing a circular hole with a straight crack was analyzed and the stress intensity factors near the crack tip obtained [Pang et al. 2018]. Furthermore, it has been demonstrated that the thermal stress around a functional defect can easily exceed the yield stresses of many thermoelectric materials [Song et al. 2019a]. These researches provide useful information regarding the mechanism controlling thermal stress around a macroscale hole or inhomogeneity in a thermoelectric material. The corresponding analysis focusing on a thermoelectric continuum at the nanoscale remains relatively absent from the literature.

At the nanoscale, it is well-known that surface effects significantly influence the corresponding stress distributions around an inhomogeneity as a result of the large surface-to-volume ratio of a representative material element [Attia 2017]. Acknowledging the increasingly important role of the use of nanosized inhomogeneities in improving the conversion efficiency of thermoelectric materials, it is important to study the reliability of thermoelectric continuum models at the nanoscale. To this end, in this paper we focus our attention on the thermal stress distribution in the vicinity of an arbitrarily shaped nanohole in a thermoelectric material. General solutions describing thermal-electric and thermoelastic fields are obtained via the use of complex variable methods. Our results indicate quite clearly that the incorporation of surface elasticity generates considerable normal and shear stresses on the boundary of various shaped nanoholes and that these stresses can be either increased or decreased by controlling the applied electric current depending on the shape of nanohole. Furthermore, we find that surface elasticity has also a remarkable effect on hoop stress around a nanohole and can dramatically suppress von Mises stress induced by heat flux. For example, the incorporation of surface elasticity can suppress the maximum von Mises stress around a particular triangular hole by about 35%. These results dramatically improve the reliability of the corresponding thermoelectric devices.

## 2. Governing equations

**2.1. Electric and thermal fields.** The temperature field  $T(x, y)$  and electric potential  $\phi(x, y)$  in a thermoelectric material represented by a Cartesian plane (described here by the generic point  $(x, y)$ ) are coupled through the Seebeck coefficient  $S$ . According to the theory of Thermodynamics, the equations governing the electric current density  $\mathbf{J}$ , heat flux  $\mathbf{Q}$  and energy flux  $\mathbf{U}$  are given by [Callen 1960]

$$-\mathbf{J} = \sigma \nabla \phi + \sigma S \nabla T, \quad (1)$$

$$\mathbf{Q} = T S \mathbf{J} - \kappa \nabla T, \quad (2)$$

$$\mathbf{U} = \mathbf{Q} + \phi \mathbf{J}, \quad (3)$$

where  $\sigma$  and  $\kappa$  are the electric conductivity and thermal conductivity, respectively. In the case of a conserved system, both the electric current density and energy flux are divergence-free:

$$\nabla \cdot \mathbf{J} = 0, \quad (4)$$

$$\nabla \cdot (\mathbf{Q} + \phi \mathbf{J}) = 0. \quad (5)$$

We assume that the parameters of our system are temperature-independent, so that (4)–(5) can be rewritten with the aid of (1)–(2) as

$$\nabla^2(\phi + ST) = 0, \quad (6)$$

$$\nabla^2 \left[ \frac{\sigma}{2} (\phi^2 + ST)^2 + \kappa T \right] = 0. \quad (7)$$

In the complex plane described by  $z = x + iy$  ( $i^2 = -1$ ), the temperature field and the electric potential in (6) and (7) can be expressed as [Song et al. 2018]

$$T = -\frac{\sigma}{\kappa} f(z) \overline{f(z)} + g(z) + \overline{g(z)} + M, \quad (8)$$

$$\phi = \frac{\sigma S}{\kappa} f(z) \overline{f(z)} + f(z) + \overline{f(z)} - S(g(z) + \overline{g(z)}) + N, \quad (9)$$

where  $f(z)$  and  $g(z)$  are complex analytic functions while  $M$  and  $N$  are real constants that denote uniform temperature and electric potential fields, respectively. Note that the overhead bar denotes the usual complex conjugate. Substituting (8)–(9) into (1)–(3), the components of electric current density, heat flux and energy flux can be expressed as

$$J_x - iJ_y = -2\sigma f'(z), \quad (10)$$

$$Q_x - iQ_y = 2\sigma f'(z) \left[ \frac{\sigma S}{\kappa} f(z) \overline{f(z)} + f(z) + \overline{f(z)} - S(g(z) + \overline{g(z)}) + N \right] - 2\sigma f(z) f'(z) - 2\kappa g'(z), \quad (11)$$

$$U_x - iU_y = -2\sigma f(z) f'(z) - 2\kappa g'(z). \quad (12)$$

From (8)–(12), we see that the quantities corresponding to the thermal and electric fields are governed entirely by the complex functions  $f(z)$  and  $g(z)$ . As such, the temperature distribution, electric potential, electric current, heat flow and energy flux in the thermoelectric material are known entirely if the two complex functions  $f(z)$  and  $g(z)$  are determined.

**2.2. Stress and displacement fields.** Thermal stress induced by unmatched thermal expansion in a thermoelectric material depends linearly on the thermal expansion coefficient  $\alpha$ , leading to the governing equation coupling the stress function  $\Phi$  and the temperature field  $T$  [Parkus 1968]:

$$\nabla^4 \Phi + E\alpha \nabla^2 T = 0, \quad (13)$$

where  $E$  is Young's modulus. The general solution of (13) is composed of a particular solution and the general solution of the corresponding homogeneous equation which is given as [Song et al. 2019c]

$$\Phi = \frac{1}{2} [\bar{z} \varphi(z) + z \overline{\varphi(z)} + \vartheta(z) + \overline{\vartheta(z)}] + \frac{E\alpha\sigma}{4\kappa} F(z) \overline{F(z)}, \quad (14)$$

where  $\varphi(z)$  and  $\vartheta(z)$  are complex analytic functions of  $z$ , and

$$F(z) = \int f(z) dz. \quad (15)$$

We introduce  $\psi(z)$  to represent the derivative of  $\vartheta(z)$ . The stress and displacement components  $\sigma_x, \sigma_y, \tau_{xy}$ ;  $u$  and  $v$  can then be derived from (14) as [Zhang and Wang 2016]

$$\sigma_x + \sigma_y = 4 \frac{\partial^2 \Phi}{\partial z \partial \bar{z}} = 2(\varphi'(z) + \overline{\varphi'(z)}) + \frac{E\alpha\sigma}{\kappa} f(z) \overline{f(z)}, \quad (16)$$

$$\sigma_y - \sigma_x + 2i\tau_{xy} = 4 \frac{\partial^2 \Phi}{\partial z^2} = 2(\bar{z}\varphi''(z) + \psi'(z)) + \frac{E\alpha\sigma}{\kappa} f'(z) \overline{F(z)}, \quad (17)$$

$$u + iv = \frac{1}{2G} [K\varphi(z) - z\overline{\varphi'(z)} - \overline{\psi(z)}] + 2\alpha \int g(z) dz - \frac{E\alpha\sigma}{4\kappa G} F(z) \overline{f(z)}, \quad (18)$$

where  $K = (3 - \mu)/(1 + \mu)$  for the plane stress problem while  $G$  and  $\mu$  are the shear modulus and Poisson's ratio, respectively. Note that  $E, \mu$  and  $\alpha$  are respectively replaced by  $E/(1 - \mu^2), \mu/(1 - \mu)$  and  $(1 + \mu)\alpha$  in the case of the plane strain problem.

**2.3. Surface elasticity.** The effects of surface elasticity are generally disregarded in the modelling of thermoelectric materials at the macroscale. However, it is well-known that the incorporation of surface elasticity into models of deformation significantly affects the stress distribution on the surface of a nanoinhomogeneity due to the large surface to volume ratio of a representative material element. According to the continuum theory of elastic material surfaces, the surface hoop stress  $\sigma_\theta^s$  is a critical quantity in the description of surface elasticity and depends linearly on the hoop strain  $\varepsilon_\theta^s$ , that is [Gurtin and Murdoch 1975]

$$\sigma_\theta^s = M^s \varepsilon_\theta^s, \quad (19)$$

where  $M^s = 2\mu^s + \lambda^s$  is a surface material constant incorporating  $\mu^s$  and  $\lambda^s$  which are referred to as surface Lamé constants. Noting (16)–(18),  $\varepsilon_\theta^s$  can be expressed as [Dai et al. 2017]

$$\begin{aligned} \varepsilon_\theta^s = \frac{1 - \mu}{E} \left( \varphi'(z) + \overline{\varphi'(z)} + \frac{E\alpha\sigma}{2\kappa} f(z) \overline{f(z)} \right) + \frac{\text{Re}[(\bar{z}\varphi''(z) + \psi'(z))e^{2i\theta}]}{2G} \\ + \frac{E\alpha\sigma}{4G\kappa} \text{Re}[f'(z) \overline{F(z)} e^{2i\theta}] + 2\alpha \text{Re}[g(z)], \end{aligned} \quad (20)$$

where the angle  $\theta$  is measured from the  $x$ -axis, and “Re” denotes the real part of a complex function.

### 3. Solution for infinite thermoelectric plate containing an arbitrary shaped nanohole

We consider an infinite thermoelectric plate containing an arbitrarily shaped hole bounded by a simple curve  $L$ . The plate is subjected to remote electric current density  $J_x^\infty, J_y^\infty$  and energy flux  $U_x^\infty, U_y^\infty$ . Without loss of generality, the origin of the Cartesian coordinate system is placed at the centroid of the hole, as shown in Figure 1 (left). The infinite thermoelectric matrix surrounding the hole can be mapped into the external of a unit circle  $L'$  in the image  $w$ -plane ( $w = \xi + i\eta$ ), as shown in Figure 1 (right), using

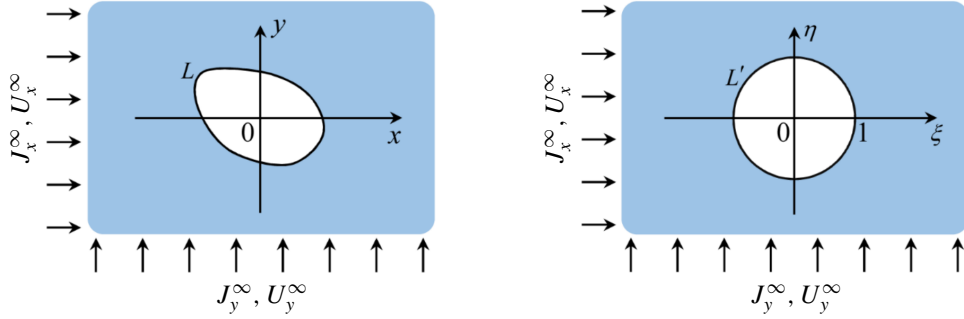


**Figure 1.** Left: infinite thermoelectric plate containing an arbitrarily shaped nanohole. Right: the image  $w$ -plane after conformal mapping.

the conformal mapping function  $\omega(w)$  given by [Muskhelishvili 1975]

$$z = \omega(w) = R \left( w + \sum_{j=1}^n m_j w^{-j} \right), \quad (21)$$

where  $R$  is real number associated with the size of hole and the complex number  $m_j$  is determined by the shape of hole.

**3.1. Boundary conditions.** We assume that the boundary of the nanohole prevents the transport of both electrons and heat, thus the boundary conditions for the normal electric current density  $J_r$  and energy flux  $U_r$  can be written as [Song et al. 2019b]

$$\int_P^Q J_r ds = 0, \quad (22)$$

$$\int_P^Q U_r ds = 0, \quad (23)$$

where  $P$  and  $Q$  are arbitrary points on  $L$ .

As stated in Section 2.3, the presence of surface elasticity influences the stress field on the surface of a nanohole. Since there is no additional loading on the boundary  $L$ , the stress boundary conditions can be expressed as [Gurtin et al. 1998]

$$\sigma_r - i \tau_{r\theta} = k \sigma_\theta^s - i \frac{d\sigma_\theta^s}{ds}, \quad (24)$$

where  $\sigma_r$  and  $\tau_{r\theta}$  are the normal and shear stresses on  $L$ , respectively, while  $k$  is the pointwise curvature along  $L$ .

**3.2. Solutions for electric and thermal fields.** The functions  $f(z)$  and  $g(z)$  can be deduced from (10) and (12) in terms of the remote current density and energy flux as

$$f(z) = -\frac{1}{2\sigma} (J_x^\infty - i J_y^\infty) z + f_0(z), \quad (25)$$

$$g(z) = -\frac{1}{8\sigma\kappa} (J_x^\infty - i J_y^\infty)^2 z^2 - \frac{1}{2\kappa} (U_x^\infty - i U_y^\infty) z + g_0(z), \quad (26)$$

where  $f_0(z)$  and  $g_0(z)$  are analytic functions in the matrix. Noting the conformal mapping function in (21) and adopting the notation that  $f(z) = f[\omega(w)]$  and  $g(z) = g[\omega(w)]$ , equations (25) and (26) can be expanded into series form as

$$f(z) = A_1 w + \sum_{j=0}^n A_{-j} w^{-j}, \quad (27)$$

$$g(z) = B_2 w^2 + B_1 w + \sum_{j=0}^n B_{-j} w^{-j}, \quad (28)$$

where

$$A_1 = -\frac{R}{2\sigma}(J_x^\infty - iJ_y^\infty), \quad B_1 = -\frac{R}{2\kappa}(U_x^\infty - iU_y^\infty), \quad B_2 = -\frac{R^2}{8\sigma\kappa}(J_x^\infty - iJ_y^\infty)^2. \quad (29)$$

Substituting (27) and (28) into the boundary conditions in (22) and (23),  $f(z)$  and  $g(z)$  can be determined as

$$f(z) = A_1 w + \frac{\bar{A}_1}{w}, \quad (30)$$

$$g(z) = B_2 w^2 + B_1 w + \frac{\bar{B}_1}{w} + \frac{\bar{B}_2}{w^2}. \quad (31)$$

The temperature, electric potential, electric current density, heat flux and energy flux around an arbitrarily shaped nanohole in a thermoelectric material can then be totally determined by substituting (30) and (31) into (8)–(12) as

$$T = -\frac{\sigma}{\kappa} \left| A_1 w + \frac{\bar{A}_1}{w} \right|^2 + 2\text{Re} \left[ B_2 w^2 + B_1 w + \frac{\bar{B}_1}{w} + \frac{\bar{B}_2}{w^2} \right] + M, \quad (32)$$

$$\phi = \frac{\sigma S}{\kappa} \left| A_1 w + \frac{\bar{A}_1}{w} \right|^2 + 2\text{Re} \left[ A_1 w + \frac{\bar{A}_1}{w} - S \left( B_2 w^2 + B_1 w + \frac{\bar{B}_1}{w} + \frac{\bar{B}_2}{w^2} \right) \right] + N, \quad (33)$$

$$J_x - iJ_y = -\frac{2\sigma}{\omega'(w)} \left( A_1 - \frac{\bar{A}_1}{w^2} \right), \quad (34)$$

$$\begin{aligned} Q_x - iQ_y = & \frac{2\sigma\phi}{\omega'(w)} \left( A_1 - \frac{\bar{A}_1}{w^2} \right) - \frac{2\sigma}{\omega'(w)} \left( A_1 w + \frac{\bar{A}_1}{w} \right) \left( A_1 - \frac{\bar{A}_1}{w^2} \right) \\ & - \frac{2\kappa}{\omega'(w)} \left( 2B_2 w + B_1 - \frac{\bar{B}_1}{w^2} - \frac{2\bar{B}_2}{w^3} \right), \end{aligned} \quad (35)$$

$$U_x - iU_y = \frac{2\sigma}{\omega'(w)} \left( A_1 w + \frac{\bar{A}_1}{w} \right) \left( \frac{\bar{A}_1}{w^2} - A_1 \right) - \frac{2\kappa}{\omega'(w)} \left( 2B_2 w + B_1 - \frac{\bar{B}_1}{w^2} - \frac{2\bar{B}_2}{w^3} \right), \quad (36)$$

where  $\omega'(w) = d\omega(w)/dw$ .

**3.3. Solution for stress distributions.** Substituting (30) and (31) into (16)–(18), the thermal stress and displacement in the matrix can be expressed as

$$\sigma_x + \sigma_y = \frac{E\alpha\sigma}{\kappa} \left| A_1 w + \frac{\bar{A}_1}{w} \right|^2 + 2(\varphi'(z) + \overline{\varphi'(z)}), \quad (37)$$

$$\sigma_y - \sigma_x + 2i\tau_{xy} = \frac{E\alpha\sigma(A_1 w^2 - \bar{A}_1)}{\kappa w^2 \omega'(w)} \int \left[ \left( \bar{A}_1 \bar{w} + \frac{A_1}{\bar{w}} \right) \overline{\omega'(w)} \right] d\bar{w} + 2(\bar{z}\varphi''(z) + \psi'(z)), \quad (38)$$

$$u + iv = 2\alpha \int \left[ \left( B_2 w^2 + B_1 w + \frac{\bar{B}_1}{w} + \frac{\bar{B}_2}{w^2} \right) \omega'(w) \right] dw + \frac{1}{2G} (K\varphi(z) - z\overline{\varphi'(z)} - \overline{\psi(z)}) - \frac{E\alpha\sigma}{4\kappa G} \left( \bar{A}_1 \bar{w} + \frac{A_1}{\bar{w}} \right) \int \left[ \left( A_1 w + \frac{\bar{A}_1}{w} \right) \omega'(w) \right] dw, \quad (39)$$

while the hoop strain in (20) can be expressed as

$$\begin{aligned} \varepsilon_\theta^s = & \frac{1-\mu}{E} \left( \varphi'(z) + \overline{\varphi'(z)} + \frac{E\alpha\sigma}{2\kappa} \left| A_1 w + \frac{\bar{A}_1}{w} \right|^2 \right) + \frac{\operatorname{Re}[(\bar{z}\varphi''(z) + \psi'(z))e^{2i\theta}]}{2G} \\ & + \frac{E\alpha\sigma}{4G\kappa} \operatorname{Re} \left[ \frac{(A_1 w^2 - \bar{A}_1)}{w^2 \omega'(w)} \int \left[ \left( \bar{A}_1 \bar{w} + \frac{A_1}{\bar{w}} \right) \overline{\omega'(w)} \right] d\bar{w} e^{2i\theta} \right] \\ & + 2\alpha \operatorname{Re} \left[ B_2 w^2 + B_1 w + \frac{\bar{B}_1}{w} + \frac{\bar{B}_2}{w^2} \right]. \end{aligned} \quad (40)$$

The integrations in (38)–(40) will generate multivalued terms which can be eliminated by introducing additional terms in  $\varphi(z)$  and  $\psi(z)$  as

$$\varphi(z) = \chi_1 \ln w + \sum_{j=1}^n C_{-j} w^{-j}, \quad (41)$$

$$\psi(z) = \chi_2 \ln w + \sum_{j=1}^n D_{-j} w^{-j}. \quad (42)$$

Here, we have disregarded  $C_0$  and  $D_0$  in (41) and (42) since they correspond to rigid displacement and thus do not influence the stresses. Noting (21), the coefficients of the multivalued terms are now identified as

$$\begin{cases} \chi_1 = \frac{4G\alpha R}{\kappa+1} (m_1 B_1 + 2m_2 B_2 - \bar{B}_1), \\ \chi_2 = \bar{\chi}_1 + \frac{E\alpha\sigma R}{2\kappa} (A_1 - m_1 \bar{A}_1) \left( A_1 w + \frac{\bar{A}_1}{w} \right). \end{cases} \quad (43)$$

Rewriting the boundary condition in (24), we have [Dai et al. 2016]

$$\varphi(z) + z\overline{\varphi'(z)} + \overline{\psi(z)} + \frac{E\alpha\sigma}{2\kappa} \overline{f(z)} F(z) = M^s \varepsilon_\theta^s e^{i\theta}. \quad (44)$$

Substituting (40)–(42) into (44), and noting that

$$e^{i\theta} = \frac{w\omega'(w)}{\rho|\omega'(w)|}, \quad e^{2i\theta} = \frac{w^2\omega'(w)}{\rho^2\overline{\omega'(w)}}, \quad (45)$$

we have

$$\begin{aligned}
& \varphi(w) + \frac{\omega(w)}{\omega'(w)} \overline{\varphi'(w)} + \overline{\psi(w)} + \frac{E\alpha\sigma}{2\kappa} \overline{f(w)} F(w) \\
&= M^s \left\{ \frac{1-\mu}{E} \left( \frac{w}{|\omega'(w)|} \varphi'(w) + \frac{w\omega'(w)}{|\omega'(w)|\overline{\omega'(w)}} \overline{\omega'(w)} + \frac{E\alpha\sigma}{2\kappa} \frac{w\omega'(w)}{|\omega'(w)|} |f(w)|^2 \right) \right. \\
&\quad + 4G \left( \frac{w^3}{\omega'(w)} \varphi''(w) - \frac{w^3\omega''(w)}{\omega'(w)} \varphi'(w) + \frac{w^3\omega'(w)}{|\omega'(w)|\overline{\omega'(w)}} \psi'(w) \right. \\
&\quad \left. + \frac{\omega(w)}{w|\omega'(w)|\overline{\omega'(w)}} \overline{\varphi''(w)} - \frac{\omega(w)\overline{\omega''(w)}}{w|\omega'(w)|\overline{\omega'(w)}} \overline{\varphi'(w)} + \frac{1}{w|\omega'(w)|} \overline{\psi'(w)} \right) \\
&\quad - \frac{E\alpha\sigma}{8G\kappa} \frac{w\omega'(w)}{|\omega'(w)|\overline{\omega'(w)}} (A_1 w^2 - \bar{A}_1) \int \left[ \left( \frac{A_1}{w} + \frac{\bar{A}_1}{w^3} \right) \bar{w} \left( \frac{1}{w} \right) \right] dw \\
&\quad + \frac{8\alpha\sigma}{8G\kappa} \frac{(\bar{A}_1 - A_1 w^2)}{w|\omega'(w)|} \int \left[ \left( A_1 w + \frac{\bar{A}_1}{w} \right) \omega'(w) \right] dw \\
&\quad \left. + 2\alpha \frac{w\omega'(w)}{|\omega'(w)|} \operatorname{Re} \left[ B_2 w^2 + B_1 w + \frac{\bar{B}_1}{w} + \frac{\bar{B}_2}{w^2} \right] \right\}. \quad (46)
\end{aligned}$$

We introduce Fourier series expansions for the  $w$ -related terms as

$$\begin{cases} \frac{1}{\omega'(w)} = \sum_{j=-n'}^{n'} \left( \frac{1}{2\pi} \int_0^{2\pi} \frac{\zeta^{-j}}{\omega'(\zeta)} d\theta \right) w^j, \\ \frac{1}{|\omega'(w)|} = \sum_{j=-n'}^{n'} \left( \frac{1}{2\pi} \int_0^{2\pi} \frac{\zeta^{-j}}{|\omega'(\zeta)|} d\theta \right) w^j, \\ \frac{1}{|\omega'(w)|\overline{\omega'(w)}} = \sum_{j=-n'}^{n'} \left( \frac{1}{2\pi} \int_0^{2\pi} \frac{\zeta^{-j}}{|\omega'(\zeta)|\overline{\omega'(\zeta)}} d\theta \right) w^j, \end{cases} \quad (47)$$

where  $\zeta = e^{i\theta}$ , and  $n'$  is selected to cover the highest power of  $w$  in (46). Since the multivalued terms in (46) will cancel each other on  $L$ , the stress boundary condition is successfully written in terms of Fourier series using (47). Equating coefficients of  $w^j$  ( $j = -n, \dots, -1, 1, \dots, n$ ) in (46), we arrive at a system of equations with respect to  $C_{-j}$  and  $D_{-j}$  ( $j = 1, \dots, n$ ). Solving this system numerically, the complex functions  $\varphi(z)$  and  $\psi(z)$  are determined completely.

#### 4. Numerical analyses and discussion

Numerical analysis is undertaken to illustrate the distribution of thermal stress around the nanohole using the material parameters listed in Table 1. For illustrative purposes, we consider the stresses around an elliptic hole, an approximately triangular hole (which we refer to as a ‘triangular hole’) and an approximately square hole (similarly referred to as a ‘square hole’) and prescribe remote electric current and energy flux in the  $y$ -direction. The conformal mapping functions corresponding to the three shapes are given by [Savin 1961]

$$\begin{cases} \omega(w) = R(w + 1/3w), & \text{elliptic hole,} \\ \omega(w) = R(w + 1/3iw^2), & \text{triangular hole,} \\ \omega(w) = R(w - 1/8w^3), & \text{square hole,} \end{cases} \quad (48)$$



sample	$\sigma$ (S/m)	$S$ ( $\mu$ V/K)	$\kappa$ (W/mK)	$E$ (GPa)	$\alpha$ (/K)	$\mu$	$M^s$ (N/m)
PbTe	$10^4$	300	1.5	58	$2 \cdot 10^{-5}$	0.29	10

**Table 1.** Material parameters of samples [Pei and Liu 2012; Ni et al. 2010].

with the area of these holes given by

$$s = \pi R^2(1 - jm_j^2), \quad (49)$$

where  $j$  corresponds to  $w^{-j}$  appearing in the conformal mapping function, and  $m_j$  is the coefficient of  $w^{-j}$ .

Comparing the state of stress around a macrohole, we can see that the surface elasticity mainly induces normal and shear stresses on the boundary of a nanohole. Consequently, we focus our investigation on the effect of electric current on the normal and shear stresses induced by surface elasticity for holes of different shapes as described in figures 2–4. In order to compare the stress fields for different shapes of hole, we set the area of each hole to be uniform at  $s = 3 \text{ nm}^2$  and subject the thermoelectric material to a remote energy flux given by  $U_y^\infty = 10^{-6} \text{ W/nm}^2$ . For the case of an elliptic hole, the maximum positive and negative normal stresses induced by surface elasticity appear at the locations  $\theta = 0.1\pi$  and  $-0.1\pi$ , respectively, while the maximum shear stress appears at  $\theta = 0$  (see Figure 2). The remote electric current has considerable influence on the normal stress, but no influence on the shear stress. In addition, our results also show that the remote electric current has the capability of suppressing the absolute value of the negative normal stress and enhancing the positive normal stress around an elliptic hole.

For the same conditions used in Figure 2, the surface elasticity generates more than 10 times the normal and shear stresses on the boundary of a triangular hole than the on the boundary of an elliptic hole (see Figure 3). With the increase of remote electric current density, the maximum normal and shear stresses transfer from the lower boundary ( $-\pi/2 < \theta < 0$ ) to the upper boundary ( $0 < \theta \leq \pi/2$ ) of a triangular hole and the maximum normal stress is enhanced by a factor of 3 when the remote electric current density changes from 0 to  $2 \cdot 10^{-6} \text{ A/nm}^2$ . In contrast to the elliptic hole, the maximum shear stress does not occur at the tip (the point of maximum curvature) of a triangular hole, as we can see from Figure 3 (right). It is worth pointing out from Figure 3 (right) that an appropriate electric current density can suppress the maximum shear stress on the boundary of the triangular hole. The remote electric

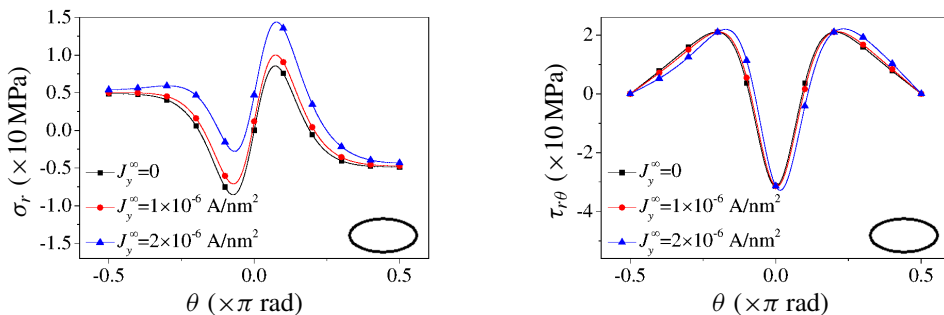


**Figure 2.** Normal stress (left) and shear stress (right) on the boundary of an elliptic hole.

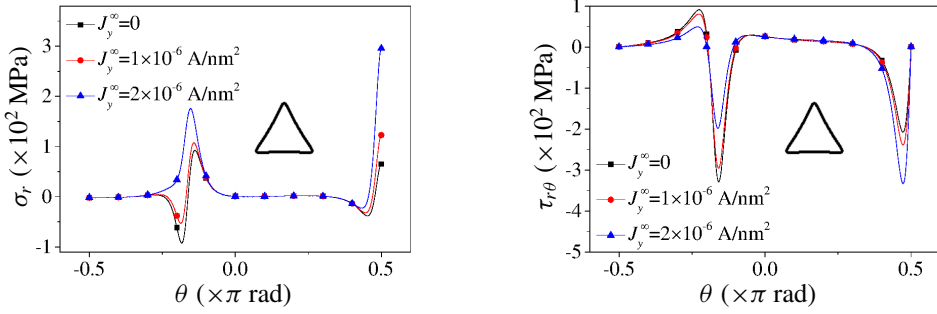


**Figure 3.** Normal stress (left) and shear stress (right) on the boundary of a triangular hole.

current suppresses maximum shear stress when  $J_y^\infty = 10^{-6}$  A/nm<sup>2</sup> but enhances maximum shear stress for the case when  $J_y^\infty = 2 \cdot 10^{-6}$  A/nm<sup>2</sup>.

The normal and shear stresses around a square hole under various values of electric current are shown in Figure 4. Comparing with figures 2 and 3 we see that the maximum normal and shear stresses induced by surface elasticity around a square hole are higher than the maximum stress around an elliptic hole although much lower than the case of a triangular hole which corresponds with the order of their maximum curvatures. Figure 4 (left) shows that the electric current greatly enhances the normal stress on the lower boundary yet suppresses normal stress on the upper boundary of a square hole. In contrast, the electric current decreases and increases shear stress on the lower and upper boundary of a square hole, respectively, as shown in Figure 4 (right).

In Figure 5,  $\sigma_r^{(1)}$  and  $\tau_{r\theta}^{(1)}$  are the maximum normal and shear stresses on  $L$  when  $R = 1$  nm. In figures 5 and 6, we further investigate the effect of surface elasticity on thermal stress with hole size. The value of the prescribed energy flux is adjusted to control the maximum temperature difference on the boundary of the hole at 1 K and the applied electric current density is adjusted to the optimal value around the hole. As is clear from Figure 5 (left), all of the maximum normal stresses decrease sharply with the increase in  $R$ , and tend to zero when  $R = 20$  nm. The size of the hole has a stronger influence on the maximum normal stress around a square hole than on that around a triangular hole. Figure 5 (right) shows that the maximum shear stresses on the boundaries of elliptic and square holes decrease with the increase of  $R$ , which is the same as for normal stress. However, in the case of a triangular hole, the maximum shear stress increases in the initial phase of the increase in size of the hole: this is because the maximum shear

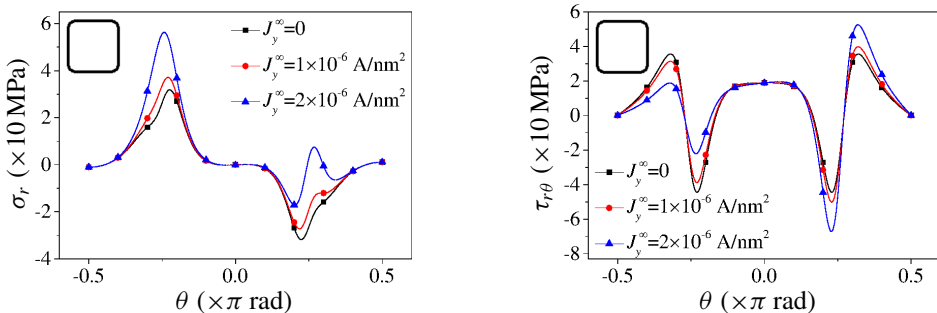


**Figure 4.** Normal stress (left) and shear stress (right) on the boundary of a square hole.

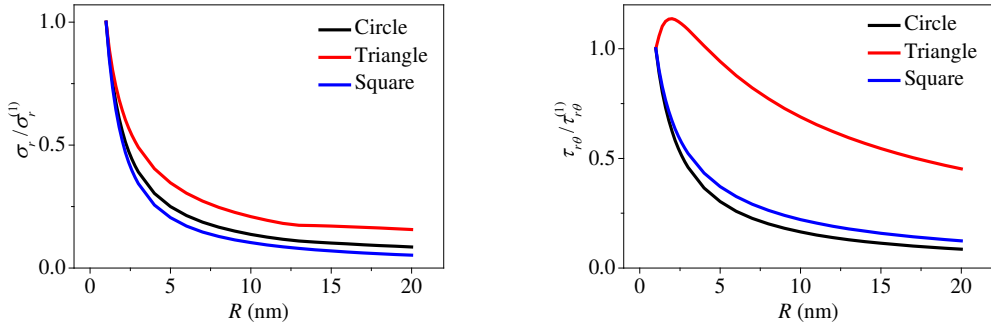


**Figure 5.** Maximum normal stress (left) and shear stress (right) versus  $R$  for different shaped holes.

stress occurs at the point of lower curvature on the boundary of triangular hole. With further increase of  $R$ , the effect of surface elasticity fades away, thus leading to a decrease of shear stresses for all shapes of hole.

In Figure 6,  $\sigma_\theta^{(0)}$  and  $\sigma_v^{(0)}$  are the maximum hoop and von Mises stresses on  $L$  when  $M^s = 0$ . We see from Figure 6 that surface elasticity has the ability to suppress maximum hoop stress induced by heat flux around nanoholes. This effect is more obvious around a triangular hole where the maximum hoop stress can be decreased by more than 50% as a result of surface elasticity. Even for the case of a square hole, the contribution of surface elasticity can decrease the maximum hoop stress by about 20%. Since the von Mises fracture criterion is often used in semiconductors, we also illustrate the effect of hole size on the von Mises stress  $\sigma_v$  using the expression [Yang 1980]:

$$\sigma_v = \sqrt{\sigma_x^2 - \sigma_x \sigma_y + \sigma_y^2 + 3\tau_{xy}^2}. \quad (50)$$

From Figure 6 (right) we see that surface elasticity can effectively suppress the maximum von Mises stress for all shapes of nanoholes. However, a particular size of nanohole is required for maximum effectiveness. For example, when  $R = 2.5$  nm, the maximum von Mises stress generated by the heat flux is reduced by no more than 65% around a triangular hole.

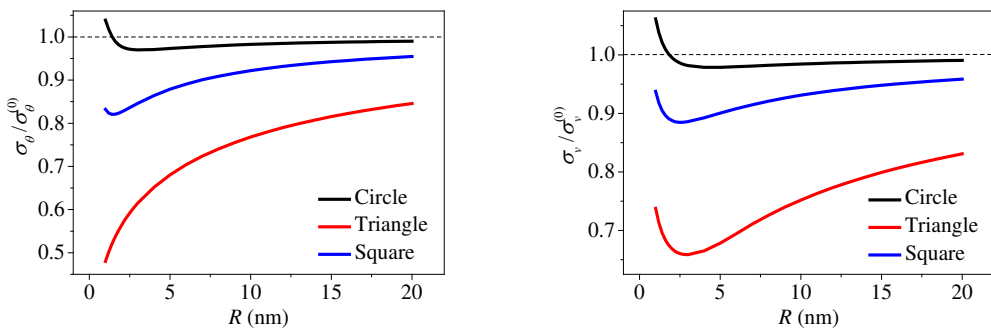


**Figure 6.** Maximum hoop stress (left) and von Mises stress (right) versus  $R$  for different shaped holes.

## 5. Conclusions

In this paper, we analyze the effect of surface elasticity on the thermal stress distribution around an arbitrarily shaped nanohole in a thermoelectric material. The electric, thermal and elastic fields in the matrix surrounding the nanohole are calculated based on complex variable methods. For a given area of nanohole, the surface elasticity generates higher normal and shear stresses around a triangular hole, but lower stresses around an elliptic hole which corresponds to the sequence of maximum curvature of the different hole shapes. The applied remote electric current can enhance or suppress the effect of surface elasticity on the thermal stress, depending on the shape and position of the boundary of the nanoholes. Detailed results show that surface elasticity has the ability of suppressing maximum hoop stress induced by heat flux around a nanohole, thus leading to significant reduction in von Mises stress. Accompanied by the appropriately chosen size of hole, surface elasticity can suppress the maximum von Mises stress around a triangular hole only by around 65%.

## Acknowledgements

K. Song appreciates the support of the China Scholarship Council. H.-P. Song and Gao acknowledge the support of the National Natural Science Foundation of China (Grant no. 11872203 and 11202099), the Priority Academic Program Development of Jiangsu Higher Education Institutions (PAPD). Schiavone thanks the Natural Sciences and Engineering Research Council of Canada for their support through a Discovery Grant (Grant no. RGPIN 155112).

## References

- [Attia 2017] M. A. Attia, “[On the mechanics of functionally graded nanobeams with the account of surface elasticity](#)”, *Int. J. Eng. Sci.* **115** (2017), 73–101.
- [Callen 1960] H. B. Callen, *Thermodynamics: an introduction to the physical theories of equilibrium thermostatics and irreversible thermodynamics*, John Wiley & Sons, New York, 1960.
- [Dai et al. 2016] M. Dai, P. Schiavone, and C.-F. Gao, “[Uniqueness of neutral elastic circular nano-inhomogeneities in antiplane shear and plane deformations](#)”, *J. Appl. Mech. (ASME)* **83**:10 (2016), 101001.
- [Dai et al. 2017] M. Dai, C.-F. Gao, and P. Schiavone, “[Closed-form solution for a circular nano-inhomogeneity with interface effects in an elastic plane under uniform remote heat flux](#)”, *IMA J. Appl. Math.* **82**:2 (2017), 384–395.
- [Gurtin and Murdoch 1975] M. E. Gurtin and A. I. Murdoch, “[A continuum theory of elastic material surfaces](#)”, *Arch. Ration. Mech. Anal.* **57**:4 (1975), 291–323.
- [Gurtin et al. 1998] M. E. Gurtin, J. Weissmüller, and F. Larché, “[A general theory of curved deformable interfaces in solids at equilibrium](#)”, *Philos. Mag. A* **78**:5 (1998), 1093–1109.
- [He and Tritt 2017] J. He and T. M. Tritt, “[Advances in thermoelectric materials research: looking back and moving forward](#)”, *Science* **357**:6358 (2017), eaak9997.
- [Kim et al. 2006] W. Kim, J. Zide, A. Gossard, D. Klenov, S. Stemmer, A. Shakouri, and A. Majumdar, “[Thermal conductivity reduction and thermoelectric figure of merit increase by embedding nanoparticles in crystalline semiconductors](#)”, *Phys. Rev. Lett.* **96**:4 (2006), 045901.
- [Kim et al. 2016] H. S. Kim, T. Wang, W. Liu, and Z. Ren, “[Engineering thermal conductivity for balancing between reliability and performance of bulk thermoelectric generators](#)”, *Adv. Funct. Mater.* **26**:21 (2016), 3678–3686.
- [Muskhelishvili 1975] N. I. Muskhelishvili, *Some basic problems of the mathematical theory of elasticity*, Noordhoff, Leyden, 1975.

- [Ni et al. 2010] J. E. Ni, E. D. Case, K. N. Khabir, R. C. Stewart, C.-I. Wu, T. P. Hogan, E. J. Timm, S. N. Girard, and M. G. Kanatzidis, “Room temperature Young’s modulus, shear modulus, Poisson’s ratio and hardness of PbTe–PbS thermoelectric materials”, *Mater. Sci. Eng. B* **170**:1–3 (2010), 58–66.
- [Özdemir et al. 2015] A. E. Özdemir, Y. Köysal, E. Özbaş, and T. Atalay, “The experimental design of solar heating thermoelectric generator with wind cooling chimney”, *Energy Convers. Manag.* **98** (2015), 127–133.
- [Pang et al. 2018] S.-J. Pang, Y.-T. Zhou, and F.-J. Li, “Analytic solutions of thermoelectric materials containing a circular hole with a straight crack”, *Int. J. Mech. Sci.* **144** (2018), 731–738.
- [Parkus 1968] H. Parkus, *Thermoelasticity*, Blaisdell Publishing Company, Waltham, Massachusetts, 1968.
- [Pei and Liu 2012] Y.-L. Pei and Y. Liu, “Electrical and thermal transport properties of Pb-based chalcogenides: PbTe, PbSe, and PbS”, *J. Alloy. Compd.* **514** (2012), 40–44.
- [Savin 1961] G. N. Savin, *Stress concentration around holes*, Pergamon Press, New York, 1961.
- [Song et al. 2015] H.-P. Song, C.-F. Gao, and J. Li, “Two-dimensional problem of a crack in thermoelectric materials”, *J. Therm. Stresses* **38**:3 (2015), 325–337.
- [Song et al. 2018] K. Song, H. P. Song, and C. F. Gao, “Improving compatibility between thermoelectric components through current refraction”, *Chin. Phys. B* **27**:7 (2018), 077304.
- [Song et al. 2019a] H. Song, K. Song, and C. Gao, “Temperature and thermal stress around an elliptic functional defect in a thermoelectric material”, *Mech. Mater.* **130** (2019), 58–64.
- [Song et al. 2019b] K. Song, H. P. Song, M. Li, P. Schiavone, and C. F. Gao, “Effective properties of a thermoelectric composite containing an elliptic inhomogeneity”, *Int. J. Heat Mass Transf.* **135** (2019), 1319–1326.
- [Song et al. 2019c] K. Song, H. P. Song, P. Schiavone, and C. F. Gao, “Electric current induced thermal stress around a bi-material interface crack”, *Eng. Fract. Mech.* **208** (2019), 1–12.
- [Wang and Wang 2017] P. Wang and B. L. Wang, “Thermoelectric fields and associated thermal stresses for an inclined elliptic hole in thermoelectric materials”, *Int. J. Eng. Sci.* **119** (2017), 93–108.
- [Xu et al. 2017] B. Xu, M. T. Agne, T. Feng, T. C. Chasapis, X. Ruan, Y. Zhou, H. Zheng, J.-H. Bahk, M. G. Kanatzidis, G. J. Snyder, and Y. Wu, “Nanocomposites from solution-synthesized PbTe–BiSbTe nanoheterostructure with unity figure of merit at low-medium temperatures (500–600 K)”, *Adv. Mater.* **29**:10 (2017), 1605140.
- [Yang 1980] W. H. Yang, “A generalized von Mises criterion for yield and fracture”, *J. Appl. Mech. (ASME)* **47**:2 (1980), 297–300.
- [Yang et al. 2015] L. Yang, Z. G. Chen, M. Hong, G. Han, and J. Zou, “Enhanced thermoelectric performance of nanostructured Bi<sub>2</sub>Te<sub>3</sub> through significant phonon scattering”, *ACS Appl. Mater. Interfaces* **7**:42 (2015), 23694–23699.
- [Yu et al. 2015] S. Yu, Q. Du, H. Diao, G. Shu, and K. Jiao, “Start-up modes of thermoelectric generator based on vehicle exhaust waste heat recovery”, *Appl. Energy* **138** (2015), 276–290.
- [Zhang and Wang 2016] A. B. Zhang and B. L. Wang, “Explicit solutions of an elliptic hole or a crack problem in thermoelectric materials”, *Eng. Fract. Mech.* **151** (2016), 11–21.

Received 5 Aug 2019. Accepted 9 Sep 2019.

KUN SONG: [ksong3@ualberta.ca](mailto:ksong3@ualberta.ca)

State Key Laboratory of Mechanics and Control of Mechanical Structures, Nanjing University of Aeronautics and Astronautics, Nanjing, 210016, China

HAO-PENG SONG: [hpsong@nuaa.edu.cn](mailto:hpsong@nuaa.edu.cn)

Department of Software Engineering, Nanjing University of Aeronautics and Astronautics, Nanjing, 210016, China

PETER SCHIAVONE: [pschiavo@ualberta.ca](mailto:pschiavo@ualberta.ca)

Department of Mechanical Engineering, University of Alberta, 10-203 Donadeo Innovation Center for Engineering, 9211-116 Street NW, Edmonton AB T6G 1H9, Canada

CUN-FA GAO: [cfgao@nuaa.edu.cn](mailto:cfgao@nuaa.edu.cn)

State Key Laboratory of Mechanics and Control of Mechanical Structures, Nanjing University of Aeronautics and Astronautics, Nanjing, 210016, China



# SUBMISSION GUIDELINES

## ORIGINALITY

Authors may submit manuscripts in PDF format online at the Submissions page. Submission of a manuscript acknowledges that the manuscript is original and has neither previously, nor simultaneously, in whole or in part, been submitted elsewhere. Information regarding the preparation of manuscripts is provided below. Correspondence by email is requested for convenience and speed. For further information, write to [contact@msp.org](mailto:contact@msp.org).

## LANGUAGE

Manuscripts must be in English. A brief abstract of about 150 words or less must be included. The abstract should be self-contained and not make any reference to the bibliography. Also required are keywords and subject classification for the article, and, for each author, postal address, affiliation (if appropriate), and email address if available. A home-page URL is optional.

## FORMAT

Authors can use their preferred manuscript-preparation software, including for example Microsoft Word or any variant of  $\text{\LaTeX}$ . The journal itself is produced in  $\text{\LaTeX}$ , so accepted articles prepared using other software will be converted to  $\text{\LaTeX}$  at production time. Authors wishing to prepare their document in  $\text{\LaTeX}$  can follow the example file at [www.jomms.net](http://www.jomms.net) (but the use of other class files is acceptable). At submission time only a PDF file is required. After acceptance, authors must submit all source material (see especially Figures below).

## REFERENCES

Bibliographical references should be complete, including article titles and page ranges. All references in the bibliography should be cited in the text. The use of Bib $\text{\TeX}$  is preferred but not required. Tags will be converted to the house format (see a current issue for examples); however, for submission you may use the format of your choice. Links will be provided to all literature with known web locations; authors can supply their own links in addition to those provided by the editorial process.

## FIGURES

Figures must be of publication quality. After acceptance, you will need to submit the original source files in vector format for all diagrams and graphs in your manuscript: vector EPS or vector PDF files are the most useful. (EPS stands for Encapsulated PostScript.)

Most drawing and graphing packages—Mathematica, Adobe Illustrator, Corel Draw, MATLAB, etc.—allow the user to save files in one of these formats. Make sure that what you’re saving is vector graphics and not a bitmap. If you need help, please write to [graphics@msp.org](mailto:graphics@msp.org) with as many details as you can about how your graphics were generated.

Please also include the original data for any plots. This is particularly important if you are unable to save Excel-generated plots in vector format. Saving them as bitmaps is not useful; please send the Excel (.xls) spreadsheets instead. Bundle your figure files into a single archive (using zip, tar, rar or other format of your choice) and upload on the link you been given at acceptance time.

Each figure should be captioned and numbered so that it can float. Small figures occupying no more than three lines of vertical space can be kept in the text (“the curve looks like this:”). It is acceptable to submit a manuscript with all figures at the end, if their placement is specified in the text by means of comments such as “Place Figure 1 here”. The same considerations apply to tables.

## WHITE SPACE

Forced line breaks or page breaks should not be inserted in the document. There is no point in your trying to optimize line and page breaks in the original manuscript. The manuscript will be reformatted to use the journal’s preferred fonts and layout.

## PROOFS

Page proofs will be made available to authors (or to the designated corresponding author) at a Web site in PDF format. Failure to acknowledge the receipt of proofs or to return corrections within the requested deadline may cause publication to be postponed.



<b>Extended higher-order sandwich panel theory for plates with arbitrary aspect ratios</b>	<b>FAISAL SIDDIQUI and GEORGE A. KARDOMATEAS</b>	<b>449</b>
<b>Applications of extended higher order sandwich panel theory for plates with arbitrary aspect ratios</b>	<b>FAISAL SIDDIQUI and GEORGE A. KARDOMATEAS</b>	<b>461</b>
<b>Instabilities in the free inflation of a nonlinear hyperelastic toroidal membrane</b>	<b>SAIRAM PAMULAPARTHI VENKATA and PRASHANT SAXENA</b>	<b>473</b>
<b>Plane strain polar elasticity of fibre-reinforced functionally graded materials and structures</b>	<b>KONSTANTINOS P. SOLDATOS, METIN AYDOGDU and UFUK GUL</b>	<b>497</b>
<b>Integrated modelling of tool wear and microstructural evolution internal relations in friction stir welding with worn pin profiles</b>	<b>ZHAO ZHANG and ZHIJUN TAN</b>	<b>537</b>
<b>Local gradient theory for thermoelastic dielectrics: accounting for mass and electric charge transfer due to microstructure changes</b>	<b>OLHA HRYTSYNA and VASYL KONDRAT</b>	<b>549</b>
<b>The effect of boundary conditions on the lowest vibration modes of strongly inhomogeneous beams</b>	<b>ONUR ŞAHİN</b>	<b>569</b>
<b>Thermal stress around an arbitrary shaped nanohole with surface elasticity in a thermoelectric material</b>	<b>KUN SONG, HAO-PENG SONG, PETER SCHIAVONE and CUN-FA GAO</b>	<b>587</b>